SYNTHESIS AND RHEOLOGY OF POLY(LACTIDE)S AND THEIR LIGNIN

COMPOSITES

by

Love-Ese Chile

B.Sc. (Hons), The University of Auckland, 2011

A THESIS SUBMITTED IN PARTIAL FULFILLMENT OF

THE REQUIREMENTS FOR THE DEGREE OF

DOCTOR OF PHILOSOPHY

in

THE FACULTY OF GRADUATE AND POSTDOCTORAL STUDIES

(Chemistry)

THE UNIVERSITY OF BRITISH COLUMBIA

(Vancouver)

August 2017

Abstract

Synthetic plastics were first introduced 180 years ago, but the materials we have produced are likely to persist on our earth for thousands of years. Global shifts in thinking have urged researchers to focus their attention on bio-derived and biodegradable polymers. One such polymer is poly(lactic acid) (PLA). Despite its environmental benefits, PLA has several material weaknesses which hinder it's use as a replacement for commodity plastics.

Highly active and selective indium catalysts for the ring-opening polymerization of lactide isomers have recently been developed by the Mehrkhodavandi group. By utilizing these catalysts, modification of tacticity and end-group functionality of PLAs are possible, permitting exploration into the effect of these modifications on chain interactions in PLA. The thermal and rheological behaviours of PLAs with different microstructures were compared. The molecular weight between entanglements was greatest for the syndiotactically enriched PLAs, giving rise to the lowest zero-shear viscosity. In addition, hetero- and isotactically enriched PLA had higher flow activation energies than syndiotactic variants, implying the inclusion of transient aggregate regions within these polymers due to enhanced L- and D-interactions.

A series of aryl-capped PLAs were synthesized by living ring-opening polymerization with a chain transfer agent using a previously reported dinuclear indium catalyst, $[(NNO)InCl]_2(\mu\text{-Cl})(\mu\text{-OEt})$ (**A**). Thermal, rheological and mechanical techniques were employed to understand the extent and strength of association caused by arylated chain ends. It is shown that the end-group has a greater effect on the properties of low molecular weight PLAs due to the larger number density of aryl end groups; significant interactions can be induced under oscillatory shear conditions in the low frequency flow regime (terminal zone).

The lignocellulosic biorefinery industry has been expanding in recent years and now provides researchers access to a range of bio-based composite materials through blending and copolymerization. Lignin-*graft*-PLA copolymers were synthesized *via* different routes and the PLA products were analyzed. Polymers were found to have cyclic structures at low lignin loading and star-like structures at higher lignin loading. Rheological studies were undertaken to derive useful structure-property relationships and optimize material properties.

Lay Summary

Synthetic plastics were first introduced 180 years ago, but the materials we have produced are likely to persist on our earth for thousands of years. Global shifts in thinking have urged researchers to focus their attention on bio-derived and biodegradable polymers. One such polymer is poly(lactic acid) (PLA). This multidisciplinary thesis links organometallic catalysis with polymer technology. The aim is to take a broader view of a research question and use what we find to create efficient catalytic systems where modifications to PLA can be easily made, and will impart useful properties in a predictable way, allowing PLA to be used wider array of consumer applications.

Preface

The work in Chapters 2 and 3 is based on a manuscript published in the journal *Macromolecules*.[1] All experiments in these two chapters were conducted by myself. The manuscript was written by myself with significant contributions from Prof. Parisa Mehrkhodavandi and Prof. Savvas G. Hatzikiriakos.

The synthesis and solution characterization of metal complexes $[(NNO)InCl]_2(\mu\text{-}Cl)(\mu\text{-}OPh_{OMe})$ (**1**), $[(NNO)InCl]_2(\mu\text{-}Cl)(\mu\text{-}OPh_{Br})$ (**4**), and $[(NNO)InCl]_2(\mu\text{-}Cl)(\mu\text{-}OPh_{NO2})$ (**5**) using one methodology in Chapter 4, was carried out by undergraduate researcher Alan Wong who was supervised by me. I completed the synthesis and characterization of the remaining metal complexes in this chapter, as well as performing all the polymerization studies. Crystals suitable for single-crystal x-ray diffraction were obtained by Alan Wong (for the three complexes previously mentioned) or myself, and the crystal structures presented in Chapter 4 were run and solved by Dr. Dinesh Aluthge, Dr. Brian Patrick and Tannaz Ebrahimi. This work has been published in *Dalton Transactions.*[2] The manuscript was written by myself with significant contributions from Prof. Parisa Mehrkhodavandi and Prof. Savvas G. Hatzikiriakos.

The work in Chapter 5 has been submitted for publication. All the experiments and data analysis in this chapter was completed by myself. The manuscript was written by myself with significant contributions by Prof. Parisa Mehrkhodavandi and Prof. Savvas G. Hatzikiriakos. All the experiments in Chapter 6 were conducted by myself. This work has not been published and the chapter was entirely written by myself.

Table of Contents

List of Tables

List of Figures

List of Schemes

List of Symbols

$[OH]_{lig}$	hydroxy concentration in lignin (mmol g^{-1})
$[\eta]$	intrinsic viscosity
a_T	horizontal shift factor
$Đ$	dispersity
δ	phase angle
$E_{a,flow}$	activation of flow energy (kJ mol^{-1})
ε_H	Hencky shear rate
γ	strain
$\dot{\gamma}$	strain rate
G'	storage modulus (Pa)
G''	loss modulus (Pa)
$|G^*|$	complex modulus (Pa)
G_N^0	plateau modulus (Pa)
η	viscosity
η^*	complex viscosity (Pa.s)
η_0	zero-shear viscosity (Pa.s)
η_E^+	extensional viscosity (Pa.s)
λ_{ave}	average relaxation time (s)
M_e	entanglement molecular weight (g mol^{-1} or kg mol^{-1})
M_n	number-average molecular weight (g mol^{-1} or kg mol^{-1})
$M_{n,GPC}$	molecular weight by GPC (g mol^{-1} or kg mol^{-1})
M_w	weight-average molecular weight (g mol^{-1} or kg mol^{-1})
$M_{n,theo}$	theoretical molecular weight (g mol^{-1} or kg mol^{-1})
ρ	density (g cm^{-3})
P_i	probability of a iso linkage within a PLA chain
P_m	probability of a meso linkage within a PLA chain
ppm	parts per million
P_r	probability of a racemic linkage within a PLA chain
P_s	probability of a syndio linkage within a PLA chain
R	gas constant (J K^{-1} mol^{-1})
R_h	hydrodynamic radius (nm)
τ	stress
T	temperature (°C or K)
T_g	glass transistion temperature (°C)
T_m	melting temperature (°C)
T_{onset}	degradation onset temperature (°C)
T_{ref}	reference temperature (°C)
T_{total}	complete degradation temperature (°C)
ω	angular frequency (rad s^{-1} or s^{-1})
wt%	weight percent

List of Abbreviations

1,5-NapOH	1,5-naphthalenediol
1,8-NapOH	1,8-naphthalenediol
a-	atactic
ATRP	atom transfer radical polymerization
biPhOH	biphenol
BnOH	benzyl alcohol
CEC	chain-end control
CTA	chain transfer agent
DACH	diaminocyclohexane
DCM	dichloromethane
diClPhOH	dichlorophene
DMF	dimethylformamide
eq.	equivalents
ESC	enantiomorphic site control
G	guaiacyl lignin residue
GPC	gel permentation chromatography
H	*para*-hydroxyphenol lignin residue
h-	heterotactic
HOMeAnth	hydrxymethylanthracene
HOMePyr	hydroxymethylpyrene
i-	isotactic
IAL	indulin AT kraft lignin
iROP	immortal ring-opening polymerization
KL	kraft lignin
LA	lactide
LDPE	low density poly(ethylene)
LiP	lignin peroxidase
LVE	linear viscoelastic
MALDI-ToF MS	matrix assisted laser desorption ionization time of flight mass spectroscopy
NapOH	naphthol
Oct	octanoate
PCL	poly(caprolactone)
PDLA	poly(D-lactide)
PDLLA	poly(D,L- lactide)
PE	poly(ethylene)
PET	poly(ethylene terephthalate)
PHB	poly(hydroxybutyrate)
PhOH	phenol

PLA	poly(lactide)
PLA-Cl	chloro end-capped PLA
PLLA	poly(L-lactide)
PMMA	poly(methyl methacrylate)
PP	poly(propylene)
PS	poly(styrene)
RIU	refractive index unit
ROP	ring-opening polymerization
S	syringyl lignin residue
s-	syndiotactic
SAOS	small amplitude oscillatory shear
SER	Sentmanat Extensional Rheometer
TBD	triazabicyclodecene
TGA	thermal gravimetric analysis
THF	tetrahydrofuran
TMB	1,3,5-trimethoxybenzene
TMDP	2-chloro-4,4,5,5-tetramethyl-1,3,2-dioxaphospholane
Upy	ureidopyrimidinone

Acknowledgements

My time spent completing this doctoral degree has been the most challenging and enriching experience of my life so far. Through the ups-and-downs I have discovered my strengths, my weaknesses and my passions. I am so happy to have this chance to express my gratitude that I did not have to do it alone.

First to my research supervisor Prof. Parisa Mehrkhodavandi, who took me into her group and through her example and guidance I learnt how to succeed in this academic setting. I am so grateful not only for her patience with my youthful idealism, but also for her constant support of my ideas for new projects and initiatives. Without her backing, I would not have had the courage to attempt a multi-disciplinary research project or had the many opportunities to engage with our community about the causes I believe in.

I would like to express deep gratitude to my co-supervisor Prof. Savvas G. Hatzikiriakos who exposed me to a whole new field of inquiry that has given me a deeper understanding of polymeric materials. With his support, I have gained an array of skills which will help me continue to connect communities and bridge the gap between fundamental and applied scientists.

A huge thank you to the members of my research groups; the old guard, Dr. Insun Yu, Dr. Kim Osten, Dr. Dinesh Aluthge, Dr. Mahmoud Ansari, and Molly Sung, who welcomed me into the group and helped me develop my fundamental laboratory techniques; as well as the avant-garde, Emiliya Mamleeva, Alex Kremer, Steve Chang, Tanja Tomkovic, Carlos Diaz Lopez, Xiaofang Zhai, and Hyuk Joon Jung, who were great colleagues and even better friends. I would like to recognize Tannaz Ebrahimi with whom I shared the experience of stepping into a completely new scientific discipline. I would like to thank her for her support in teaching me polymer rheology and her encouragement when the new subject got particularly confusing. I also

had the opportunity to work with some very bright undergraduate researchers, Garion Hicks, Sam Kaser, Thales Oliveira and Alan Wong who taught me both patience and the joy of mentoring.

Thank you to my parents Rebecca and Love Chile, who supported me not only with their generosity but also with their love and experience. And to my brothers, Denen and Junior Chile, and Slade Young, in them I see reflections of myself and who I strive to be.

Being so far away from home, I came to find a new family of friends. With Elise Caron, Maria Cleveland, Nick Hein, Jan Kozicky, Kaitlyn Lovering, Brenna Milne, and Janet Ochola, I commiserated my tribulations and celebrated my triumphs. Thank you for sharing with me both tears and laughter.

"Only love can hurt like this."

To my brother, my nephew, my uncle, and all those we honour by creating a sustainable future.

Chapter 1: General introduction.

1.1 Biopolymers

Modern society has become inextricably entwined with plastics.[3] Since 1839, with the development of vulcanized rubber by Goodyear, and Eduard Simons' discovery of poly(styrene), synthetic polymeric materials have been integrated into every technological advancement across all industries. Designed to have strength, elasticity and durability, synthetic polymers have solved more problems than they have caused.[4] However, the issues associated with their use, such as environmental persistence,[5,6] non-renewable feedstocks,[7] lack of disposal methods[8] and toxicity,[9,10] have long been said to outweigh the benefits of their on-going use.[3]

The new paradigm of biorefineries[11,12] has emerged from a wide-spread shift in focus to develop circular economies[13] and materials made from renewable resources.[14] Based on the conversion of biomass to chemical building blocks, there is potential to empower local and regional economies by creating new industries, through which materials can be synthesized and manufactured within a recovery cycle.

This re-thinking has led to the investigation of renewable polymers[15] (*i.e.* polymers derived mostly or entirely from biomass)[15,16] and biodegradable polymers (*i.e.* polymers which are capable of being decomposed by bacteria or other living organisms).[17] A review of the literature reveals four major categories of exploration: biomass-derived polymers, monomers from microbial production, monomers from renewable sources and monomers from non-renewable sources. Each of these categories have been extensively studied, but for this thesis two of these "biopolymers" will be discussed, poly(lactide) and lignin (Figure 1.1).
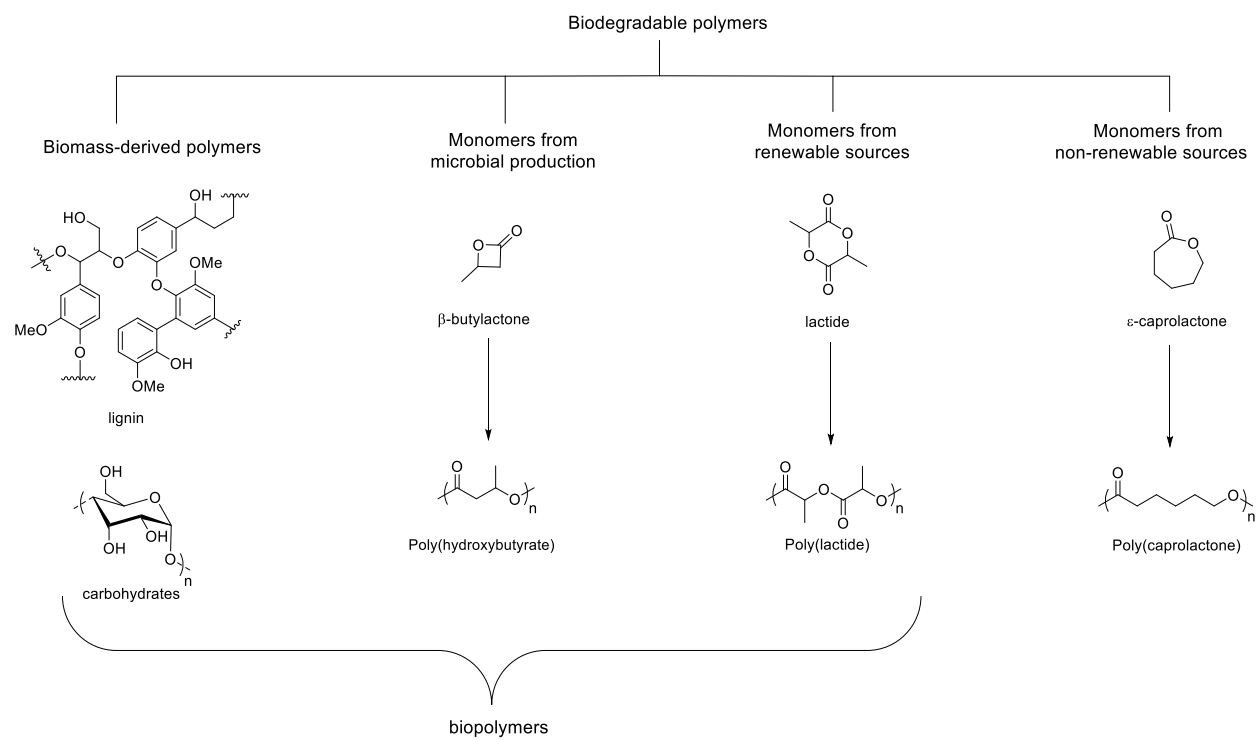
Figure 1.1 Four categories of biodegradable polymers found in the literature.[17]

1.1.1 Poly(lactide): Synthesis, characterization, biodegradation and application.

Poly(lactide), or PLA, is a biodegradable polymer whose ester linkages are inherently susceptible to hydrolysis and subsequent degradation.[18] The use of PLA has various advantages including, production from renewable agricultural sources, recyclability *via* hydrolysis or alcoholysis,[19] reduction of land-fill levels and ability to tailor physical properties by material modification.[20-26]

The linear monomer, lactic acid (2-hydroxy propionic acid) is produced industrially *via* homofermentation of carbohydrates such as glucose or lactose, found in beet sugar and corn starch.[27,28] High production yields of lactic acid have been attained when using bacteria from the *Lactobacillus* genus, which have become the industry standard.[29,30] Fermentation occurs under low oxygen concentration, at pH and temperatures of around 5.4 - 6.4 and 38 - 42 °C, respectively.[28,29]

PLA is commonly synthesized *via* two routes: a) polycondensation of lactic acid or b) ring-opening polymerization (ROP) of the cyclic dimer, lactide (LA) (Figure 1.2).[28] Direct polycondensation of lactic acid gives low molecular weight PLA, which is prone to hydrolysis by water generated in the reaction. Due to its low molecular weight, this material is not useful for many commercial applications.[29] Azeotropic distillation processes remove water from the reaction as it is generated, and have been used industrially to achieve high molecular weight PLA from lactic acid. However, this process requires the use of solvents and is energy intensive, making it less economically viable.[18]
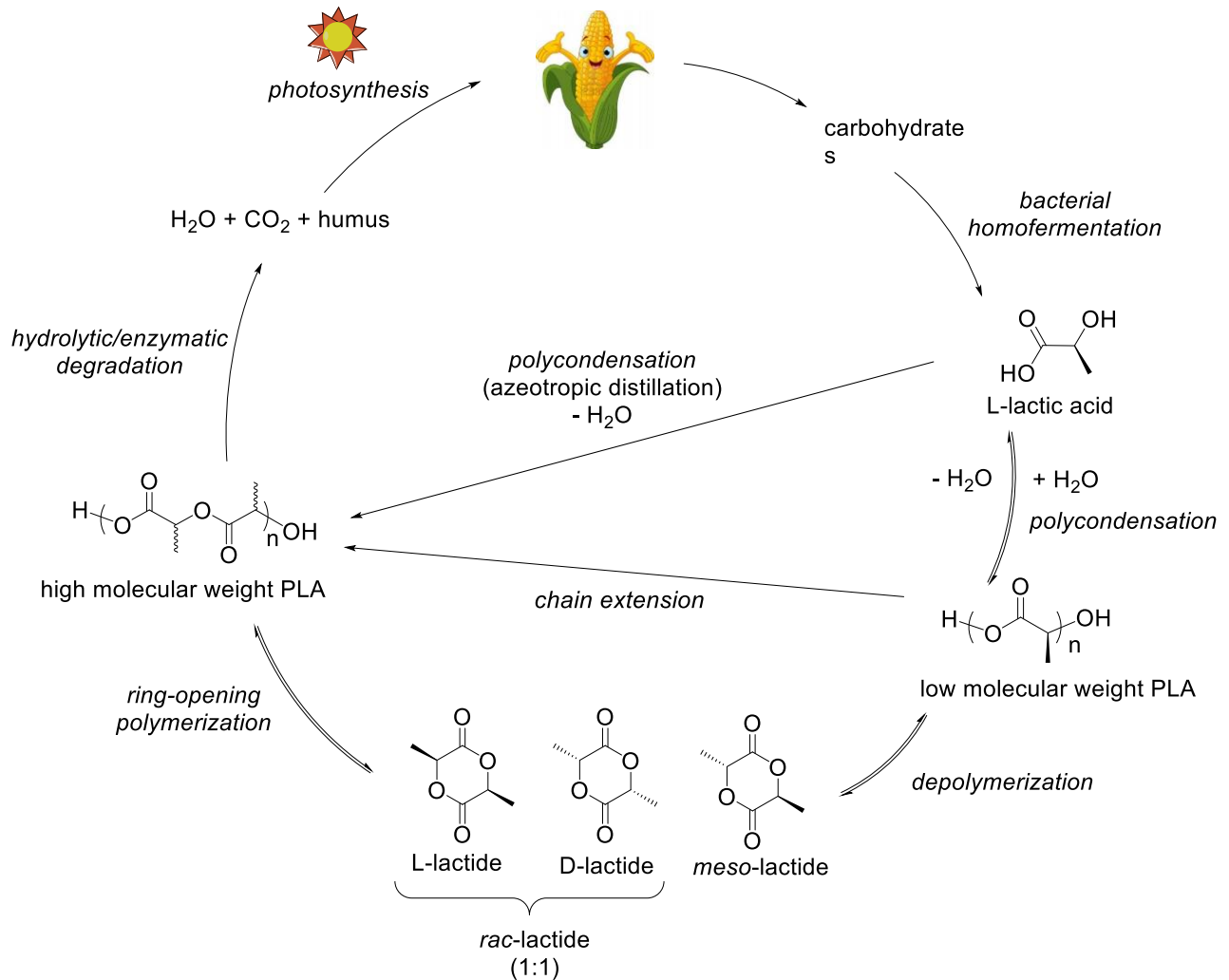
Figure 1.2 Production cycle for poly(lactide).

Natureworks LLC, the leading producer of lactic acid polymer technology, synthesizes 8×10^6 tons/year of PLA using a proprietary synthesis conducted in the melt phase rather than in solution.[31] Lactic acid is first polymerized to low molecular weight PLA *via* continuous condensation. Depolymerization of oligomeric PLA with tin(II) carboxylates or alkoxides produces lactide, which can undergo ROP with tin octanoate (SnOct₂) to form high molecular weight PLA.[18,29] Three stereoisomers of lactide exist: D- and L-LA, where both stereocentres have

the same configuration, and *meso*-LA, where the two stereocentres have opposite configurations. Racemic-lactide (*rac*-LA) is a 1:1 mixture of D- and L-LA (Figure 1.2).

Different reactivity among the three isomers has been observed (further explored in Chapter 2),[1,32,33] and the disparity in reactivity was attributed to dissimilar structural configurations adopted by the isomers. L- and D-LA have twisted boat geometries[34] whereas *meso*-LA assumes a more twisted planar geometry that stabilizes its ground state.[32] Thermal properties reflect the observed differences in solid-state conformation; in that melting temperatures for L- and D-LA are ~50 °C higher than that for *meso*-LA (94 °C vs. 47.5 °C).[35]

ROP of these three isomers can form PLA chains with a variety of microstructures (or different chain tacticity): isotactic PLA where all the stereocentres along the chain have the same configuration, syndiotactic PLA where stereocentres alternate throughout the chain, heterotactic PLA which has stereocentres that are doubly alternating, and atactic PLA with stereocentres which are randomly distributed along the polymer chain (Figure 1.3).
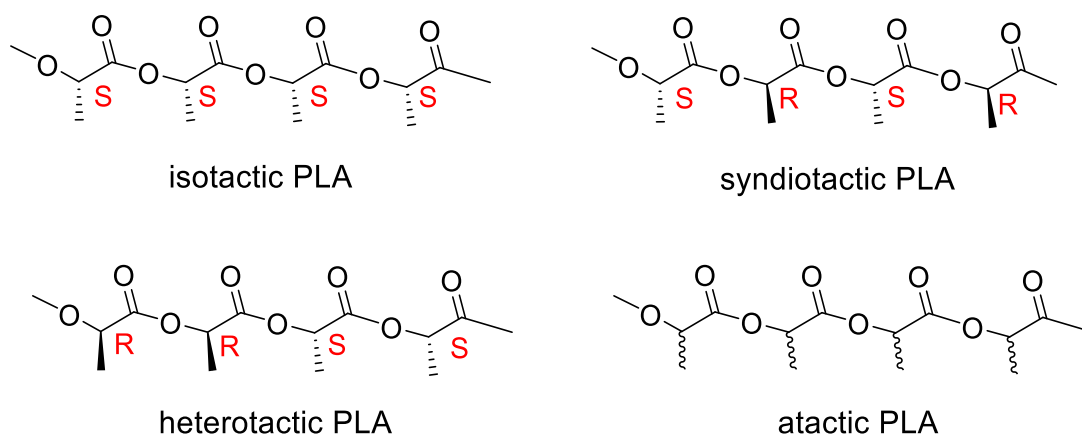
Figure 1.3 Microstructures observed for poly(lactide).

Industrial synthesis of PLA is more commonly achieved *via* the ROP of LA using homoleptic metal alkoxide complexes such as tin(II) octanoate and aluminum(III) isopropoxide. These complexes are very active and produce high molecular weight PLA but transesterification side reactions break down the growing chains causing high polydispersity in the final polymer ($Đ >$ 2.0). Using enantiopure feedstocks of L-LA allows the formation of highly isotactic PLA using these simple catalysts; however, they are not stereoselective towards *rac*-LA, giving mostly atactic PLA.

In the last few decades, a number of examples of well-defined coordination complexes that effectively control the molecular weight distribution and stereochemistry of PLA have been reported.[36-38] The first notable example came from Spassky and co-workers who, in 1996, reported the synthesis of a chiral aluminum salen binaphthalene complex that was highly stereoselective for the ROP of *rac*-lactide, and the resulting polymer was shown to have 88% optical purity.[39]

Generally, polymerization of LA with metal catalysts occurs through a coordination-insertion mechanism (Figure 1.4). Lactide coordinates to the metal centre and becomes activated to nucleophilic attack by either an internal or external alkoxide. A ring-opening event occurs which generates a polymeryl propagating species which can continue polymerization.

Stereocontrol in coordination complex systems arises through two mechanisms, enantiomorphic site control, where chiral ancillary ligands impart stereoselectivity, and chain-end control, where stereochemistry of the last enchained monomer selects for the next incoming monomer.[40-42]
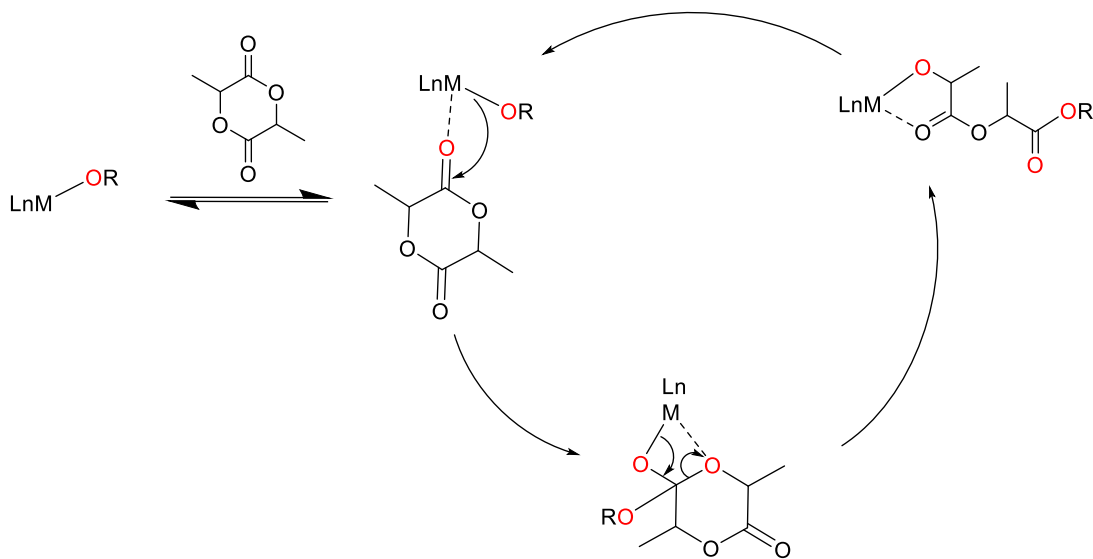
Figure 1.4 Coordination-insertion mechanism for the ROP of lactide by metal catalysts.

As a variety of PLA microstructures can be generated from the three LA isomers, a method to distinguish between them and quantify PLA tacticity was developed. Work done in 1992 by Kricheldorf *et al.*[33] and continued by Thakur and co-workers,[43-46] used ^{1}H, ^{13}C{^{1}H} and heteronuclear correlation NMR techniques to characterize PLA chains of various chain tacticity. Vert *et al.* employed Bernoullian statistics to investigate the different possible chain sequences based on the stereochemistry of the starting monomer.[34] These chain sequences are defined as tetrad sequences, where a tetrad is a hypothetical four-unit oligomer, each of which has a certain probability of occurring within a PLA chain (Table 1.1). The level of stereocomplexity, or tacticity, occurring within a polymer chain can be determined by combining the probabilities of observing the various tetrad sequences with integration data obtained from the ^{1}H{^{1}H} NMR or ^{13}C{^{1}H} NMR spectra (Figure 1.5).[47]

7

Bernoullian statistics operate under the assumption that enchainment of one monomer does not affect enchainment of the next; this assumption does not always hold true, and depends on the stereocontrol mechanism operating in the system.

Table 1.1 Tetrad probabilities for lactide isomers, based on Bernoullian statistics.[a, b]

Possible tetrads from *rac*-lactide[b]	Bernoullian probability	Possible tetrads from *meso*-lactide[c]	Bernoullian probability
(structure) R R R R — m m m	$\dfrac{P_r P_m}{2} + P_m{}^2$	(structure) R S R S — s s s	$\dfrac{P_s P_i}{2} + P_i{}^2$
(structure) S R R R — r m m	$\dfrac{P_r P_m}{2}$	(structure) S R S S — s s i	$\dfrac{P_s P_i}{2}$
(structure) S S S R — m m r	$\dfrac{P_r P_m}{2}$	(structure) S S R S — i s s	$\dfrac{P_s P_i}{2}$
(structure) R S S R — r m r	$\dfrac{P_r{}^2}{2}$	(structure) R S S R — s i s	$\dfrac{P_s{}^2}{2}$
(structure) S S R R — m r m	$\dfrac{P_m P_r + P_r{}^2}{2}$	(structure) S S R R — i s i	$\dfrac{P_i P_s + P_s{}^2}{2}$

[a] Bernoullian probability equations from Coates 2002.[47] [b] When discussing *rac*-lactide, literature convention uses m/r notation, m denotes a meso linkage where the lactyl units have same configuration and r denotes a racemic linkage where two bound units have the opposite configuration. [c] When discussing *meso*-LA, literature conventions use s/i notation, i denotes an iso linkage where the lactyl units have same configuration and s denotes a syndio linkage where two bound units have the opposite configuration.
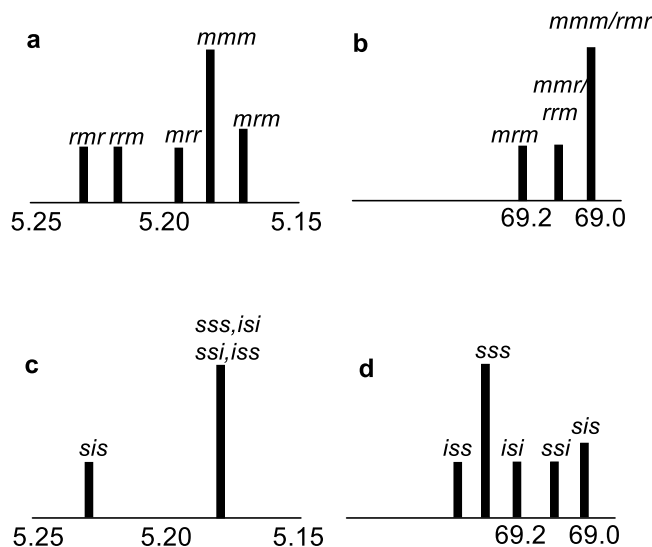
Figure 1.5 Schematic diagrams of PLA tetrad resonances corresponding to the methine region in (a) homonuclear decoupled ^{1}H NMR of PLA from *rac*-lactide; (b) ^{13}C{^{1}H} NMR of PLA from *rac*-lactide; (c) homonuclear decoupled ^{1}H NMR of PLA from *meso*-lactide; (d) ^{13}C{^{1}H} NMR *meso*-lactide.[48]

Most consumer plastics are resistant to microbial attack, however, the ester linkages within PLAs chain structure make it much more susceptible to biodegradation.[28] Degradation and compostability of PLA has been explored under a variety of conditions. In animal models, hydrolysis breaks PLA down to soluble oligomers which are metabolized by cells.[49,50] When placed in landfills or in waste water streams, PLA sheets were still present after 15 months, though they were partially degraded, displaying lower molecular weight and obvious visual physical break-down.[51,52] Industrial composting conditions were found to be ideal for PLA degradation. One study investigated PLA with a molecular weight of 152 kg mol^{-1} which was placed in a vegetable compost with a temperature, moisture content, and pH of 45-70 °C, 40-55% and 4-8, respectively. The polymer had been broken down to chains of 4.5 kg mol^{-1} in 17 days, and total degradation was observed after 34 days.[52] Under compost conditions, decomposition begins with random non-enzymic chain scission which breaks down the main polymer chain and can be

9

accelerated in acidic or basic environments. Low molecular weight oligomers generated then diffuse from the bulk polymer and are consumed by micro-organisms.[35]

Solid PLA can be either amorphous or semi-crystalline, as a rule, PLAs with optical purity greater than 78% are usually crystallizable.[53] PLA crystals exist as polymer helices in orthorhombic unit cells. Stereodefects introduce 'kinks' into the helical confirmation which reduces crystallinity and glass transition temperatures. Physical, mechanical and degradation properties of PLA are highly dependent on the transition temperatures, and thus are impacted by PLA stereoregularity.[18] By controlling properties such as branching, D-isomer content and dispersity,[53] commercial producers have formulated PLA resins that can be transformed into films and fibers using current processing technologies such as injection molding, extrusion and fiber spinning.[28] The physical properties of PLA are often compared to poly(styrene) (PS) and poly(ethylene terephthalate) (PET) as it is strong with high modulus but is brittle with low toughness (plastic deformation) (Table 1.2).

Due to its inherent hydrolysablility, coupled with its high strength, PLA has found application as consumer articles (*i.e.* feminine hygiene products and nappies), in packaging (*i.e.* compost bags and cold water bottles), medicine (*i.e.* bone sutures and drug delivery micelles)[54] and agricultural applications (as matrices for controlled herbicide delivery).[28] However, there have been drawbacks to the widespread acceptance of PLA because of its inferior moisture barrier properties (for long-term use), low thermal stability and brittle nature.[31,55-58] Research in this field is currently focused on the rubber toughening of PLA to improve thermal stability and mechanical properties. These challenges are being targeted from two perspectives: molecular chemists tune polymer properties by adjusting PLA crystallinity, functionality and composition using concepts and tools from

organometallic and coordination chemistry; applied material scientists achieve PLA plasticization through the use of additives and melt-blending.

A variety of highly active (high turnover frequency), productive (high turnover number) and selective (high tacticity and molecular weight control) single-site metal initiators have been developed to achieve stereoregular PLAs.[36,37,59] Varying stereoregularity and crystallinity have had a marginal effect on improving the rubber toughness of PLA and most organometallic systems are not industrially viable due to low water tolerance, catalyst recovery, and melt phase selectivity.[15] Regardless, these systems give access to easily tunable, well-defined polymers, allowing researchers to investigate novel PLAs and their structure-property relationships.[11]

Melt blending with small molecules, PLA oligomers and flexible polymers is an economic and convenient method to improve the toughness of PLA and has been successful in forming a variety of commercially available PLA resins.[28] However, the formation of useful blends is complicated by the size, volume fraction, properties and interfacial adhesion of the dispersed phase.[56] Small molecules and oligomers have also been shown to migrate to the surface of the melt during processing, leading to diminished properties of the final material, [56] and generally increases in toughness are linked with decreases in strength and modulus compared to the native polymer.

Table 1.2 Comparison of mechanical and thermal properties for common consumer plastics.[29,31,55]

	PLLA	PDLLA	PS	LDPE	PET
Mechanical properties					
Yield strength (MPa)	59	44	35	20	31
Tensile strength (MPa)	70	53	46	8 – 20	47
Elongation at break (%)	7	5.4	3 – 4	100 – 1000	30 – 300
Thermal properties					
Glass transition (°C)	63	51	95	-100	75
Melting temperature (°C)	178	--	240	180	250
Processing temperature (°C)	210	190	230	280	255

1.1.2   Lignin: Structure, isolation, characterization and biodegradation.

Lignin is the second most abundant polymer available from bio-mass.[60] A constituent of most plants, lignin binds cellulose and hemicellulose while imparting strength and rigidity to cell walls. Its abundance has provoked researchers to investigate the use of lignin as a component in polymeric materials.[61]

Lignin is comprised from phenyl propane units originating from three aromatic alcohol precursors or monolignols: *para*-coumaryl alcohol, coniferyl alcohol and sinapyl alcohol.[60,62] These alcohols end up as three lignin residues (Figure 1.6). Biologically mediated radical coupling reactions[63] (Figure 1.7) bond the monolignol units to form a highly branched, 3-dimensional macromolecule held together by abundant hydrogen-bonding interactions between methoxy and hydroxy groups (Figure 1.8).[62]

The composition of lignin (Figure 1.6), specifically the ratio of *para*-hydroxyphenyl (**H**), guaiacyl (**G**) and syringyl (**S**) residues, depend on the species and environment of the plant source. Hardwood[*] lignin contains mostly **G** and **S** units with trace amounts of **H** units. Guaiacyl units make up most of softwood[†] lignin, although low levels of **H** units are also incorporated. Grasses generally consist of primarily **G** and **S** units.[62,64]

---

[*] Flowering plants, *eg.* cherry trees.

[†] Seed bearing plants, *eg.* oak trees.

Monolignols

para-coumaryl alcohol   coniferyl alcohol   sinapyl alcohol

Lignin residues

p-hydroxyphenol   guaiacyl   syringyl
H   **G**   **S**

R$_1$, R$_2$ = H or lignin
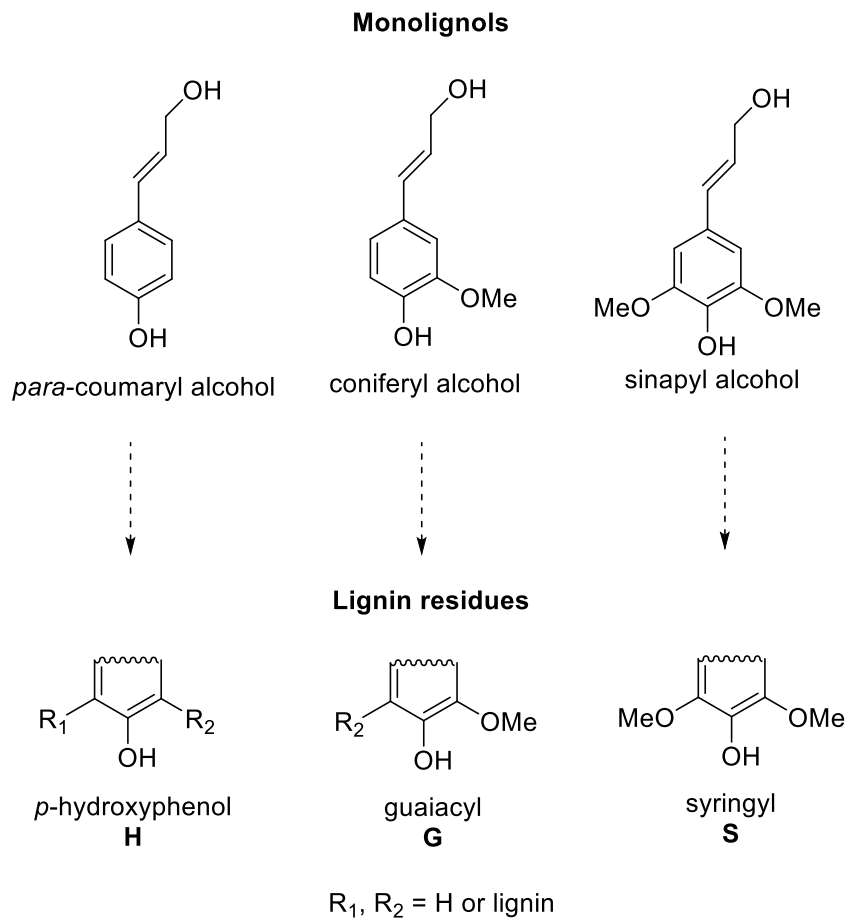
Figure 1.6 Three main monolignols: *para*-coumaryl alcohol, coniferyl alcohol and sinapyl alcohol, which become *para*-hydroxyphenyl (**H**), guaiacyl (**G**) and syringyl (**S**) units within the lignin framework.[64]
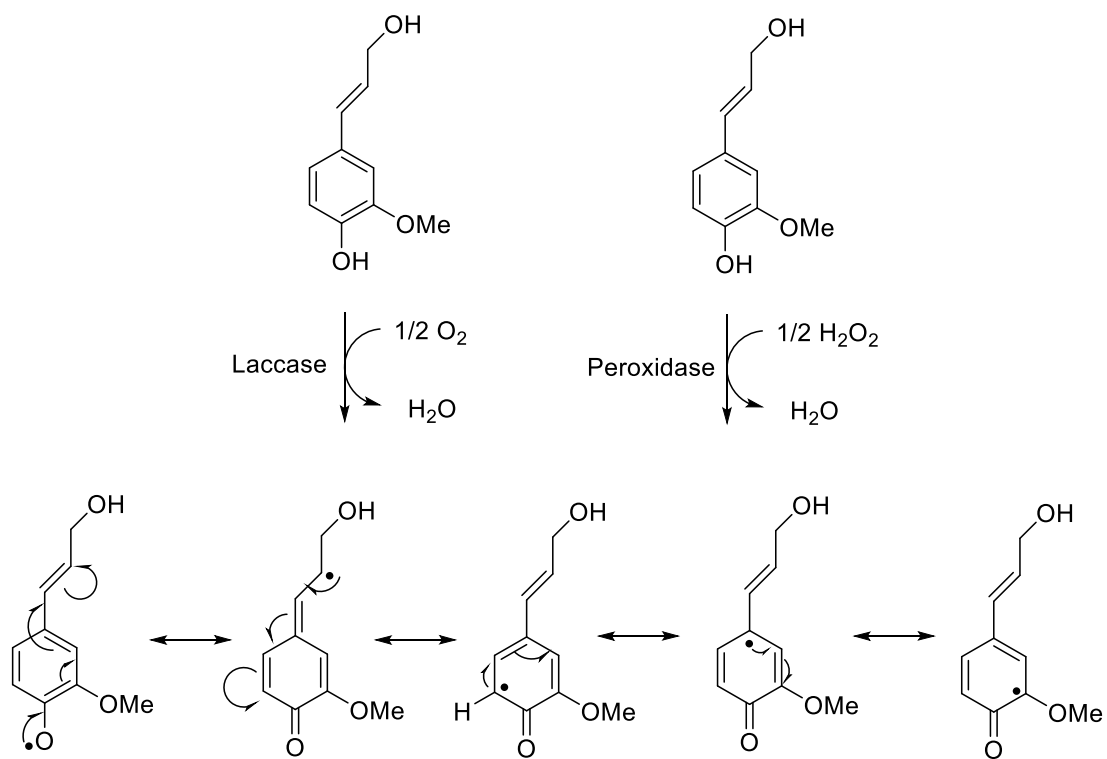
Figure 1.7 Enzymatic radical pathways for coniferyl alcohol.[65]
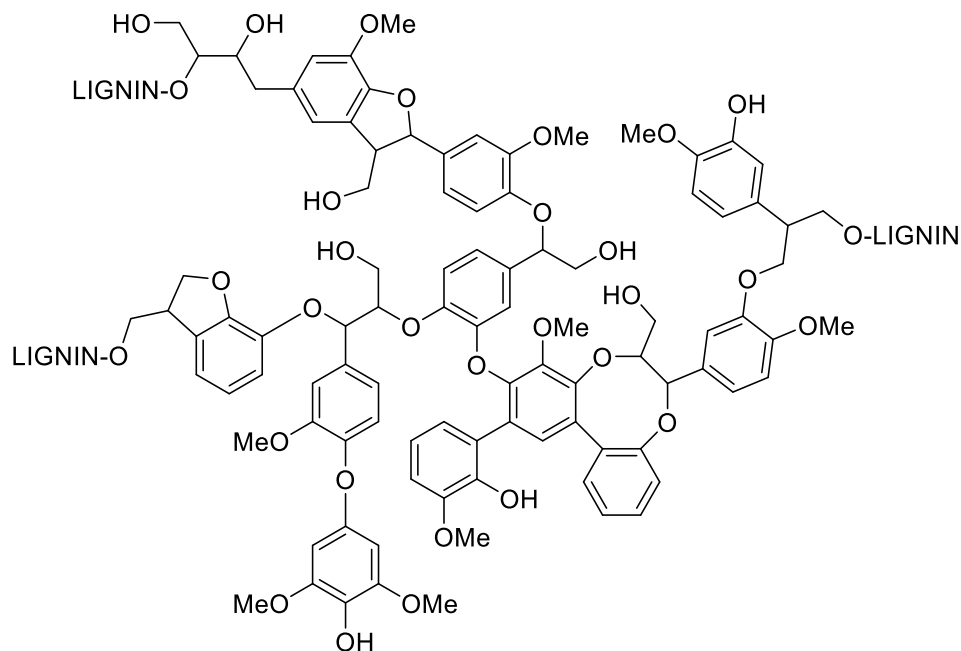
Figure 1.8 Schematic representation of lignin after radical coupling of monolignols.[66]

Lignin has an irregular and complex structure that makes it insoluble in organic solvents. Historically, analysis of its chemical structure has been difficult to determine. Argyropoulos *et al*. developed a novel technique which utilizes ^{31}P NMR spectroscopy to characterize the hydroxyl groups in lignin (Scheme 1.1).[67] Phosphitylation of hydroxy groups using 2-chloro-4,4,5,5-tetramethyl-1,3,2-dioxaphospholane (TMDP) is achieved in the presence of a base such as pyridine.[68] Phosphitylated hydroxyls are compared to an internal standard (usually cyclohexanol) to quantify the concentration of hydroxy species, in mmol g^{-1} (Figure 1.9).

Scheme 1.1 Phosphitylation of lignin using 2-chloro-4,4,5,5-tetramethyl-1,3,2-dioxaphospholane (TMDP).
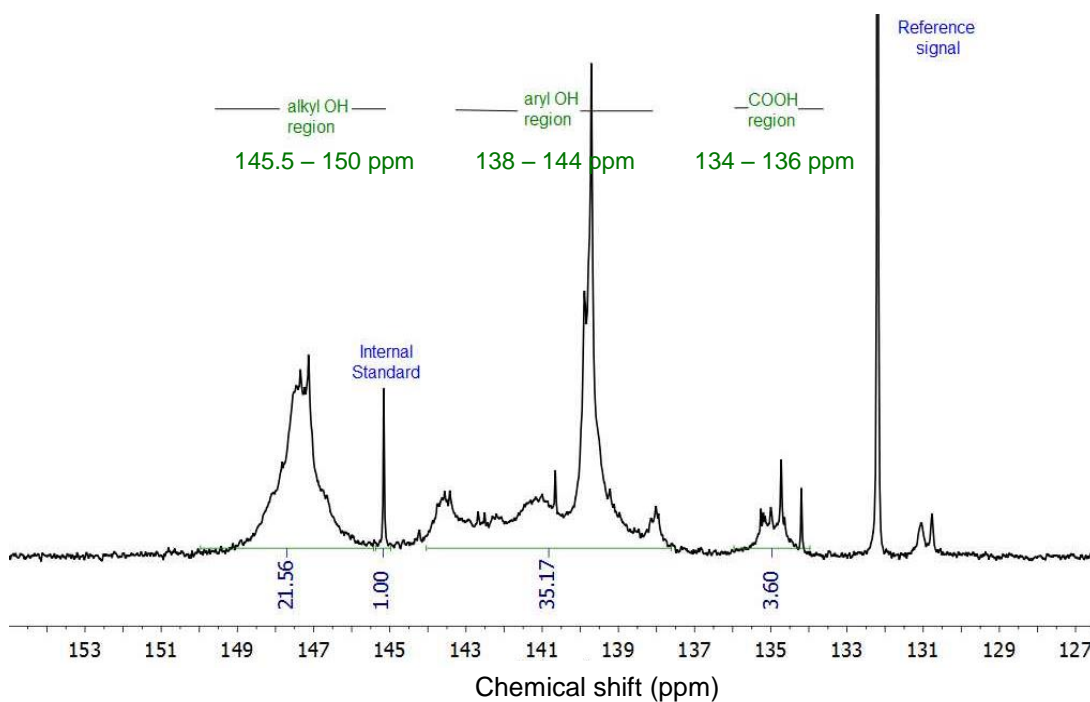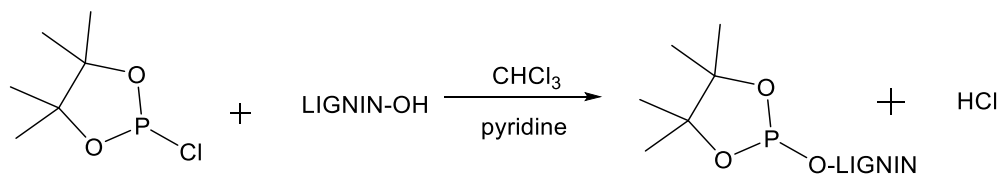
Figure 1.9 ^{31}P NMR spectrum (CHCl$_3$/pyridine, 25 °C, 121 MHz) for phosphitylated lignin, derivatized with 2-chloro-4,4,5,5-tetramethyl-1,3,2-dioxaphospholane (TMDP). IS = internal standard (cyclohexanol), 145.2 ppm. Reference = phosphitylated water, 132.2 ppm. Alkyl-OH signals found 145.5 – 150 ppm; aryl-OH signals found = 138 – 144 ppm, carboxylic acid-OH signals found 134 – 136 ppm.

Lignocellulosic biomass is a composite of lignin, hemi-cellulose and cellulose and is a feed-stock for the pulp and paper industry.[64] Pulping (delignification) processes are used to remove lignin allowing fibrous cellulose to be separated for the production of paper and its related products. Pulping relies on breaking lignin-cellulose bonds *via* cleavage of ester and ether bonds to release the lignin from other plant cell components.
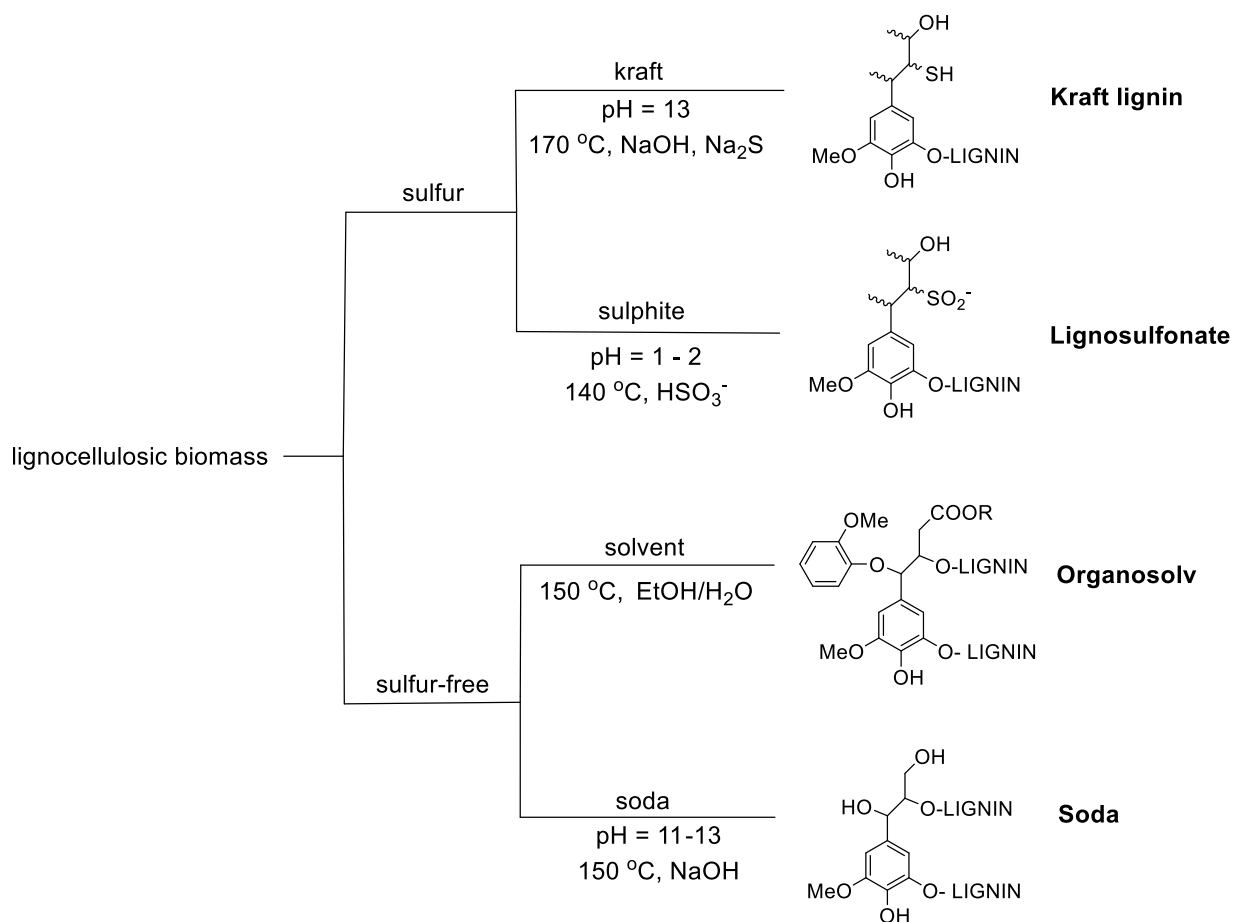
Figure 1.10 Biomass extraction processes to produce the four classes of technical lignin, kraft, lignosulfonate, organosolv and soda.[64,69]

Two methods exist for extraction of lignin from biomass: sulfur and sulfur-free processes. These processes generate four classes of technical lignin used in academia and industry (Figure 1.10).

Sulfur processes are used primarily on wood sources, and are the main delignification techniques used by the pulp and paper industry. In these processes, lignin is cooked in the presence of 'white liqour', a basic solution containing NaOH and Na_2S. Following acidification, kraft lignin can be isolated; however, this type of lignin is contaminated with residual levels of sulfur (1-2 %). Cooking can also be done in an acidic white liquor containing aqueous SO_2 (HSO_3^-), and produces a class of lignins called lignosulfonates. This lignin has higher sulfur content due to the presence of sulfonate groups on aliphatic side chains. The abundance of sulfonate groups make lignosulfonates soluble in water making it a useful dispersant and binder for industrial applications. These cooking processes depolymerize lignin so the final structure has significantly lower molecular weight and is chemically different to that of natural lignin.[64,65,69]

Sulfur-free processes are more often used for grasses and occasionally hardwoods. The structure of lignin produced from these methods are more similar to that of the plant-bound polymer.[64] Ethanol/water dissolves lignocellulosic biomass at high temperature and after precipitation with a non-solvent, organosolv lignin is isolated. This class of lignin has the highest purity and shows high solubility in organic solvents. Under alkaline conditions, cooking produces the final class of technical lignin, soda lignin, which have structures most similar to native lignin. Both these classes have the potential to produce useful building blocks for chemical synthesis, which has spurred investigation into their selective degradation.[66]

One role of lignin in plant cells is to protect against degradative enzymes, which means it is inherently recalcitrant towards chemo- and biodegradation.[70] Lignin is biosynthesized *via* a radical mechanism and as such is sensitive to radiative degradation. In biological systems, lignases utilize peroxide radical pathways to degrade lignin (Scheme 1.2).[71] Thermophillic ligninolytic microfungi excrete peroxidases that generate radicals and initiate the break-down of lignin macrostructure. The white-rot fungus (*Pycnoporus cinnabarinus*) breaks down wood and lignin in natural environments.[72] Studies of the activity of this fungus under industrial composting conditions showed this microbe cannot withstand the ideal composting temperatures (40-50 °C).[73,74]

Scheme 1.2 Oxidative cleavage of lignin structure by lignin peroxidase (LiP).
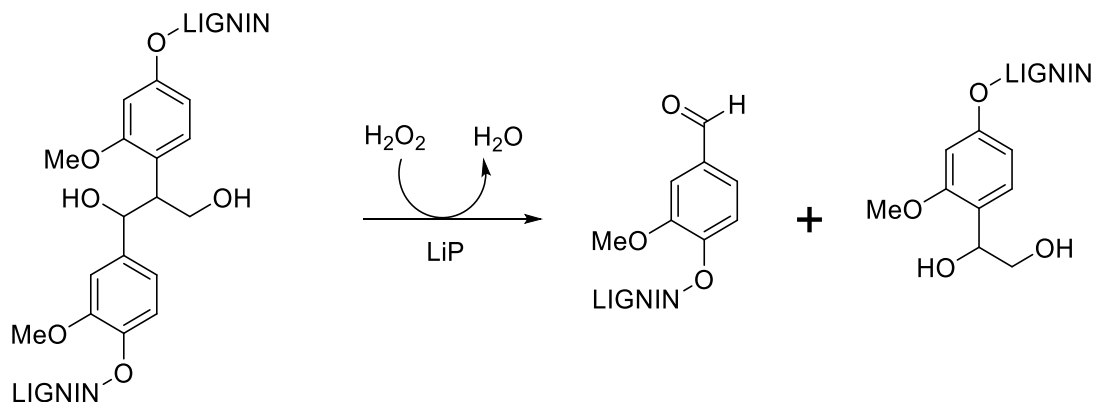
Currently most lignin produced in the pulp and paper industry is burned to off-set energy costs,[61] with only 1-2% being used for specialty products. Recently there has been a surge of interest to increase the value of this cheap and renewable source of polymeric material.[69,75,76] Direct use of lignin in materials is hindered by its highly disordered aromatic structure which makes it thermally strong and brittle and thus difficult to process.[77] However, these structural properties have led to lignin being used as a filler in a variety of green composites,[16,65] in particular

to improve the properties of other bio-derived and biodegradable polymers such as PLA.[26,78] The effect of unmodified lignin incorporation into PLA blends has been investigated with a variety of lignin sources and though greater thermal stability of the composites has been shown,[79-82] the overall mechanical properties were diminished or remain unchanged compared to neat PLA due to poor stress transfer as a result of insufficient compatibilization between lignin and the polymer matrix.[61,64,76,80,83-86]

1.2 Polymer rheology

Rheology is the study of the deformation and flow of materials when external forces are applied.[87] An important aspect of polymer rheology is the study of how viscoelastic behaviour changes with respect to temperature, molecular weight and polymer microstructure. These parameters can give an indication of how the polymer will behave during industrial processing as well as shedding light on potential end-use behaviour.

1.2.1   Polymer processing technologies.

Thermoplastics have been used for consumer products and packaging because they have useful properties such as being reformable, light-weight, heat sealable and variable in their barrier properties.[88] Thermoplastic materials display temperature and time dependent behaviour. At low temperatures, polymer chains have little mobility and show glass-like response. Once stretched, polymer chains cannot fully relax back to their equilibrium positions making the material brittle. As the temperature is increased, polymer chains have more free volume allowing them to move cooperatively.[89] Polymer behaviour moves into a glass transition region where the material softens. Above the glass transition temperature, T_g, amorphous polymers show rubbery elastic behaviour and at high temperature the chains are highly mobile and the material behaves as a low viscosity liquid (Figure 1.11). Semi-crystalline polymers show further softening above their T_gs but chains only become fully mobile past their melting temperature, T_m, when crystalline regions are broken and chains move freely (Figure 1.11).[90] The variable behaviour of thermoplastics means they can be easily processed at temperatures well above the glass transition where they behave as viscous melts.
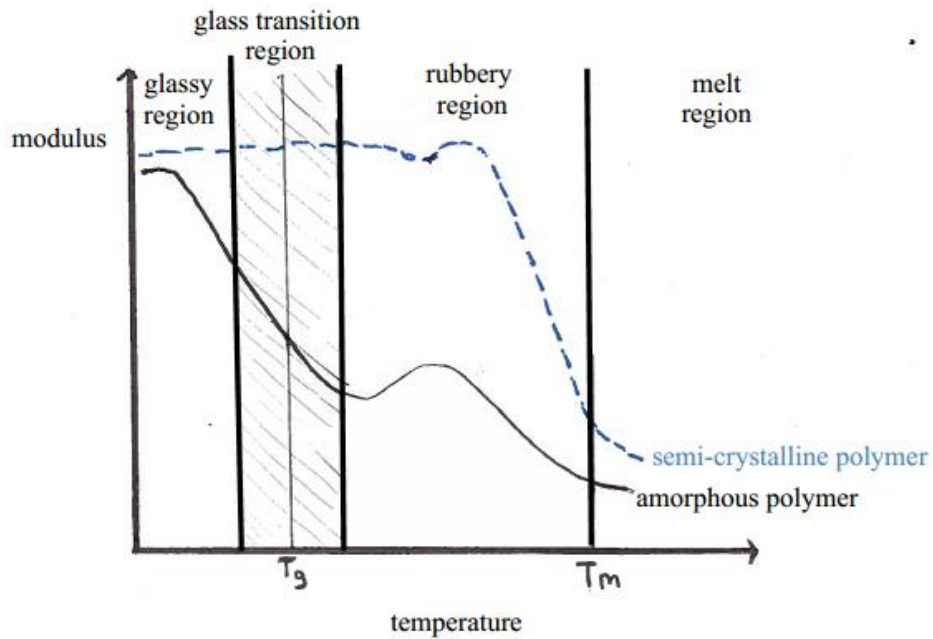
Figure 1.11 Modulus vs. temperature for an amorphous polymer (black solid line) and a semi-crystalline polymer (blue dashed line).

Extrusion is an important technique for continuous melt phase processing and is often coupled to other forming machine systems such as injection or blow molders.[91] Screw extruders are commonly used for industrial processing (Figure 1.12). Polymer pellets are fed through a hopper into a heated barrel where a screw rotates, forcing pellets to move forward. The action of the screw works to mix the pellets into a homogenous melt flow. Molten polymer leaves the screw out the front of the barrel and moves through a die and into a forming machine.[92]
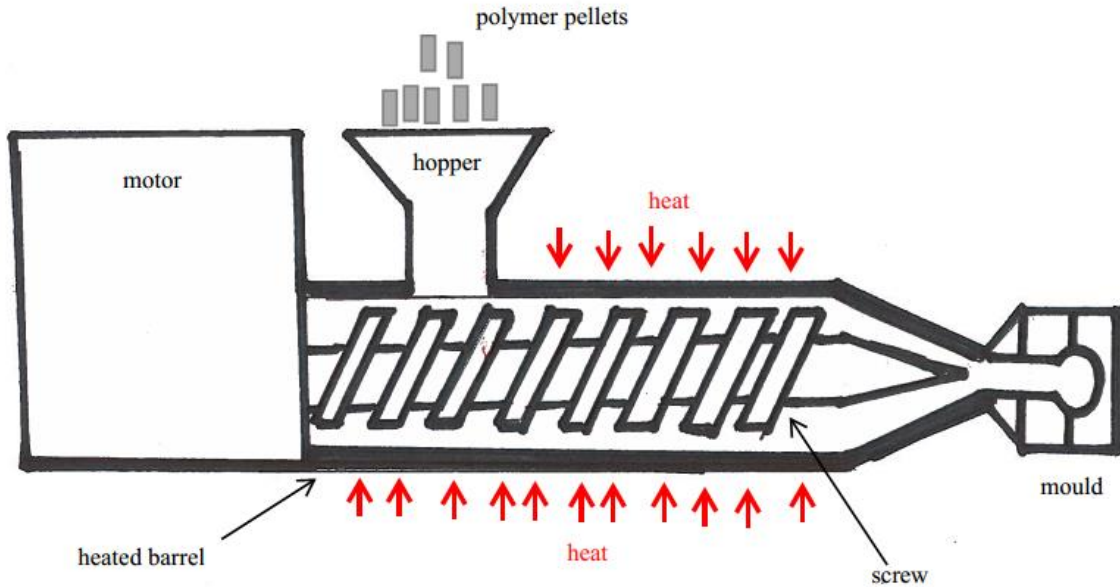
Figure 1.12 Schematic of a single screw-extruder.

Injection and blow molding are processing techniques commonly used to produce consumer plastics. Molten polymer flows directly into a mold where it cools and hardens to form injection molded products. In blow molding, a preform is first filled with molten polymer before air flow is used to axially stretch the polymer to fit the preform (Figure 1.13).[92]
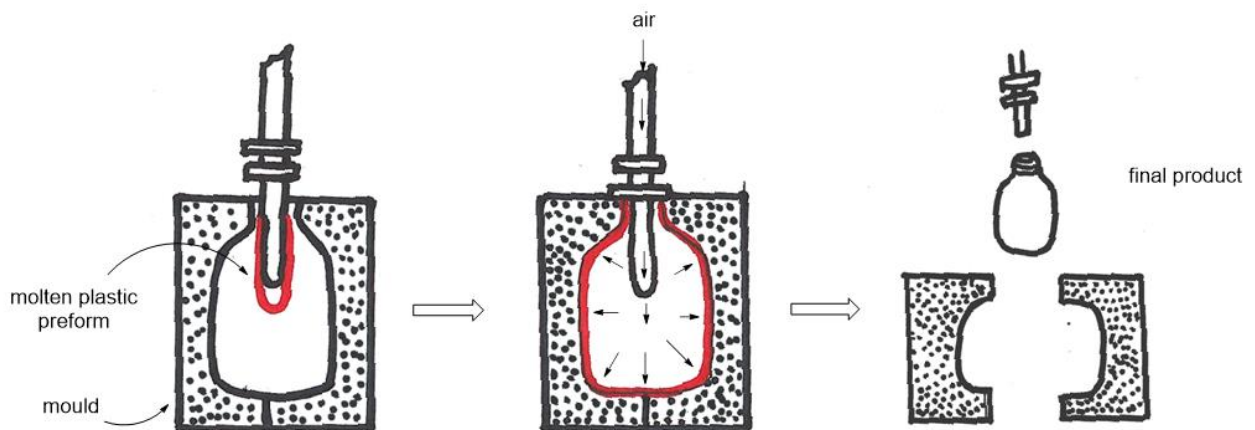
Figure 1.13 Schematic of a blow mold.

24

To avoid flow instabilities and non-uniform melts, polymers require a level of thermal stability and melt strength at processing temperatures.[93] Rheological properties are useful when comparing and evaluating the performance of polymers during processing. Sensitive to microstructure changes, rheological analyses can help researchers predict and control polymer properties.[91]

1.2.2 Polymer viscoelasticity.

Polymer melts display complex flow behaviour; acting as viscous liquids by dissipating energy when a force is applied, as well as acting as elastic solids by storing applied energy. This dual behaviour identifies them as viscoelastic materials.[87] Viscoelastic properties are often described in terms of the elastic component, or storage modulus G', and the viscous component, or loss modulus G". The behaviour of a material depends on which of the two moduli dominate at a given temperature or deformation frequency.[90] At low temperatures G' often dominates over G", meaning that the material shows solid response. Increasing the temperature takes the material response through a cross-over transition where G" begins to dominate and the polymer shows more fluid response (Figure 1.14).
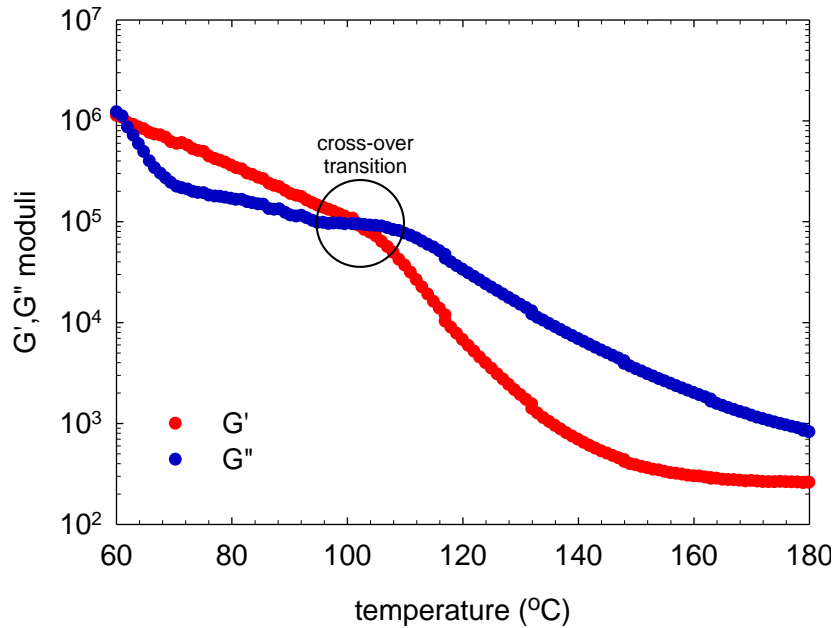
Figure 1.14 Plot of the linear viscoelastic moduli, G' and G" of a thermoplastic polymer. At temperatures below 100 °C, the storage modulus dominates; thus, the material behaves as an elastic solid. Above 100 °C the material behaves as a viscous fluid.

The viscoelastic behaviour of polymer melts also depends on the deformation time and frequency.[90] Long deformation times allow chains to respond to applied stresses and chains relax to dissipate the energy. As such, G" is observed to dominate and the material shows viscous liquid response. As deformations get shorter (frequencies increase), polymer behaviour moves through a cross-over region ω_c. After this point deformations are faster than relaxation and energy is stored within chain segments, thus solid response where G' dominates is observed (Figure 1.15).
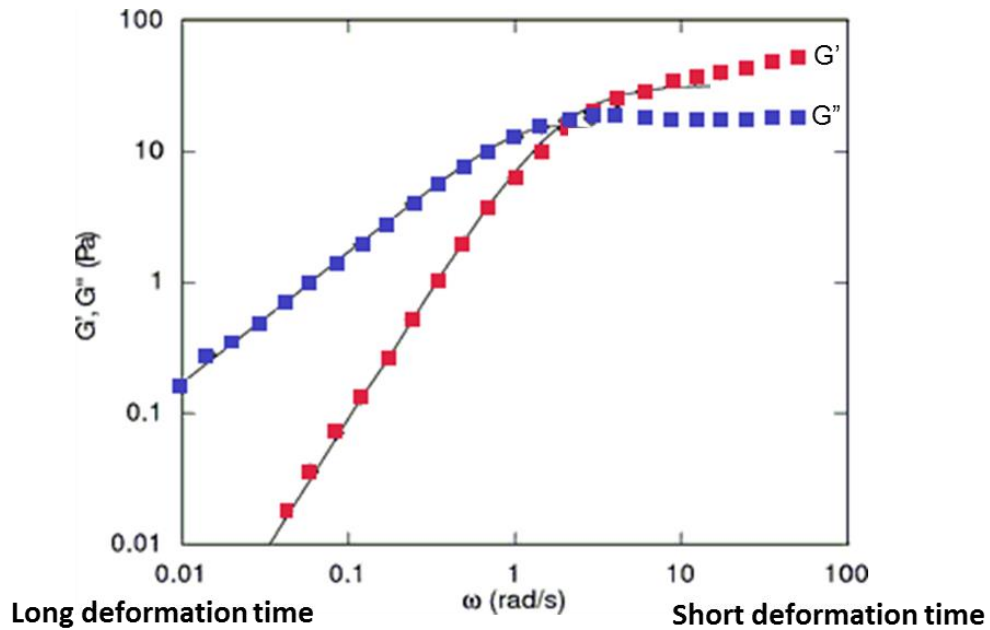
Figure 1.15 Plot of the linear viscoelastic moduli, G' (■) and G'' (■) of a hypothetical thermoplastic polymer. At deformation frequencies lower than 1 rad s^{-1} the loss modulus dominates thus the material behaves as a viscous liquid. Above 10 rad s^{-1} the material behaves as an elastic solid.

1.2.3 Polymer viscosity.

When put in motion, liquid molecules slide past each other causing internal friction and flow resistance called viscosity. Viscosity is a property that involves resistance to continuous deformation. Polymeric materials exhibit both viscous resistance to deformation and elastic energy storage.[94] The viscosity of polymeric materials can be determined by inducing a shearing rate, $\dot{\gamma}$ and measuring the resulting stress, τ in the sample using a parallel plate rheometer (Figure 1.16). In this configuration, two circular plates are arranged in the same vertical axis with a polymeric sample placed in the space between them. The upper plate is rotated at a specific angular velocity, resulting in a shear force being applied to the sample. The shear stress can be related to the torque

27

required to rotate the upper plate and the shear rate to the rotational speed. The relationship between viscosity, shear stress and shear rate is described in Equation 1.1 below:

$$\eta = \tau / \dot{\gamma}$$

Equation 1.1 where η is the viscosity, τ is the shear stress and $\dot{\gamma}$ is the strain rate. [90]
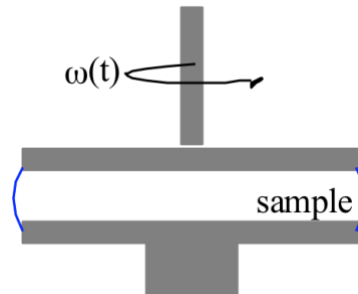
Figure 1.16 Schematic of parallel plate rheometer.

Viscosity values are not constant and depend on conditions such as temperature and time. Ideal viscous or Newtonian flow behaviour, occurs when viscosity is independent of shear rate (*i.e.* water). Conversely, non-Newtonian fluids display viscous response which is dependent on the shear rate. Pseudo-plastic or shear thinning materials show a *decrease* in viscosity with increasing rate of shear whereas dilatant or shear-thickening materials show an *increase* in their viscosity with shear rate (Figure 1.17).[94]
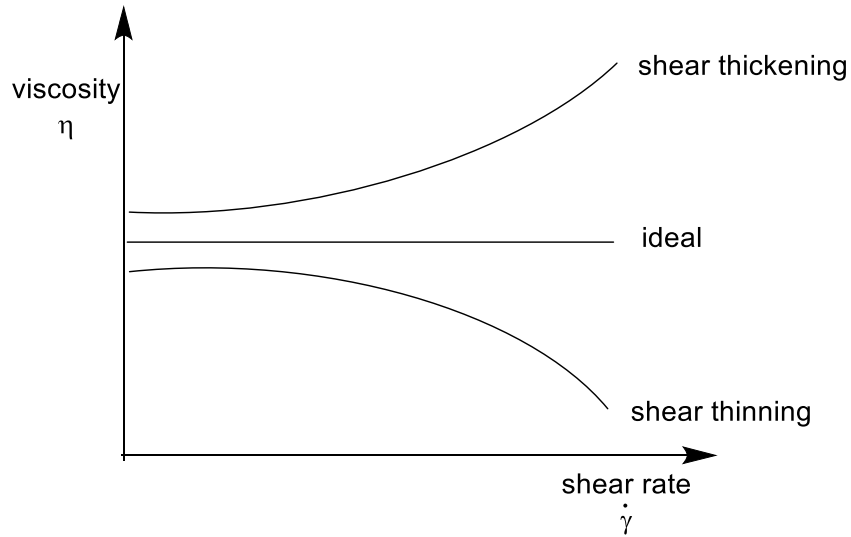
Figure 1.17 Viscosity curves for ideally viscous, shear thinning and shear thickening flow behaviour.

1.2.4   Small amplitude oscillatory shear (SAOS) experiments.

Deformations which do not perturb a polymer past its equilibrium position fall into the linear viscoelastic regime. These deformations are usually of low strains ($< 20\%$) and at low oscillatory frequency (< 100 rad s^{-1}). Oscillatory tests probe chain-chain interactions and are most important when characterizing molecules and correlating their viscoelastic properties with molecular structure.[90]

Consider the parallel plate rheometer presented in Figure 1.16. If a sinusoidal oscillatory strain, γ is applied (Equation 1.2), the resultant stress, τ can be recorded as a function of time (Equation 1.3).

$$\gamma\,(t) = \gamma_0 \sin\,(\omega t)$$

Equation 1.2 where γ(t) is the strain as a function of time, γ_0 is the initial strain, ω is the deformation frequency and t is time.

$$\tau(t) = \tau_0 \sin(\omega t + \delta)$$

Equation 1.3 where $\tau\,(t)$ is the stress as a function of time, τ_0 is the initial stress, ω is the deformation frequency, t is time and δ is the phase shift or mechanical loss angle.

An entirely elastic material will not show a time lag between the applied strain and the resultant stress (δ = 0), whereas in Newtonian fluids, the stress lags the strain by 90° (δ = 90). As mentioned above, polymeric materials exhibit elastic storage which retards viscous resistance and as such, viscoelastic materials exhibit a phase lag between deformation and response (Equation 1.4).

$$\tau(t) = \gamma_0\,[G'(\omega)\,\sin(\omega t) + G''(\omega)\,\cos(\omega t)]$$

Equation 1.4 where $\tau\,(t)$ is the stress as a function of time, γ_0 is the initial strain, G'(ω) is the elastic response (storage modulus), G''(ω) is the viscous response (loss modulus), ω is the deformation frequency, t is time and δ is the phase shift or mechanical loss angle.

From SAOS experiments, linear viscoelastic (LVE) moduli, G' and G'', can be obtained. These two terms can be used to acquire various other useful parameters which give broader descriptions of linear viscoelastic behaviour.

Complex modulus, |G*|, considers both the viscous and elastic response to describe the entire viscoelastic behaviour (Figure 1.18). Similarily, the damping factor, tan(δ), is the ratio of the loss

to storage moduli and describes the two parts of viscoelastic behaviour.[94] Other parameters often used to describe viscoelastic behaviour are the complex viscosity η^*, a deformation frequency dependent viscosity term, and the zero-shear viscosity η_0, the viscosity when no stress is applied, determined by the limits of the linear viscoelastic region.[90]
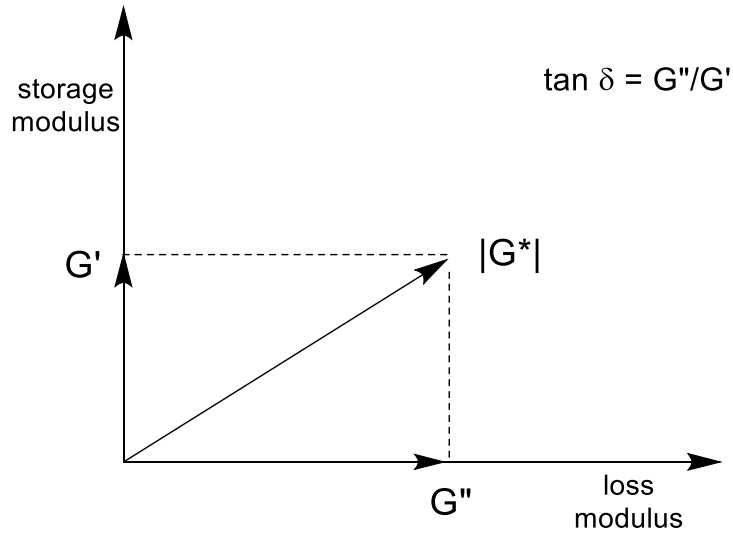
Figure 1.18 Vector diagram showing the relationship between the complex modulus |G*|, the loss and storage moduli, G" and G'.

As rheological properties are dependent on temperature, as such, experiments performed over a range of temperatures can be used to attain a complete map of how a material behaves. These isothermal data can be superimposed by introducing a horizontal a_T, and vertical shift factors b_T, required to bring the data into master curves at a reference temperature. a_T describes the temperature dependence of the LVE properties and follows an Arrhenius trend, from which the activation of flow energy, $E_{a,flow}$ can be calculated (Equation 1.5).[90]

$$a_T = \exp\{E_{a,flow}/R(1/T - 1/T_{ref}\}$$

Equation 1.5. where $E_{a,flow}$ is the activation energy for flow, R is the universal constant of the ideal gas law, and T_{ref} is the reference temperature.

1.2.5   Uniaxial extensional rheology.

Extensional deformations align polymer chains and if deformation time exceeds the rate of molecular relaxation, strain hardening can occur. This effect comes about when polymer chains resist deformation, causing a sharp increase in viscosity before failure. Strain hardening is useful because a polymer can harden upon being stretched into a mold, improving strength and barrier properties.[88] Normally, strain hardening is observed when long-chain branching or network structures are present within the polymer. These structures increase relaxation times by reducing the number of relaxation modes,[21] meaning that there are fewer ways in which the polymer can relax to its equilibrium configuration.

A Sentmanat Extensional Rheometer Universal Testing Platform (SER)[95] can be used to explore strain hardening in polymer melts. A polymer is loaded onto the instrument by placing it between two drums. Rotating one drum applies a uniaxial elongation to the polymer (Figure 1.19). Elongational viscosity or tensile strength growth coefficient, η_E^+, can be plotted against time to reveal strain hardening, which is seen as an upturn in viscosity (Figure 1.20). This effect is influenced by both extensional rate and temperature. Fast extensions do not allow chains time to respond to deformation and are more likely to show strain hardening. Likewise, at low temperature polymer chains have less mobility and can also show strain hardening.
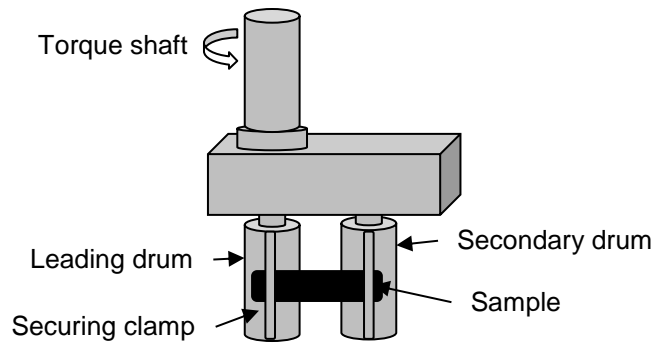
Figure 1.19 Sentmanat Extensional Rheometer Universal Testing Platform (SER).[95]
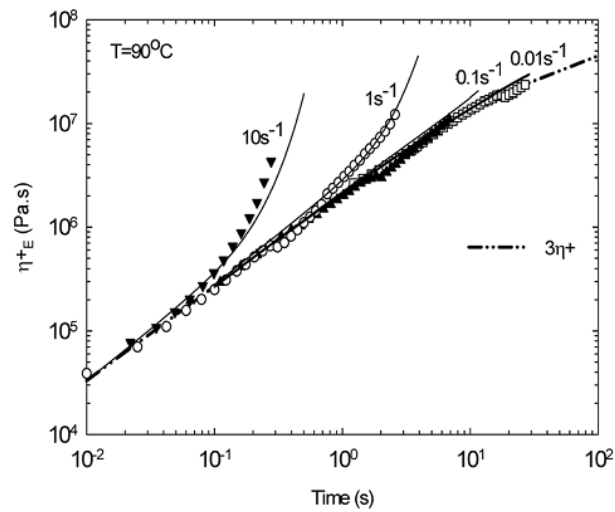
Figure 1.20 Plot of the elongational viscosity η_E^+ vs. time for a hypothetical polymer. At low strain rates, no strain hardening is observed. At strain rates greater than 1 s^{-1}, strain hardening is present.

1.3 Scope of thesis

This multidisciplinary thesis links organometallic catalysis with polymer rheology. The aim is to take a broader view of a research question and use what I find to create efficient catalytic systems where modifications to PLA can be easily made, and will impart useful properties in a predictable way, allowing PLA to be used wider array of consumer applications. In particular, I aim to use molecular chemistry to probe catalysis and polymer synthesis, in order to tune PLA properties.

The thesis begins with an analysis of the ring-opening polymerization of lactide isomers with dinuclear indium catalysts. Chapter 2 describes how catalysis operates in order to design better systems that can attain highly stereoregular PLA. This analysis of stereocontrol and stereochemistry, is followed by a comparison of the structure-property relationships for stereoregular PLAs (Chapter 3). Seeing the influence of interchain interactions on polymer properties, I targeted a series of functionalized polymers. Aryl initiators were synthesized to gain better understanding of how polymerization behaviour changes when using phenolic catalysts and initiators (Chapter 4). By exploiting a facile synthesis, functionality was installed as polymer end-groups. The chain-chain interactions imparted by end-group aggregation is explored in Chapter 5. Using insight gained from examining aryl initiators for the ROP of LA, an effort to incorporate lignin into PLA composite materials is described in Chapter 6.

Chapter 2: Living ring-opening polymerization of *meso*-lactide using indium initiators.[‡]

2.1 Introduction

2.1.1 Controlled tacticity *via* ring-opening polymerization of lactide monomers.

L-(+)-lactic acid can be synthesized industrially by the bacterial fermentation of D-glucose found in corn sugar (see section 1.1.1). High temperature polycondensation followed by metal-catalyzed depolymerization of oligomers, yields lactide (LA). Racemization during the depolymerization process forms three isomers of lactide: D-LA, L-LA and *meso*-LA (Figure 2.1).[88] Catalytic ring-opening polymerization (ROP) of the different lactide isomers produces poly(lactide) (PLA) whose microstructure or tacticity depend on the catalysts' preference for one enantiomer over the other.[34,36]

Homopolymerization of enantiopure D- or L-LA forms isotactic PLA where all chiral centres along the chain have the same stereochemistry. Highly ordered isotactic stereo-block PLA can be synthesized through the sequential copolymerization of two isotactic units. Ring-opening polymerization of the racemic mixture of enantiomers, *rac*-LA, gives varying degrees of stereo-gradient PLA depending on the stereo-control mechanisms acting during polymerization.[96] Lack of stereo-control leads to random incorporation of D- and L-LA from *rac*-LA forming largely disordered amorphous atactic PLA where configurations of stereocentres are randomly distributed

along the polymer chain. Heterotactic microstructures can be obtained from *rac*-LA through the alternating inclusion of D- and L-LA into the growing polymer chain (Figure 2.1).

Isotactic PLA has been reported to show high crystallinity, indicating the presence of significant chain-chain interactions which give rise to regions of order and aggregation of polymer chains.[96-101] By tailoring the microstructure, desirable properties may be imparted to the resulting polymer (discussed further in Chapter 3).[88] Consequently, reports of catalysts achieving well-ordered microstructures are very common in the literature.[36,59] Following these advances, and with the associated increase in commercial PLA production, the use of *meso*-LA as a monomer has become more prevalent.[37] Researchers have been investigating the ring-opening polymerization of *meso*-LA to determine if polymers with useful properties can be obtained from this abundant starting material.

Ring-opening polymerization of *meso*-LA has the possibly of forming polymers within three categories of microstructures: atactic, heterotactic and syndiotactic PLA (Figure 2.1). Syndiotactic PLA has a complex alternating arrangement of stereocentres along the polymer chain making this type of microstructure more difficult to synthesize and thus less common.[102,103] To achieve purely syndiotactic PLA from *meso*-LA, ring-opening should occur predominately at one of the two enantiotopic sites; conversely, heterotactic PLA can be obtained from *meso*-LA if ring-opening alternates between the two enantiotopic acyl oxygen sites (Figure 2.1, sites a and b).[104] If there is no preference for either enantiomorphic site during polymerization, then atactic PLA is formed. Due to their stereoregularity, syndiotactic polymers are typically crystalline and have enhanced mechanical properties compared to amorphous polymers.[102]
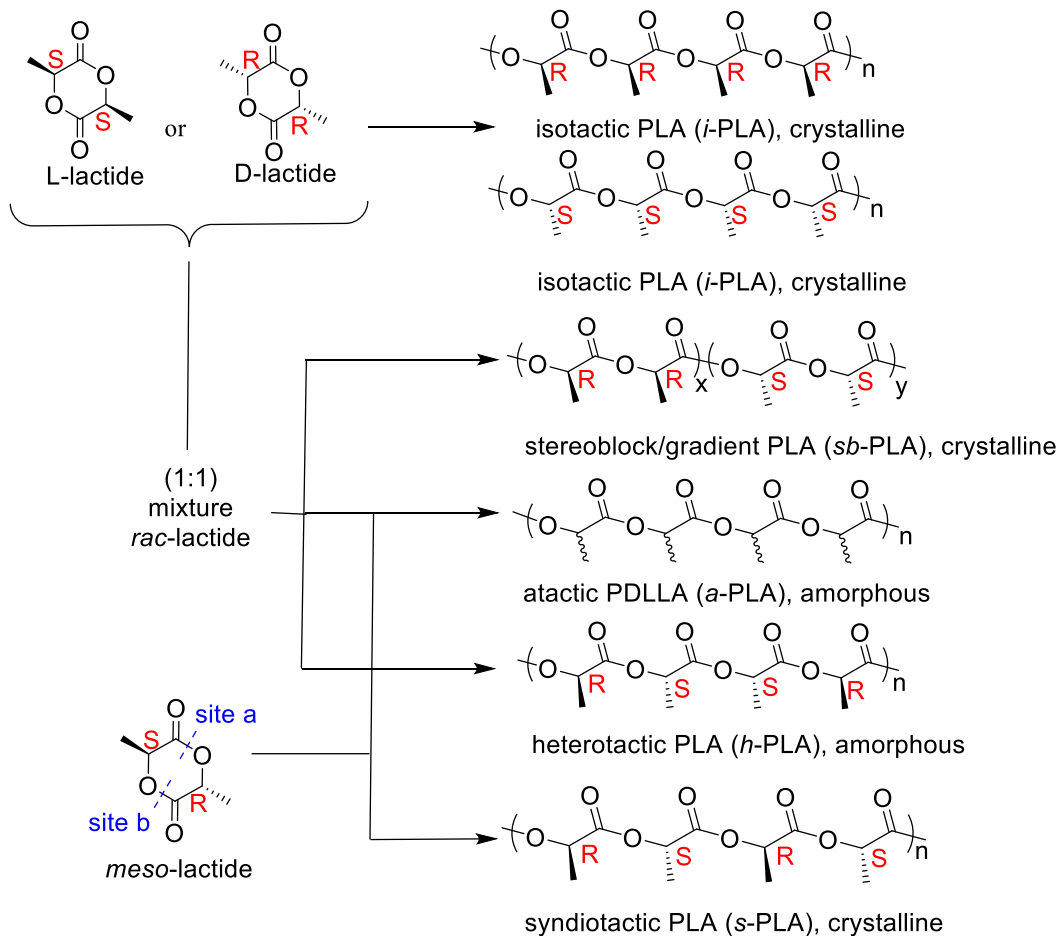
Figure 2.1 Stereoisomers of lactide and the possible microstructures of poly(lactic acid).

2.1.2   Mechanisims for stereocontrol.

Stereocontrol in metal-catalyzed ring-opening polymerization of lactide arises through two mechanisms: enantiomorphic site control (ESC) and chain-end control (CEC). In ESC, selectivity in the ring-opening event is promoted by utilizing ancillary ligands that prefer one enantiotopic site over the other. This differs from CEC where the stereocentre of the last monomer in a propagating chain selects for the next incoming monomer.

Due to the range of ordered and random microstructures reported for both chiral and achiral catalysts, it can be said that these two mechanisms are not independent and both may play an important role at different points in the polymerization process.[32] As both mechanisms contribute to the final microstructure, stereodefects can be incorporated into the polymer chain due to a mismatch in stereocentres when an incoming monomer is enchained. Even small degrees of stereo-irregularity can dramatically decrease the physical properties of the resulting polymer.[29] Therefore, controlling and determining the number of stereodefects along the polymer chain is crucial for synthesizing PLA with desirable properties.

2.1.3   Determining poly(lactide) tacticity.

Historically optical polarimetry has been used to determine the optical rotation of the polymer in solution, this gives the enantiomeric purity and an estimation of the level of stereoregularity within a PLA sample.[32,39] Enantiomeric purity does not fully capture the configurational structures occurring within PLA, and early researchers determined that more information about chain tacticity and the stereo-control mechanism can be gained through inspection of the NMR spectra of the polymers.[34]

The level of stereocomplexity occurring within a polymer chain is expressed by two parameters: P_i defined as the probability of having an *iso* linkage where two adjacent lactyl units have the same stereochemistry (often reported as P_m when discussing *rac*-LA), and P_s defined as the probability of having a *syndio* linkage where the lactyl units have opposite configuration (often reported as P_r when discussing *rac*-LA). A probability value close to one implies high levels of

order, while values close to 0.5 imply atacticity. Bernoullian statistics[§] can be used to describe the various possible tetrad chain sequences[**] dependent on the stereochemistry of the starting monomer (Figure 2.2).[43-46] Tacticity values can be calculated from analysis of the methyl region of the homonuclear decoupled $^1H\{^1H\}$ NMR spectra, where resonances for each possible tetrad sequence are observable after removal of scalar coupling between methine and methyl protons (Figure 2.3).[105] The relative integrations can be substituted into Equation 2.1 and Equation 2.2 (derived from Bernoullian probabilities in Table 1.1) to determine the P_i and P_s values.
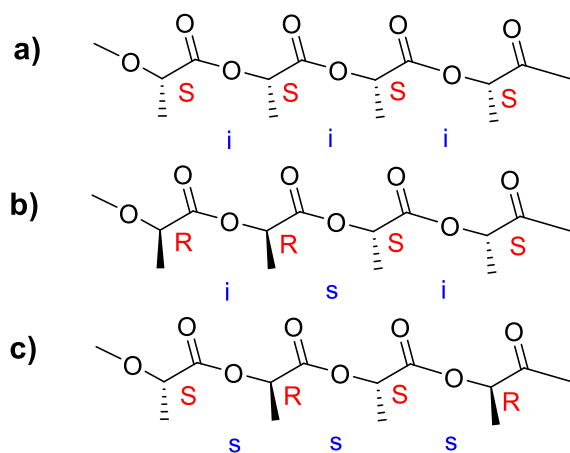
Figure 2.2 Examples of tetrad sequences from the ring-opening polymerization of lactide. a) isotactic PLA b) heterotactic PLA and c) syndiotactic PLA. i indicates an *iso* linkage where two bound lactyl units have the same arrangement s indicates a *syndio* linkage where the lactyl units have opposite configuration.

[§] Bernoullian statistics assume that the configuration of each newly enchained monomer is independent of the previous monomer, an assumption which does not always hold true (see section 1.1.1, page 8)

[**] A tetrad sequence is four bound lactyl units (Figure 2.2).
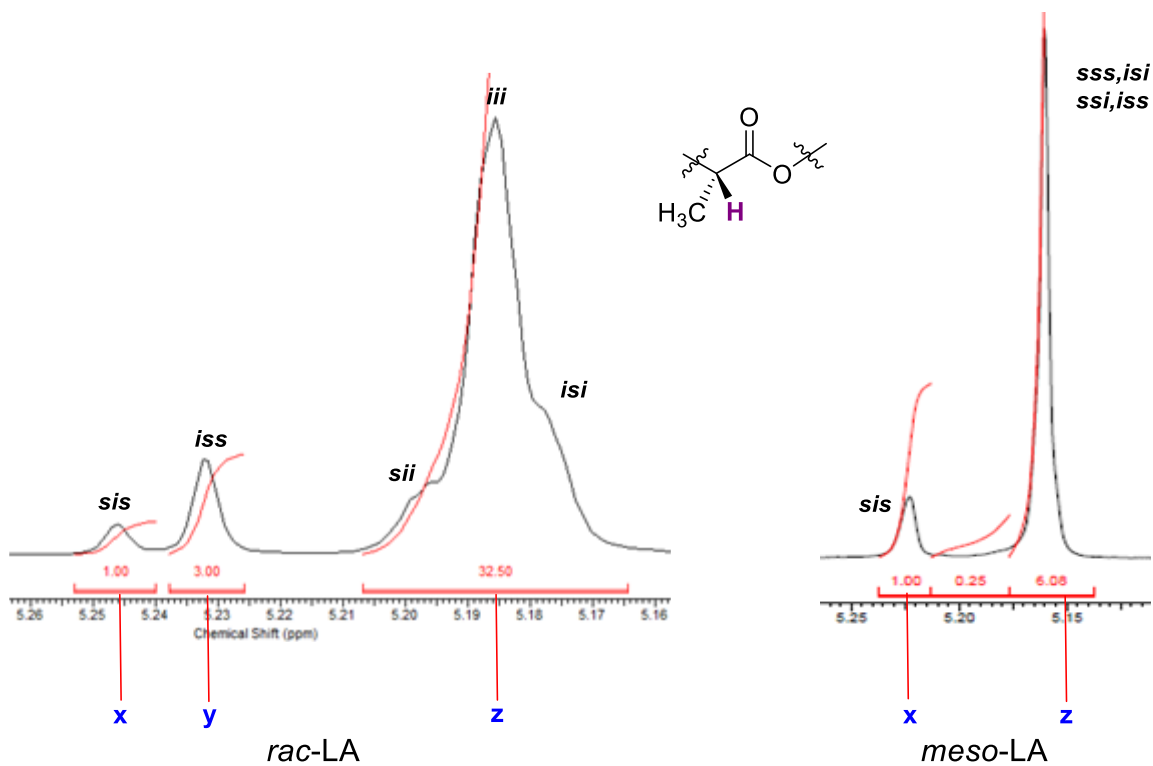
Figure 2.3 ^{1}H[^{1}H] NMR spectra (CDCl$_3$, 25 °C, 600 MHz) of PLA samples resulting from ring-opening polymerization of different lactide isomers. The chemical shifts for the methine proton (shown in purple) depend on the tetrads (labelled in black) in which it is found.

$P_i = [iii]$ $a = x + y + z$

$P_s = [sis] + [isi]$

$$P_s = \left(\frac{2x}{a}\right)^{\frac{1}{2}}$$

$$P_i = \left(\frac{2y}{a}\right) \div P_i$$

Equation 2.1 Equation to calculate tacticity for polymers formed from *rac*-LA.

$P_i = [sis]$ $a = x + z$

$P_s = [sss] + [ssi/iss/isi]$

$$P_i = \sqrt{\frac{2x}{a}}$$

$$P_s = \frac{2\left(\frac{z}{a} - P_i{}^2\right)}{P_i}$$

Equation 2.2 Equation to calculate tacticity for polymers formed from *meso*-LA.

40

As stated above, purely syndiotactic PLA is obtained by ring-opening *meso*-LA predominately at one of the two enantiotopic acyl-oxygen sites. A catalyst's preference for one site can be determined by the rate at which the catalyst ring-opens at one position over the other (Figure 2.4, a vs. b).[106] This enantiotopic selectivity ratio can be quantified by the α-value (the probability of ring-opening at one site over the other) and is determined experimentally by comparing the ratio of the integrations for the [sss] and [sis] tetrads or by examining the rate of polymerization for L- and D-LA.
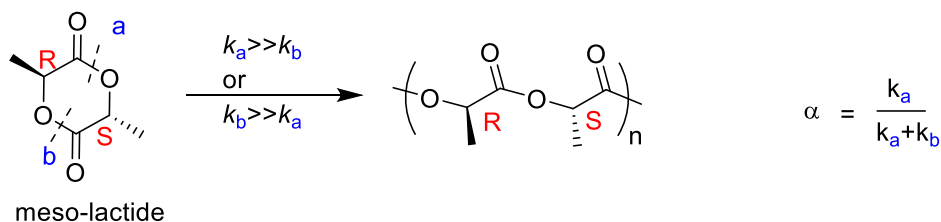
Figure 2.4 A catalyst's preference for a certain enantiomeric site is determined by the rate at which it ring-opens at one site over the other (a vs. b), quantified by the α-value.[106]

The chain tacticity arising from catalytic systems with high enantiomorphic site control, can be approximated by substituting the α-value into Equation 2.3 below. These equations, however, underestimate the influence of defect tetrad peaks and, if used with catalyst systems which operate through any degree of chain-end control, the calculated polymer tacticity will be artificially inflated.

$P_i = [sis]$

$$\alpha = \frac{z}{(x + z)}$$

$P_s = [sss] + [ssi/iss/isi]$

$$[sss] = \tfrac{1}{2}[\alpha^3 + (1 - \alpha)^3 + \alpha^2 + (1 - \alpha)^2]$$

$$[sis] = \alpha(1 - \alpha)$$

$$[ssi/iss/isi] = 3(\tfrac{1}{2}[\alpha^2(1 - \alpha) + \alpha(1 - \alpha)^2])$$

Equation 2.3 Equation to calculate tacticity for polymers formed from *meso*-LA using the enantiotopic selectivity ratio, α-value.[103]

Insertion errors are corrected differently depending on the stereocontrol mechanism. Examination of defect tetrad peaks in the methine region of the $^{13}C\{^1H\}$ NMR spectrum can give an indication of which control mechanism dominates during polymerization. In systems operating under CEC, defects are propagated until the next insertion error occurs, giving a ratio of 1:1:1 for the defect tetrads iis:isi:sii (Figure 2.5). When considering CEC systems polymerizing *meso*-lactide, the same ratio applies to the defect tetrads ssi:sis:iss (Figure 2.6).

In ESC, because the tacticity is determined by the chirality at the metal centre, mistakes are corrected with the next insertion, giving a 1:2:1:1 ratio for the defect tetrads iis:isi:sis:sii when polymerizing *rac*-lactide (Figure 2.5), and ssi:sis:isi:iss when polymerizing *meso*-lactide (Figure 2.6).

To wholly characterize and compare polymers of different tacticity, it is important to supplement NMR analysis with other techniques such as differential scanning calorimetry, viscometry or rheology (see Chapter 3).
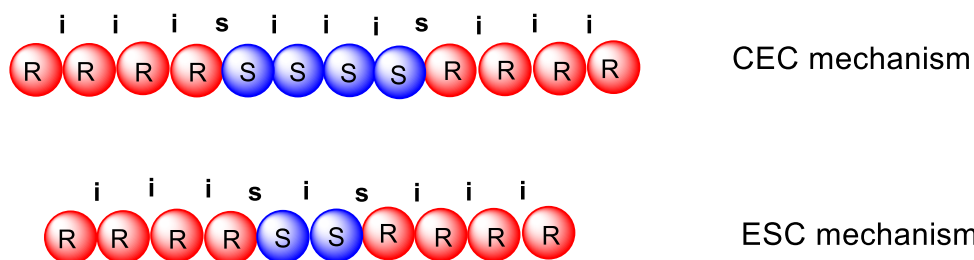
Figure 2.5 Possible insertion errors from ROP of *rac*-lactide *via* chain-end control (CEC) and enantiomorphic site control (ESC) (where i denotes isotactic enchainment, (relative stereochemistry of adjacent lactyl units are the same) and s denotes syndiotactic enchainment (relative stereochemistry of adjacent lactyl units are different)).
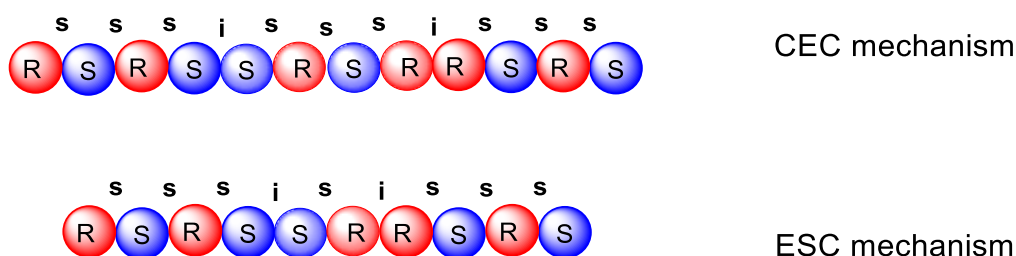
Figure 2.6 Possible insertion errors from ROP of *meso*-lactide *via* chain-end control (CEC) and enantiomorphic site control (ESC) (where i denotes isotactic enchainment, (relative stereochemistry of adjacent lactyl units are the same) and s denotes syndiotactic enchainment (relative stereochemistry of adjacent lactyl units are different)).

2.1.4   Catalysts for synthesizing PLA with controlled microstructure.

In the last few decades a number of examples of coordination complexes which effectively control the molecular weight distribution and stereochemistry of lactide isomers have been reported (major contributions are summarized in Figure 2.7).[27] The first notable example comes from Spassky and co-workers who in 1996 reported the synthesis of a chiral aluminum salen binaphthalene complex which was highly stereoselective for the ROP of *rac*-lactide.[39] The resulting polymer had 88% optical purity and showed good molecular weight control due to suppression of transesterification reactions. Following this landmark report, many researchers

have made important contributions to this field. Their reports convey a variety of ligand motifs to support a range of metals from the main group,[48,107-109] transition,[110-113] and lanthanide[114] metals, achieving highly isotactic or heterotactic PLA with good control over molecular weights while using mild reaction conditions.[27]

Despite the vast amount of work going into the polymerization of *rac*-LA, there are far fewer examples of stereoselective catalysts for the ROP of *meso*-LA.[37] The landmark catalyst in this field was reported by Ovitt and Coates in 1999. In this report, a chiral aluminum salen binaphthalene complex (Figure 2.7 **I**[39]) catalyzed the ROP of *meso*-LA, affording highly syndiotactic PLA in 14 h at 70 °C ($P_s = 0.96$, $Đ \approx 1.1$).[103,106] Two years after their pioneering report, Coates *et al.* described a series of zinc(II) alkoxides bearing easily functionalized bulky β-diiminate (BDI) groups which were shown to catalyze the ROP *meso*-LA, giving syndiotactically enriched polymer at 0 °C in under 4 hours ($P_s = 0.76$, $Đ \approx 1.1$).[115]
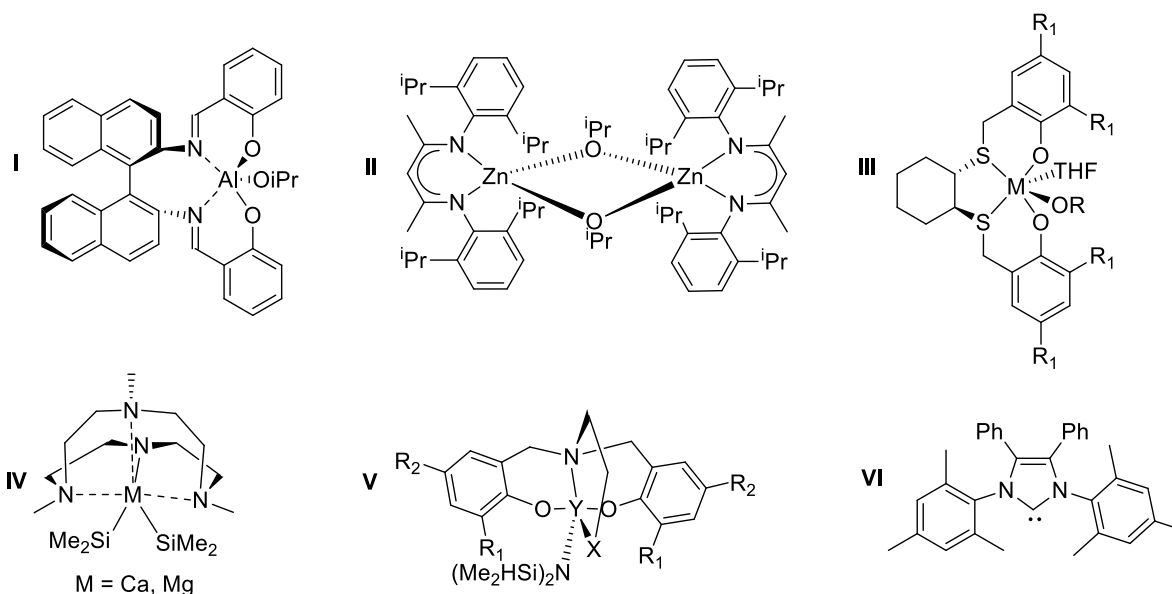
Figure 2.7 Catalysts reported for the ROP of *meso*-lactide. **I**–Coates 1999[103] **II**–Coates 2001[115] **III**– Okuda 2010[116] and 2012 [117] **IV**–Okuda 2011[118] **V**–Carpentier 2006[119] **VI**–Hendrick 2006.[104]

In 2010, Okuda *et al.* communicated the synthesis of Group 3 metal complexes bearing (OSSO)-bis(phenolate) ligands with varying levels of rigidity in their backbones. These catalysts polymerized *meso*-LA to form moderately to highly syndiotactic PLA in under an hour at room temperature (P_s = 0.71-0.93); however, they did not show good control of molecular weight ($Đ$ = 1.3-2.2).[116] By switching to Group 4 metals, the OSSO-type catalysts showed improved molecular weight control ($Đ$ = 1.0-1.2) and high heteroselectivity towards *meso*-LA at 100 °C in toluene (P_i = 0.90).[117] Further work from Okuda and co-workers demonstrated how scandium complexes supported by sterically dominating tetradentate cyclen-derived (NNNN) macrocycles were highly active towards *meso*-LA giving moderately syndiotactic PLA at room temperature (P_s = 0.74, $Đ$ = 1.7-2.1).[118]

Other systems have shown varied success for the polymerization of *meso*-LA. In 2006, Carpentier *et al.* described the synthesis of yttrium complexes supported by flexible dianionic alkoxy-amino-bisphenolate ligands which catalyzed the polymerization of *meso*-LA to give modest syndiotactic enrichment (P_s = 0.75) under ambient conditions (20 °C) in less than an hour, albeit with decreased control over molecular weight ($Đ \approx 1.2$).[114] Hillmyer and Tolman diverged from the use of bulky supporting ligands in 2009 and reported a simple salt system using $InCl_3$, benzyl alcohol and triethylamine which formed a catalytic species *in situ* that subsequently polymerized *rac*-lactide to give highly heterotactic PLA (P_i = 0.96); however only atactic PLA was achieved from the polymerization of *meso*-LA (P_s = 0.56).[120,121] By exploiting a metal-free system, high levels of heterotacticity (P_i = 0.83, $Đ \approx 1.3$) at −40 °C were achieved by Hendrick and co-workers who used an organocatalyst comprising of *N*-heterocyclic carbenes.[104]

The origin of selectivity in these systems is often unclear. Systems reported by Coates generate differently ordered PLA microstructures when using an enantiopure complex compared to a racemic version of the same catalyst (Figure 2.7 **I**).[47,103] For these systems it has been proposed that stereoselectivity for the catalysts arises mainly through enantiomorphic site control. Shown in Figure 2.7 **II** and **V** are two achiral coordination complexes, a bulky β-diiminate (BDI) zinc complex and a yttrium complex supported by a dianionic alkoxy-amino-bisphenolate ligand, which show a preference for ordered microstructures most likely occurring through chain-end control. [115,122]

Even with the concerted effort to control the polymerization of *meso*-LA, the systems discussed above either show insufficient molecular weight control *or* require elevated temperatures and long reaction times to achieve high monomer conversions. The Mehrkhodavandi group has reported two families of indium catalysts active for the ROP of *rac*-LA (Chart 2.1) The first-generation catalyst is a dinuclear asymmetrically bridged diaminophenolate system $[(NNO)InCl]_2(\mu\text{-Cl})(\mu\text{-OEt})$ (**A**) (Chart 2.1), which exerts moderate isoselectivity ($P_m \sim 0.6$, $Đ \approx 1.0$) for the ROP of *rac*-LA.[123,124] The second generation catalysts $[(ONNO)In(OEt)]_2$ (**B**) are more active and show greater stereocontrol towards *rac*-LA giving isotactically enriched polymers ($P_m \sim 0.75$, $Đ \approx 1.5$).[125]

In the following sections the ring-opening polymerization behaviour of chiral catalysts **A** and **B** towards *meso*-LA and an examination of the resulting syndiotactically enriched polymers will be discussed.

Chart 2.1 Chiral indium based catalysts (*RR/RR*)-[(NNO)InCl]$_2$(μ-Cl)(μ-OEt) (**A**) and (*RR/RR*)-[(ONNO)In(μ-OEt)]$_2$ (**B**).

(±)/(RR/RR)-[(NNO)InCl]$_2$(μ-Cl)(μ-OEt) (**A**)   (±)/(RR/RR)-[(ONNO)In(μ-OEt)]$_2$ (**B**)
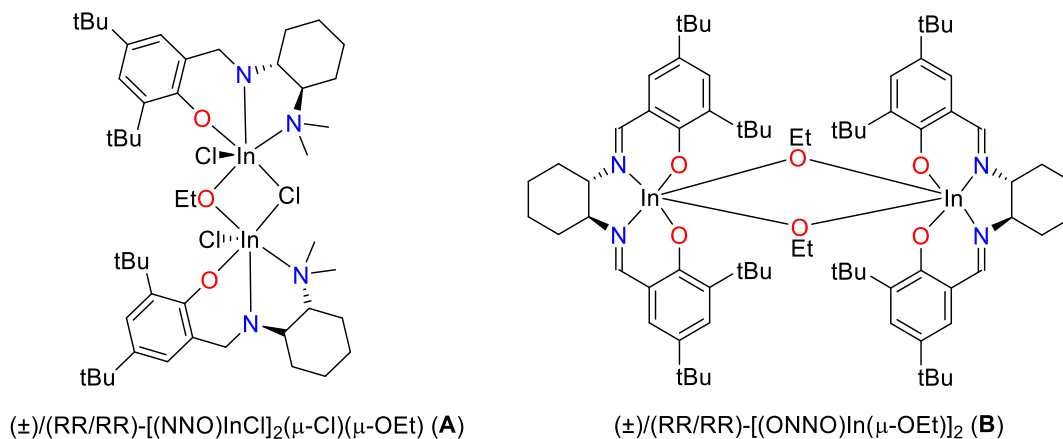
2.2 Results and discussion

2.2.1   Purification of *meso*-lactide.

Meso-LA is a by-product of lactide production from L-lactic acid. During monomer processing, substantial amounts of *meso*- and D-LA are produced. When *meso*-LA is isolated, it is contaminated with significant amounts of D- and L-LA. These impurities can cause the incorporation of *rac*-LA units into the growing polymer causing stereodefects in the chain. Stereodefects interrupt the chain sequence, decreasing the crystallinity and diminishing polymer properties. To adequately analyse how the catalysts behave towards *meso*-LA, rigorous purification of *meso*-LA is necessary.

Meso-LA, obtained from Purac Inc., was analysed by ^{1}H NMR spectroscopy and was shown to contain on average 12% *rac*-LA impurities (Figure 2.8). Sublimation of *meso*-LA was successful in removing *rac*-LA impurities, but this technique was slow and low yielding. A more

47

efficient method of purification was achieved by drying a solution of *meso*-LA in DCM over MgSO$_4$ followed by re-isolation *via* vacuum filtration. After at least five recrystallizations from warm dry isopropanol, *meso*-LA with >95% purity (by GC-MS) can be obtained (see appendix A).
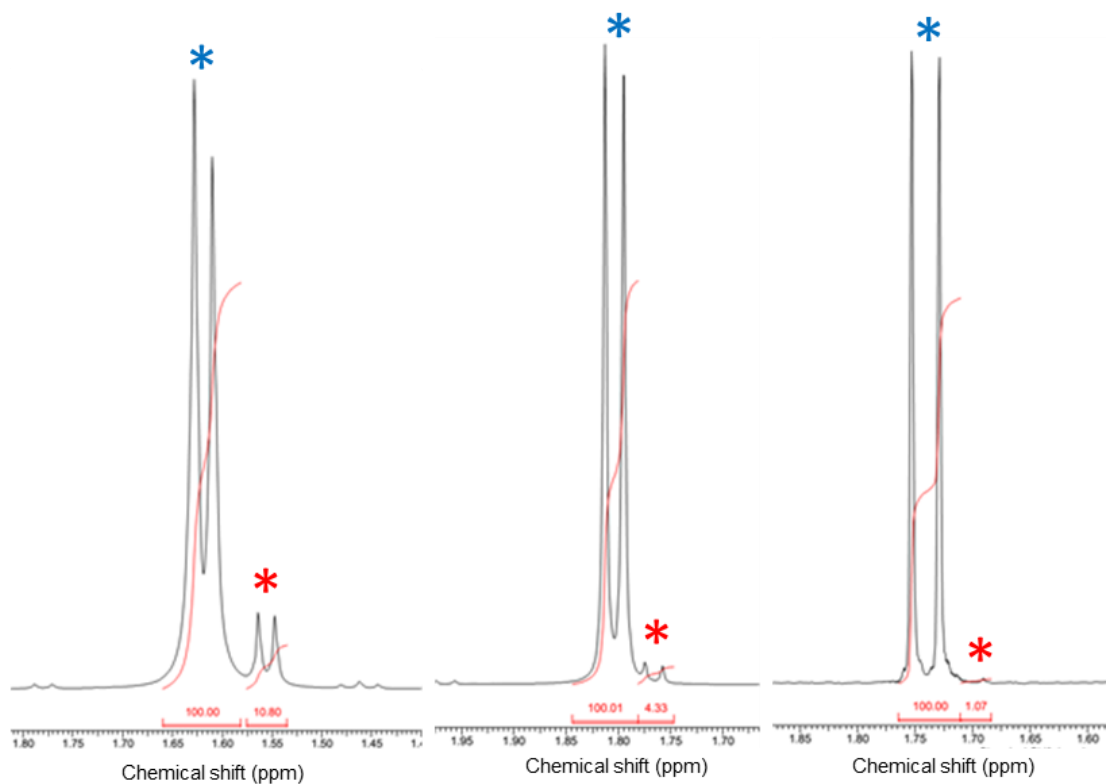
Figure 2.8 ^{1}H NMR spectra (CDCl$_3$, 25 °C, 300 MHz) of *meso*-lactide (blue star) and diminishing *rac*-lactide impurity (red star) a) after drying b) after three recrystallizations from [i]PrOH c) after five recrystallizations from [i]PrOH.

2.2.2 Polymerization of *meso*-lactide with tetra- and tridentate indium alkoxide complexes.

The racemic and enantiopure versions of proligands: asymmetrically substituted trans-diaminocyclohexane ($\pm$)- or (*RR*)-H(NNO) and a tetradentate diimino-diol ($\pm$)- or (*RR*)-H$_2$(ONNO), can be prepared according to known methods.[40,123,125] Deprotonation of these proligands with benzyl potassium followed by addition of one equivalent of indium trichloride yields the respective indium chloride species. Racemic and enantiopure alkoxy complexes, [(NNO)InCl]$_2$(μ-Cl)(μ-OEt)] ($\pm$)- and (*RR/RR*)-**A** and [(ONNO)In(μ-OEt)]$_2$ ($\pm$)- and (*RR/RR*)-**B** can then be obtained by reaction with potassium or sodium ethoxide, respectively (Scheme 2.1 and Scheme 2.2, only the *RR/RR* enantiomers are shown).

Scheme 2.1 Synthesis of *RR/RR*-[(NNO)InCl]$_2$(μ-Cl)(μ-OEt)] (*RR/RR*)-**A**.
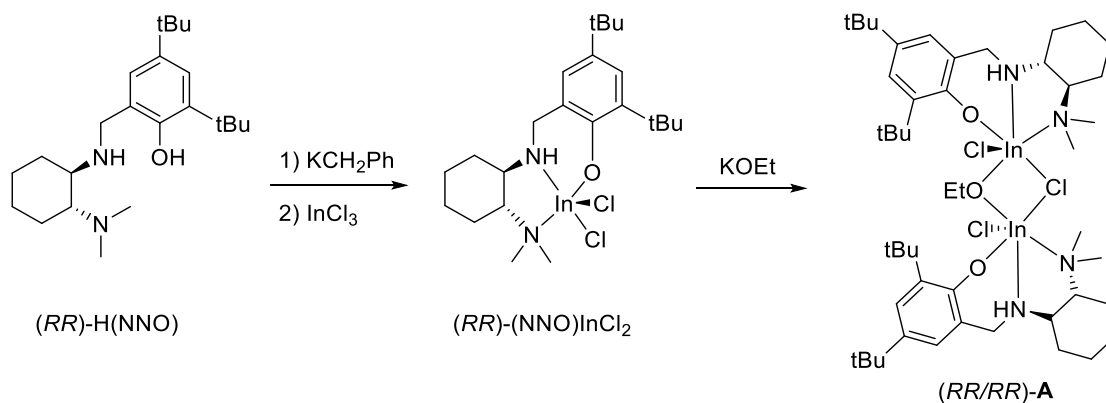
Scheme 2.2 Synthesis of *RR/RR*-[(ONNO)In(μ-OEt)]₂ (*RR/RR*)-**B**.

(*RR*)-H₂(ONNO)　　　　(*RR*)-(ONNO)InCl　　　　(*RR/RR*)-**B**
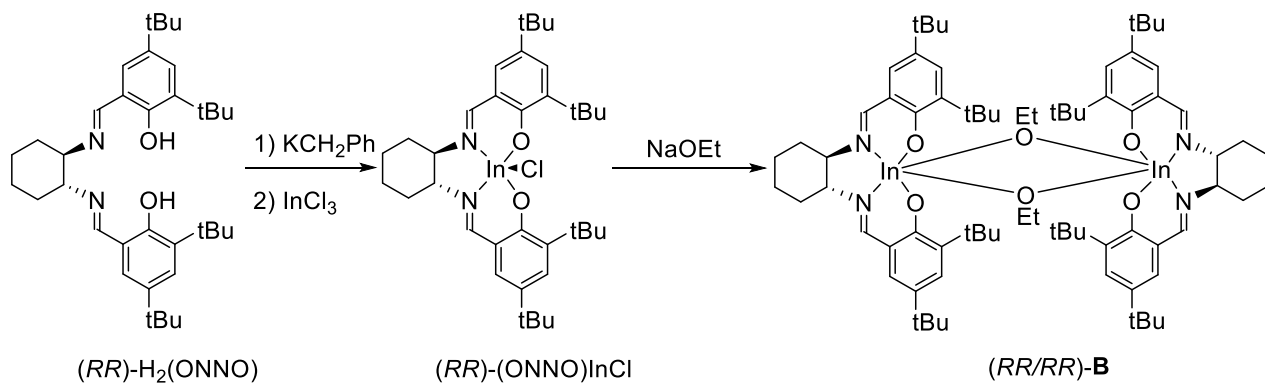
Polymerization reactions with the appropriate volumes of **A** and **B** (2.8 mM) and *meso*-LA (2.78 M) were carried out in DCM at room temperature for 16 and 4 h, respectively (Table 2.1 and Table 2.2). Conversions and polymer tacticity were determined by ^{1}H and ^{1}H{^{1}H} NMR spectroscopy (CDCl₃, room temperature). Molecular weight (M_n) and dispersity ($Đ$) are obtained *via* gel permeation chromatography (GPC).

Polymers formed from the reaction of (±)- or (*RR/RR*)-**A** with *meso*-LA show good agreement between the calculated and experimental molecular weights (Figure 2.9). Low molecular weight distributions ($Đ$ < 1.10) indicate that the polymerization is living as previously observed for *rac*-LA.[40,123] Polymerizations with **B** show less control over molecular weight at higher monomer loadings than those carried out with **A** due to previously described depolymerization reactions catalysed with **B** as observed by transesterification detected MALDI-ToF mass spectrometry data and dispersity values greater than 1.10 (Figure 2.9).[126]
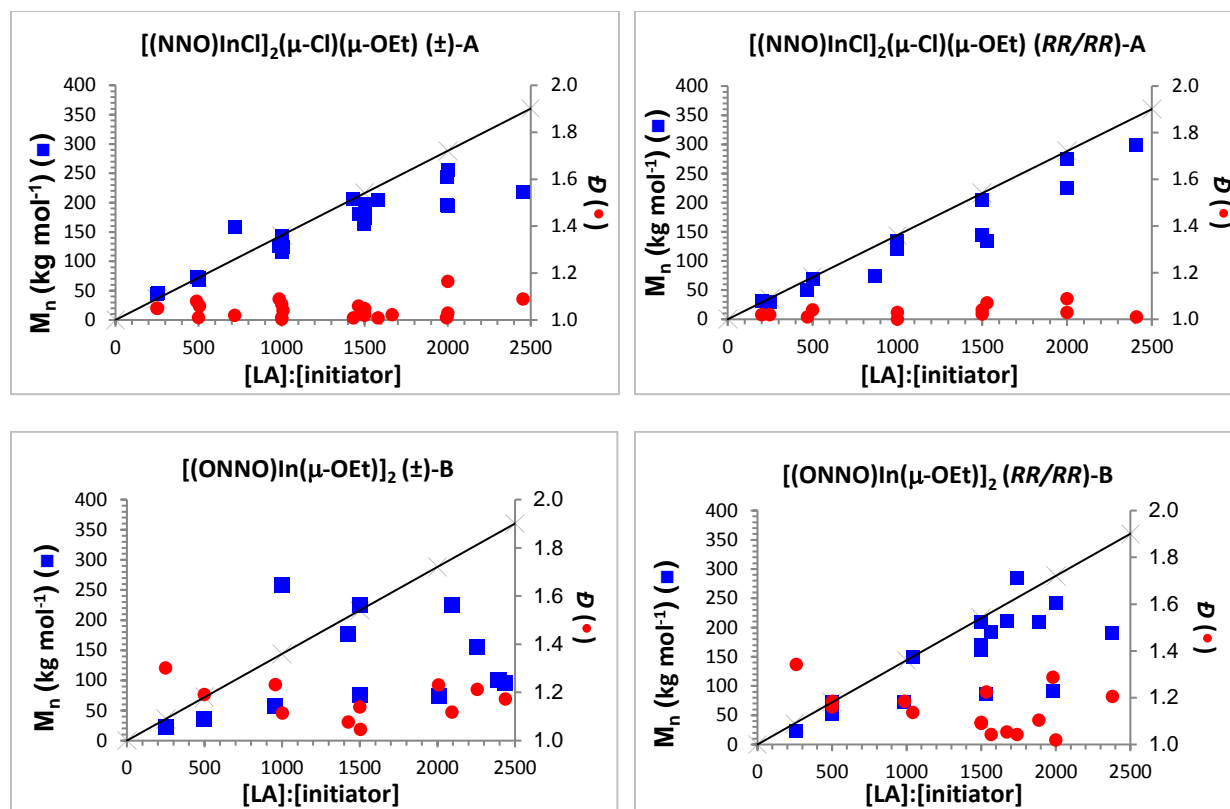
Figure 2.9 Plot of observed PLA M_n (■) and $Đ$ (●) as functions of added *meso*-LA for (±)- (*RR/RR*)-**A** (top) and for (±)- (*RR/RR*)-**B** (bottom). (M_n = number averaged molecular weight, $Đ$ = dispersity index). The black line indicates theoretical M_n values based on the [LA]:[initiator] ratio at 100% conversion. All reactions were carried out at room temperature for 16 h (**A**) or 4 h (**B**) in DCM and polymer samples were obtained at >90% conversion.

Analysis of the methine region of polymers resulting from catalyst **A** by $^1H\{^1H\}$ NMR spectroscopy elucidates the microstructures of isolated material (Figure 2.10). Over the range of monomer to initiator ratios, the PLA produced by (*RR/RR*)-**A** shows syndiotactic enrichment (0.71 > P_s > 0.73). PLAs isolated from (±)-**A** display little syndiotacticity, with P_s values of 0.54-0.56 (Table 2.1, entries 8-14). This trend is opposite to that seen with *rac*-LA where (±)-**A** shows greatest isoselectivity.

Table 2.1 Polymerization of lactide with dinuclear indium complexes ($\pm$)-**A** and (*RR/RR*)-**A**.[††]

Entry	Catalyst	[LA]:[initiator]	$M_{\text{n,theo}}$ (g mol^{-1})^a	$M_{\text{n,eGPC}}$ (g mol^{-1})^b	$P_s{}^c$	$P_s{}^d$	$Đ$
1	(*RR/RR*)-**A**	250	35400	30200	0.71	0.83	1.02
2	(*RR/RR*)-**A**	470	66400	50300	0.71	0.83	1.04
3	(*RR/RR*)-**A**	870	79800	73800	0.72	0.83	1.00
4 ^{e}	(*RR/RR*)-**A**	1000	146000	136000	0.76	0.86	1.00
5	(*RR/RR*)-**A**	1500	21800	204000	0.72	0.82	1.04
6	(*RR/RR*)-**A**	2000	284000	275000	0.73	0.84	1.03
7	(*RR/RR*)-**A**	2400	344000	299000	0.73	0.84	1.07
8	($\pm$)-**A**	250	35300	44300	0.55	0.81	1.02
9	($\pm$)-**A**	490	69600	72700	0.55	0.81	1.01
10	($\pm$)-**A**	990	141000	127000	0.56	0.80	1.01
11	($\pm$)-**A**	1006	144000	112000	0.58	0.81	1.10
12	($\pm$)-**A**	1500	213000	198000	0.56	0.82	1.02
13	($\pm$)-**A**	2000	281000	255000	0.56	0.82	1.03
14	($\pm$)-**A**	2500	350000	219000	0.53	0.82	1.09

Reactions were carried out in DCM at 25 °C to greater than 90% conversion, [**A**]$_o$ ≈ 2.8 mM; ^{a} Calculated from $M_{\text{n,theo}}$ = (144 g mol^{-1} × conversion × [LA]/[initiator]). ^{b} Absolute molecular weights were determined by triple detector GPC (gel permeation chromatography) *via* Universal Calibration (THF 4 mg mL^{-1}, flow rate = 0.5 mL min^{-1}, dn/dc = 0.044 mL g^{-1}). ^{c} Calculated from ^{1}H{^{1}H} NMR spectra using Equation 2.2.[46] ^{d} Calculated from ^{1}H{^{1}H} NMR spectra using Equation 2.3.[103] ^{e} Experiment carried out at 0 °C for 48 hours.

[††] Tacticity values in this table differ from those published in Chile, L.-E.; Mehrkhodavandi, P.; Hatzikiriakos, S. G.; *Macromolecules* **2016**, *49*, 909.
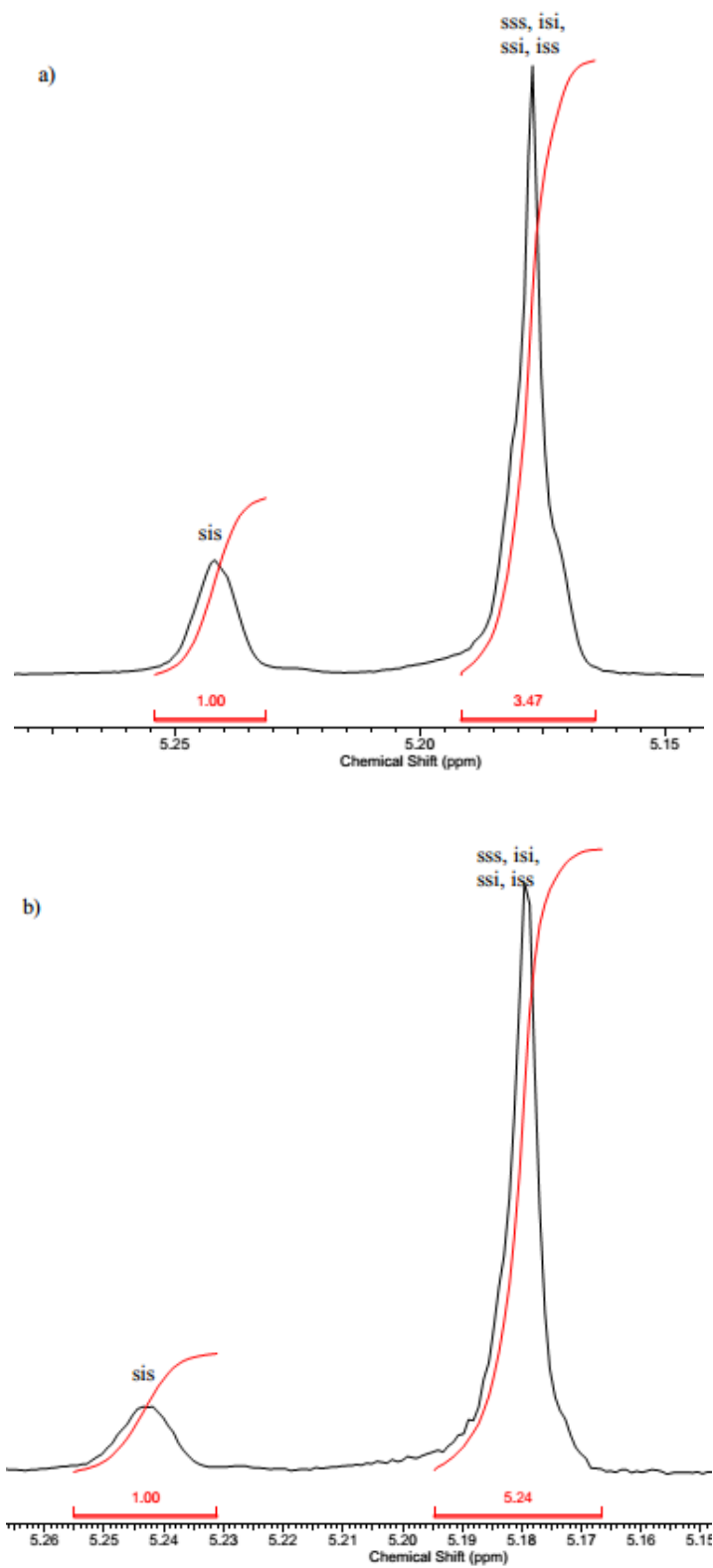
Figure 2.10 ¹H{¹H} NMR spectra (CDCl₃, 25 °C, 600 MHz) of polymers generated from a) (±)-**A** and b) (*RR/RR*)-**A**.

There have been cases reported where greater stereoselectivity has been observed at lower temperatures. Hendrick *et al.* observed a marked increase in syndioselectivity (P_i = 0.62 to 0.83) by reducing polymerization temperatures from 25 °C to −40 °C.[104] A zinc β-diiminate (BDI) complex investigated by Coates imparts moderate syndiotacticity at 0 °C (P_s = 0.76), but no room temperature experiments with *meso*-LA were reported.[115] Polymerizations with (*RR/RR*)-**A** exhibit modest syndiocontrol. So, low temperature experiments at 0 °C were conducted for 48 hours in an attempt to enhance selectivity. Good agreement with calculated molecular weights and high conversions are seen, but a significant increase in syndiotacticity was not observed (Table 2.1, entries 4 and 11).

Inspection of the $^{13}C\{^1H\}$ NMR spectrum of polymers generated from (*RR/RR*)-**A**, confirms that the sss tetrad is the major linkage present in the polymer chain, giving more evidence towards this catalyst being syndioselective. The presence of all four other defect peaks indicates both CEC and ESC stereocontrol mechanisms are in action during polymerization, but the higher ratio of the sis peak compared to the isi peak implies that ESC is the major mechanism acting in this system (Figure 2.11).

Included in Table 2.1 are P_s values calculated using Equation 2.3 for comparison. Syndioselective catalyst (*RR/RR*)-**A**, shows P_s values which differ by 13%, whereas in the less selective system, (±)-**A**, the variance is close to 30%, illustrating the limitations of the using enantiotopic selectivity to approximate these values.
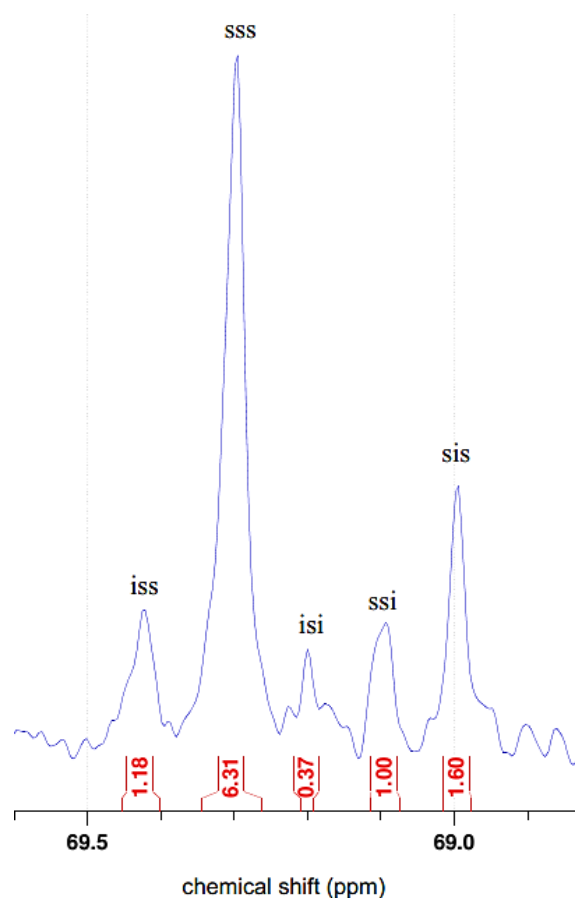
Figure 2.11 Inverse-gated $^{13}C\{^1H\}$ NMR spectrum (CDCl$_3$, 25 °C, 100 MHz) for a polymer generated from (*RR/RR*)-**A**.

Both enantiopure and racemic versions of catalyst **B** are isoselective for the ring-opening polymerization *rac*-LA, forming polymers with P_m values of ~ 0.73. These isorich polymers have good molecular weight control for [LA]:[initiator] ratios of up to 1000 albeit with high dispersities (*Đ* ~1.5).[125] Catalyst **B** displays nominal syndiocontrol towards the polymerization of *meso*-LA compared with catalyst **A**, giving moderately heterotactic polymers with P_s values ranging from 0.35 to 0.39 for (±)-**B** and 0.42 to 0.43 for (*RR/RR*)-**B** (Table 2.2 and Figure 2.12).

Analysis of the defect tetrads in the $^{13}C\{^1H\}$ NMR spectra for polymers generated from (±)-**B** confirms that the isi and sis tetrads are most prominent, giving rise to the heterotactic

microstructure (Figure 2.13). The presence of all four defect tetrads is an indication that both CEC and ESC are acting during polymerization, though from the defect peaks alone, it is difficult to postulate which mechanism is dominant. Using the enantiotopic selectivity approximation only holds true for systems acting through ESC, and that this approximation completely fails with catalyst **B**, predicating moderate syndiotacticity (Table 2.2). These results suggest that CEC is the major control mechanism acting during polymerization of *meso*-LA.

Table 2.2 Polymerization of *meso*-lactide with dinuclear indium complexes (±)-**B** and (*RR/RR*)-**B**.[‡‡]

entry	Catalyst	[LA]:[initiator]	$M_{n,theo}$ (g mol^{-1})^a	$M_{n,GPC}$ (g mol^{-1})^b	$P_s{}^c$	$P_s{}^d$	$Đ$
1	(*RR/RR*)-**B**	250	35300	30200	0.51	0.77	1.02
2	(*RR/RR*)-**B**	490	69900	48900	0.43	0.77	1.22
3	(*RR/RR*)-**B**	980	141000	74700	0.43	0.76	1.25
4	(*RR/RR*)-**B**	1400	201000	103000	0.43	0.78	1.22
5	(*RR/RR*)-**B**	1800	260000	105000	0.42	0.78	1.18
6	(*RR/RR*)-**B**	2300	328000	121000	0.42	0.78	1.26
7	(±)-**B**	250	35300	31600	0.46	0.77	1.22
8	(±)-**B**	490	70600	52500	0.39	0.76	1.17
9	(±)-**B**	800	115000	52100	0.35	0.77	1.14
10	(±)-**B**	1300	190000	110000	0.34	0.77	1.13
11	(±)-**B**	2000	283000	143000	0.35	0.77	1.17
12	(±)-**B**	2500	353000	146000	0.35	0.77	1.14

Reactions were carried out in DCM at 25 °C to greater than 90% conversion, [**B**]$_o$ ≈ 2.7 mM; ^{a} Calculated from $M_{n,theo}$ = (144 g mol^{-1} × conversion × [LA]/[initiator]). ^{b} Absolute molecular weights were determined by triple detector GPC (gel permeation chromatography) *via* Universal Calibration (THF 4 mg mL^{-1}, flow rate = 0.5 mL min^{-1}, dn/dc = 0.044 mL g^{-1}). ^{c} Calculated from ^{1}H{^{1}H} NMR spectra using Equation 2.2.[46] ^{d} Calculated from ^{1}H{^{1}H} NMR spectra using Equation 2.3.[103]

[‡‡] Tacticity values in this table differ from those published in Chile, L.-E.; Mehrkhodavandi, P.; Hatzikiriakos, S. G.; *Macromolecules* **2016**, *49*, 909.
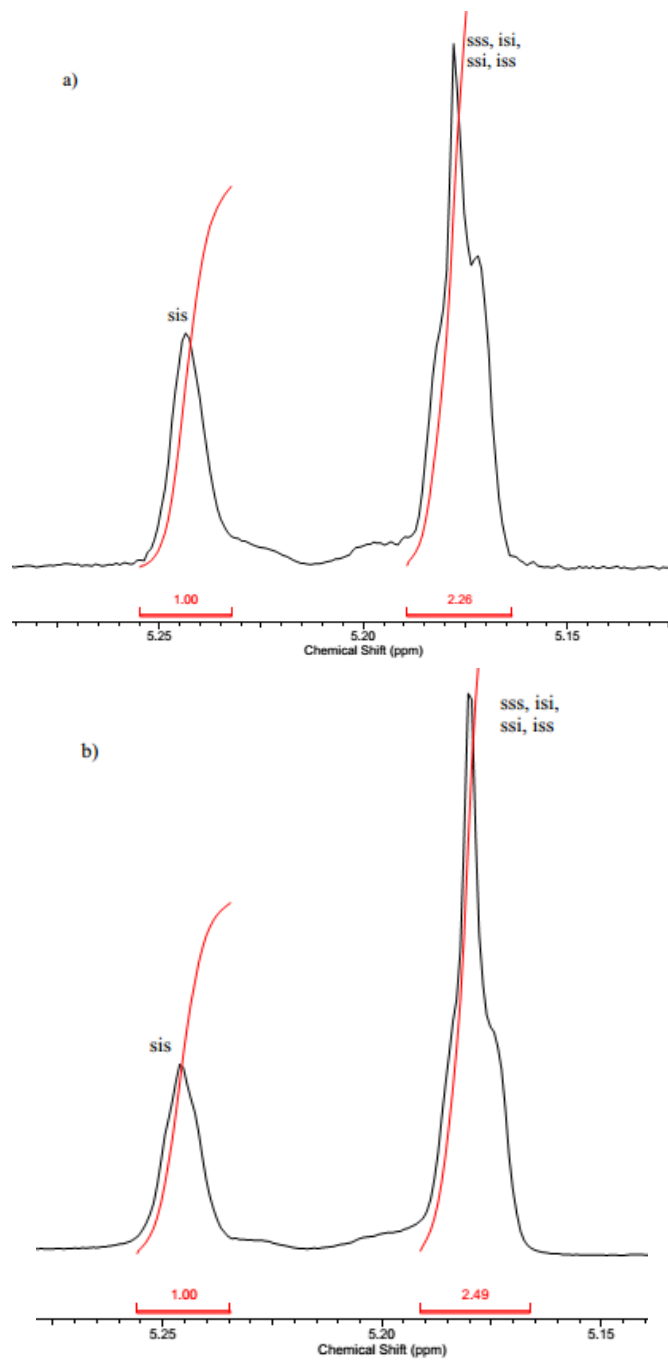
Figure 2.12 ^{1}H{^{1}H} NMR spectra (CDCl$_3$, 25 °C, 600 MHz) of polymers generated from a) (±)-**B** and b) (*RR/RR*)-**B.**
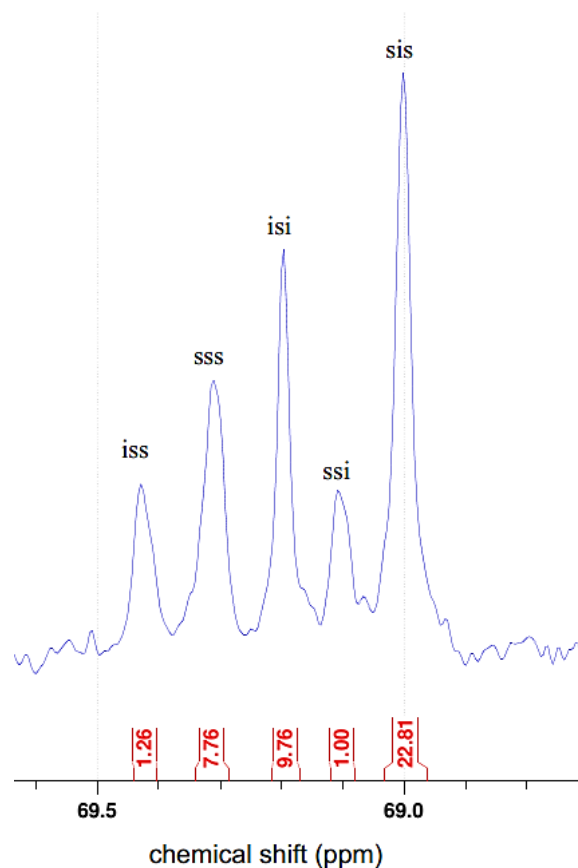
Figure 2.13 Inverse-gated $^{13}C\{^1H\}$ NMR spectrum (CDCl$_3$, 25 °C, 100 MHz) for a polymer generated from (±)-**B**.

2.2.3   In situ studies.

Polymerization of *meso*-LA using (±)- and (*RR/RR*)- analogues of complexes **A** and **B** can be monitored *in situ* using ^1H NMR spectroscopy. To determine the propagation rate, k_{obs}, experiments were performed at room temperature in CDCl$_3$ with a monomer to initiator ratio of 200 and monitored to at least 90% conversion. The plots of ln[LA] vs. time for all catalysts are linear after a short initiation period for catalyst **A**, and a longer period for **B** (Figure 2.14, Table 2.3). The long initiation period for **B** is due to dissociation of the dimer prior to polymerization.[127] The linear relationship between concentration and time implies that first order kinetics (with

respect to the monomer) is obeyed for these systems. Table 2.3 compares rates of reaction for all catalysts and the difference LA isomers. Generally, *meso*-LA is polymerized at a slower rate compared to the other isomers.[33] In the solid state, L- and D-LA adapt twisted boat geometries to minimize the interaction between the two carbonyl oxygens.[128] This distorted structure increases ring strain within the monomer which drives ring-opening polymerization. Meso-LA, with two different configurations at the stereocentres, adopts a more twisted planar geometry, stabilizing its ground state.[32] The ~4 kcalmol^{-1} difference in ground-state energy translates to a slower rate of living ring-polymerization for *meso*-LA compared to the other two isomers (Table 2.3).

Polymerization rate kinetics were explored to elucidate the mechanisms through which catalyst **A** acts (Figure 2.4). (±)-**A** was previously shown to be a racemic mixture of (*RR/RR*)-**A** + (*SS/SS*)-**A** and not a heterochiral dimer and thus, if acting through ESC, one enantiomer of the catalyst should favour the coordination of only one isomer of LA.[40] Confirming this finding, a high selectivity factor for the polymerization of L-LA vs. D-LA with (*RR/RR*)-**A** ($k_L/k_D \sim 14$) was shown, but this only resulted in atactic PLA from *rac*-LA.[40] Figure 2.15 shows the energies for species in the polymerization of *rac*-LA with (*RR/RR*)-**A** as determined by DFT calculations by Maron *et al.* in 2013.[129] The rate-determining step was shown to be the nucleophilic addition of the propagating alkoxide into the carbonyl C-O bond (k_1). The energy of a matched pair is stabilized compared to a mismatch ($NA_L < NA_D$). However, similar energies were calculated for the ring-opening pathways for both a match and a mismatch (k_2) which would result in the generation of atactic PLA from *rac*-LA despite the high selectivity factor.
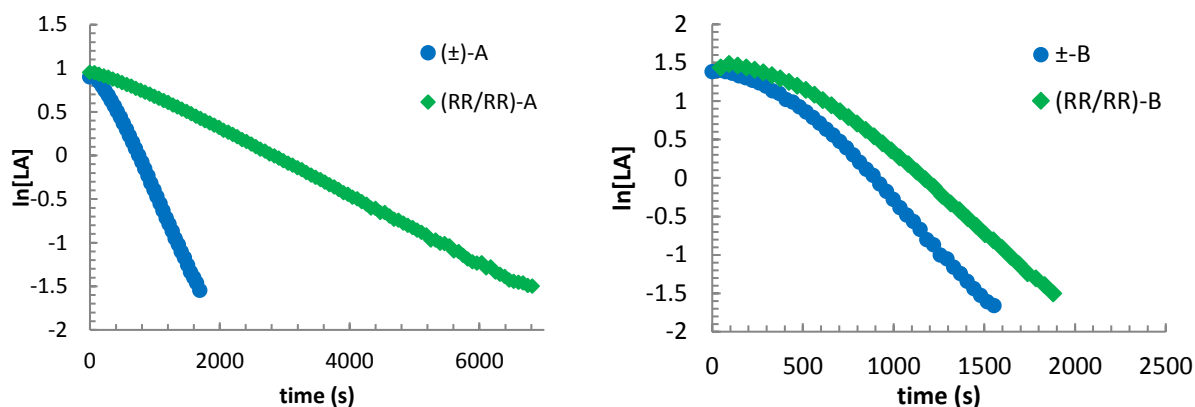
Figure 2.14 Plot of ln[LA] versus time for polymerization of *meso*-LA catalysed with a) left, (±)-**A** (•) and (*RR/RR*)-**A** (◆) and b) right, (±)-**B** (•) and (*RR/RR*)-**B**(◆). Reactions were carried out in an NMR tube at 25 °C and followed to 90% conversion. 1,3,5-trimethoxybenzene (TMB) was used as internal standard. All reactions were carried out with 200 eq. of LA in CDCl$_3$ at 25 °C and followed to 90% conversion by ^{1}H NMR spectroscopy [**A**] = 0.0023 M, [LA] = 0.46 M. [**B**] = 0.0018 M, [LA] = 0.36 M. The value of k_{obs} was determined from the slope of ln[LA] vs. time, averaged from at least three experiments.

Table 2.3 Rates of polymerization of lactide isomers with various catalysts.

Entry	Catalyst	k_{obs} (× 10^{-3} s^{-1}) for			$P_s{}^a$	$P_m{}^b$
		meso-LA	*rac*-LA	L-LA		
1	(±)-**A**	1.61(0.03)^c	1.72(0.16)^d	2.98(0.09)^d	0.52	0.61
2	(*RR/RR*)-**A**	0.35(0.5)^c	0.62(0.16)^d	3.4(0.6)^d	0.73	0.48
3	(*SS/SS*)-**A**	0.31(0.03)^c	0.70(0.05)^d	0.27(0.7)^d	0.71	0.49
4	(±)-**B**	2.52(0.02)^e	2.3(0.5)^f	2.6(0.5)^e	0.36	0.74
5	(*RR/RR*)-**B**	2.24(0.01)^e	0.46(0.09)^f	2.2(0.5)^e	0.42	0.77

Values shown in parentheses are standard errors. ^{a} P_s values shown for *meso*-LA. ^{b} P_m values shown for *rac*-LA. ^{c}[LA] = 0.46 M. [catalyst] = 0.0023 M. ^{d} [LA] = 0.46 M. [catalyst] = 0.0024 M;[40] ^{e} [LA] = 0.36 M. [catalyst] = 0.0018 M.[125] ^{f}[LA] = 0.45 M. [catalyst] = 0.0023 M.[122] $^{c-f}$Reactions were carried out in an NMR tube at 25 °C and followed to 90% conversion. 1,3,5-trimethoxybenzene (TMB) was used as internal standard. The value of k_{obs} was determined from the slope of ln[LA] vs. time, averaged from three experiments.
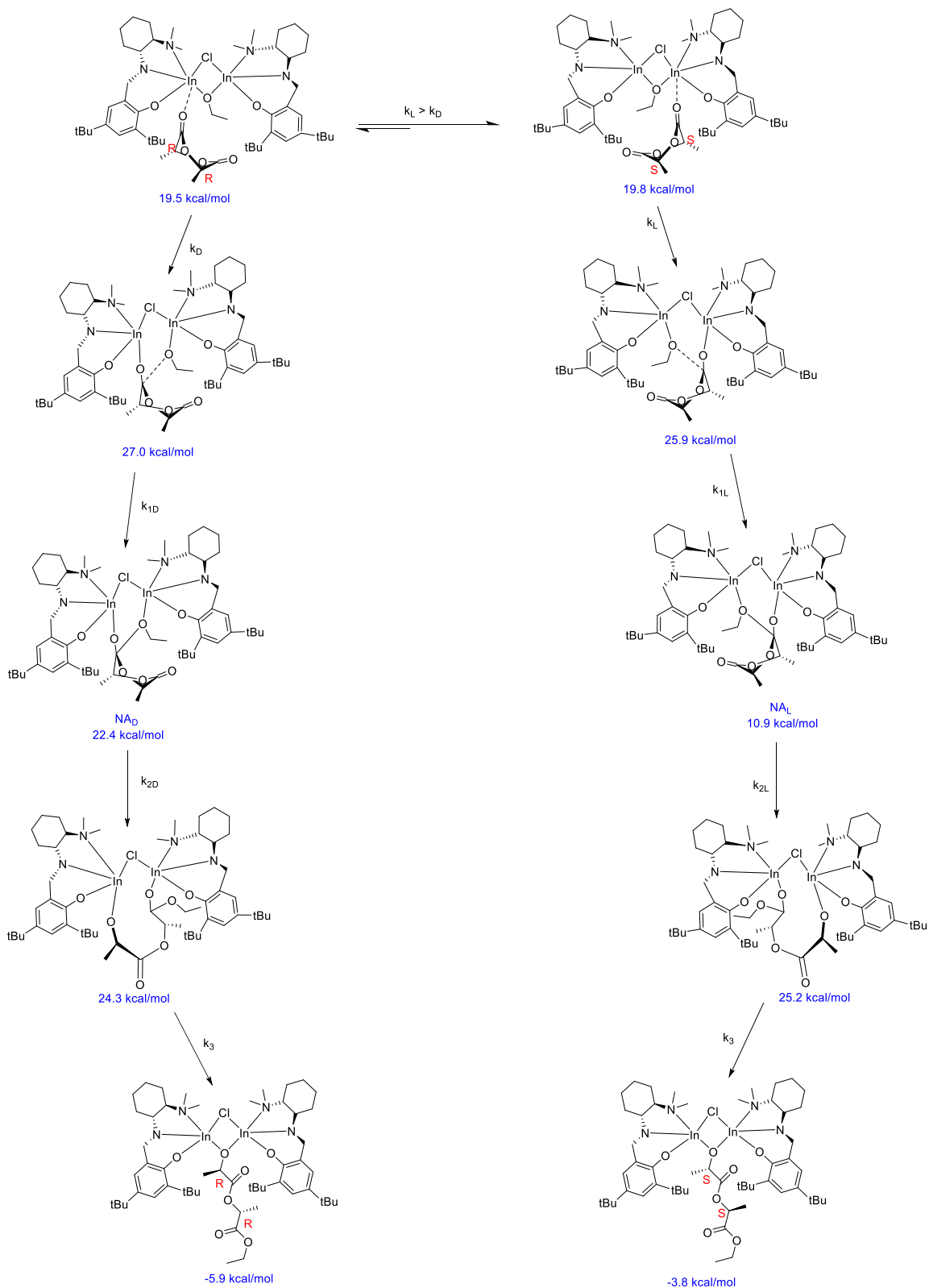
Figure 2.15 Mechanism for ring-opening of L- or D-LA by (*RR/RR*)-**A**.[129]

The k_{obs} value for polymerization of *meso*-LA with (*RR/RR*)-**A** is over five times slower than its racemic analogue, (±)-**A** (Figure 2.14, Table 2.3, entries 1-2). The smaller k_{obs} value observed for (*RR/RR*)-**A** translates to a greater syndiotacticity for the enantiopure catalyst, contrasting the observed behaviour towards *rac*-LA. Based on the analysis of the theoretical calculations discussed above, this observation implies that: a) kinetic preference for the different acyl-oxygen sites in *meso*-LA is either more significant that than between D- and L-LA, giving rise to different energies for nucleophilic addition products or b) *meso*-LA has a significantly different energy pathway for ring-opening compared to the other isomers. Either of these deductions could account for the difference in stereoselectivity between lactide isomers.

Catalysts (±)- and (*RR/RR*)-**B** exhibit higher rates for the ROP of *meso*-LA than (±)- and (*RR/RR*)-**A**, which is consistent with their relative rates of polymerization of *rac*-LA (Figure 2.14). (*RR/RR*)-**B** shows a k_L/k_D of 5, much lower than that of (*RR/RR*)-**A**, nonetheless this k_{rel} translates to moderate isoselectivites and heteroselectivities (Table 2.3).[40,125] DFT studies of this catalyst system are not available but the similarities in stereoselectivity between isomers may be due to the dissociation of the pre-catalyst dimer in the presence of monomer coupled with having a flexible ligand which may promote the CEC mechanism.[127]

2.3 Conclusions

Two series of dinuclear indium coordination complexes were employed to investigate the catalytic ring-opening polymerization of *meso*-lactide. Catalyst **A** showed good molecular weight control for the ring-opening polymerization of *meso*-LA. Polymerization of *meso*-LA with (*RR/RR*)-**A** generated PLA with the highest syndiotacticity of all complexes in this study. Defect peak analysis showed that enantiomeric site control is the main mechanism acting during ring-

opening polymerization. Catalyst **B** showed less control over molecular weight and displayed similar levels of iso- and heterotactic control, likely due to dissociation of the pre-catalyst dimer during initiation. Correlation of polymerization rate to syndioselectivity was attempted, but the interplay between enantiomorphic site control, chain-end control, kinetic and thermodynamic influences during polymerization make this relationship non-trivial.

2.4 Experimental

General considerations. All air and moisture sensitive manipulations were carried out in an MBraun glovebox or using standard Schlenk line techniques. A Bruker Avance 300 or 400 MHz spectrometer was used to record ^{1}H NMR spectra. A Bruker Avance 600 MHz spectrometer was used to acquire homonuclear decoupled ^{1}H{^{1}H} NMR spectra of PLA. ^{1}H NMR chemical shifts are given in ppm versus residual protons in deuterated CDCl$_3$ (δ 7.27).

Molecular weights, hydrodynamic radii and intrinsic viscosities were determined by GPC-MALS-RI-Viscometer using an Agilent liquid chromatograph equipped with a Agilant 1200 series pump and autosampler, three Phenogel 5 μm Narrow Bore columns (4.6 × 300 mm with 500 Å, 10^3 Å and 10^4 Å pore size), a Wyatt Optilab differential refractometer, Wyatt tristar miniDAWN (laser light scattering detector) and a Wyatt ViscoStar viscometer. The column temperature was set at 40 °C. A flow rate of 0.5 mL/min was used and samples were dissolved in THF (*ca*. 4 mg/mL). The measurements were carried out at laser wavelength of 690 nm at 25 °C. Data were processed by ASTRA software (Wyatt Technology).

Materials. THF was taken from an IT Inc. solvent purification system with activated alumina columns and degassed before use. HPLC grade DCM was purchased from Fisher Chemicals and

was dried over CaH_2, transferred under vacuum, and degassed before use. $CDCl_3$ was purchased from Cambridge Isotope Laboratories Inc. and dried over CaH_2, transferred under vacuum, and degassed *via* three freeze−pump−thaw cycles before use. 2-Propanol was purchased from Fisher Chemicals and was dried over 3 Å molecular sieves. Indium(III)trichloride was purchased from Sigma-Aldrich and was used as received. Rac-LA and *meso*-LA were a gift from PURAC America Inc. Rac-LA was recrystallized thrice from hot dried toluene. Racemic and enantiopure complexes **A** and **B** were prepared according previously reported methods.[40,125]

Purification of *meso*-lactide. *Meso*-LA (50 g) was fully dissolved in DCM; magnesium sulphate (anhydrous) was added to the solution, which was then stirred for 10 min. The excess solid was removed from white suspension *via* vacuum filtration and the solvent removed from the filtrate under reduced pressure to yield a white crystalline powder. This powder was recrystallized from dry 2-propanol five to seven times, to yield *meso*-LA with >95% purity.

Polymerization of *meso*-LA with catalyst A. A 20 mL scintillation vial was equipped with a magnetic stir bar. *Meso*-lactide (290 mg, 2.7 mmol) was dissolved in 2 mL of DCM and to this, a solution of the catalyst (2.0 mg, 0.002 mmol) in 2 mL of DCM was added. The solution was stirred at room temperature for 16 h. Solvent was removed under reduced pressure and the conversion was determined using ^{1}H NMR spectroscopy. The polymer was then dissolved in minimal DCM and precipitated using excess of cold methanol at least three times to remove residual catalyst. The polymer sample was then dried under vacuum for 48 h.

Polymerization of *meso*-LA with catalyst B. A 20 mL scintillation vial was equipped with a magnetic stir bar. *Meso*-lactide (620 mg, 4.3 mmol) was dissolved in 2 mL of DCM and to this, a solution of the catalyst (2.0 mg, 0.001 mmol) in 2 mL of DCM was added. The solution was

stirred at room temperature for 4 h to minimise transesterification and back-biting reactions. Solvent was removed under reduced pressure and the conversion was determined using ^{1}H NMR spectroscopy. The polymer was then dissolved in minimal DCM and precipitated using excess of cold methanol at least three times to remove residual catalyst. The polymer sample was then dried under vacuum for 48 h.

In situ observation of ROP of *meso*-LA. All samples for NMR scale polymerization were prepared in Young's' cap sealed NMR tubes under an N_2 atmosphere. The NMR tube was charged with a stock solution of catalyst in CDCl$_3$ (0.25 mL, 0.001 mmol) and frozen in liq. N_2. CDCl$_3$ (0.25 mL) was added and again frozen to create a barrier between the catalyst and the monomer layers. Finally, a stock solution of *meso*-LA (0.50 mL, 0.45 mmol) and the internal standard 1,3,5-trimethoxybenzene (5 mg, 0.03 mmol per 0.50 mL) in CDCl$_3$ was added and frozen. The sealed and evacuated NMR tube was immediately taken to the NMR spectrometer (400 MHz Avance Bruker Spectrometer). The sealed tubes were thawed and the polymerization monitored at 25 °C until greater than 90% conversion.

Chapter 3: Comparison of the rheological properties of isotactic, syndiotactic, and heterotactic poly(lactide)s.[§§]

3.1 Introduction

In the previous chapter, tri- and tetradentate indium complexes were used for the stereocontrolled ring-opening polymerization of lactide isomers to achieve stereoregular poly(lactide)s. The enantiopure tridentate catalyst showed moderate syndioselectivity towards *meso*-lactide, acting primarily through enantiomorphic site control. On the other hand, the tetradentate catalysts showed heteroselectivity by acting through chain-end control. The effect of stereoregularity on chain-interactions and polymer properties will be further probed in the following sections.

3.1.1 Influence of polymer tacticity on chain packing and thermal properties

Stereoselective catalyst systems with good molecular weight control have allowed researchers to the investigate the effect of chain-packing and crystallinity on the properties of stereoregular polymers.[130] Four polymers that form microstructures similar to those exhibited by poly(lactide) are: poly(propylene) (PP), poly(styrene) (PS), poly(methyl methacrylate) (PMMA) and poly(hydroxybutyrate) (PHB) (Chart 3.1).

Chart 3.1 Common polyolefins that form polymers with various microstructures.

poly(propylene)
PP

poly(styrene)
PS

poly(methyl methacrylate)
PMMA

poly(hydroxybutyrate)
PHB
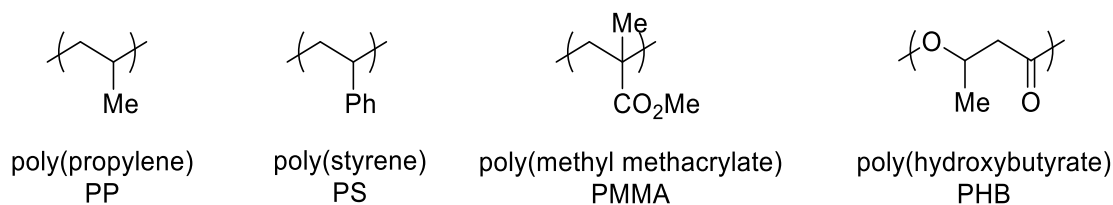
Syndiotactic polyolefins are reported to have two major chain conformations, helical and zig-zag planar (Figure 3.1).[131-134] This chain packing forms crystalline regions within the polymer matrix which impart greater strength[135] and elasticity[136,137] with respect to their isotactic counterparts. Thermal transitions such as melting temperature, T_m and glass transition temperature, T_g are dependent on the presence of regions of order and thus are strongly influenced by microstructure.

helical chain packing   zig-zag chain packing
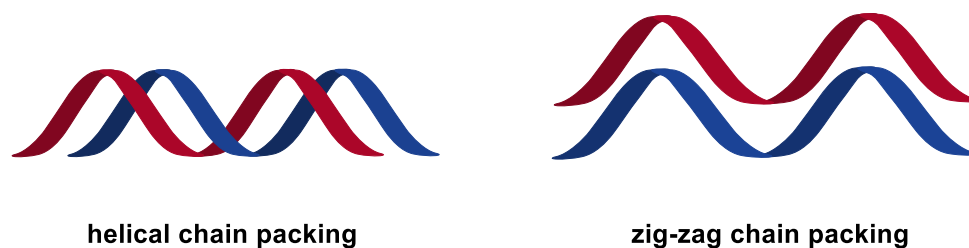
Figure 3.1 Chain packing conformations reported for syndiotactic polyolefins.

Higher thermal transition temperatures for s-PMMA[138] and s-PS[135] compared to i-PMMA and i-PS were ascribed to strong intermolecular bonding from favourable electronic interactions between side groups on adjacent chains (Table 3.1).[136]

Table 3.1 Trends in thermal transitions for different microstructures of three common polyolefins (all values in °C).

	PP		PS[c]		PMMA[d]		PHB[e]	
	Isotactic	Syndiotactic	Isotactic	Syndiotactic	Isotactic	Syndiotactic	Isotactic	Syndiotactic
T_g	4.5[a]	6.7[a]	99	100	61	131	--	--
T_m	151[b]	139[b]	240	270	--	--	183	155

[a] Mülhaupt 1997[139] [b] Ward 1995[136] [c] Malanga 1998[102] [d] Schultz 1998[140] [e] Ebrahimi 2016[137]

Reports of syndiotactic PLA (s-PLA) are scarce in the literature (see 2.1.4 above) with only two groups reporting melting temperatures for highly syndiotactic polymers.[48,103] Although highly heteroselective catalysts have been investigated,[107,114,115,117,120,121,141-156] there has only been one report of the thermal properties for heterotactic PLAs (h-PLA).[150]

3.1.2 Polymer tacticity and its influence on rheological properties.

Rheological measurements on polymer melts are useful for characterization due to the strong correlation between viscoelastic behaviour and molecular structure. Stereoregularity is expected to influence the entanglement of polymer chains and consequently rheological parameters such as zero-shear viscosity, η_0, plateau modulus, G_N^0 and activation of flow energy ($E_{a,flow}$).

An early report by Weese *et al.* assessed the melt rheology of stereoregular PMMA and showed that increasing the syn-content of the polymer enhanced the zero-shear viscosity and plateau modulus compared to their isotactic counterparts.[157] Similar enhancements were shown for s-PP by Eckstien *et al.* in 1997[139] and 1998[158] whereby s-PP had an increased $E_{a,flow}$ compared to i-PP (55 kJ mol^{-1} vs. 15 kJ mol^{-1}) and showed zero-shear viscosity 10 times higher than i-PP.

A more recent report comparing rheological properties of syndiotactic and isotactic poly(styrene) (PS)[159] showed that entanglement molecular weight, M_e is dependent on tacticity, with s-PS having the lowest M_e (14500 g mol^{-1}), therefore giving rise to the highest zero-shear viscosity and energy barrier to flow. These results were in line with earlier studies exploring the viscoelastic properties of poly(propylene) homo-[160] and copolymers.[161] These accounts concluded that syndiotactic polymers exhibit higher activation energies of flow, $E_{a,flow}$ compared to their isotactic and atactic counterparts, implying a higher sensitivity of rheological properties on temperature. Tacticity dependence on rheological properties was also found in solutions of poly(vinyl alcohol),[162] indicating that increasing degrees of syndiotacticity enhances chain stiffness as well as the entanglement density of the polymer chain.

Poly(hydroxybutyrate) (PHB) is another polyester capable of forming polymers with various microstructures. Recently Ebrahimi *et al.* reported the effect of tacticity on the thermorheological properties of PHBs, showing that the large M_e for i-PHBs translates to a low melt strength while syndiotactically enriched PHBs have a much smaller M_e and larger entanglement density, which imparts the material with strength and elasticity.[137]

3.1.3   Rheological properties of poly(lactide)s.

Comprehensive studies of the viscoelastic behaviours and mechanical properties of isotactic, isotactic stereocomplex, and atactic PLA have been reported.[21,22,163-166] Isotactic PLA (i-PLA) has a highly-ordered microstructure, with G_N^0, ranging around 0.9 ± 0.2 MPa, and M_e of approximately 4400 g mol^{-1}. These properties impart i-PLAs with chain stiffness and strength but leave the material brittle, with an elongation at break of just 3%.

There are no rheological and mechanistic studies of the useful processing properties of syndiotactic or heterotactic PLAs. In the following sections, stereo-selective systems are used to produce PLAs with varying levels of stereoregular microstructures with the aim of correlating tacticity with the thermorheological behaviour of the materials.

3.2 Results and discussion

3.2.1 Synthesis of PLAs with various microstructures.

Families of atactic, syndiotactic, isotactic and heterotactic PLAs with varying molecular weights were synthesized and rheological studies carried out to generate a comprehensive correlation between polymer microstructures determined by *in situ* NMR spectroscopic methods (P_m / P_s)[***] to bulk polymer properties (Table 3.2). The rheological properties of isotactic and isotactically enriched PLA have been thoroughly investigated,[15,16,159-171] thus these samples were only used for comparisons.

The current study compares: a) syndiorich PLAs (s-PLA) generated from polymerization of *meso*-LA with (*RR/RR*)-[(NNO)InCl]$_2$(μ-Cl)(μ-OEt)] ((*RR/RR*)-**A**); b) isorich gradient PLAs (i-PLA) generated from polymerization of *rac*-LA with catalyst (*RR/RR*)-[(ONNO)In(μ-OEt)]$_2$ ((*RR/RR*)-**B**); c) essentially atactic PLA (a-PLA) (with a slight heterotactic bias, $P_r = 0.60$) generated from polymerization of *rac*-LA with tin octanoate; and d) highly heterotactic PLA (h-PLA) generated from polymerization of *rac*-LA with an InCl$_3$/amine/alcohol system (Table 3.2).[120,121] The polymers are assigned labels based on their molecular weight and tacticity; for

---

[***] See Chapter 2.

example, 155-het-60 denotes heterotactic polymers with M_n of 155 kg mol^{-1} and P_r of 0.60. All polymers were isolated by precipitating thrice from DCM with cold MeOH before being dried under vacuum for two days to remove any trace amounts of solvent. Subsequently, polymers were compression molded to a width of 0.4-0.6 mm at 150 °C for rheological measurements.

Synthesis of highly syndiotactic PLA with an enantiopure aluminum salen binaphthylamine isopropoxide complex (**I**) was attempted (Figure 3.2).[39,103] These catalysts form highly syndiotactic PLA at low molecular weights (M_n ~ 12 kg mol^{-1}). To achieve high molecular weights required for rheological measurements ($M_n > 100$ kg mol^{-1}), higher monomer loading and longer reaction times were required. Under these conditions a decrease in syndio-enrichment was observed (Figure 3.3, $P_s = 0.77$). We attribute this decrease in syndiotactic control to the greater extent of polymer exchange which has been reported to occur at long reaction times.[106]
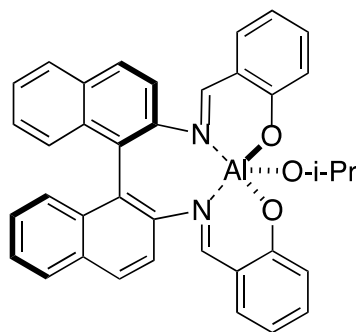
Figure 3.2 (-)-Salen binathphylamine alkoxide complex (**I**) reported to be highly syndioselective towards *meso*-LA by Coates *et al.* in 1999.[103]
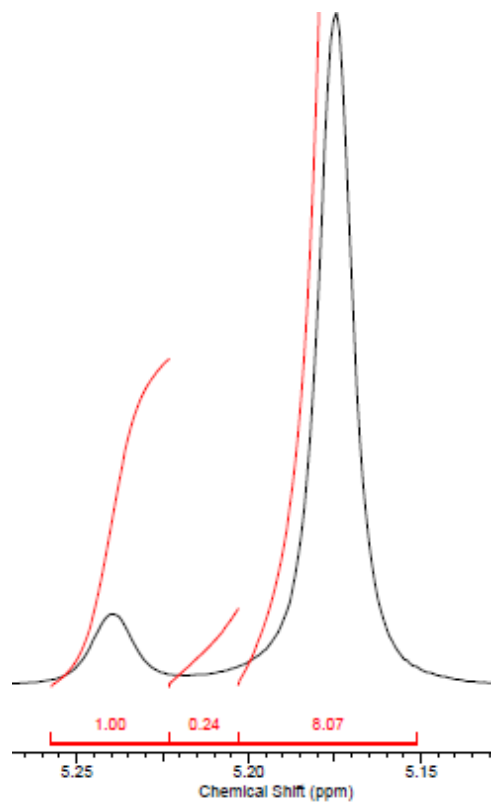
Figure 3.3 ^{1}H {^{1}H} NMR spectrum of polymer produced from reaction of (-)-salen binaphthylamine alkoxide complex (**I**) with *meso*-lactide. Using Equation 2.2, the polymer tacticity was calculated to be $P_s = 0.77$.

Table 3.2 Polymerization data for various microstructured PLAs used for themorheological experiments.

entry	catalyst	sample	$M_{n,GPC}$ (g mol^{-1})^a	tacticity^b	Đ^a	
1 ^{c}	Sn(Oct)$_2$	50-het-60	49900	$P_r = 0.56$	1.11	Atactic PLAs
2 ^{c}	Sn(Oct)$_2$	155-het-60	155000	$P_r = 0.60$	1.12	(het-60)
3 ^{c}	Sn(Oct)$_2$	249-het-60	249000	$P_r = 0.57$	1.14	
4 ^{c}	Sn(Oct)$_2$	352-het-60	353000	$P_r = 0.55$	1.10	
5 ^{c}	InCl$_3$/NEt$_3$/BnOH	148-het-96	148000	$P_r = 0.95$	1.04	Heterotactic PLAs
6 ^{c}	InCl$_3$/NEt$_3$/BnOH	182-het-96	182000	$P_r = 0.96$	1.05	(het-96)
7 ^{c}	InCl$_3$/NEt$_3$/BnOH	255-het-96	255000	$P_r = 0.95$	1.02	
8 ^{c}	InCl$_3$/NEt$_3$/BnOH	295-het-96	295000	$P_r = 0.94$	1.05	
9 ^{d}	(RR/RR)-**A**	130-syn-72	130000	$P_s = 0.73$	1.01	Syndiotactic PLAs
10 ^{d}	(RR/RR)-**A**	147-syn-72	147000	$P_s = 0.72$	1.02	(syn-72)
11 ^{d}	(RR/RR)-**A**	224-syn-72	224000	$P_s = 0.72$	1.02	
12 ^{d}	(RR/RR)-**A**	279-syn-72	279000	$P_s = 0.71$	1.01	
13 ^{d}	(RR/RR)-**B**	67-iso-72	66700	$P_m = 0.73$	1.06	Isotactic PLAs
14 ^{d}	(RR/RR)-**B**	100-iso-72	100000	$P_m = 0.72$	1.02	(iso-72)
15 ^{d}	(RR/RR)-**B**	104-iso-72	104000	$P_m = 0.72$	1.08	
16 ^{d}	(RR/RR)-**B**	119-iso-72	118600	$P_m = 0.71$	1.04	

^{a} Absolute molecular weights were determined by triple detector GPC (gel permeation chromatography) *via* Universal Calibration (THF 4 mg mL^{-1}, flow rate = 0.5 mL min^{-1}, dn/dc = 0.044 mL g^{-1}). ^{b} Calculated from ^{1}H{^{1}H} NMR spectra. ^{c} Reactions were carried out in toluene at 70 °C. ^{d} Reactions were carried out in DCM at 25 °C. ^{e} 155-het-60 denotes heterotactic polymers with a molecular weight of 155 kg mol^{-1} and a P_r value of 0.60.

3.2.2 Thermal study of stereoregular poly(lactide)s.

Thermogravimetric analysis (TGA) and differential scanning calorimetery (DSC) were used to determine the thermal properties for PLA samples with different degrees of tacticity. Studies on poly(styrene) revealed no evidence that tacticity effects the degradation pathway as these mechanisms are dependent on repeat unit rather than microstructure. However, the authors did note a weak tacticity effect on the thermal stability of PS, where atactic PS displayed the low stability while isotactic PS showed the highest thermal stability.[167] Contrary to the studies with PS, the syn-72 polymers show the highest degradation onset temperature, T_{onset} thus better thermal stability compared to the other microstructures (Table 3.3 and Figure 3.4).
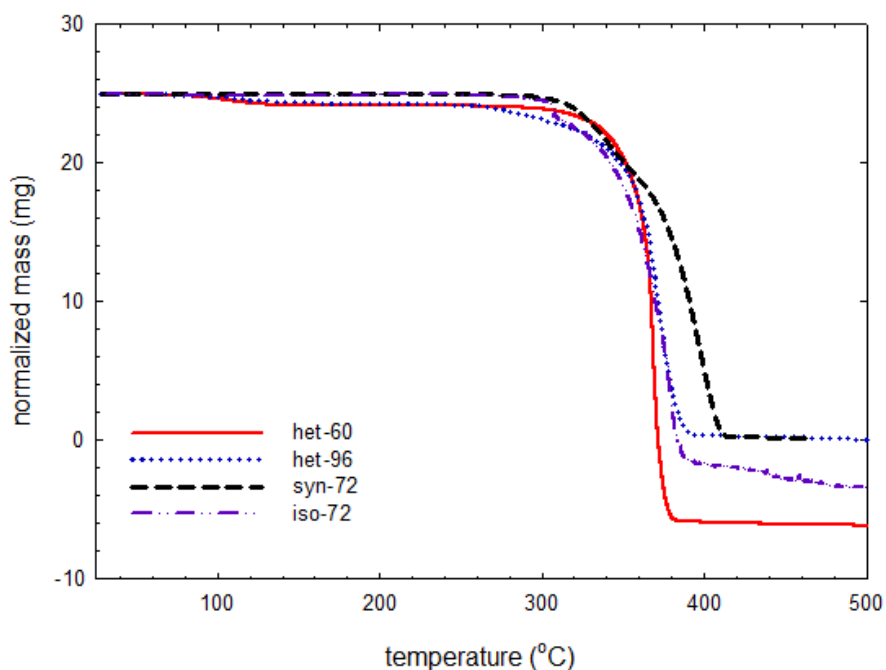
Figure 3.4 TGA heating traces for the various microstructured PLAs. Thermogravimetric analysis was performed on approximately 20 mg of material. Samples were heated to 500 °C at a rate of 20 °C/min to determine the degradation onset temperature (temperature at which there is 5% weight loss), $T_{onset.}$

Glass transition temperatures, T_g are highly dependent on the presence of strong inter-chain interactions and are thus influenced by tacticity.[89,138,140] Based on previous observations of syndiotactic PS and PMMA, it was expected that extended blocks of syndiotactic units would allow the formation of aggregates, increasing the T_g of s-PLA compared to other PLA microstructures. In the current study, all the polymers studied are amorphous and only show glass transitions in their DSC traces (Figure 3.5). In contrast to what was seen for other syndiotactic polymers, a significant effect of tacticity on glass transition temperatures was observed (Table 3.3). Isotactically enriched PLA, iso-72 exhibited the highest T_g of the polymers studied, likely due to the strong interactions between PLLA and PDLA domains within the stereo-gradient polymer backbone (Table 3.3, entry 5).[96,99,100] As a comparison, values were obtained for purely isotactic PLA which also displays a high glass transition temperature (Table 3.3, entry 6).[29] Syn-72 PLA displayed the lowest T_g (comparable to atactic PLA), indicating lasting chain aggregates are scarce within the polymer matrix. Highly syndiotactic PLA reported by Coates *et al.* in 1999 shows a T_g lower than that of heterotactic and isotactic PLAs,[103] implying that even large syndiotactic aggregates do not impart as much strength as isotactic domains.

Although heterotactic PLAs are prevalent in the literature,[36,37] there is only one report of a melting temperature after annealing (P_r = 0.95, T_g = ~46 °C, T_m = ~120 °C).[150] Heterotactic PLA, het-96, exhibits the second highest T_g (37.9 °C), indicating that although this microstructure enhances chain interactions, it cannot readily form highly crystalline regions. This may be due to the structure of aggregate domains within h-PLA. However, this microstructure has not been thoroughly explored so there is no information to indicate how these aggregate structures arise.

Table 3.3 Thermal properties of PLAs of varying stereoregularity.

Entry		T_{onset} (°C)[a]	T_g (°C)[b]	T_m (°C)[b]
1	het-60	258(11)	31.9	--
2	het-96	290(5)	37.9	--
3	syn-72	323(2)	30.8	--
4	syn-96[c]	--	34	151
5	iso-72	319(6)	46.2	--
6	iso-100[d]	310	55	175

Values shown in parentheses are standard deviations. [a]Thermogravimetric analysis was performed on approximately 20 mg of material. Samples were heated to 500 °C at a rate of 20 °C/min to determine the degradation onset temperature (temperature at which there is 5% weight loss, T_{onset}) [b]Thermal analysis of samples was performed by using a differential scanning calorimeter (DSC) with *ca.* 2 mg of sample. Samples heated to 170 °C at 10 °C/min and cooled to 25 °C at 5 °C/min to determine T_g and T_m. Glass transition and melting temperatures calculated from second heating scans. [c]Coates 1999.[103] [d]Garlotta 2001.[29]
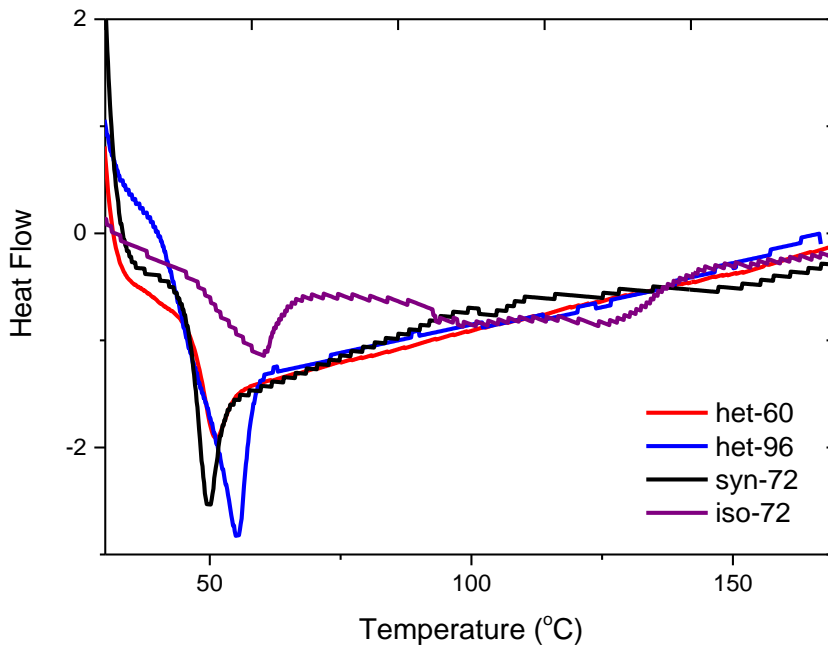
Figure 3.5 DSC traces for various microstructured PLAs studied. Samples heated to 170 °C at 10 °C/min and cooled to 25 °C at 5 °C/min under a nitrogen atmosphere to reduce sample degradation. Glass transition and melting temperatures calculated from second heating scans. *ca.* 2 mg of sample used.

3.2.3   Solution viscosity.

The average values of the intrinsic viscosities, $[\eta]$, and the weight-average molecular weight, M_w, obtained from light-scattering GPC analysis are plotted in Figure 3.6. The slope of the linear regression line (exponent of the Mark-Houwink equation) is 0.73, which agrees with the values reported by Dorgan *et al.* for PLAs in THF.[22,163,164] For linear polymers with random coil conformation, the exponent of the Mark-Houwink equation has a value from 0.5 in a poor solvent to 0.8 in a good solvent.[138,168] It can also be seen that the intrinsic viscosities of the isotactic PLAs are higher compared to heterotactic PLAs which in turn are higher than those of syndiotactic counterparts with the latter possessing the lowest intrinsic viscosity of all different types of PLAs. This is attributed to the different chain conformations, although the slopes of 0.75-0.76 for all the different families imply good solvent conditions and random coil conformation.[138]
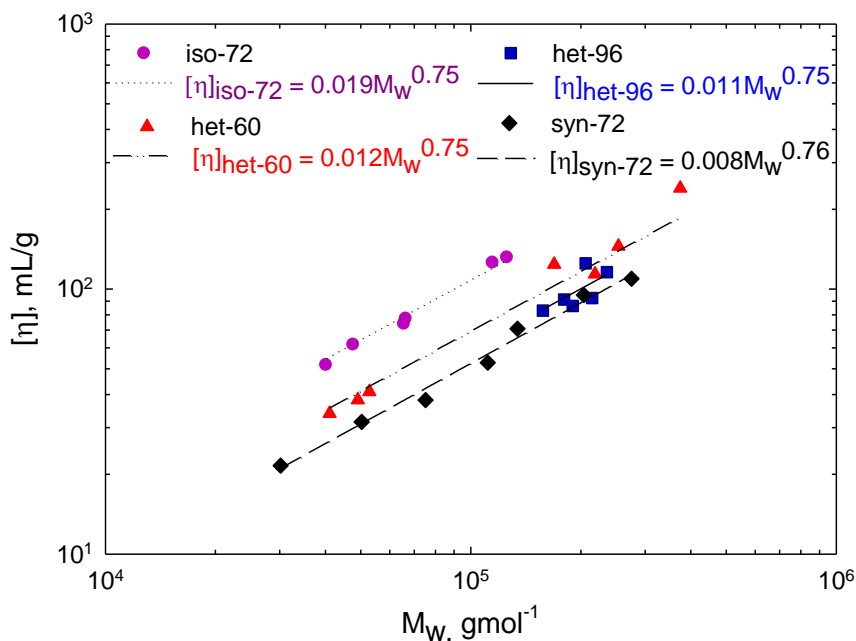
Figure 3.6 Log-log plot of intrinsic viscosity of various types of PLAs as a function of the molecular weight.

The hydrodynamic radius dependence on the weight-averaged molecular weight for the range of polymers studied is shown in Figure 3.7. The scaling relation for heterotactic (het-96) and atactic (het-60) PLAs is $R_h = 0.017M_w^{0.55}$, in agreement with trends for amorphous PLAs reported by Othman and co-workers.[22] The radii of iso-72 polymers are higher than those expected by this relation while the radii of syn-72 polymers are lower. This result correlates well with the calculated mass dependence of the intrinsic viscosity plotted in Figure 3.6.
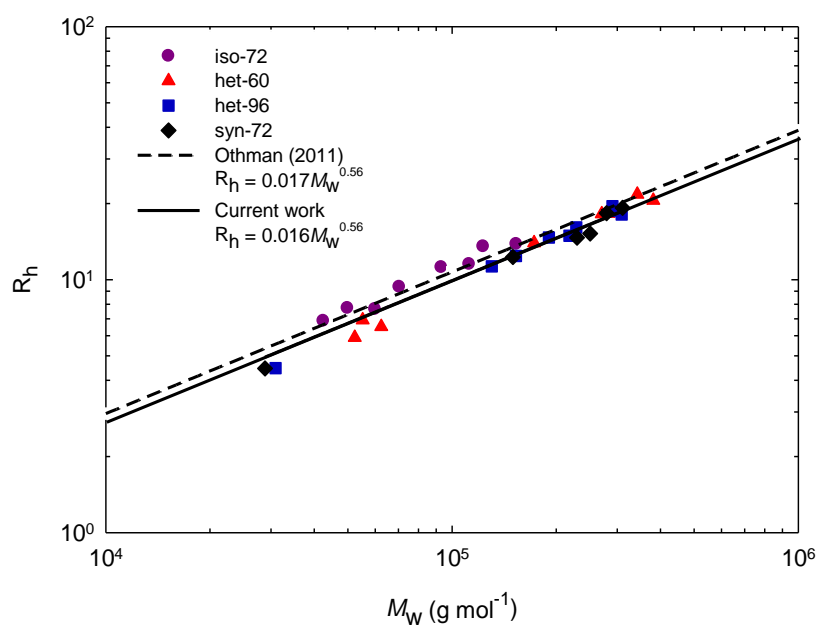
Figure 3.7 Characteristic hydrodynamic radius (R_h) as a function of molecular weight and tacticity. The radii of the iso-PLA are the highest while those of syndio-PLA are the lowest, in agreement with the intrinsic viscosity data plotted in Figure 3.6.

3.2.4   Linear viscoelasticity of PLAs with varying microstructures.

An important aspect of polymer rheology is the study of how viscoelastic behaviour changes with respect to temperature, molecular weight and polymer microstructure. Of particular significance is

establishing structure-property relationships *i.e.* zero-shear viscosity vs. molecular weight, useful also in assessing the processing properties of materials. Currently there are no reports of these properties for heterotactic or syndiotactic PLA.

The thermal stability of stereoregular PLAs under shear stress was probed in isothermal time sweep experiments at 180 °C over 60 minutes. A parallel plate rheometer was used at a constant frequency of 0.5 rad s^{-1} and strain amplitude of 2%. The complex modulus, |G*| , a measure of resistance to deformation sensitive to structural changes, is plotted against time in Figure 3.8.

Heterotactic (het-96) and atactic (het-60) PLAs show a steady decrease in complex modulus and associated melt strength over the experimental time frame. Subsequent GPC analysis conducted on the collected material showed a 20% decrease in molecular weight consistent with the fundamental relationship of $\eta_0 \propto M_w^{3.4}$ for linear macrostructures. Isotactically enriched PLA (iso-72) and syndiotactic (syn-72) samples showed stable melt strength over the experimental time frame, however, a small decrease in molecular weight and a broadening of dispersity values was observed after the test.[†††]

[†††] Linear viscoelastic (LVE) measurements last about 20 minutes, during which time the decrease in molecular weight is estimated to be 6%. A molecular weight decrease of this size has a minimal impact on the reported LVE properties.
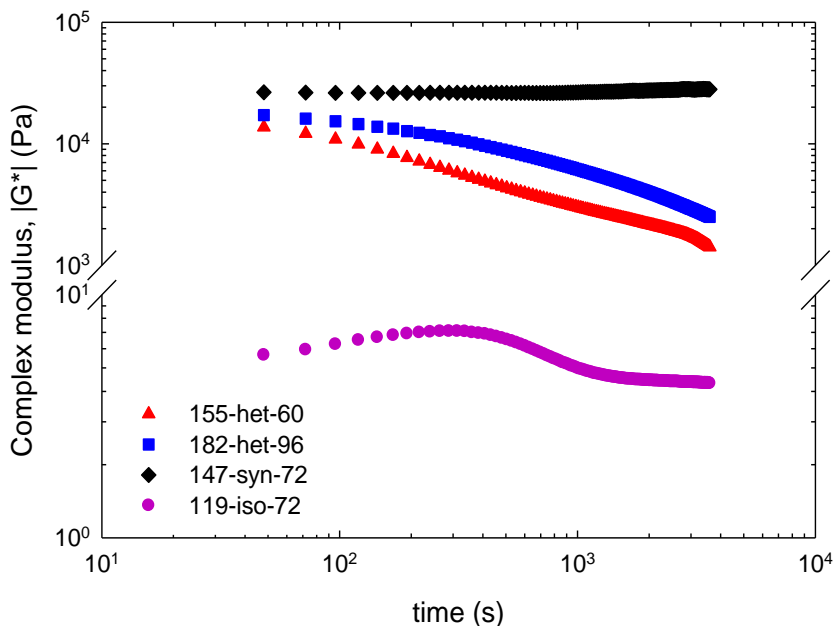
Figure 3.8 Complex modulus, |G*| vs. time for stereoregular PLAs.

Dynamic linear viscoelastic measurements were focussed on the comprehensive characterization of syndiotactic and heterotactic PLAs and comparison with isotactic and atactic PLAs.[20-22,163-165,169] These measurements were conducted within the linear viscoelastic regime at temperatures in the range of 70-190 °C and at angular frequencies ranging from 0.01 to 100 rad s^{-1} with a constant strain of 2% and a gap of 0.5 mm was used to minimize edge effects.

The isothermal frequency sweep measurements for each microstructure show an expected decrease in complex viscosity with temperature and the materials display shear-thinning behaviour. All stereoregular PLAs studied were found to be thermorheologically simple, allowing for the application of the time-Temperature superposition to generate master curves. Figure 3.9 shows a representative master curve for the linear viscoelastic moduli, G' and G", as well and the complex viscosity at the reference temperature of 150 °C for het-96 (Figure 3.9a) and syn-72 (Figure 3.9b) polymers. Deformation frequency trends for the loss modulus are very similar for both heterotactic

and syndiotactically enriched PLAs where the loss moduli reach a plateau value (plateau modulus) at high frequencies ($10^1 – 10^6$ s^{-1}). Similar trends are observed for the storage modulus which increases with increase of frequency, reaching a maximum and minimum value at higher frequencies typical of linear monodisperse polymers. It can be seen from the characteristic slopes of 1 and 2 for G' and G'', respectively, that the terminal zone at small deformation frequencies (and long deformation times) has been reached.

The linear viscoelastic moduli of syn-72 and het-96 polymers with varying molecular weights are shown in Figure 3.10 and Figure 3.11, respectively. Trends observed in these plots are in line with those reported for isotactic PLAs,[22] whereby, with increasing molecular weight plateau regions in both storage and loss moduli become more defined, occurring over a larger frequency ranges, in addition terminal zones shift to lower frequencies. (Figure 3.10 and Figure 3.11). All these observations are typical of linear monodisperse polymers.
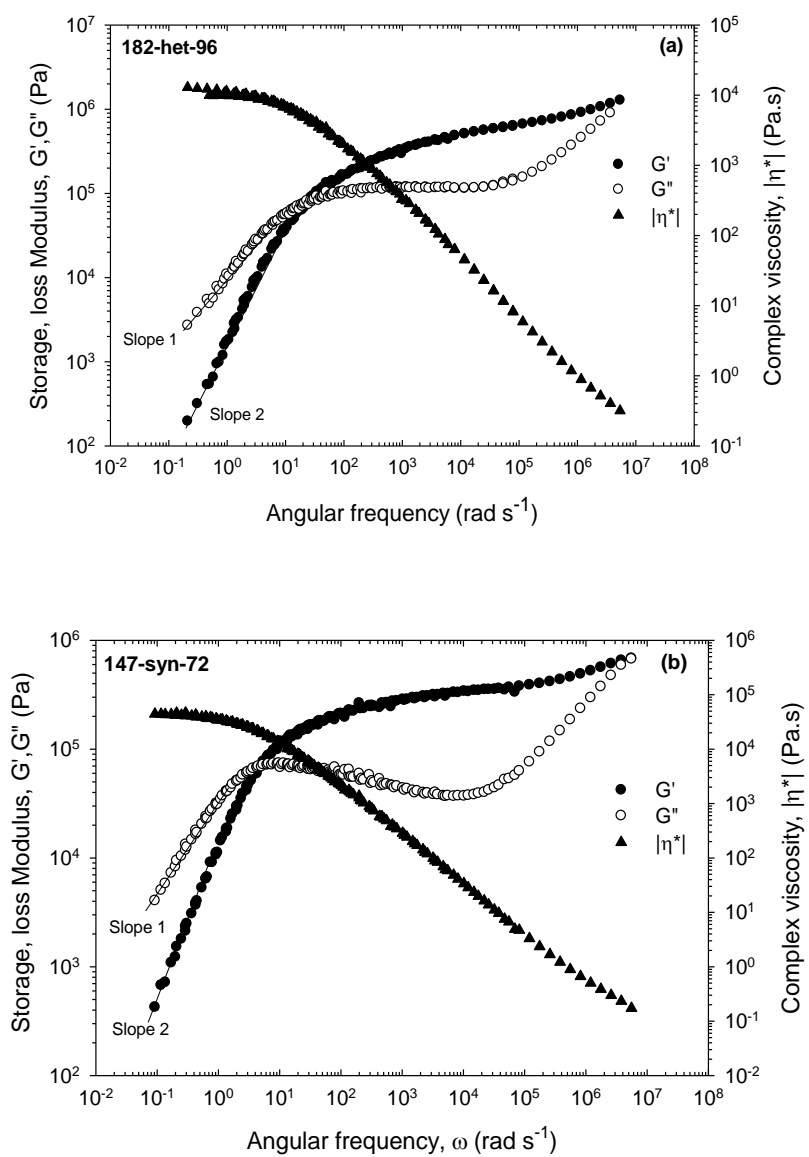
Figure 3.9 Master curve of the linear viscoelastic moduli, G' and G" and complex viscosity, |η*|, (T_{ref} = 150 °C) for (a) 182-het-96 (Table 3.2, entry 6) and (b) 148-syn-72 (Table 3.2, entry 10).
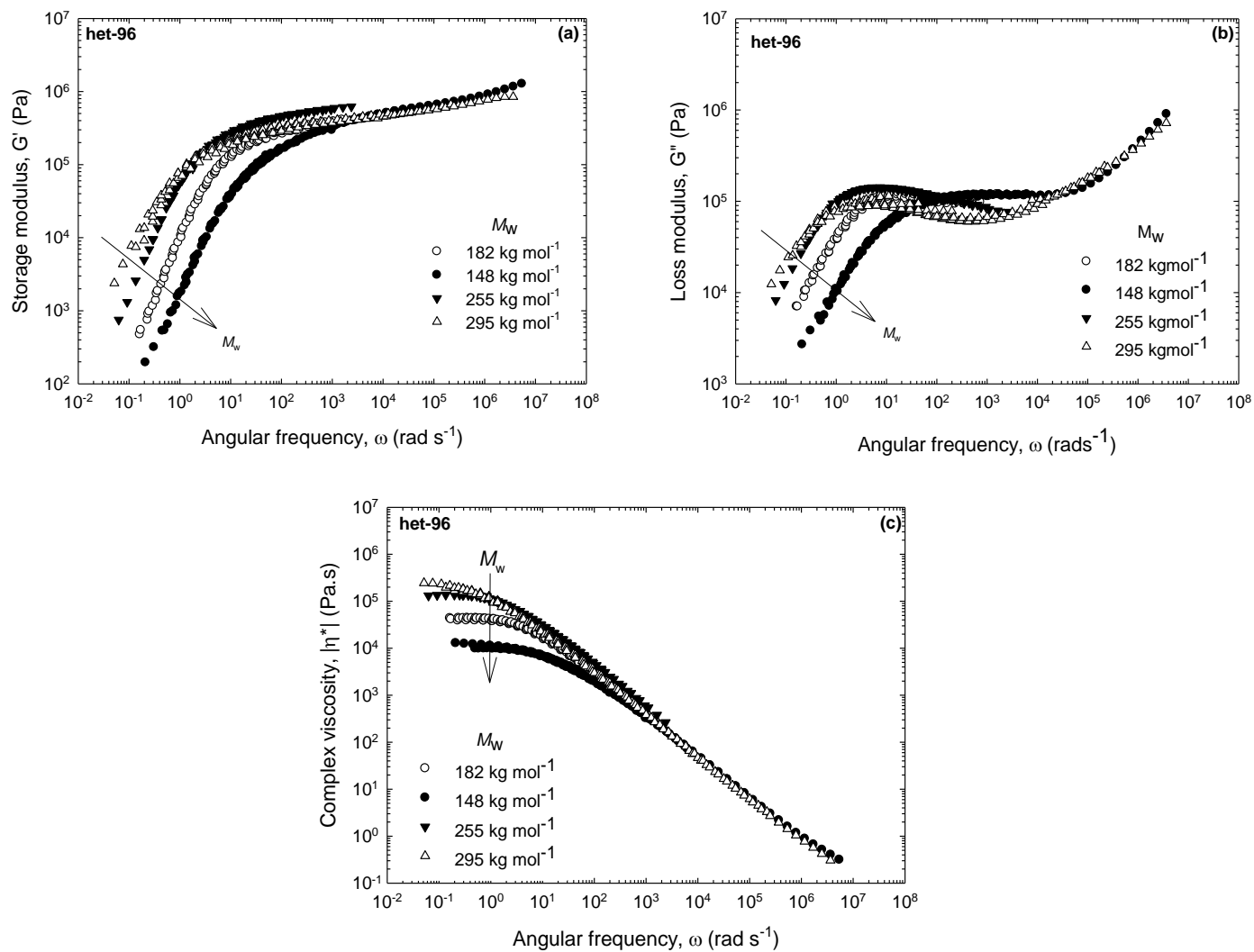
Figure 3.10 Master curves of the linear viscoelastic moduli for het-96 polymers (T_{ref} = 150 °C). (a) Loss modulus vs. angular frequency (b) storage modulus vs. angular frequency (c) complex viscosity vs. angular frequency.
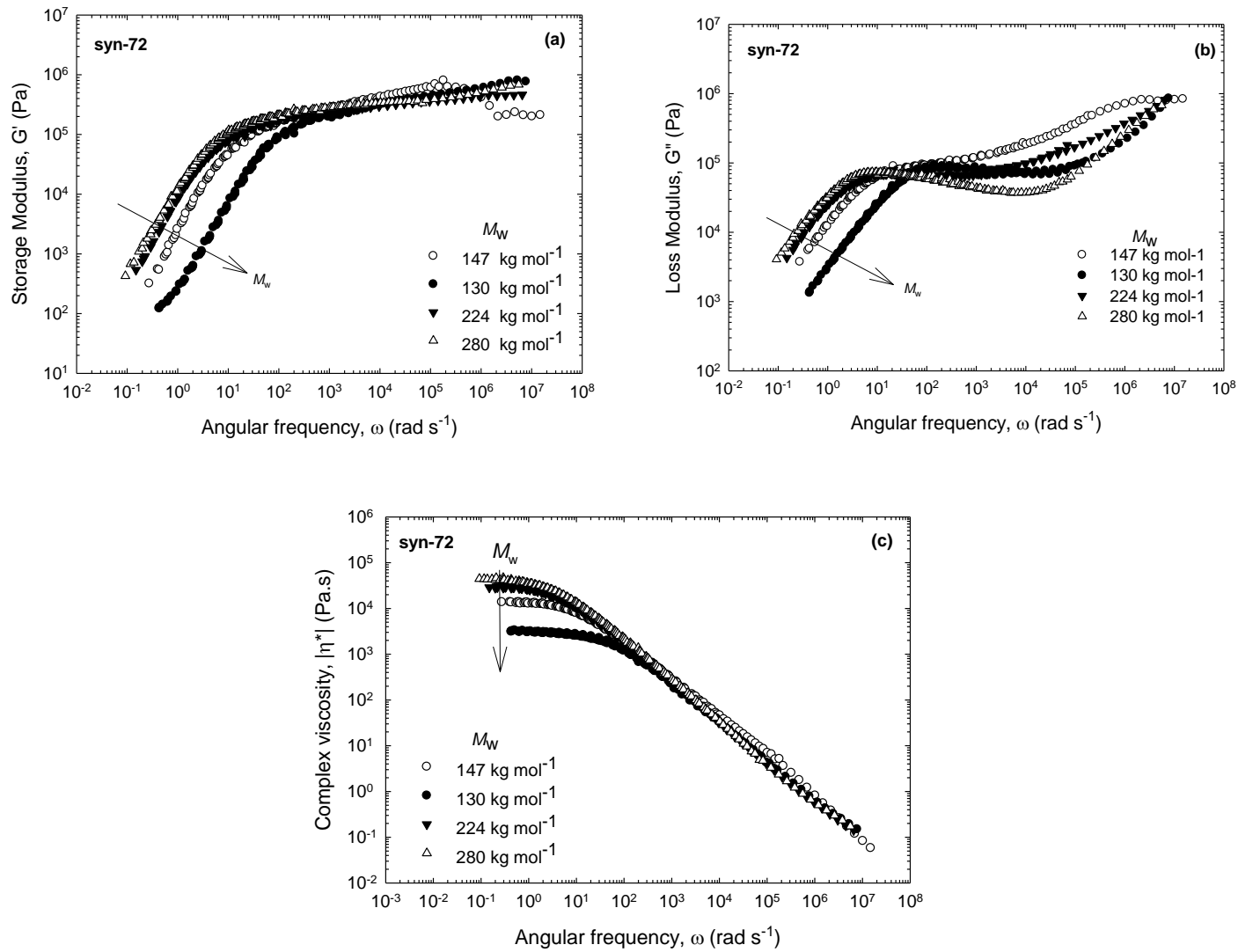
Figure 3.11 Master curves of the linear viscoelastic moduli for syn-72 polymers ($T_{ref} = 150$ °C). (a) Loss modulus vs. angular frequency (b) storage modulus vs. angular frequency (c) complex viscosity vs. angular frequency.

Reports comparing the viscoelastic behaviours of syndiotactic and isotactic poly(propylene) homo- and copolymers[139,161,170] showed that increasing the degree of syndiotacticity increases chain stiffness as well entanglement density, imparting strength to these polymers, observed by an increase in the plateau modulus, G_N^0.[136]

The plateau moduli, G_N^0 for the various microstructures studied were obtained from the minima of van Gurp-Palmen plots (Figure 3.12). From the G_N^0, molecular weight between entanglements, M_e, can be calculated using:

$$M_e = \frac{\rho RT}{G_N^0} \qquad (1)$$

where ρ is the melt density (g/cm^3) at the chosen reference temperature, obtained using the relationship:[22]

$$\rho(t) = 1.2836\, e^{(-7.7 \cdot 10^4 T)} \qquad (2)$$

Plateau moduli for PLAs with varying levels of isotacticity calculated by Dorgan and co-workers fell within the range of 1.0 MPa ± 0.2.[164] Moderately isotactic PLA, iso-72, agrees with these values (G_N^0= 0.97 MPa). In contrast to work on s-PS, moderately syndiotactic PLA displaying the lowest plateau modulus and largest M_e exhibits lower chain stiffness compared to heterotactic and atactic polymers.[159] Heterotactic and atactic polymers display similar plateau moduli and M_e thus are expected to have comparable chain stiffness (Table 3.4).
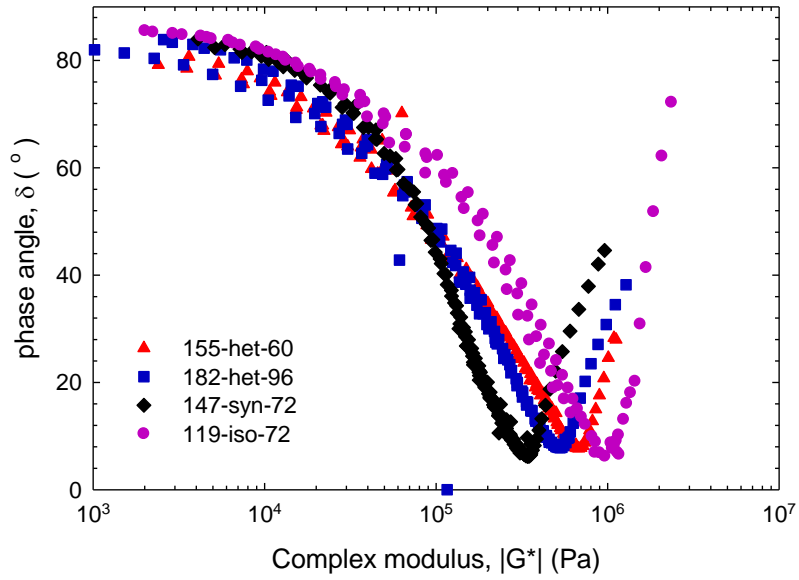
Figure 3.12 Van Gurp-Palmen plots of the various microstructured PLAs.
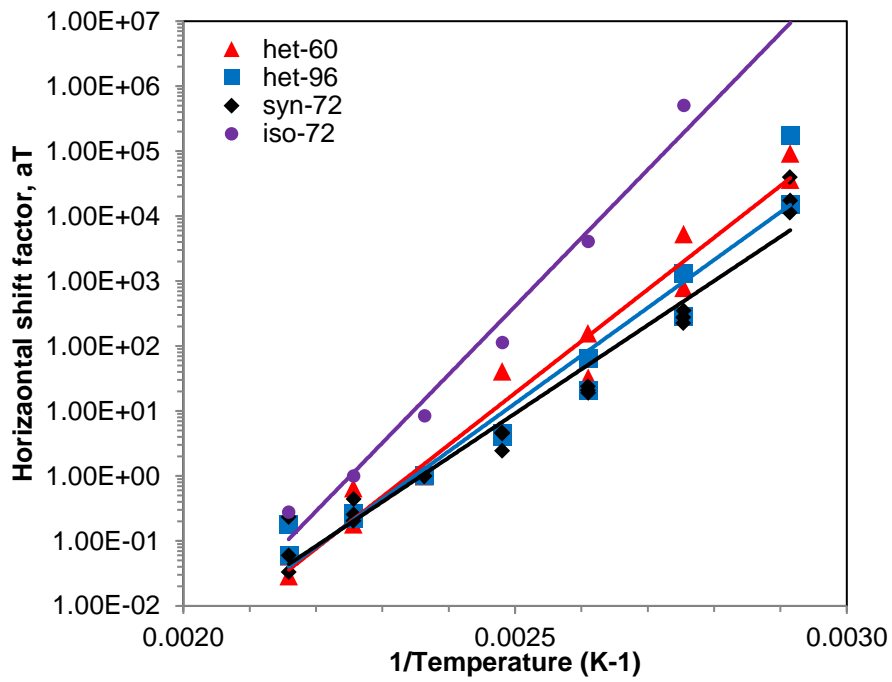
Figure 3.13 The horizontal shift factors, a_T for PLAs listed in Table 3.4 at the reference temperature of 150 °C. Lines represents single fitting of the data used to calculate flow activation energy, $E_{a,flow.}$

Table 3.4 Comparison of rheological properties of PLA, PS and PP in this work and obtained from the literature.

entry	polymer	$G_N^0 (10^5 \text{ Pa})^a$	$M_e (\text{g mol}^{-1})^b$	$E_a (\text{kJ mol}^{-1})^c$
1	het-60	0.58	6900	152.7 (0.5)
2	het-96	0.52	7700	141.0 (0.9)
3	syn-72	0.34	11800	130.2 (0.6)
4	iso-72	0.97	4100	167.9 (0.6)
5^d	a-PP	0.42	7050	--
6	s-PP	0.87^e	3400^e	50.6^d
7^d	i-PP	0.43	6900	38.7
8^f	a-PS	0.24	17900	97(9)
9^f	s-PS	0.30	14500	53 (5)
10^f	i-PS	0.16	27200	99

Values shown in parentheses are standard errors. ^{a} Calculated from minimum of van Gurp-Palmen plot (Figure 3.12). ^{b} Obtained from equation 1 and 2 ^{c} Calculated from the slope of the horizontal shift factor, a_T vs. 1/Temperature plot (Figure 3.13) ^{d} Jing 2004.[160] ^{e} Hadjichristidis 1992.[171] ^{f} Wang 2011.[159] To obtain the G_N^0 and M_e the reference used for the PS and PP samples are 280 °C and 190 °C, respectively.

Complex viscosities for the various tacticity polymers studied at the reference temperature of 150 °C are shown in Figure 3.14. This plot shows that the terminal zone has been reached for all different microstructures and thus zero shear viscosities can be directly determined from the experimental data.

Previous work in our group on linear PLAs with varying levels of isotacticity showed that the zero-shear viscosities (η_0) of PLAs scale to 3.4 power with M_w.[22] In a subsequent report, it was also shown that PLA enantiomeric diblock copolymers also follow this power law;[166] both of these results are in agreement with pioneering work carried out by Dorgan *et al.* in 2005.[164] Figure 3.15 shows a plot of zero-shear viscosity, η_0 against weight averaged molecular weight, M_w for the various microstructures studied. The trend lines drawn in Figure 3.15 for the iso- and syndio- PLAs

are best fit with a fixed exponent of 3.4 that is well established for the atactic PLAs. Although the effect of tacticity on the zero-shear viscosity might be smaller than the experimental error and thus difficult to conclude from the graph, the isotactic and heterotactic polymers appear to have a higher zero-shear viscosity compared to syndiotactic polymers, in agreement with the intrinsic viscosity comparison presented in Figure 3.6.
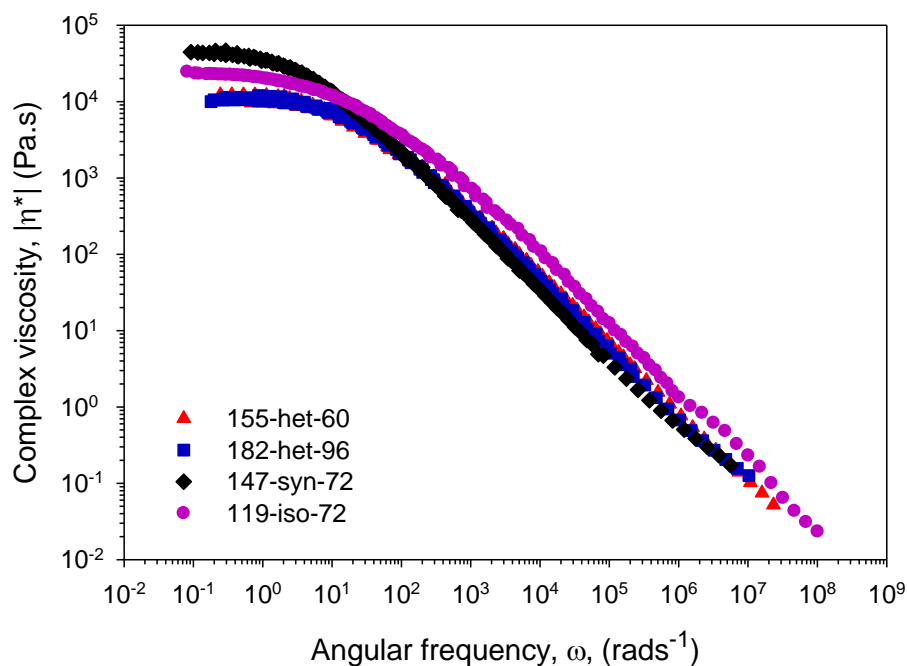
Figure 3.14 Complex viscosity vs. angular frequency master curves for the different microstructure PLAs at approximately a fixed molecular weight value ($T_{ref} = 150\ °C$).
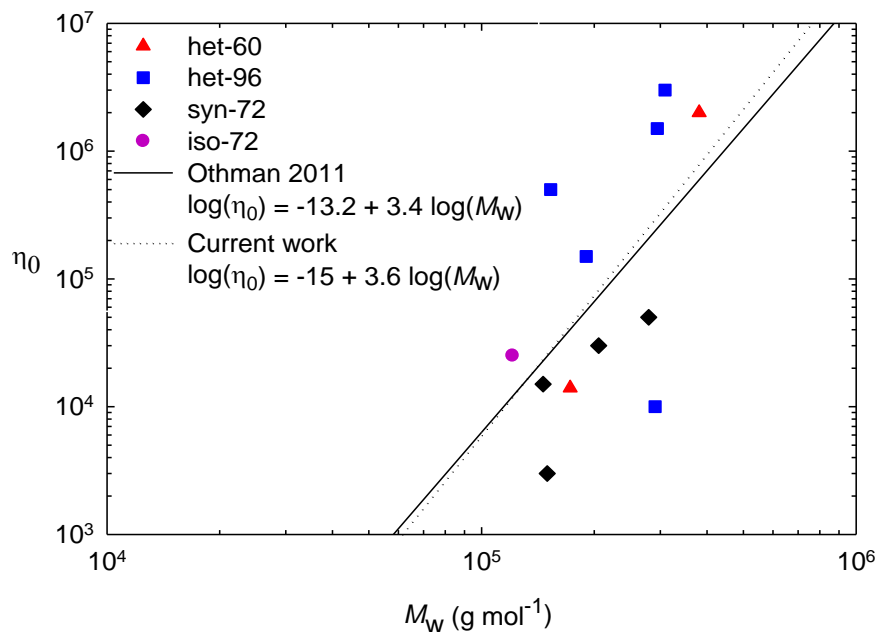
Figure 3.15 Zero-shear viscosity, η_0, versus weight averaged molecular weight for PLAs with different microstructures.

Horizontal shift factors, a_T determined from the time-temperature superposition were found to agree with those reported in the literature[166] and followed an Arrhenius trend, $a_T \propto \exp\{E_a/R(1/T - 1/T_{ref})\}$, where E_a is the activation energy for flow, R is the universal constant of the ideal gas law, and T_{ref} is the reference temperature (Figure 3.13). The obtained a_T values were plotted against the reciprocal of temperature and this was used to calculate the flow activation energy for all the microstructures studied (Table 3.4).

The activation barrier of flow is highest for the isotactically enriched PLA (Table 3.4, entry 4). This is evidence that strong chain interactions between regions of L- and D-units form aggregates, which need more energy to break apart and allow the material to flow. The small flow activation energy displayed by the syndiotactically enriched material (Table 3.4, entry 3) can be an indication that lasting aggregates are not formed between the syndiotactic units within the

polymer chains. The high energy barrier observed for atactic PLA can be explained by the statistical distribution of the different tacticities within its structure (Table 3.4, entry 1). Depending on the synthetic conditions used to make this material, it may contain enough regions of iso- or hetero-enrichment to form transient aggregates, resulting in higher activation energy compared to the heterotactic PLA (Table 3.4, entry 2).

Relevant properties for PS and PP (similar polymers to PLA in application scope) obtained from the literature (Table 3.4) are shown in an attempt to compare to the present results, particularly for the effect of tacticity on entanglement molecular weight, molecular stiffness and plateau modulus. Poly(propylene) has a small methyl side group, similar to PLA, and the reported materials display comparable molecular weights between entanglements than the various PLAs apart from s-PLA. However, they (PPs) display significantly lower activation flow energies due to the absence of interactions *i.e.* PLLA with PLDA. Conversely, PS with a bulky phenyl side ring is shown to exhibit entanglement molecular weights comparable only with s-PLA, yet lower activation of flow energies are also observed. Dipole-dipole and hydrogen-bonding are the dominating interactions which govern chain interactions within PLA. These results indicate the large effect of hydrogen-bonding on the viscosity of PLA compared to commodity polyolefins.

3.2.5 Uniaxial extensional rheology

Poor melt strength is one of the factors limiting the application of PLA as a replacement for commodity plastics like poly(ethylene terephthalate) and poly(styrene). Early work by Green and Tobolosky describes the motion of highly entangled polymers as a system of transient interconnections extending throughout the polymer.[172] Poly(lactide) with its ability for strong

91

hydrogen-bonding interactions between regions of stereoregularity within polymer chains is a good example of this type of system (Figure 3.16). The extensional viscosity of polymeric materials is greatly influenced by the presence of chain interactions at different chain scales, thus can be used as a measure to probe the effect of microstructure on the melt properties of PLA.
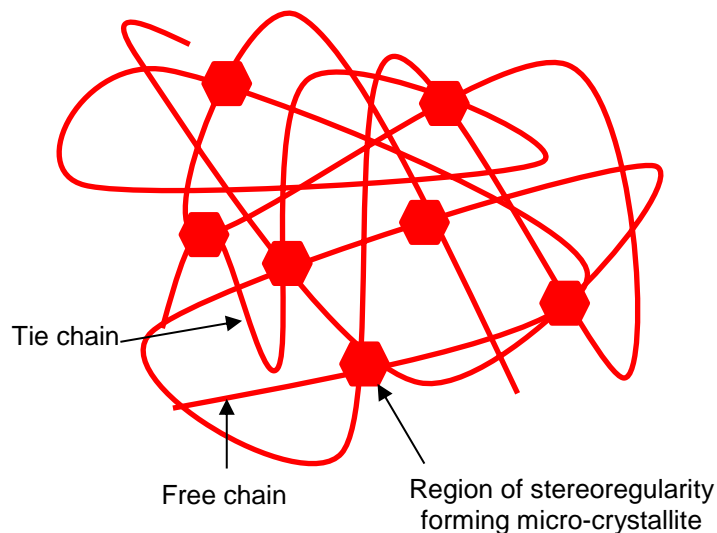
Figure 3.16 Illustration of micro-crystallites forming transient cross-links between polymer chains.

Strain-hardening for short linear polymers is unusual. Palade and Dorgan however, showed that *high* molecular weight isotactic PLA does exhibit strain-hardening at relatively low strain rates[173] and in 2004, Yamane reported that the formation of stereocomplex micro-crystallites in PLLA/PDLA blends results in temporary cross-links between polymer chains allowing for strain-hardening.[24] In addition, the time scales of the deformation compared with the terminal relaxation times of the polymers might also favor the occurrence of strain-hardening. Extensional tests at low temperatures are useful in illustrating the effect of microstructure on the melt strength of PLA as any strain-hardening will be amplified.

Uniaxial extensional tests were carried out at 70, 90 and 110 °C at Hencky strain rates of 0.01 - 10 s^{-1}. Strain-hardening was most significantly observed at strain rates of 10 s^{-1}. Figure 3.17 shows the log-log plots of extensional viscosity vs. time at the three temperatures.[‡‡‡] Only syn-72 PLAs do not show strain-hardening at 70 °C, indicating a lack of significant chain interactions to increase chain entanglement within the material. Both atactic and h-PLAs have enough internal order for transient aggregates to form due to intermolecular interactions and thus exhibit strain-hardening (Figure 3.17a). As the temperature is increased to 90 °C, extra thermal energy affords polymer chains more free volume in which to move. At this temperature atactic PLAs no longer exhibit strain-hardening but, isotactic and heterotactic-PLAs retain enough of their aggregate and these chain interactions manifest as strain-hardening (Figure 3.17b). At 110 °C only the strong interactions between L- and D-regions within the isotactically enriched materials remain; all other PLAs have lost their internal order (Figure 3.17c).

Strain-hardening behaviour can be observed when the molecular relaxation time exceeds the characteristic time of deformation.[21,165] For a Hencky strain rate of 10 s^{-1}, the characteristic deformation time is 0.1 s. The average relaxation times for each of the polymers studied were calculated from the linear viscoelastic experiments (LVE) experiments and are shown in Table 3.5. It is seen that the average relaxation times are high at 70 °C and 90 °C (5-10 s) explaining the presence of strain-hardening at 10 s^{-1} (with characteristic time of deformation of 0.1 s). Another contributing factor to strain-hardening is the interactions between L-and D-regions with formations of stereocomplex aggregates. It seems that these interactions are stronger in the case of isotactic

---

[‡‡‡] Uniaxial extensional experiments were unable to be performed on iso-72 at 70 ˚C due to material constraints.

PLAs, and thus, strain-hardening persists even at temperatures of 110 °C at all extensional rates (Figure 3.18). This is not the case for the other types of stereoregular PLAs where at 110 °C there is no observable strain-hardening (see appendix A).

Table 3.5 Average relaxation times for various polymers studied calculated from linear viscoelastic experiments.

entry		λ_{ave} (s)		
		70 °C	90 °C	110 °C
1	het-60	9.97	4.72	2.79
2	het-96	7.29	4.65	1.48
3	syn-72	9.46	7.26	2.70
4	iso-72	--	7.22	2.97
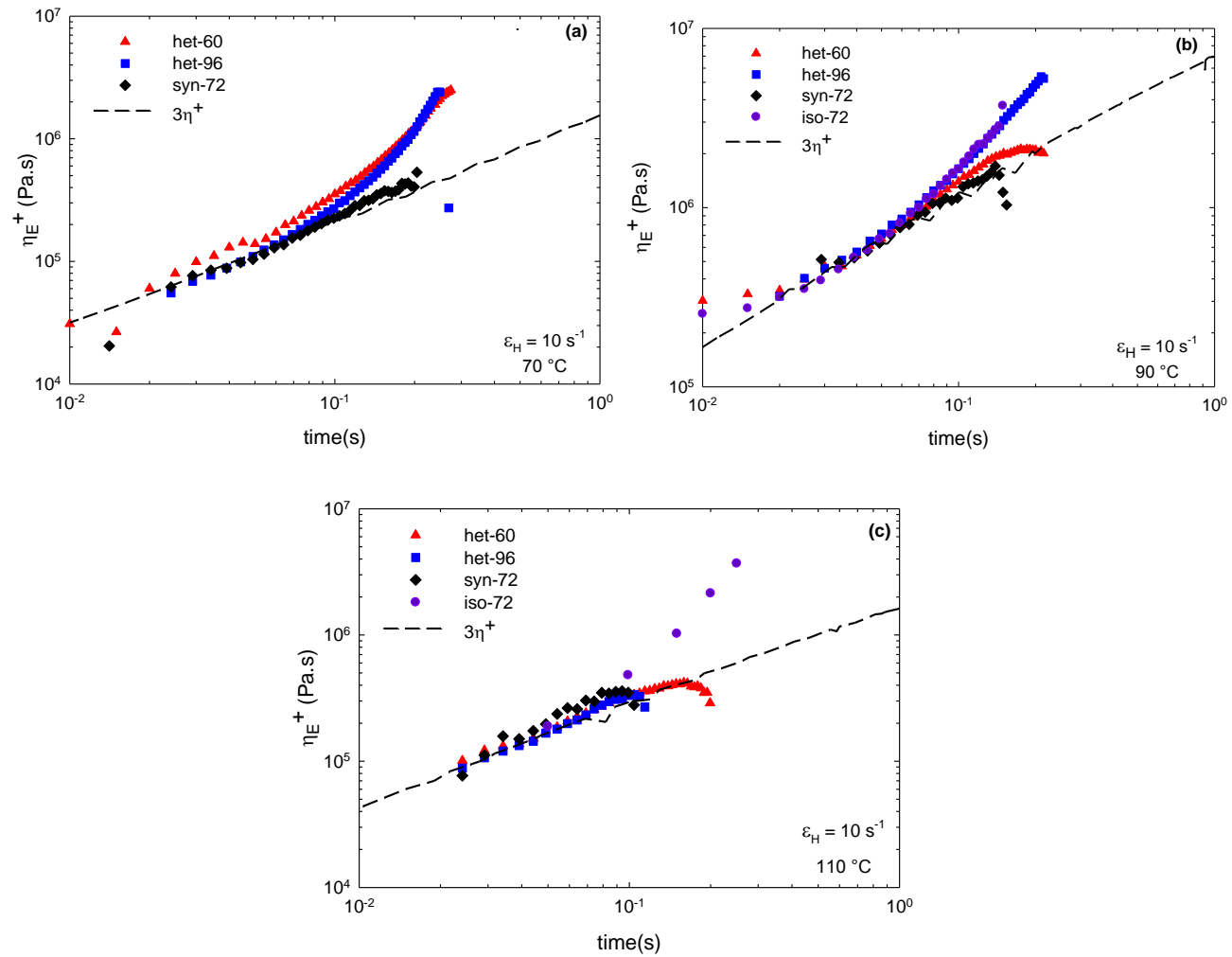
Figure 3.17 Elongational viscosity as a function of time at Hencky strain rate of 10 s^{-1} for differently microstructured poly(lactide)s at (a) 70 °C, (b) 90 °C and (c) 110 °C. Uniaxial elongation experiments on iso-72 were unable to be performed at 70 °C.
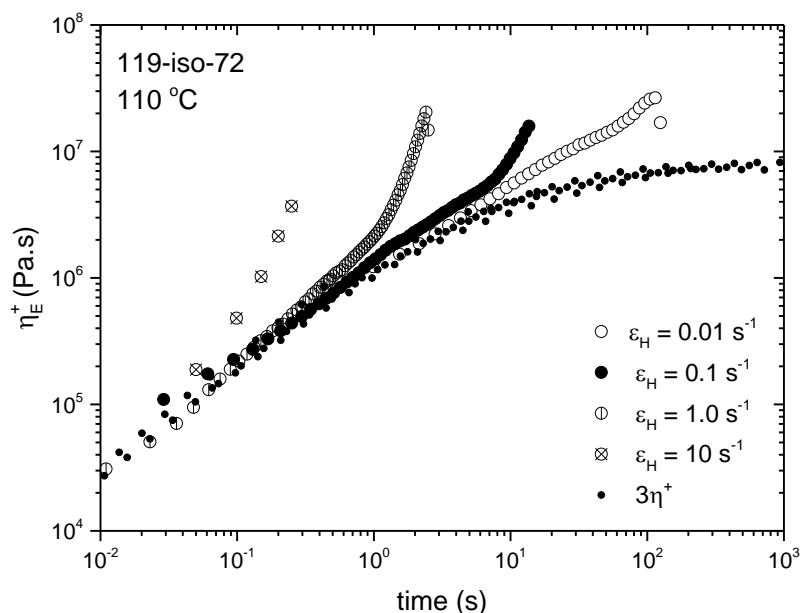
Figure 3.18 Elongational viscosity as a function of time at Hencky strain rates from 0.01 to 10 s^{-1} for iso-enriched PLA (Table 3, entry 4). It is noted that strain-hardening is present at all Hencky strain rates (not the case for all other PLA types) indicating the stronger interaction of L- and D- regions.

3.3 Conclusions

Known stereoselective systems were used to produce PLAs with varying stereoregularity and the relationship between tacticity and the thermal and rheological behaviour of these materials was investigated. Comparisons of thermal properties showed that to achieve large aggregate regions, chain packing from isotactic and heterotactic domains are superior to those of syndiotactic domains, as evidenced by the different glass transition temperatures. The linear viscoelastic properties of PLA showed greater dependence on the level of isotactic rather than syndiotactic linkages present in the polymer chain, with isotactically enriched polymers having higher flow activation energy than syndiotactically enriched polymers. Heterotactic PLAs (h-PLA) exhibited

nascent aggregate domains which were observed by an increase in flow activation energy compared to syndiotactic PLA (s-PLA).

Plateau moduli were determined from van Gurp-Palmen plots and the influence on molecular weight between entanglements, M_e, was discussed. Our results showed that the measured M_e is lowest for i-PLA and highest for s-PLA. Syndiotactic PLAs possess the lowest entanglement density for a given M_w (highest M_e), which gives rise to the lowest zero-shear viscosity. In addition, h-PLA and i-PLA have higher $E_{a,flow}$, than s-PLA. This is consistent with h- and i-PLA having larger aggregate regions than s-PLA. These results are further confirmed by the solution and melt viscosity data.

Furthermore, it was determined that strain-hardening was possible for h- and i-PLA, showing that transient aggregates due to enhanced L- and D- interactions, more common in isotactically and heterotactically enriched polymers compared to syndiotactic polymers, can increase the relaxation times. As a result, strain-hardening was present for i–PLA even at temperatures as high as 110 °C.

Academic researchers in the organometallic chemistry literature have been basing their expectations of the properties of PLA on studies of polyolefins capable of forming different microstructures. This study on PLAs with similar iso- and syndiotactic enrichment show that this assumption is incorrect and that syndiotactic PLAs do not have enhanced properties compared to their isotactic counterparts.

There may be an enhancement in the properties of highly syndiotactic PLAs, but considering the minute number of reports of these materials, achieving highly syndiotactic PLAs from *meso*-lactide does not seem favourable compared to forming heterotactic PLAs.

3.4 Experimental

General Methods. All air and moisture sensitive manipulations were carried out in an MBraun glovebox or using standard Schlenk line techniques. A Bruker Avance 300 or 400 MHz spectrometer was used to record ^{1}H NMR spectra. A Bruker Avance 600 MHz spectrometer was used to acquire homonuclear decoupled ^{1}H{^{1}H} NMR spectra of PLA. ^{1}H NMR chemical shifts are given in ppm versus residual protons in deuterated $CDCl_3$ (δ 7.27). Molecular weights, hydrodynamic radii and intrinsic viscosities were determined by GPC-MALS-RI-Viscometer using an Agilent liquid chromatograph equipped with a Agilant 1200 series pump and autosampler, three Phenogel 5 μm Narrow Bore columns (4.6 × 300 mm with 500 Å, 10^3 Å and 10^4 Å pore size), a Wyatt Optilab differential refractometer, Wyatt tristar miniDAWN (laser light scattering detector) and a Wyatt ViscoStar viscometer. The column temperature was set at 40 °C. A flow rate of 0.5 mL/min was used and samples were dissolved in THF (*ca.* 4 mg/mL). The measurements were carried out at laser wavelength of 690 nm at 25 °C. Data were processed by ASTRA software (Wyatt Technology). Molecular masses were determined using a Bruker Autoflex time-of-flight mass (TOF) spectrometer equipped with MALDI ion source. A differential scanning calorimeter (DSC) Q1000 (TA Instruments) was employed to measure the glass transition (T_g) and melting (T_m) temperatures. Thermogravimetric analysis (TGA) traces were collected on a PerkinElmer Pyris 6 TGA with a nitrogen flow rate of 20 mL/min. Shear measurements were performed using a MCR 501 rheometer equipped with 8 mm parallel plates. Uniaxial extensional measurements were performed using the SER-2 extensional fixture attached to an Anton Paar MCR 502 rheometer.

Materials. THF was taken from an IT Inc. solvent purification system with activated alumina columns and degassed before use. HPLC grade DCM was purchased from Fisher Chemicals and

was dried over CaH_2, transferred under vacuum and degassed before use. $CDCl_3$ was purchased from Cambridge Isotope Laboratories Inc. dried over CaH_2, transferred under vacuum and degassed through three freeze−pump−thaw cycles before use. 2-Propanol was purchased from Fisher Chemicals and was dried over 3Å molecular sieves before use. Indium (III) trichloride was purchased from Sigma-Aldrich and was used as received. Triethylamine and benzylalcohol were purchased from Sigma-Aldrich and were dried over CaH_2, transferred under vacuum and degassed before use. Rac-LA and *meso*-LA were a gift from PURAC America Inc. Rac-LA was recrystallized twice from hot dried toluene prior to use. Racemic and enantiopure complexes **A** and **B** were prepared according previously reported methods.[40,125]

Purification of *meso*-lactide. *Meso*-LA (50 g) was fully dissolved in DCM; magnesium sulphate (anhydrous) was added to the solution which was then stirred for 10 min. The excess solid was removed from white suspension *via* vacuum filtration and the solvent removed from the filtrate under reduced pressure to yield a white crystalline powder. This powder was recrystallized from dry 2-propanol five to seven times, to yield *meso*-LA with >95% purity (by GC-MS).

Polymerization of *meso*-LA with catalyst A. A 20 mL scintillation vial was equipped with a magnetic stir bar. *Meso*-lactide (290 mg, 2.7 mmol) was dissolved in 2 mL of DCM and to this a solution of the catalyst (2.0 mg, 0.002 mmol) in 2 mL of DCM was added. The solution was stirred at room temperature for 16 h. Solvent was removed under reduced pressure and the conversion was determined using ^{1}H NMR spectroscopy. The polymer was then dissolved in minimal DCM and precipitated using excess of cold methanol at least three times to remove residual catalyst. The polymer sample was then dried under vacuum for 48 h. No stabilizers were added.

Polymerization of *rac*-LA with catalyst B. A 20 mL scintillation vial was equipped with a magnetic stir bar. *Rac*-lactide (620 mg, 4.3 mmol) was dissolved in 2 mL of DCM and to this, a solution of the catalyst **B** (2.0 mg, 0.001 mmol) and in 2 mL of DCM was added. The solution was stirred at room temperature for 4 h to minimise transesterification and back-biting reactions. Solvent was removed under reduced pressure and the conversion was determined using ^{1}H NMR spectroscopy. The polymer was then dissolved in minimal DCM and precipitated using excess of cold methanol at least three times to remove residual catalyst. The polymer sample was then dried under vacuum for 48 h. No stabilizers were added.

Polymerization of *meso*-LA with aluminum salen binaphthylamine alkoxide catalyst (I). A vacuum adapted flask was equipped with a magnetic stir bar and charged with *meso*-lactide (1190 mg, 8.2 mmol) and stirred in 4 mL of toluene. To this, a solution of the catalyst (4.4 mg, 0.008 mmol) in 4 mL toluene was added. The reaction mixture was stirred at 80 °C for 20 h under N_2. Solvent was removed under reduced pressure and the conversion was determined using ^{1}H NMR spectroscopy. The polymer was then dissolved in minimal DCM and precipitated using excess of cold methanol at least three times to remove residual catalyst. The polymer sample was then dried under vacuum for 48 h.

Synthesis of heterotactic PLA. A vacuum adapted flask was equipped with a magnetic stir bar and was charged with *rac*-lactide (2.6 g, 0.02 mol) and stirred in 5 mL of toluene. InCl$_3$ (2 mg, 0.009 mmol), benzyl alcohol (0.9 µL, 0.009 mmol) and triethylamine (2.5 µL, 0.020 mmol) were then added and the volume made up to 15 mL with toluene. The reaction mixture was stirred at 80 °C for 72 h under N_2. Solvent was removed under reduced pressure and the conversion was determined using ^{1}H NMR spectroscopy. The polymer was then dissolved in minimal DCM and

precipitated using excess of cold methanol at least three times to remove residual catalyst. The polymer sample was then dried under vacuum for 48 h. No stabilizers were added.

Synthesis of atactic PLA. A vacuum adapted flask was equipped with a magnetic stir bar and charged with *rac*-lactide (2.0 g, 0.01 mol) and stirred in 5 mL of toluene. $Sn(oct)_2$ (4.5 μL, 0.04 mmol) was then added and the volume made up to 15 mL. The reaction was then stirred at 80 °C for 72 h under N_2. Solvent was removed under reduced pressure and the conversion was determined using ^{1}H NMR spectroscopy. The polymer was then dissolved in minimal DCM and precipitated using an excess of cold methanol at least three times to remove residual catalyst. The polymer sample was then dried under vacuum for 48 h. No stabilizers were added.

DSC measurement of polymers. Approximately 2-3 mg of polymer was weighed and sealed in an aluminum pan. Experiments were carried out under a nitrogen atmosphere. The samples were heated at a rate of 10 °C/min from 25 to 170 °C and held isothermally for 5 min to destroy any residual nuclei before cooling at 5 °C/min. The glass transition and melting temperatures were obtained from the second heating sequence, performed at 10 °C/min.

TGA measurement of polymers. Approximately 20 mg of polymer was weighed into a ceramic crucible. Experiments were carried out under a nitrogen atmosphere at a flow rate of 20 mL/min. The samples were heated at a rate of 20 °C/min from 25 to 500 °C.

Linear viscosity measurements. All polymer samples were compression molded at 150 °C into discs with diameters of 16-50 mm and thickness 0.4–0.6 mm. The dynamic linear viscoelastic measurements were carried out within the linear viscoelastic regime at temperatures in the range from 70 to 190 °C. The dynamic measurements were conducted in the range of 0.01–100 rad s^{-1} at a strain of 2%. A gap of 0.5 mm was used to minimize edge effects and ensure a reasonable aspect

ratio of plate radius and gap. Dynamic time sweep measurements were carried out at an angular frequency of 0.5 rad s^{-1} at 180 °C to examine the thermal stability of the samples. The rheological measurements were performed under nitrogen atmosphere to minimize degradation of the polymer samples during testing.

Uniaxial extensional measurements. Samples with diameters of 16-50 mm and thickness 0.4–0.6 mm were prepared by the same procedure used for shear measurements. Individual polymer specimens were then cut to a width of 1.5 – 3.5 mm. Measurements were conducted at 70, 90 and 110 °C at Hencky shear rates of 0.01 s^{-1}, 0.1 s^{-1}, 1.0 s^{-1} and 10 s^{-1}.

Chapter 4: Aryl initiators for the living ring-opening polymerization of rac-lactide.[§§§]

4.1 Introduction

The preceding chapters examined the polymerization behaviour of dinuclear indium complexes capable of stereoselective living ring-opening polymerization of cyclic esters (Chapter 2). This was followed by description of structure-property relationships for these materials, established by investigating the effect of tacticity on the rheological properties of poly(lactide) (Chapter 3). The next chapters aim to expand this study by exploring the role of aryloxy initiators on the living and immortal ring-opening polymerization of lactide with the ultimate aim of incorporating complex arylated bioproducts in this process (see Chapter 6).

4.1.1 PLA synthesis *via* living ring-opening polymerization with a chain transfer agent.

Metal-mediated living ring-opening polymerization (ROP) is characterized by linear growth in molecular weight with respect to conversion.[174,175] Figure 4.1 shows the coordination-insertion mechanism for the ROP of lactide with dinuclear indium catalyst $[(NNO)InCl]_2(\mu\text{-}Cl)(\mu\text{-}OEt)$ (**A**). In this mechanism, lactide coordinates to one of the metal centres activating the monomer for nucleophilic attack by the bridging alkoxide which inserts into the carbonyl C-O bond. A subsequent ring-opening event generates a propagating species which continues the polymerization. Propagation continues until all monomer is depleted and the catalyst is only

---

quenched with the addition of excess alcohol. Systems acting through this mechanism are useful as they generate polymers with low molecular weight distributions and chain ends which remain active, revived with addition of more monomer. Through this route, block co-polymers[176] with a variety of structures can be easily synthesized.
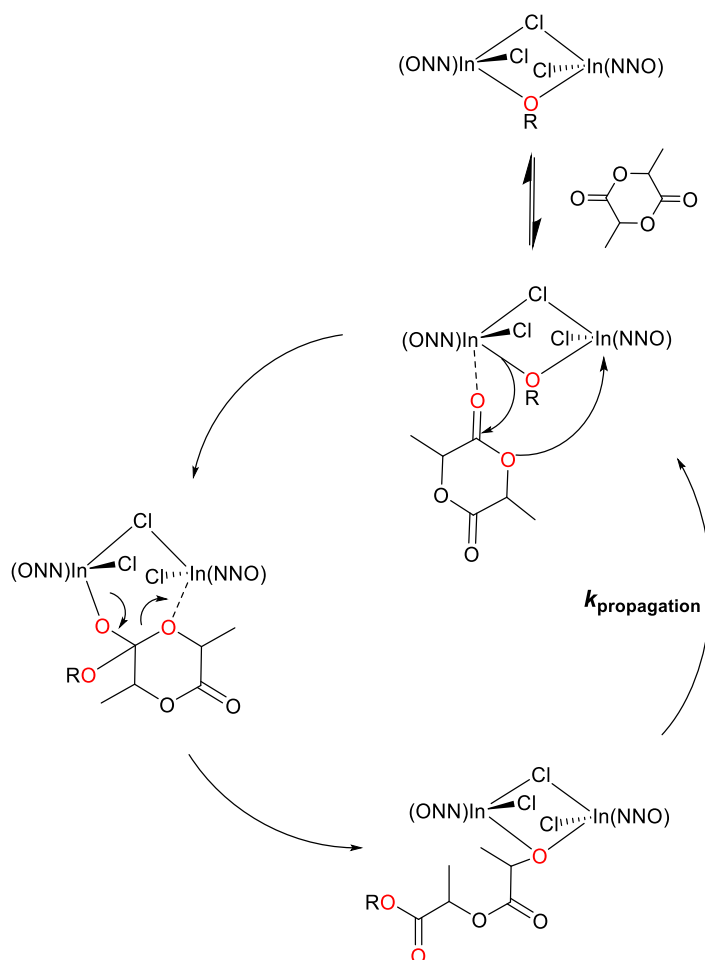
Figure 4.1 Coordination-insertion mechanism for the living ROP of lactide with dinuclear indium catalyst (**A**).

As mentioned previously, poly(lactide) or PLA has emerged as a useful bio-sourced and biodegradable polymer with applications in a wide variety of fields,[11,15,17,18,177-181] packaging (films), 3-D printing (filaments), and biomedical (tissue, implants and drug delivery). However, PLA has the drawback of lacking sites to impart extra functionality which could further improve

PLA properties and application scope. One efficient method to functionalize PLA that circumvents this issue, first reported by Inoue *et al.*,[182] is living ring-opening polymerization (ROP) with a chain transfer agent (CTA) (also known as immortal ROP (iROP)). In the modified mechanism, a propagating species can undergo reversible chain transfer with a CTA in solution. If this transfer reaction is faster than propagation, the altered propagating species can continue polymerization, incorporating the CTA onto the polymer chain-end (Figure 4.2). [182,183] Along with highly tuneable catalysts,[184,185] immortal polymerization has been a powerful methodology for generating multi-functionalized biodegradable polymers with varied architectures.[183,186-190]

One way to generate architectural density in immortal ROP systems is to include lignocellulosic alcohols. The lignocellulosic biorefinery industry has been expanding[75,191,192] and now provides researchers access to a large number of bio-based composite materials through blending and co-polymerization.[77,83,193] One interesting case is the use of lignin functionalized PLA[194-198] as an alternative to the widely-used phenol formaldehyde resins and adhesives.[199] Understanding and controlling the reactivity of phenolic[200-202] bioproducts as CTAs in immortal polymerization can expand their application scope (see Chapter 6).[200-203]
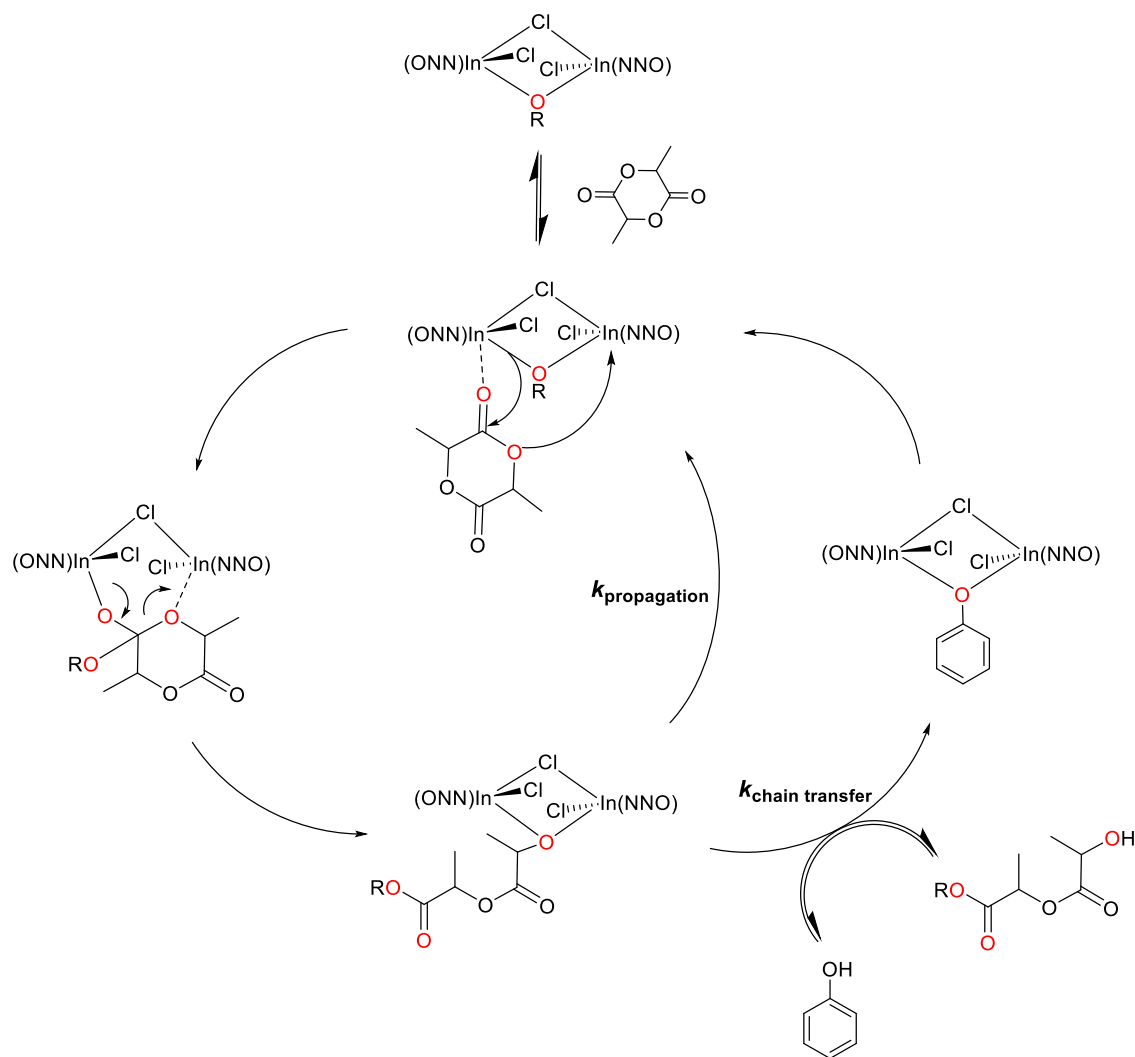
Figure 4.2 Coordination-insertion mechanism for the immortal ROP of lactide with dinuclear indium catalyst (**A**).

4.1.2 Aryloxy initiators in lactide ring-opening polymerization.

The use of aromatic alcohols as CTAs[197,204-209] and phenoxy derivatives as initiators[112,210-231] for the ROP of lactones has been less explored due to their lower nucleophilicity.[211] Byers *et al.*[232] have reported the use both of internal and external phenoxy derivatives with their bis(imido)pyridine iron complexes and found a decreasing trend in activity with the electron

106

withdrawing character of the phenols (Chart 4.1C). There are few examples of main group complexes with aryloxy-initiator ligands that are active for the ROP of lactones.[233-238]

The following sections explore the role of aryloxy initiators on the living and immortal polymerization of lactide with the ultimate aim of incorporating complex arylated products in this process. A family of indium complexes with *para*-substituted phenoxy initiators was synthesized and the effect of these substitutions on the living ring-opening polymerization of lactide investigated. Immortal ROP of lactide with a range of arylated alcohols as CTAs is explored as are the possible limitations of the system in incorporating more complex species such as diols.

[(NNO)InCl]$_2$(μ-Cl)(μ-OEt) (**A**)   **C**
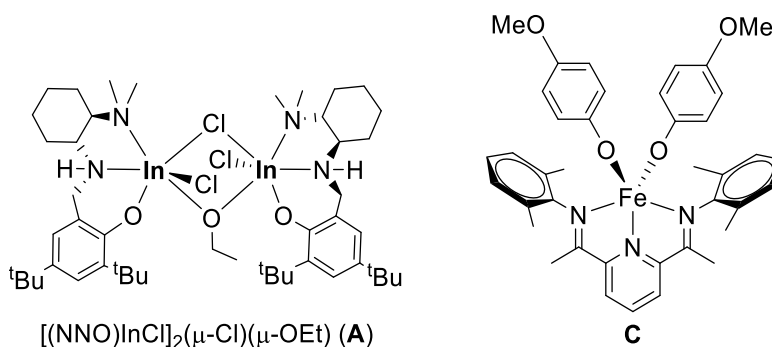
Chart 4.1 Dinuclear indium complexes [(NNO)InCl]$_2$(μ-Cl)(μ-OEt) (**A**)[40,123,239] and bis(imido)pyridine iron complex (**C**).[232]

4.2 Results and discussion

4.2.1 Synthesis racemic phenoxy-bridged indium complexes 1-5.

A series of phenoxy bridged complexes, analogous to complex **A**, was synthesized to investigate the role of phenyl initiators on the ROP of lactide. Reaction of ($\pm$)-(NNO)InCl$_2$ and KOPh$_R$ (Ph$_R$ = *para*-C$_6$H$_4$R; R = OMe, Me, H, Br, NO$_2$) forms the asymmetrically bridged complexes [(NNO)InCl]$_2$(μ-Cl)(μ-OPh$_R$) (R = OMe (**1**), Me (**2**), H (**3**), Br (**4**), NO$_2$ (**5**)) (Scheme 4.1, Route 1). Alternatively, these complexes can be synthesized by reaction of [(NNO)InCl]$_2$(μ-

Cl)(μ-OEt) (**A**) with a phenol through an exchange reaction (Scheme 4.1, Route 2). In Route 1, reactions involving electron poor phenoxy substituents favour the formation of the mono-phenoxy complexes **4** and **5**, which are obtained in higher yields than more electron rich complexes **1** and **2**, which readily form bis-phenoxy bridged dinuclear complexes as a by-product . The formation of bis-phenoxy species is evidenced by the presence of extra peaks in the aromatic region (6-8 ppm) of the ^{1}H NMR spectra of the crude products (Figure 4.3). Complexes **1-5** were purified *via* recrystallization from solutions of CHCl$_3$:pentane (2:3).
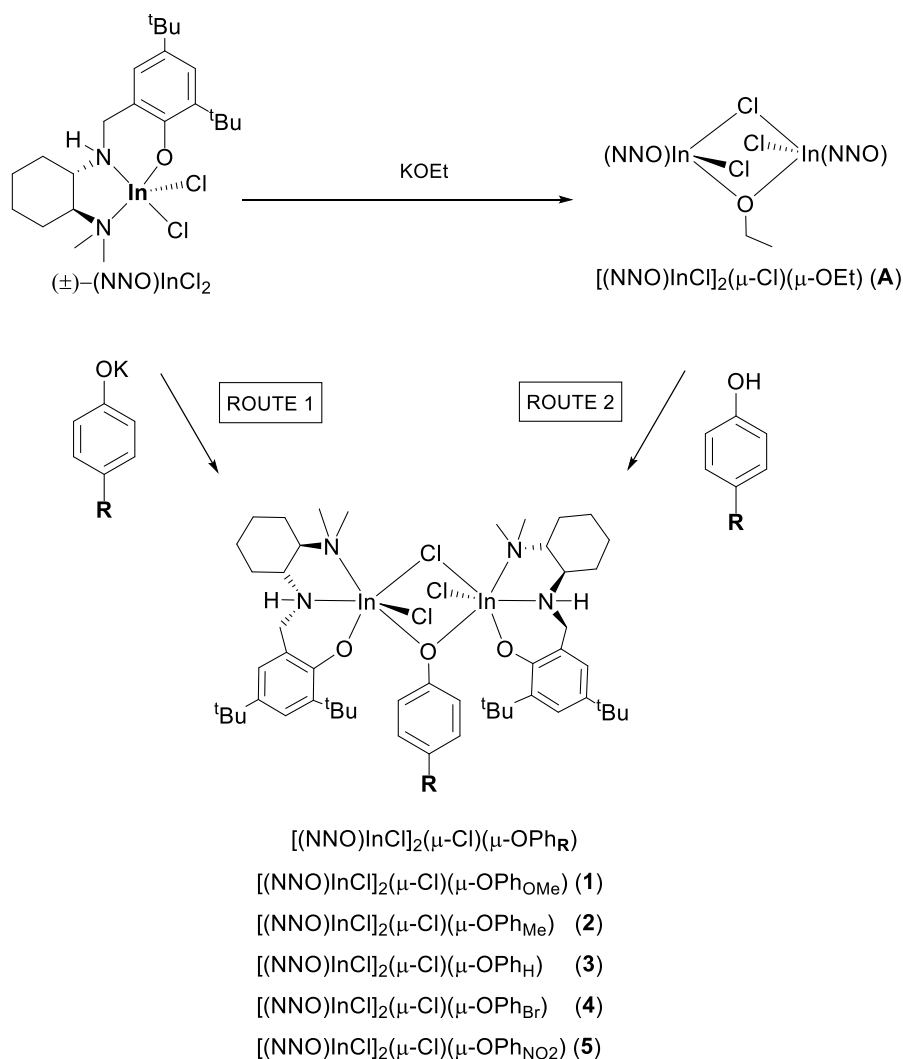
Scheme 4.1 Synthesis of dinuclear indium complexes [(NNO)InCl]$_2$(μ-Cl)(μ-OPh$_R$) (R = OMe, Me, H, Br, NO$_2$).
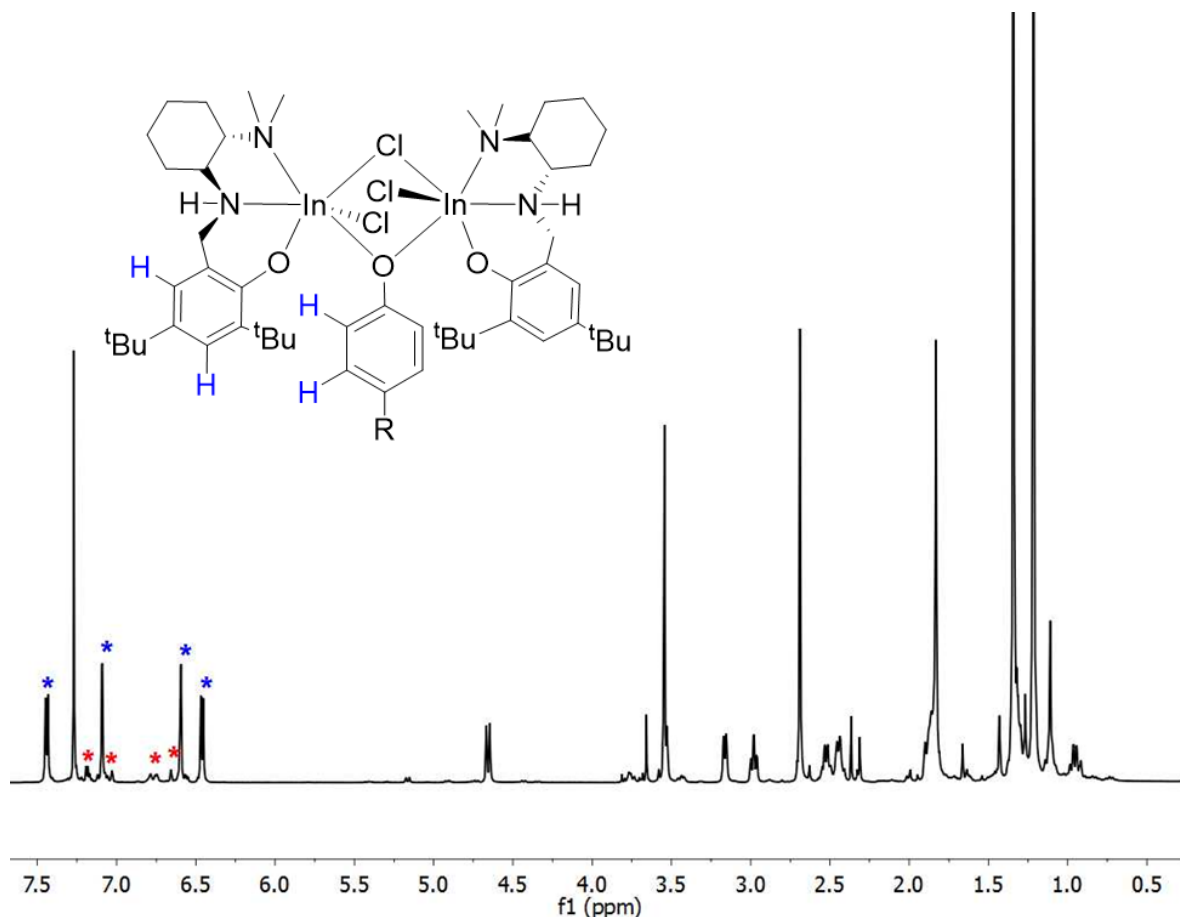
Figure 4.3 ^{1}H NMR (CDCl$_3$, 25 °C, 400 MHz) spectrum of crude reaction mixture containing (±)-[(NNO)InCl]$_2$(μ-Cl)(μ-OPh$_{OMe}$) (**1**) (blue stars). Extra peaks in the aromatic region (6-8 ppm) are assigned to the bis-phenoxy complex (red stars).

4.2.2 Solution structures of phenoxy-bridged indium complexes 1-5.

Complexes **1**–**5** have been fully characterized by ^{1}H, ^{13}C{^{1}H}, ^{1}H–^{1}H COSY, ^{1}H–^{13}C HSQC NMR spectroscopy and show similar solution structures to complex **A** and its related compounds[77-79] (see appendix B). The ^{1}H NMR spectra of complexes **1**–**5** are consistent with a mono-phenoxy bridged species with 1 : 1 ratios of the backbone NH-C*H$_2$*-Ar protons (doublets at approximately 3.7 and 4.7 ppm) and the bridging phenolic protons Ph-*H* (multiplets at 6-8 ppm). Compared to the parent complex (**A**), the loss of electron density with the substitution of the ethoxy bridge for

a phenoxy bridge causes an upfield shift of resonances on the ^{1}H NMR spectra of complexes **1–5**.

Diastereotopic splitting of the two doublets at 3-5 ppm for the NH-CH_2-Ar protons increases with

the electron-donating ability of the bridging phenol (Figure 4.4).
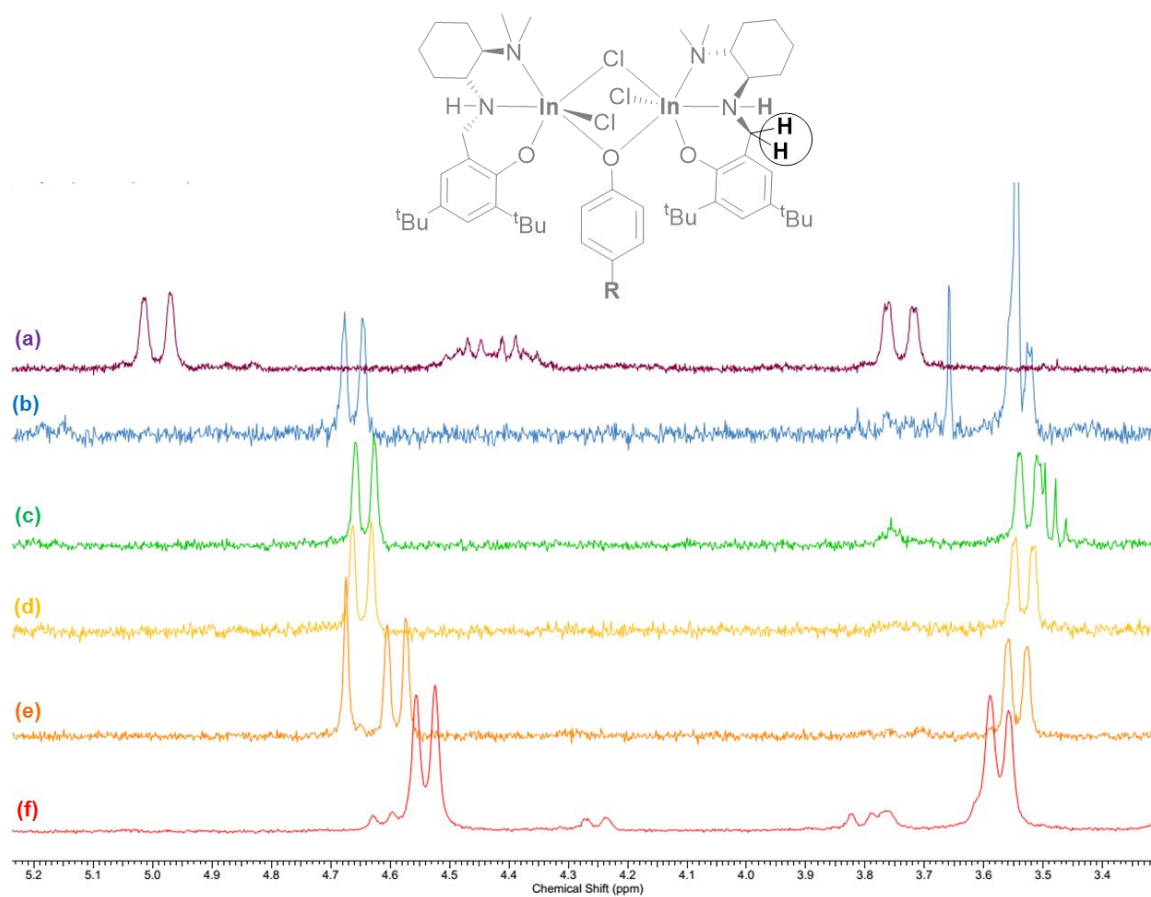
Figure 4.4 ^{1}H NMR spectra (CDCl$_3$, 25 °C, 400 MHz) of diastereotopic ligand NH-CH_2-Ar protons for (a) [(NNO)InCl]$_2$(μ-OEt)(μ-Cl) (**A**), (b) [(NNO)InCl]$_2$(μ-OPh$_{OMe}$)(μ-Cl) (**1**), (c) [(NNO)InCl]$_2$(μ-OPh$_{Me}$)(μ-Cl) (**2**), (d) [(NNO)InCl]$_2$(μ- OPh$_H$)(μ-Cl) (**3**), (e) [(NNO)InCl]$_2$(μ-OPh$_{Br}$)(μ-Cl) (**4**), and (f) [(NNO)InCl]$_2$(μ-OPh$_{NO2}$)(μ-Cl) (**5**).

Another notable feature of the ^{1}H NMR spectra of complexes **1-5** is the AB aryl coupling

constants ($^3J_{H-H}$) for the Ar-*H* protons of the ligand which narrow when shifting from alkyl to aryl

bridging moieties (2.51 Hz for complex **A** versus 2.35 Hz for complexes **1–5**) (Figure 4.5).
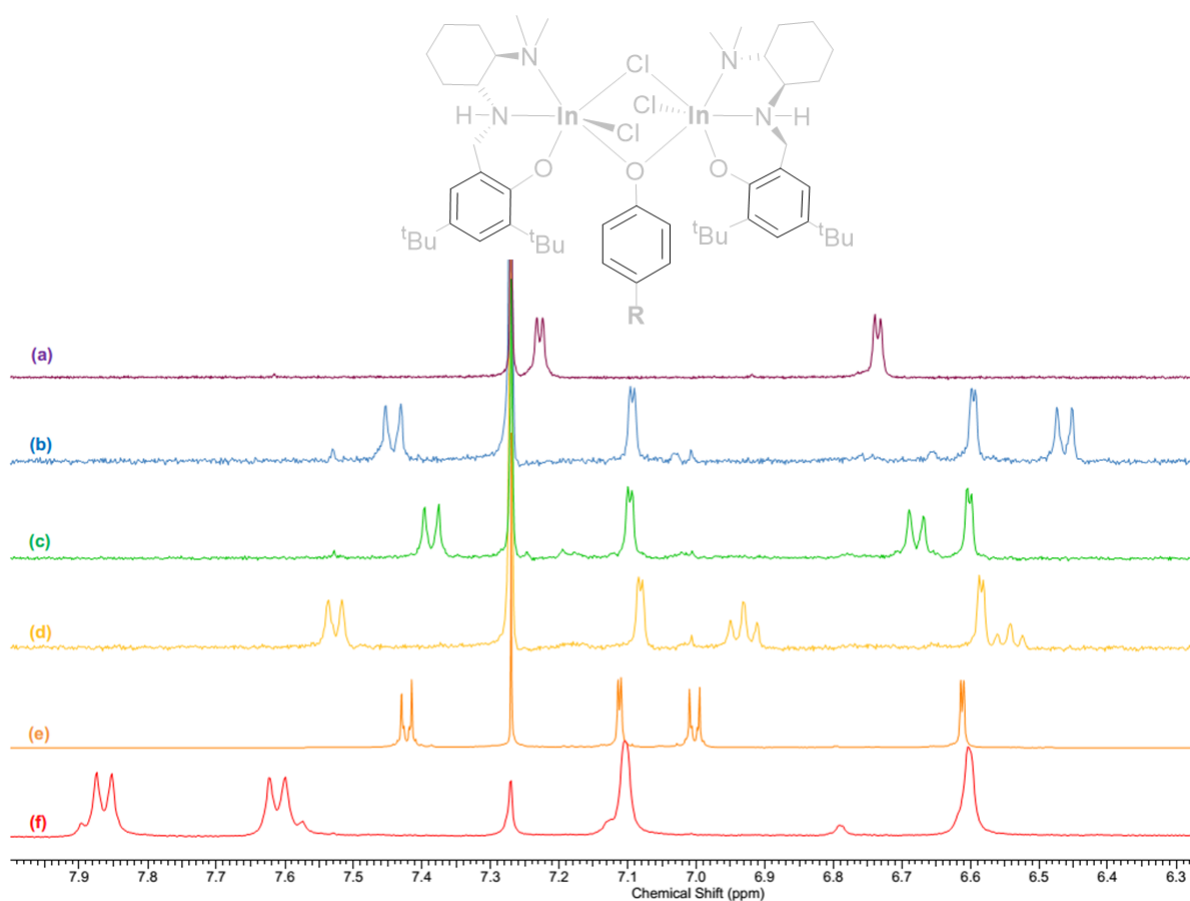
Figure 4.5 ^{1}H NMR spectra (CDCl$_3$, 25 °C, 400 MHz) bridging phenolic protons for (a) [(NNO)InCl]$_2$)(μ-Cl)(μ-OEt) (**A**), (b) [(NNO)InCl]$_2$)(μ-Cl)(μ-OPh$_{OMe}$) (**1**), (c) [(NNO)InCl]$_2$)(μ-Cl)(μ-OPh$_{Me}$) (**2**), (d) [(NNO)InCl]$_2$)(μ-Cl)(μ-OPh$_H$) (**3**), (e) [(NNO)InCl]$_2$)(μ-Cl)(μ-OPh$_{Br}$) (**4**), and (f) [(NNO)InCl]$_2$)(μ-Cl)(μ-OPh$_{NO2}$) (**5**).

4.2.3 Solid-state structures of phenoxy-bridged indium complexes 1-5.

Single-crystal x-ray diffraction analysis was conducted to support the solution characterization. Crystals of complexes **2**–**5** synthesized from racemic ligands were obtained from slow evaporation of toluene solutions at room temperature. All are asymmetric homochiral dinuclear indium complex with (*R,R*) ligand configuration at each distorted octahedral indium centre. There is a "cis" relationship between the phenoxy groups of the ligand, where they are on

111

the same side of the dimeric structure (Figure 4.6 - Figure 4.9). This arrangement is observed for

all related compounds generated from racemic ligands in this family.[77-79]
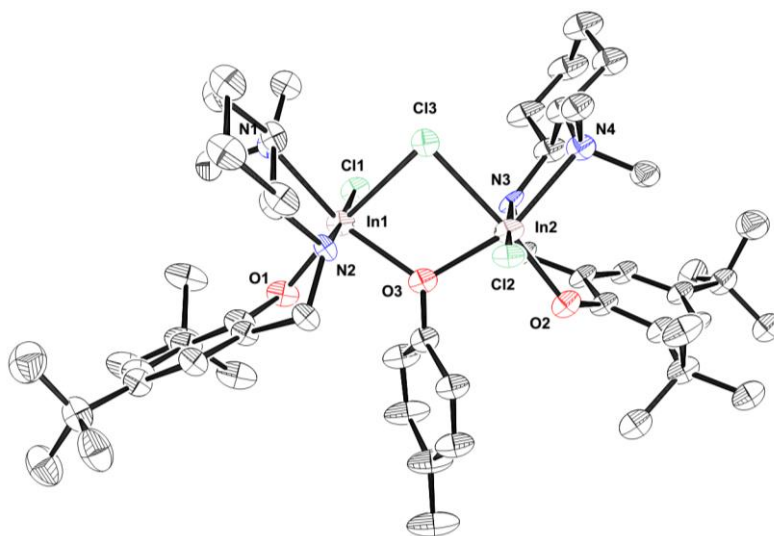
Figure 4.6 Molecular structure of [(NNO)InCl]$_2$(μ-Cl)(μ-OPh$_{Me}$) (**2**) depicted with ellipsoids at 50% probability (H atoms and all solvent molecules omitted for clarity).
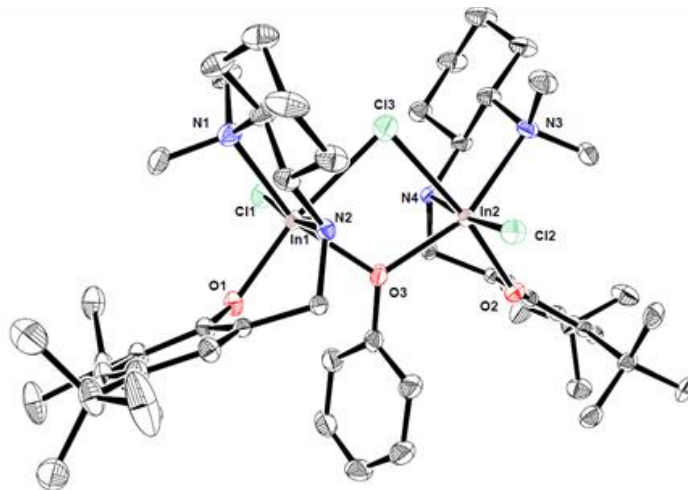
Figure 4.7 Molecular structure of [(NNO)InCl]$_2$(μ-Cl)(μ-OPh$_H$) (**3**) depicted with ellipsoids at 50% probability (H atoms and all solvent molecules omitted for clarity).
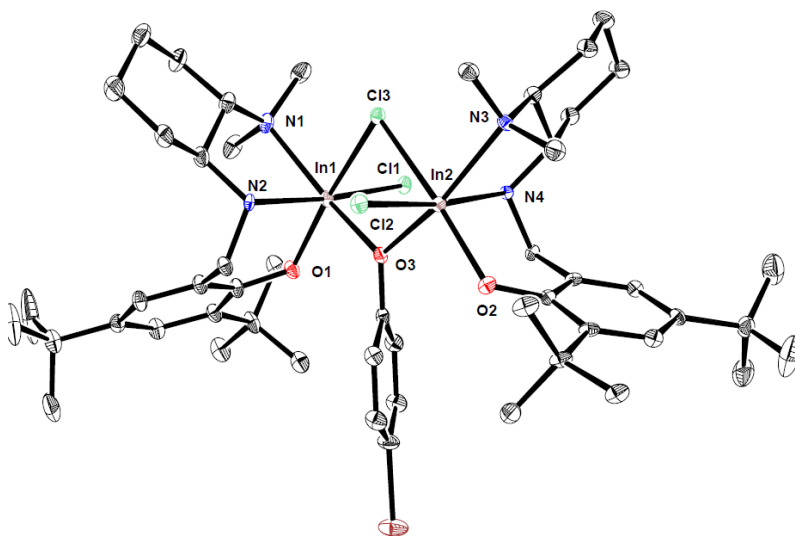
Figure 4.8 Molecular structure of [(NNO)InCl]$_2$(μ-Cl)(μ-OPh$_{Br}$) (**4**) depicted with ellipsoids at 50% probability (H atoms and all solvent molecules omitted for clarity).
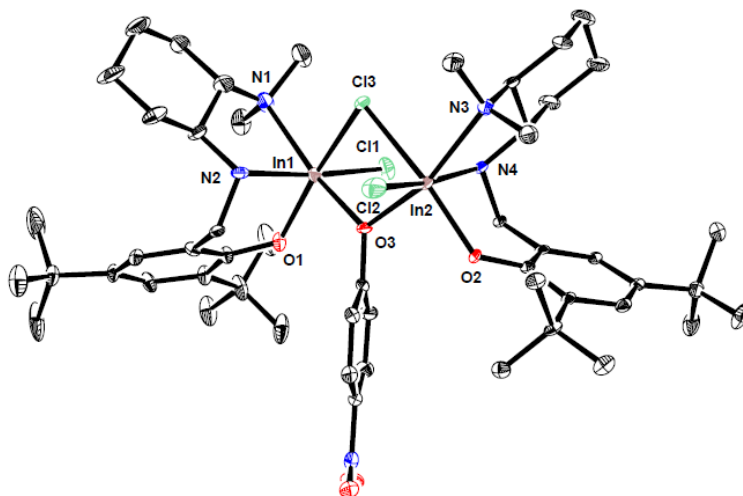
Figure 4.9 Molecular structure of [(NNO)InCl]$_2$(μ-Cl)(μ-OPh$_{NO2}$) (**5**) depicted with ellipsoids at 50% probability (H atoms and all solvent molecules omitted for clarity).

Table 4.1 Selected solid-state structural data for indium catalysts (**A, 2-6**).
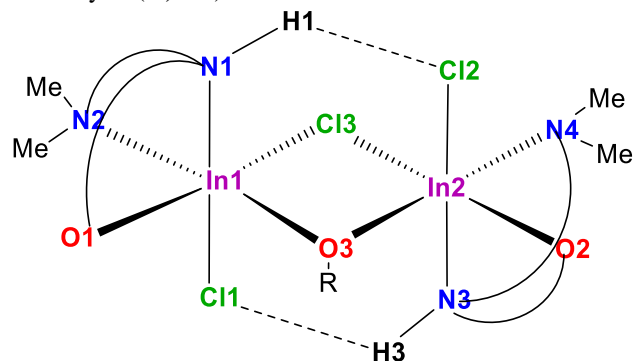
Complex	R=	In-O3(Å)	In-Cl3 (Å)	H-Cl (Å)	O1-In-Cl3 (deg)	O3-In-O1 (deg)	N1-H-Cl2 (deg)
A	C_2H_5	2.112(8), 2.129(8)	2.667(3), 2.636(4)	2.445, 2.788	166.8(2), 167.0(2)	93.0, (3), 93.0(3)	163.5, 131.8
2	C_6H_4Me	2.198(1), 2.174(1)	2.165(4), 2.423(3)	2.657, 2.914	171.7(3), 172.0(3)	94.9(4), 94.7(4)	160.6, 153.0
3	C_6H_5	2.186(2), 2.174(2)	2.602(9), 2.645(9)	2.729, 2.819	170.6(6), 169.2(6)	93.7(8), 94.4(8)	155.7, 153.8
4	C_6H_4Br	2.191(3), 2.186(3)	2.620(1), 2.630(1)	2.594, 2.907	170.7(1), 168.6(1)	93.3(1), 92.5(1)	158.2, 154.4
5	$C_6H_4NO_2$	2.193(4), 2.203(4)	2.613(1), 2.625(1)	2.484, 3,752	165.4(1), 167.7(1)	89.7(1), 77.2(1)	143.9, 139.2
6	$C_{13}H_{11}O_2Cl_2$	2.218(2), 2.247(2)	2.633(7), 2.594(7)	2.474, --	169.3(6), 173.8(6)	95.1(8), 98.9(8)	144.9, --

Errors are shown in parentheses. Data shown for both halves of non-symmetric structures. [a] Two molecules are present in the unit cell. Both show the same geometry.

Table 4.1 compares selected bond lengths and angles obtained from the X-ray crystal structures, the number in brackets are for the second half of unsymmetrical molecules. The phenoxy-bridged complexes **2–5** show longer In-O3 bonds than the alkoxy-bridged complex **A**, increasing with electron deficiency of the bridging phenol (2.174 Å (**2**) vs. 2.203 Å (**5**)). The *para*-substituted phenols are weaker nucleophiles compared to ethanol, which leads to longer and weaker bonds to the indium centre. An associated shortening of the In-Cl3 bond is also observed (2.423 Å (**2**) vs. 2.625 Å (**5**)) implying that this bond strengthens to alleviate the electron deficiency of the indium metal centre. In addition, with increasing electron deficiency of the phenol, the deviation from octahedral geometry increases: the O1-In-Cl3 angle becoming less linear (171.7° (**2**) vs. 165.4° (**5**)) and the O2-In-O3 bond becoming more acute (94.9° (**2**) vs. 89.7° (**5**)). This effect culminates in complex **5** having the most distorted octahedral geometry, and showing different reactivity to the other complexes in the series (Figure 4.9).

In previous work from our group,[41] it was of interest to probe the effect of internal hydrogen bonding within the complexes on the ring-opening polymerization of lactide. Table 4.1 attempts a comparison of the H1-Cl2 bond lengths and related angles. Parent complex **A** has a H1-Cl2 distance of 2.445 Å, comparable to that of complex **5** (2.484 Å) and the N1-H1-Cl2 bond angle for complex **A** is comparable to that of complex **2** (163.5° and 160.6°, respectively) suggesting that hydrogen-bonding is present in these systems. However, there does not appear to be any trend with the electron-withdrawing character of the bridging phenol. The reactivity towards *rac*-LA for these complexes does not correlate to the trends in hydrogen bonding strength, further supporting an earlier finding from our group showing that although these hydrogen-bonding interactions are important for the stability of the dimeric species, they are unlikely a factor contributing to the reactivity of these systems.[41]

4.2.4 Living ring-opening polymerization (ROP) of lactide using catalysts 1–5.

The efficiency of the different initiators **1**-**5** for the ring-opening polymerization of up to 2000 equivalents of racemic lactide (*rac*-LA) was examined at room temperature (Scheme 4.2 and Table 4.2). Phenoxy-bridged complexes display less control over the polymerization of *rac*-LA compared to catalyst **A**, giving polymers with higher-than-expected molecular weights at low monomer loadings, which is indicative of a slow initiation step (Figure 4.10). Catalysts with electron rich bridging phenols (**1**-**2**) show the best control over molecular weight; conversely, catalysts **4** and **5** with electron deficient bridging phenols give polymers with molecular weights which largely deviate from the theoretical molecular weights. In addition, as expected for the least nucleophilic initiator, the *para*-nitrophenol bridged complex **5** is significantly less active than the other four phenoxy catalysts, only reaching 10-20% conversion after 3-4 days (Table 4.2, entries 18-22). These observations are in line with those reported for complex **B** and its analogues, where a similar change in activity was shown as the electron-withdrawing ability of the *para* substituent was altered.[232]

Scheme 4.2 Ring-opening polymerization of *rac*-lactide with complexes **1**-**5**.

R = OMe (**1**), Me (**2**), H (**3**), Br (**4**), NO$_2$ (**5**)
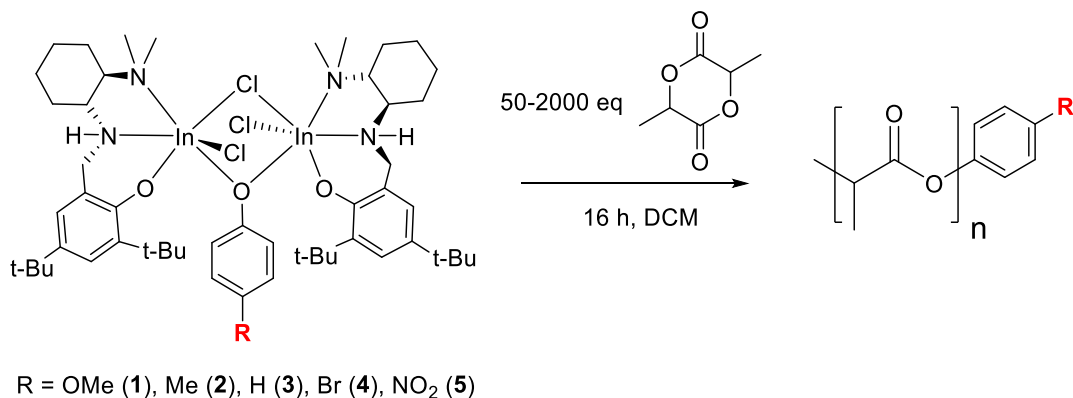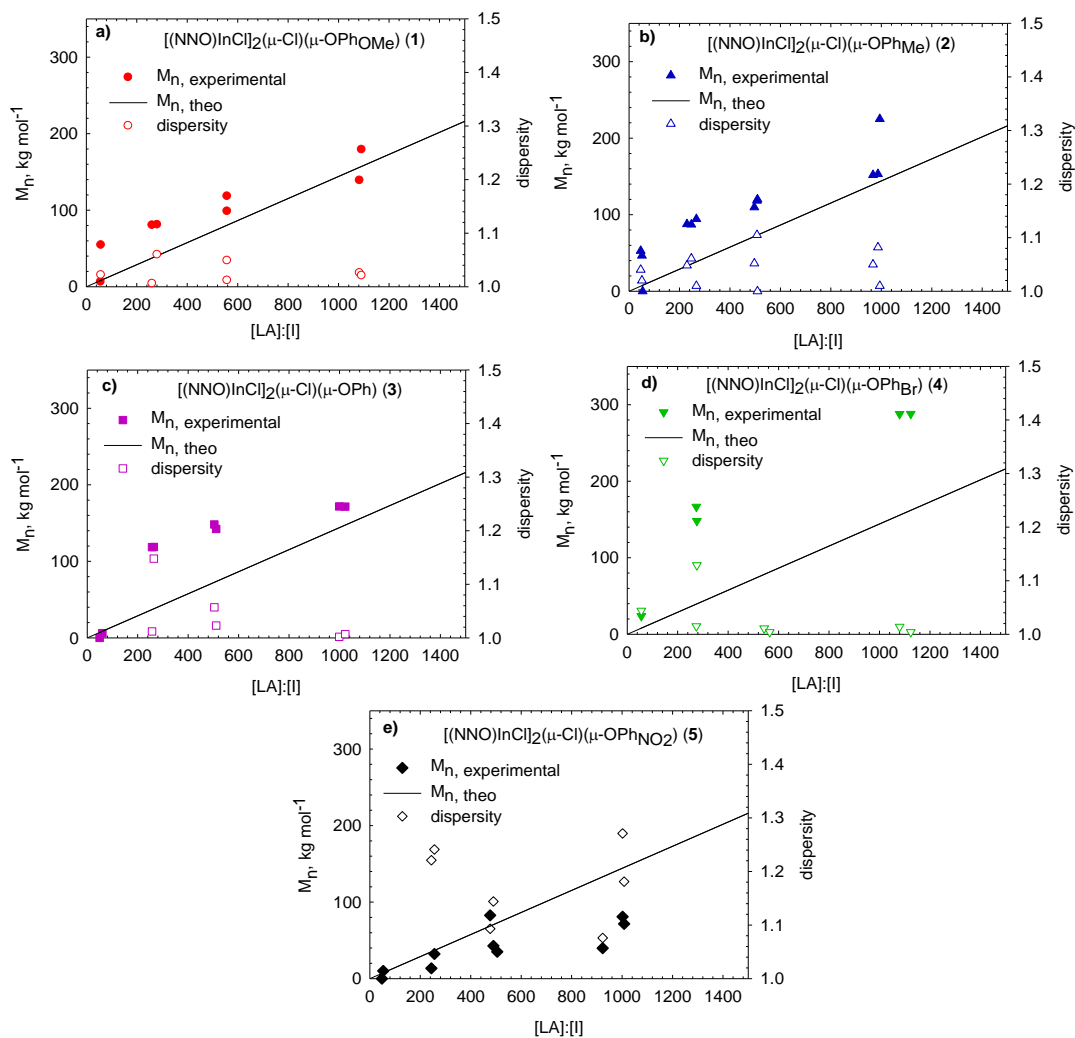
Figure 4.10 Plots of observed PLA M_n (closed symbols) and dispersity (open symbols) as functions of added *rac*-LA for a) [(NNO)InCl]$_2$(μ-OPh$_{OMe}$)(μ-Cl) (**1**), b) [(NNO)InCl]$_2$(μ-OPh$_{Me}$)(μ-Cl) (**2**), c) [(NNO)InCl]$_2$(μ-OPh$_H$)(μ-Cl) (**3**), d) [(NNO)InCl]$_2$(μ-OPh$_{Br}$)(μ-Cl) (**4**), and e) [(NNO)InCl]$_2$(μ-OPh$_{NO2}$)(μ-Cl) (**5**). (M_n = number averaged molecular weight). The line represents theoretical M_n values based on the monomer:initiator ratio at 100% conversion. All reactions were carried out room temperature in DCM.

117

Table 4.2 Living ring-opening polymerization data of *rac*-lactide with complexes **1-5.**

entry	Cat	Time (h)	Conv. (%)^a	[M]/[I]	$M_{n,theo}{}^b$	$M_{n,GPC}{}^c$	$Đ^c$
1	**1**	18	78	58	6550	54600	1.02
2	**1**	18	93	260	35000	80500	1.01
3	**1**	18	95	560	76400	98700	1.01
4	**1**	18	97	1100	152000	139000	1.03
5	**2**	18	86	54	6690	52800	1.04
6	**2**	18	89	270	34300	87200	1.06
7	**2**	18	97	500	71200	118000	1.11
8	**2**	18	97	990	139000	153000	1.08
9	**2**	18	95	2070	284000	225000	1.01
10	**3**	4	21	49	1480	6180^d	*na*
11	**3**	4	95	260	35200	119000	1.01
12	**3**	4	98	510	72200	142000	1.02
13	**3**	4	98	1020	145000	172000	1.01
14	**4**	18	12	56	990	23700	1.04
15	**4**	18	93	270	36700	167000	1.02
16	**4**	18	97	540	75900	231000	1.01
17	**4**	18	98	1080	153000	288000	1.01
18	**5**	72	12	53	930	10100	1.01
19	**5**	72	8.6	240	3020	13500	1.22
20	**5**	72	11	490	7600	42800	1.14
21	**5**	72	17	1000	25000	80900	1.27
22	**5**	96	23	1010	33400	71600	1.18

Reactions were carried out in DCM, 25 °C. ^{a} Monomer conversions determined by ^{1}H NMR spectroscopy. ^{b} Calculated from $M_{n,theo} = (144$ g mol^{-1} × conversion × [LA]/[initiator]) + M_{ROPh}. ^{c} Absolute molecular weights were determined by triple detector GPC (gel permeation chromatography) *via* Universal Calibration (THF 4 mg mL^{-1}, flow rate = 0.5 mL min^{-1}, dn/dc = 0.044 mL g^{-1}). ^{d} Molecular weight determined from MALDI-ToF analysis.

To confirm that the phenoxy initiators remain as the polymer chain ends, polymer samples were analysed using ^{1}H NMR spectroscopy and MALDI-ToF mass spectrometry. Chain end analysis of polymer samples generated with catalyst **3** (50 equiv. *rac*-LA) by ^{1}H NMR spectroscopy shows aryl signals that do not belong to free phenol or to **3** (Figure 4.11). MALDI-

ToF analysis revealed a major series of peaks separated by 144 mass units with phenol at the end-group. The minor series is separated by 72 mass units, implying there is some transesterification occurring during the polymerization (Figure 4.12).
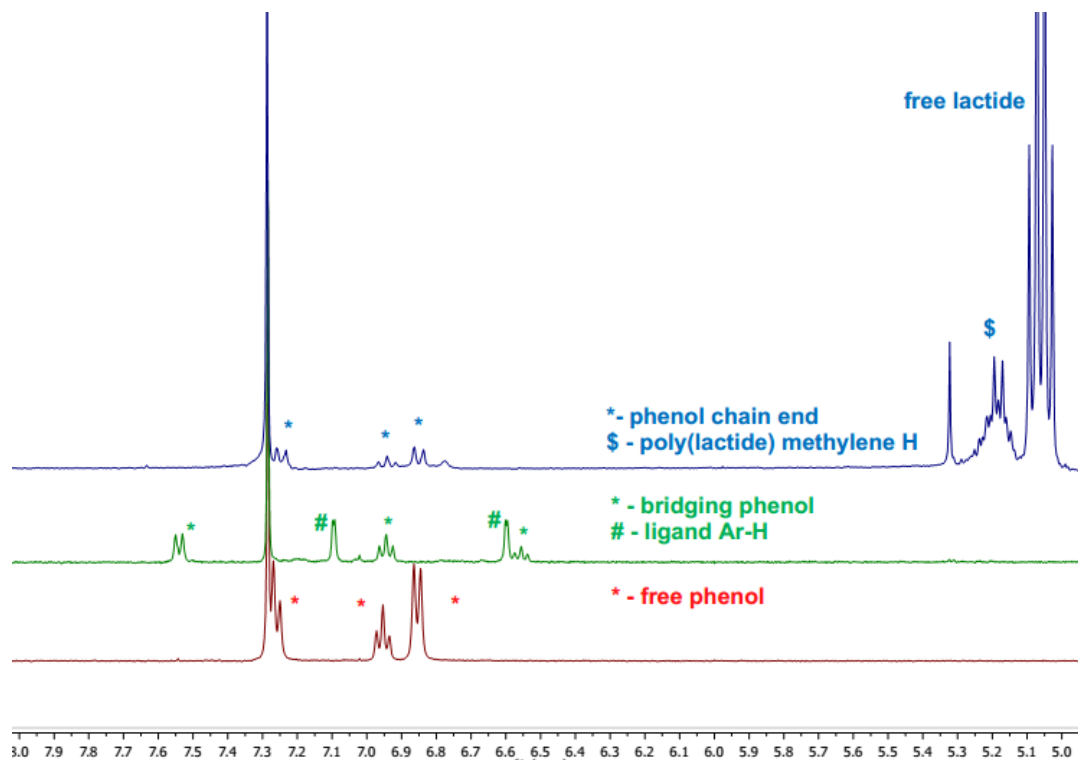
Figure 4.11 ^{1}H NMR spectrum (CDCl$_3$, 25 °C, 400 MHz) of free phenol (red spectrum) overlaid with ^{1}H NMR spectrum (CDCl$_3$, 25 °C, 400 MHz) of [(NNO)InCl]$_2$(μ-Cl)(μ-OPh$_H$) (**3**) (green) and ^{1}H NMR spectrum (CDCl$_3$, 25 °C, 400 MHz) of the polymerization reaction mixture (blue, Table 4.2. entry 10).
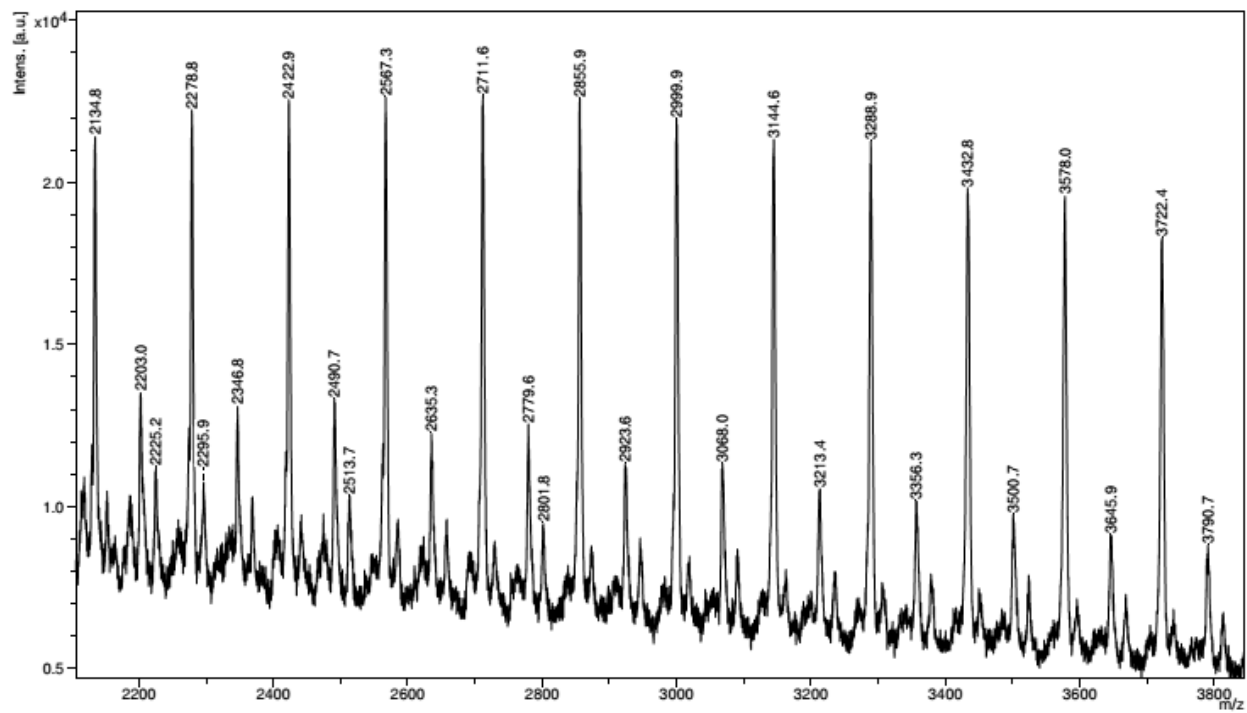
Figure 4.12 MALDI-ToF spectrum from polymerization of [LA]:[**3**] = 49:1 (Table 4.2, entry 10). A_n = [144.13LA]$_n$ + 94.11HOPh + ^{23}Na$^+$
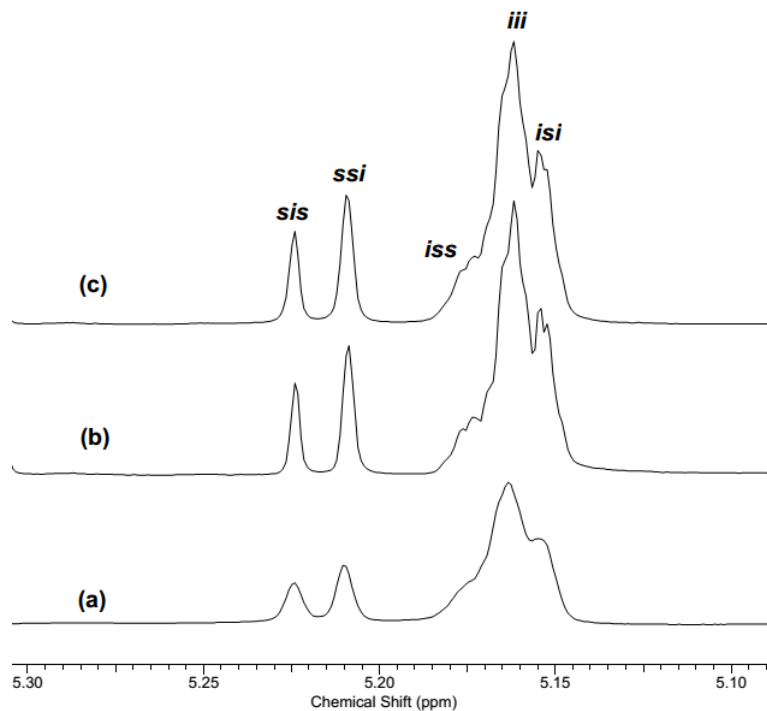
Figure 4.13 ^{1}H{^{1}H} NMR (CDCl$_3$, 25 °C) spectrum of the methylene region of PLAs generated from a) (±)-[(NNO)InCl]$_2$(μ-Cl) (μ-OEt) (**A**), b) (±)-[(NNO)InCl]$_2$(μ-Cl) (μ-OPh$_{OMe}$) (**1**) (±)-[(NNO)InCl]$_2$(μ-Cl) (μ-OPh) (**3**).

The tacticity of polymers formed from the aryl initiators can be determined by inspecting the methylene region (3-5 ppm) of the ^{1}H{^{1}H} NMR spectra. From analysis of defect tetrad patterns, polymers generated from both alkyl and aryl initiators showed the same distribution of tetrad peaks implying the same stereocontrol mechanism is acting in all the systems (Figure 4.13).

4.2.5 *In situ* polymerization studies.

Polymerization of *rac*-LA using catalysts **1**-**4** ([LA]:[I] = 50:1) was monitored using ^{1}H NMR spectroscopy at room temperature. The plots of ln[LA] vs. time for all catalysts show an initiation period followed by a linear propagation period. Initiation times correlate with the electron-deficiency of the bridging phenoxide, thus catalyst **1** displays a shorter initiation period than catalysts **2**-**4** (Figure 4.14).

121
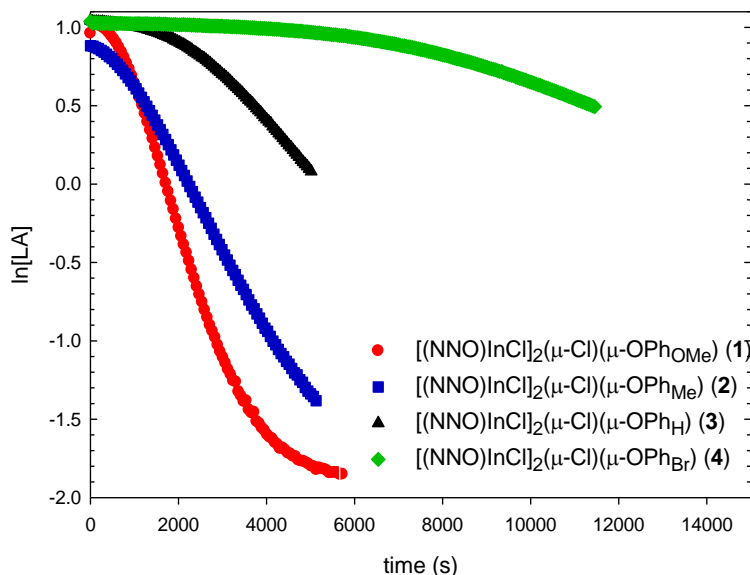
Figure 4.14 Plot of ln[LA] versus time for polymerization of *rac*-LA catalyzed with **1** (●) **2** (■), **3** (▲) and **4** (◆). Reactions were carried out in an NMR tube at 25 °C. 1,3,5-trimethoxybenzene (TMB) was used as internal standard. All reactions were carried out with 50 eq. of LA in CD$_2$Cl$_2$ at 25 °C and followed by ^{1}H NMR spectroscopy. [**1**] = 0.0039 M, [LA] = 0.19 M. [**2**] = 0.0043 M, [LA] = 0.21 M. [**3**] = 0.0037 M, [LA] = 0.22 M. [**4**] = 0.0041 M, [LA] = 0.22 M. The value of k_{obs} was determined from the slope of ln[LA] vs. time, averaged from at least three experiments.

The estimated rates of propagation, k_{obs}, were determined from the slope of ln[LA] vs. time (averaged from at least three experiments). The observed rates for **1-4** are one order of magnitude slower than that for catalyst **A** (Table 4.3). The higher-than-expected molecular weights observed in the polymers generated with phenoxy-bridged catalysts is indicative of their incomplete activation.

Previously reported computational studies on the polymerization of lactide isomers with catalyst **A** showed that the rate determining step is the insertion into the carbonyl C-O bond by the bridging ethoxy moiety.[129] The longer initiation period of the phenoxy bridged catalysts can be attributed to the lower nucleophilicity of the phenoxy compared to the ethoxy moieties. This lower

nucleophilicity may mean that not all the complex molecules are being activated leading to a lower concentration of the active catalytic species in the reaction medium.

After the initial insertion of the aryloxide, similar propagation species exist in solution. The difference in the observed propagation rates is likely due to different concentrations of active catalyst present that also causes the observed higher-than-expected molecular weights.

Table 4.3 Propagation rates for the ROP of *rac*-LA with complexes **A** and **1-4**.

entry	Catalyst	k_{obs} ($\times 10^{-4}\,s^{-1}$)
1	A	18.9(5)
2	1	8.5(8)
3	2	5.3(2)
4	3	3.3(2)
5	4	1.1(1)

Values shown in parentheses are standard errors. Reactions carried out in an NMR tube at 25 °C with 1,3,5-trimethoxybenzene (TMB) as internal standard with 50 equivalents of LA in CD$_2$Cl$_2$ at 25 °C. [**A**] = 0.0046 M, [LA] = 0.22 M. [**1**] = 0.0039 M, [LA] = 0.19 M. [**2**] = 0.0043 M, [LA] = 0.21 M. [**3**] = 0.0037 M, [LA] = 0.22 M. [**4**] = 0.0041 M, [LA] = 0.22 M. The value of k_{obs} was determined from the slope of ln[LA] vs. time, averaged from at least 3 experiments (see appendix B).

4.2.6 Immortal ring-opening polymerization (ROP) of lactide with catalyst A and aromatic alcohols.

One of the main goals of this study was to investigate the use of aromatic alcohols in the immortal ROP of *rac*-LA. Shifting from alkyl alcohols to using aryl alcohols does have an effect on the initiation step of the living ROP (as shown in 4.2.5). Therefore, it was of interest to examine the influence of phenols on the chain transfer reaction needed to achieve immortal ROP. To probe the kinetics of exchange, the substitution reaction between catalyst **A** and phenol (HOC$_6$H$_5$), *para-*

methoxyphenol (HOC$_6$H$_4$OMe) and *para*-bromophenol (HOC$_6$H$_4$Br) was followed by *in situ* ^{1}H NMR spectroscopy (Scheme 4.3).

Scheme 4.3 Alkoxy-phenoxy exchange reaction with complex **A** and *para*-substituted phenol.
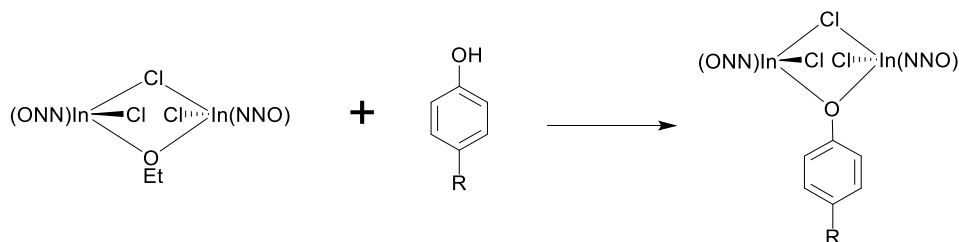
A 1:1 mixture of [**A**]:[aryl alcohol] was dissolved in CDCl$_3$ and the loss of the bridging ethoxy moiety for **A** was monitored at room temperature for 60 minutes (Figure 4.15). Plots of ln[**A**] versus time show an initial decrease in the [**A**] followed by a steady state (Figure 4.16). The slope of this graph gives an indication of the chain-transfer step (6.8(4) × 10^{-4} s^{-1} ([**A**] + phenol)) which is on the same order as the propagation rate k_{obs}, for catalysts **1**-**4**.
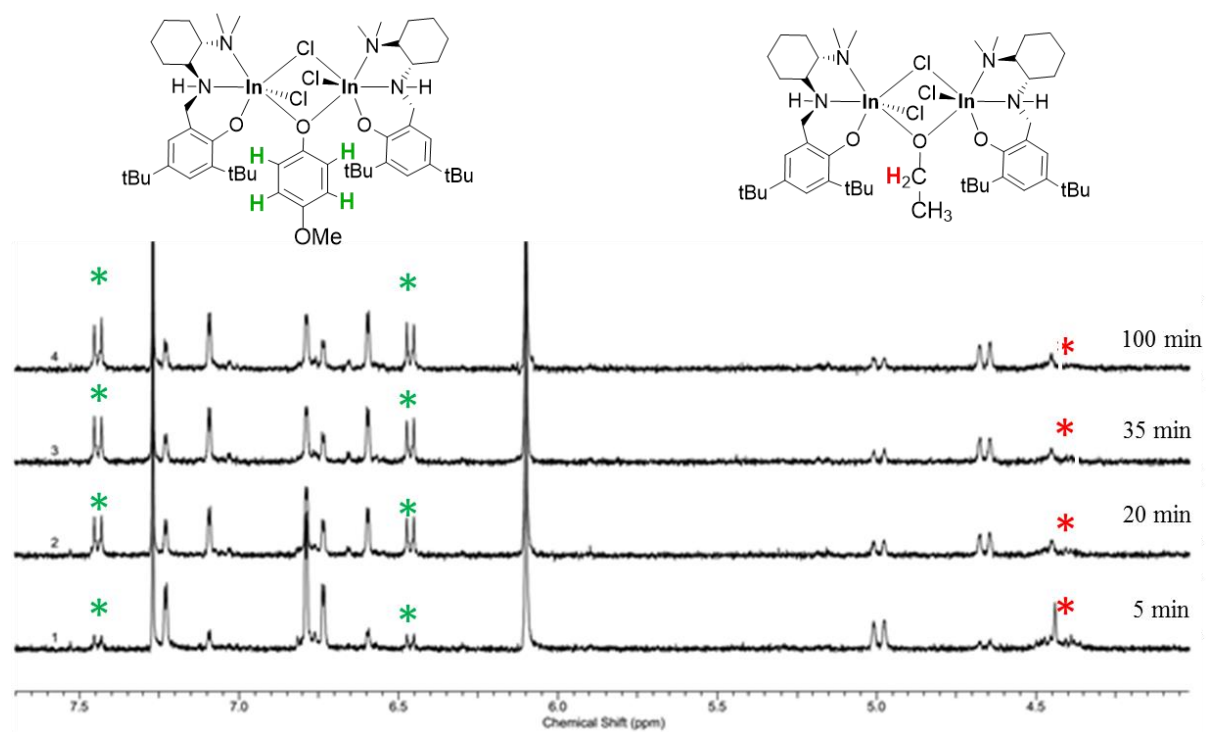
Figure 4.15 ^{1}H NMR (CDCl$_3$, 25 °C) spectrum of the alkoxy-phenoxy exchange reaction with complex **A** and *para*-methoxy phenol. The loss of the bridging ethoxy peaks (denoted by red stars) and the emergence of bridging phenoxy signals (denoted by green stars) were monitored and used to calculate the rate of exchange, $k_{exchange}$.
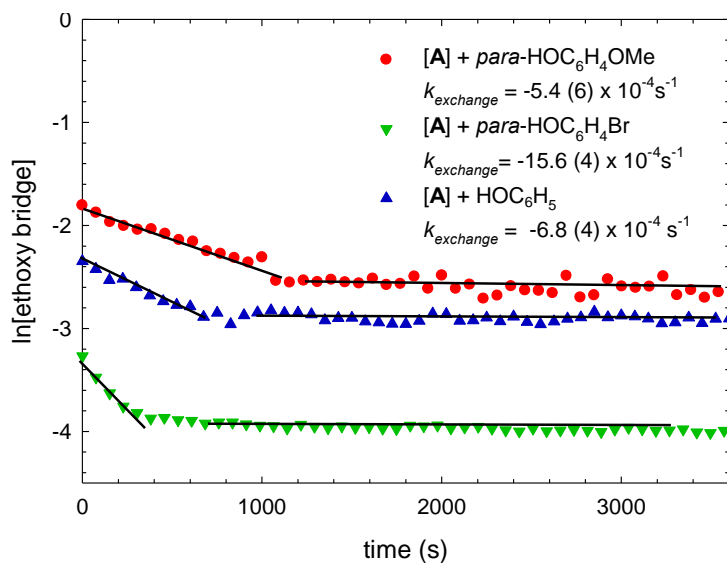
Figure 4.16 Plot of ln[**A**] versus time for exchange between catalyst **A**, HOC$_6$H$_4$OMe (●) and HOC$_6$H$_4$Br (▼) and HOC$_6$H$_5$ (▲). Reactions carried out in an NMR tube (CDCl$_3$, 25 °C). 1,3,5-trimethoxybenzene (TMB) was used as internal standard. [**A**] = 0.0046 M, [HOC$_6$H$_4$OMe] = 0.0050 M, [HOC$_6$H$_4$Br] = 0.0059 M, [HOC$_6$H$_5$] = 0.00411 M. The value of $k_{exchange}$ was determined from the slope of ln[**A**] vs. time, averaged from three experiments.

To probe the immortal ROP reaction further, a polymerization with a ratio of 10500:1:20 ([LA]:[**A**]:[phenol]) in DCM at room temperature was performed and aliquots were taken at regular intervals over 8 hours. The extracted aliquots were quenched and precipitated with wet methanol and analysed using GPC analysis (Figure 4.17 and Figure 4.18). GPC peaks shift to short elution times which correlates to an increase in molecular weight. This linear growth with respect to conversion is expected of a living process.
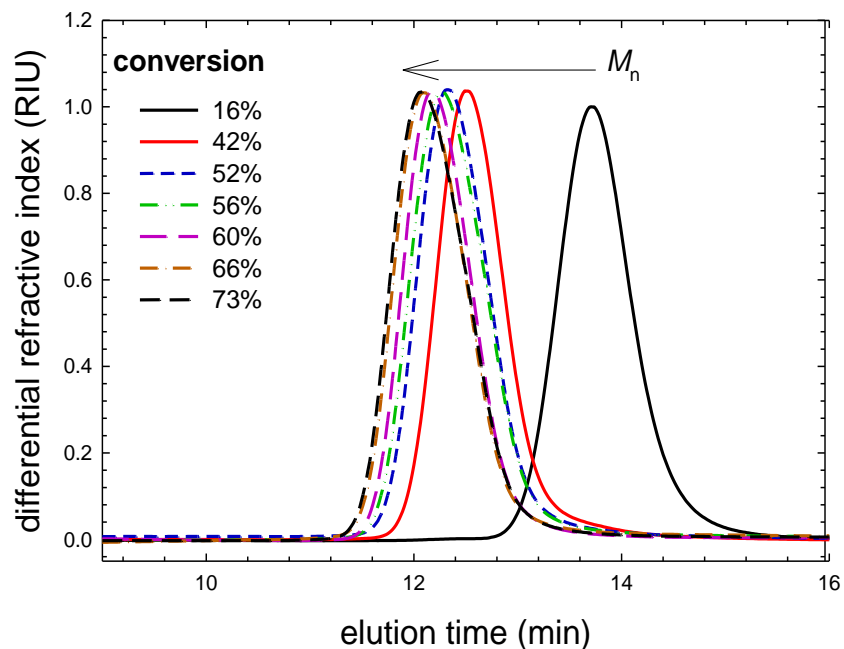
Figure 4.17 GPC traces with respect to conversion for the immortal ROP of lactide with **A** and phenol as the CTA ([LA]:[**A**]:[phenol] = 10500:1:20).
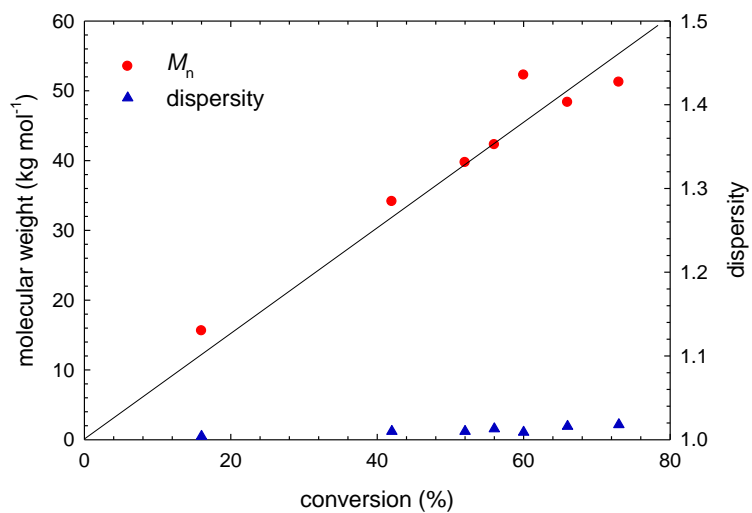
Figure 4.18 Plot of molecular weight and dispersity with respect to conversion for the immortal ROP of lactide with **A** with phenol ([LA]:[**A**]:[phenol] = 10500:1:20).

The immortal ring-opening polymerization of *rac*-LA was attempted with four different aromatic diols as chain transfer agents (CTAs) at room temperature (Chart 4.2). Under an inert atmosphere, solutions of *rac*-LA and CTA in DCM were prepared. After a homogenous solution had been obtained, appropriate amounts of complex **A** were added and the resulting reaction mixtures were stirred at room temperature. Catalyst to CTA ratios were kept constant at 1:20, while catalyst to monomer ratios were varied from 1050 to 21000 to generate polymer chains 50 to 1000 units in length. The resulting polymers using phenol (PhOH), showed excellent control over molecular weight and dispersity, compared to the living polymerization with aryl initiators (Table 4.4 and Figure 4.19). The initiating species in the immortal ROP reaction is complex **A** with a bridging ethoxy moiety. As the initiator is an alkoxide, it is expected that all the catalyst in solution is activated unlike with complexes **1-5** leading to well-defined polymers.

Chart 4.2 Aromatic diols used as chain transfer agents (CTAs) for the immortal ROP of *rac*-LA.

| biphenol | dichlorophene | 1,8-naphthalenediol | 1,5-naphthalenediol |
| biPhOH | diClPhOH | 1,8-NapOH | 1,5-NapOH |
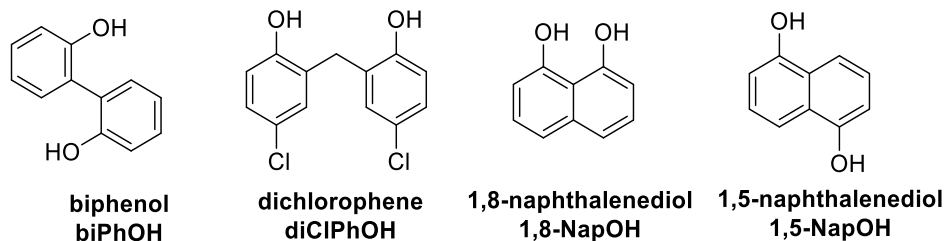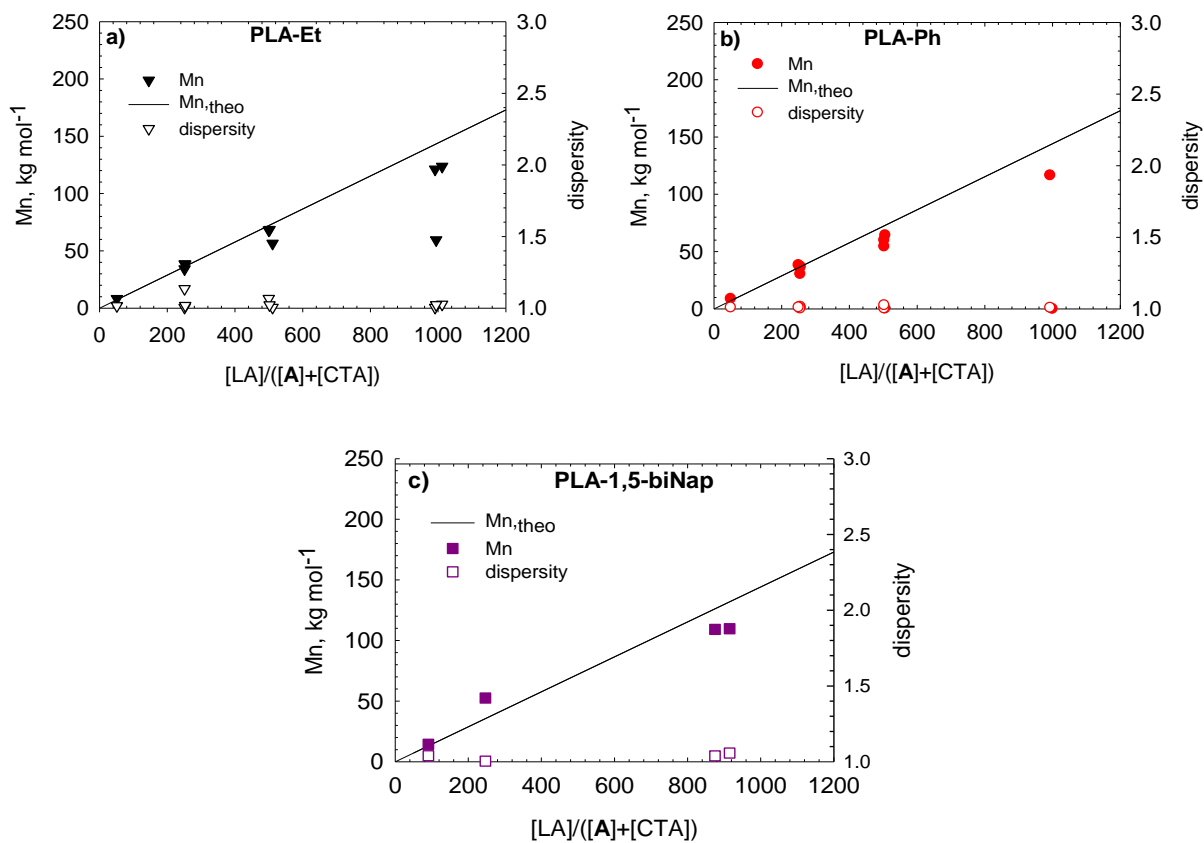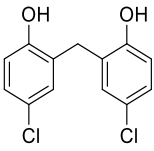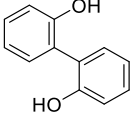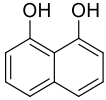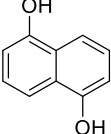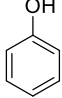
Figure 4.19 Plots of observed PLA M_n (closed symbols) and dispersity (open symbols) as functions of [LA]:([**A**]+[CTA]) for (a) CTA = ethanol (PLA-Et), (b) CTA = phenol (PLA-Ph), (c) CTA = 1,5-naphthalenediol (PLA-1,5-Nap)

Table 4.4 Molecular weight data for immortal ROP of *rac*-LA with various aryl chain transfer agents.

Entry	CTA	Time (h)	Conv. (%)[a]	[LA]/([A]+[CTA])	$M_{n,theo}$ (g mol^{-1})[b]	$M_{n,GPC}$ (g mol^{-1})[c]	$Đ$[c]
1	dichlorophene diClPhOH	168	0	71	--	--	--
2[d]		65	44	79	5310	3160[e]	--
3	biphenol biPhOH	168	0	53	--	--	--
4	1,8-naphthalenediol 1,8-NapOH	168	0	45	--	--	--
5[i]		65	33	26	1400	8750[e]	--
6	1,5-naphthalenediol 1,5-NapOH	18	93	91	12200	14400	1.04
7		18	99	875	125000	109000	1.04
8		18	98	1730	245000	197800	1.01
9	phenol PhOH	18	99	49.8	7080	8750	1.01
10		18	92	255	33800	30400	1.00
11		18	98	993	140000	117000	1.01
12		18	97	503	70300	54400	1.00

Reactions carried out in DCM at room temperature. [a] Monomer conversions determined by ^{1}H NMR spectroscopy. [b] Calculated from $M_{n,theo} = (144$ g mol$^{-1} \times$ conversion $\times$ [LA]/([A]+[CTA])$+ M_{OR}$. [c] Absolute molecular weights were determined by GPC−MALS−RI (gel permeation chromatography−multi-angle light scattering−refractive index) *via* Universal Calibration (THF 4 mg mL^{-1}, flow rate = 0.5 mL min^{-1}, dn/dc = 0.044 mL g^{-1}). [d] Reactions carried out in THF. [e] Molecular weights obtained from MALDI-ToF mass spectrum.

End-group fidelity was confirmed by ^{1}H NMR spectroscopy and MALDI-ToF mass spectrometry. The ^{1}H NMR spectra show peaks in the aromatic region corresponding to the aryl-chain ends (Figure 4.20– Figure 4.22). The integrations of the aromatic peaks and the methylene

proton signals (5.10-5.25 ppm) are in agreement with the calculated molar ratios of [LA]:([**A**]+[CTA]).

The MALDI-ToF mass spectrum for a selected 1,5-Nap-PLA sample is shown in Figure 4.24. This spectrum shows one major series of peaks separated by 72 mass units, indicative of chain transfer occurring during reaction. From analysis of the peak masses, this series is assigned to PLA with a 1,5-naphthalenediol chain-end (Figure 4.24).
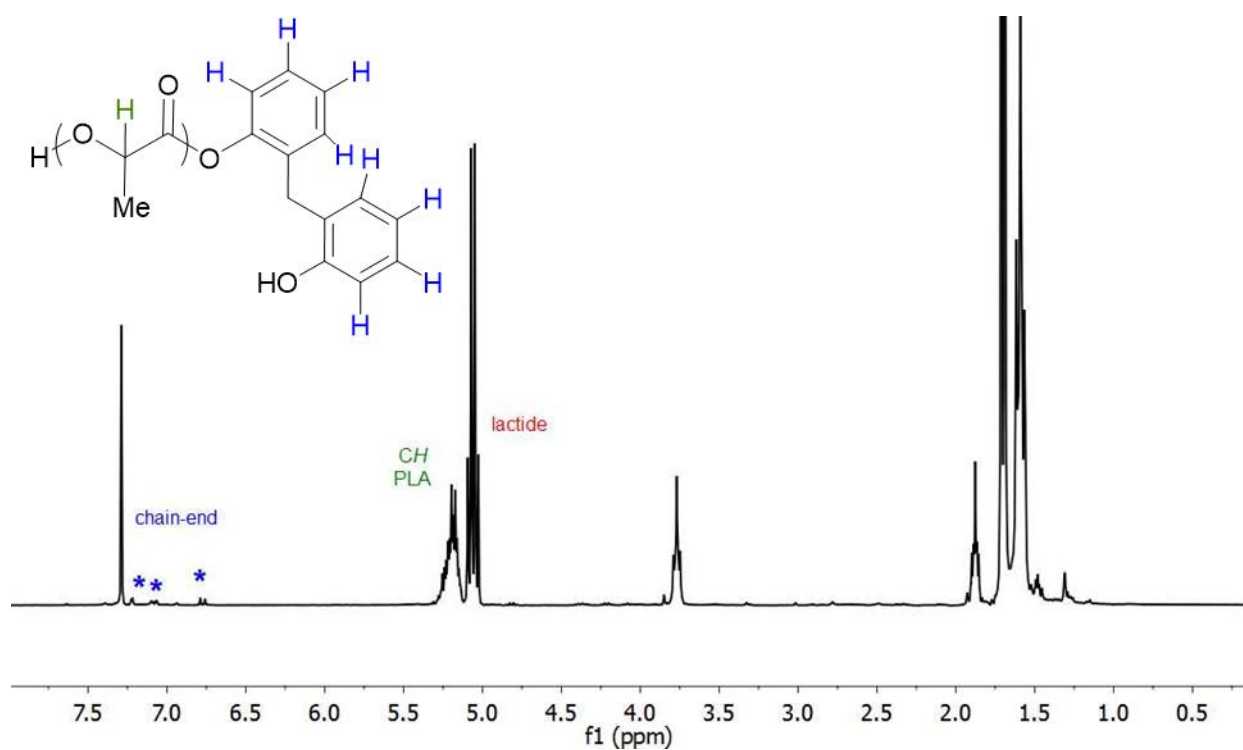
Figure 4.20 ^{1}H NMR (CDCl$_3$, 25 °C, 400 MHz) spectrum of PLA isolated from polymerization with [LA]:[**A**]:[diClPhOH] ratios of 237:1:2 (Table 4.4, entry 2).

131
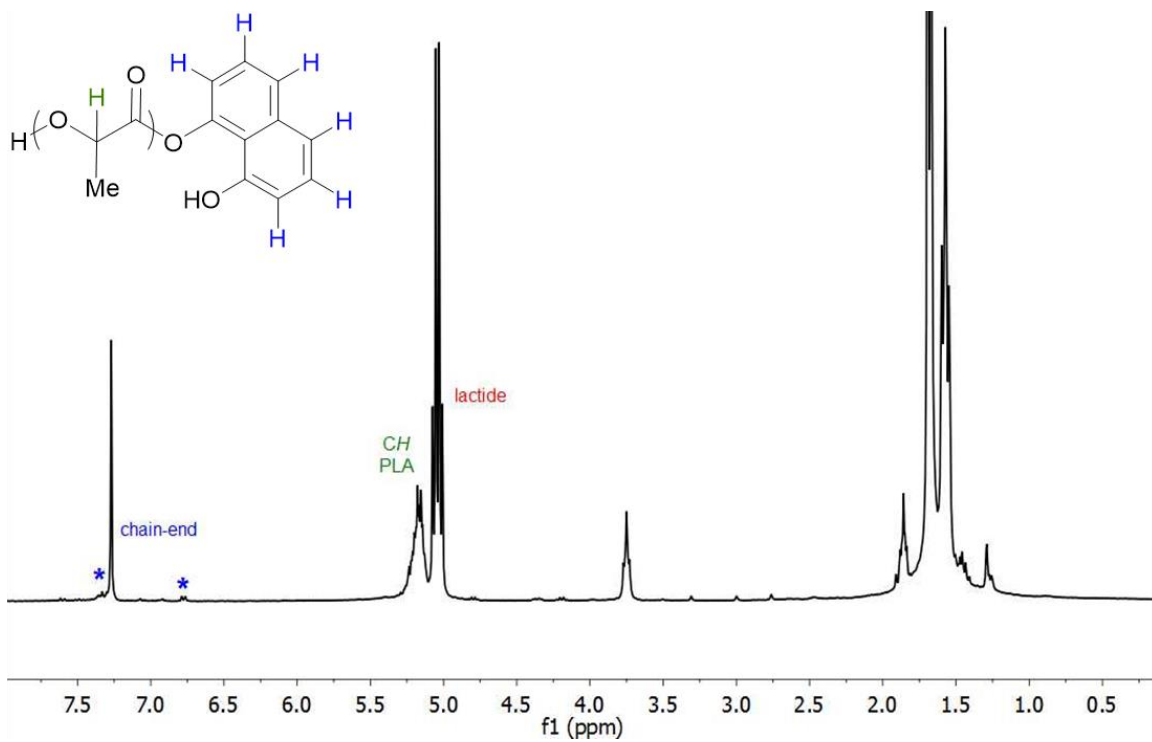
Figure 4.21 ^{1}H NMR (CDCl$_3$, 25 °C) spectrum of PLA isolated from polymerization with [LA]:[**A**]:[1,8-NapOH] ratios of 78:1:2 (Table 4.4, entry 5).
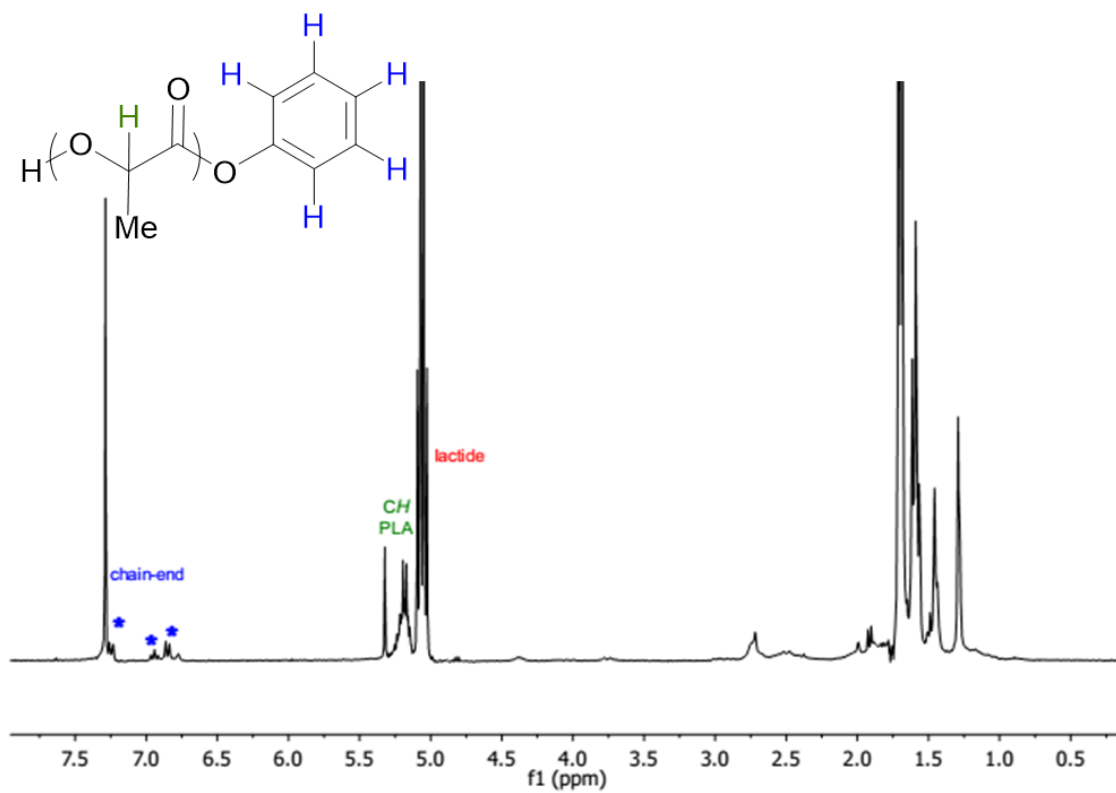
Figure 4.22 ^{1}H NMR (CDCl$_3$, 25 °C) spectrum of PLA isolated from polymerization with [LA]:[**A**]:[PhOH] ratios of 1050:1:20 (Table 4.4, entry 9).
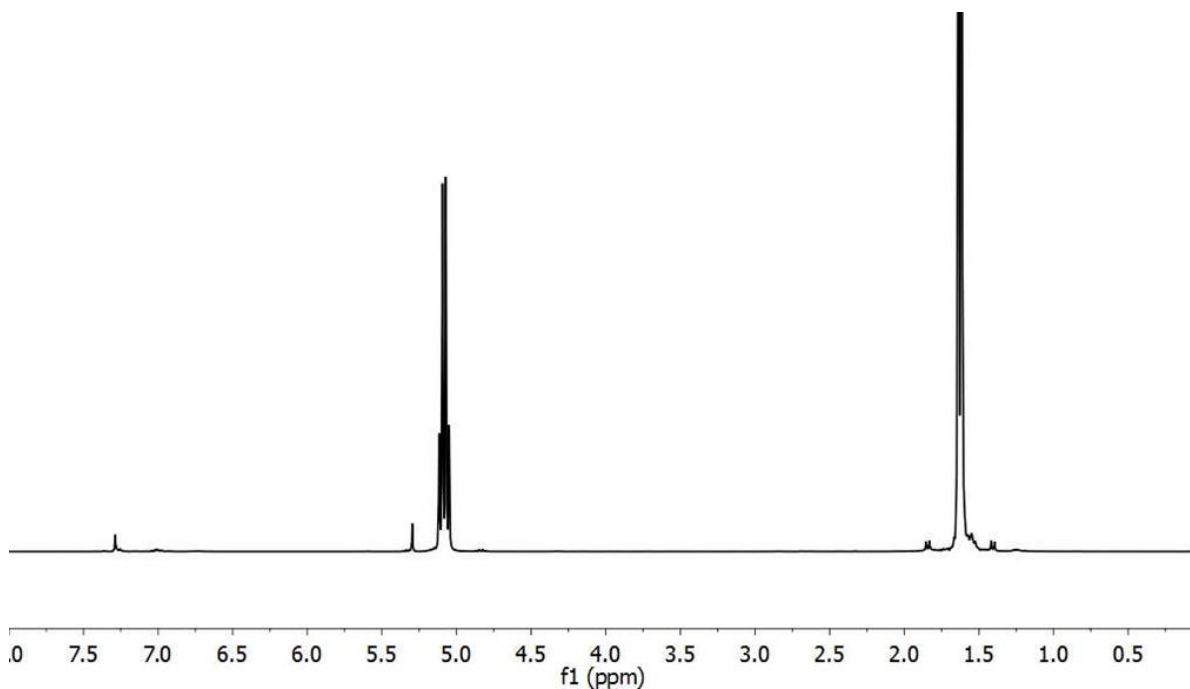
Figure 4.23 ^{1}H NMR (CDCl$_3$, 25 °C) spectrum of unconverted lactide isolated from polymerization with [LA]:[**A**]:[biPhenOH] ratios of 583:1:10 (Table 4.4, entry 3).
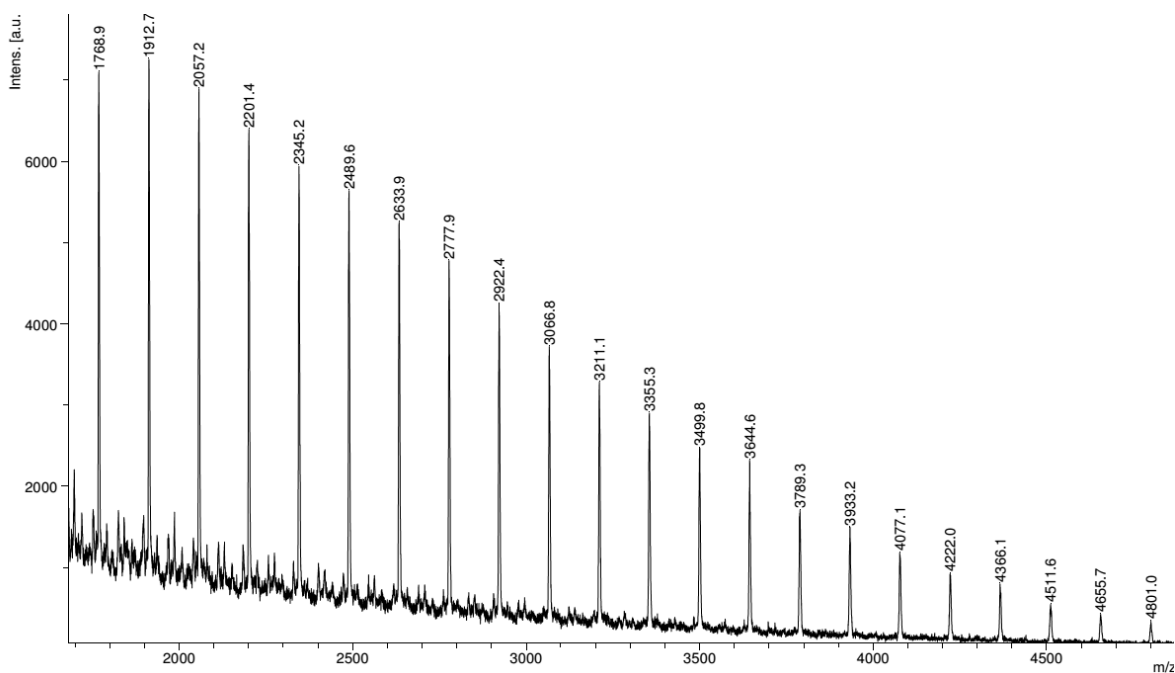
Figure 4.24 MALDI-ToF mass spectrum for a selected PLA-1,5-Nap sample. A$_n$ = [72.07 LA]$_n$ + 160.17 1,5-Nap + ^{23}Na$^+$

Of the diols used as CTAs, only 1,5- naphthalenediol was incorporated into the polymer chain under the initial reaction conditions; the biphenol, dichlorophene and 1,8-naphthalenediol completely hindered the polymerization activity in DCM. Previously reported computational studies showed that both metal centres are active during polymerization with complex **A**.[129] Chelation of the diols to one or both metals would be expected to hinder polymerization.

One such species was isolated. Reaction of **A** with 2 equivalents of dichlorophene in toluene at room temperature for 16 h forms the dinuclear complex [(NNO)InCl]$_2$(μ-Cl)(κ^2,μ-diClPh) (**6**) (Scheme 4.4). The ^{1}H NMR spectrum of complex **6** shows separate signals for each ligand on the two metal centres, indicating a breakdown in symmetry compared to the previous complexes in the series (Figure 4.25).

Scheme 4.4 Synthesis of [(NNO)InCl]$_2$(μ-Cl)(κ^2,μ-diClPh) (**6**).

[(NNO)InCl]$_2$(μ-Cl)(μ-OEt) (**A**)   [(NNO)InCl]$_2$(μ-Cl)(κ^2-μ-diClPh) (**6**)
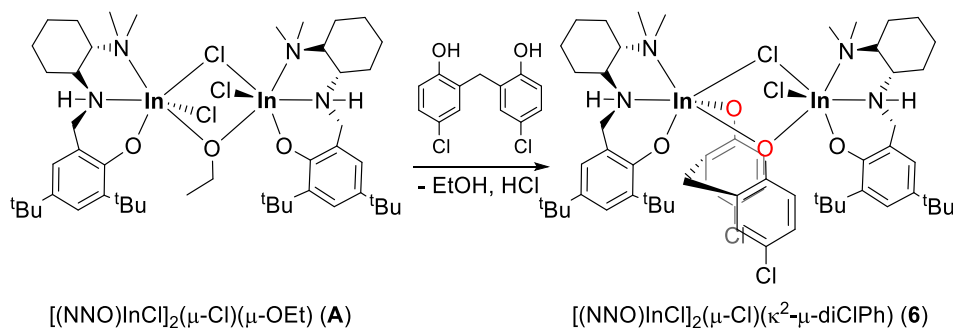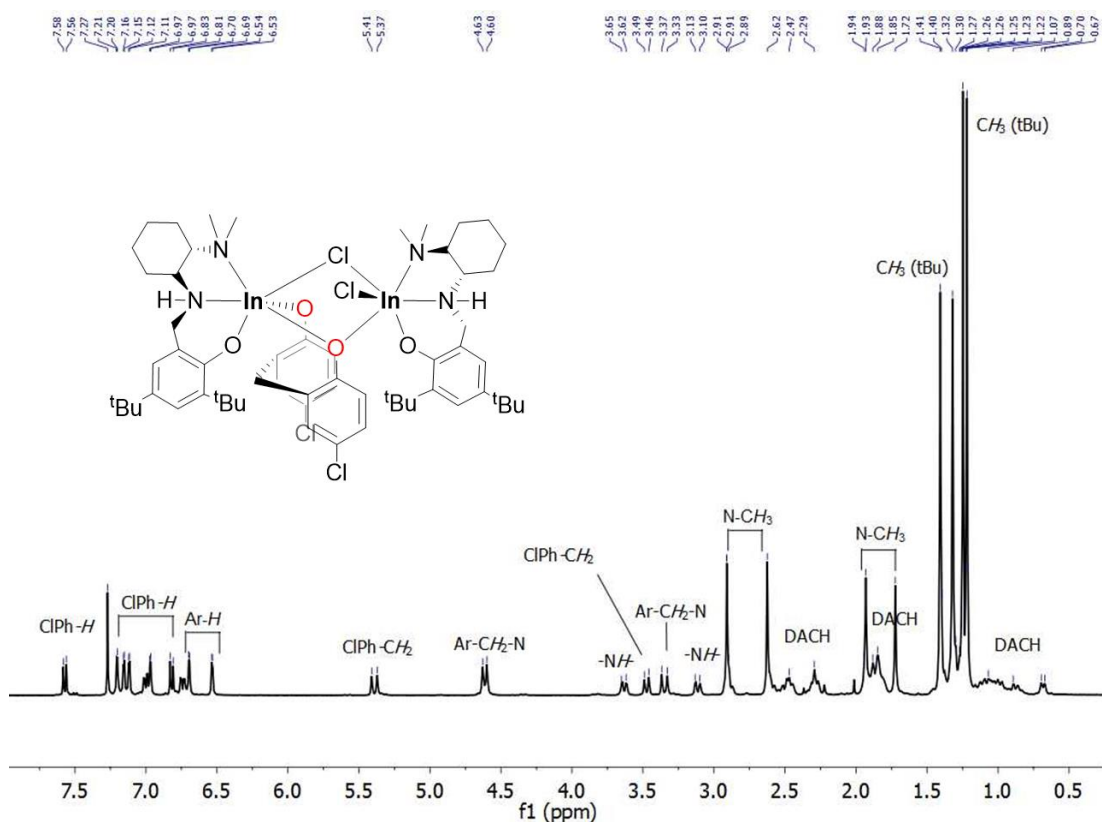
Figure 4.25 ^{1}H NMR (CDCl$_3$, 25 °C, 400 MHz) spectrum of ($\pm$)-[(NNO)InCl]$_2$(μ-Cl)(κ^2,μ-diClPh) (**6**)

Single crystals suitable for X-ray crystallography were obtained from the slow evaporation of a toluene solution. The solid-state structure of **6** shows a deprotonated dichlorophene molecule chelated to one indium centre with one of the oxygen atoms bridging both indium centres (Figure 4.26). Compound **6** displays the same asymmetric homochiral dinuclear structure with distorted octahedral indium centres as other complexes in this family and the "cis" relationship between the phenoxy groups of the ligand is maintained (Table 4.1).
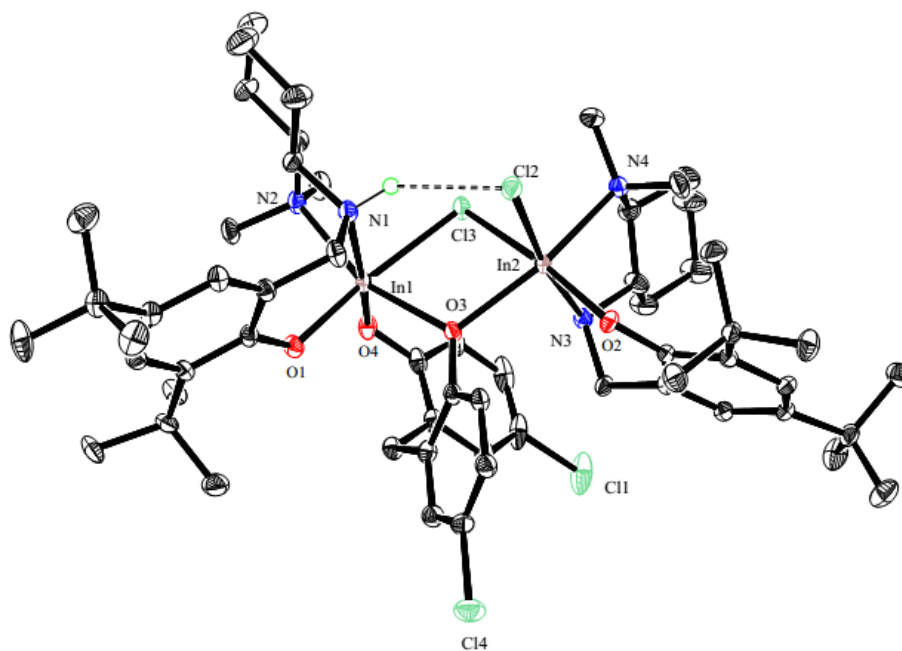
Figure 4.26 Molecular structure of [(NNO)InCl]$_2$(μ-Cl)(κ^2,μ-diClPh) (**6**) depicted with ellipsoids at 50% probability (H atoms and all solvent molecules omitted for clarity).

Related complex [(NNO)InCl]$_2$(μ-Cl)(κ^2,μ-biPh) can be generated from reaction of complex **A** with biphenol. Although [(NNO)InCl]$_2$(μ-Cl)(κ^2,μ-biPh) was not further characterized, a similar structure to that of **6** is assumed, based on the ^{1}H NMR spectrum (Figure 4.27). The chelating initiator explains the lack of reactivity in this system. In contrast, 1,5-naphthalenediol with hydroxyl groups on opposite sides of the naphthalene ring is active as a chain transfer agent. (Table 4.4, Figure 4.19c and Figure 4.24).
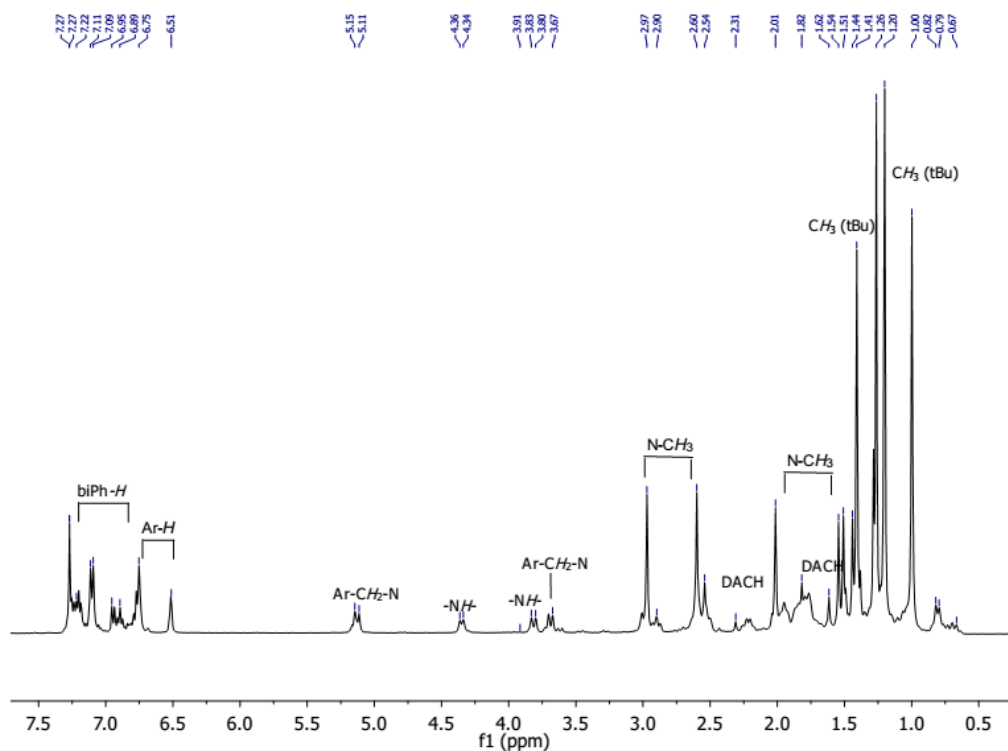
Figure 4.27 ^{1}H (CDCl$_3$, 25 °C, 400 MHz) spectrum of (±)-[(NNO)InCl]$_2$(μ-Cl)(κ^2,μ-biPh).

To further confirm that these stable chelate species were shutting down reactivity, immortal ROP using **A** and CTAs dichlorophene and 1,8-naphthalenediol was conducted in THF. These conditions did allow for the generation of polymeric materials (Table 4.4, entries 2 and 5). We attribute this effect to the blocking of a coordination site by solvent molecules, disallowing the formation of the chelating complex. Additionally, reaction of the stable chelate complex **6** with *rac*-LA in THF also generated polymer, albeit with only 30% conversion after 5 days, showing that coordinating solvents can disrupt the chelate leading to polymer growth (Figure 4.28 and Figure 4.29).
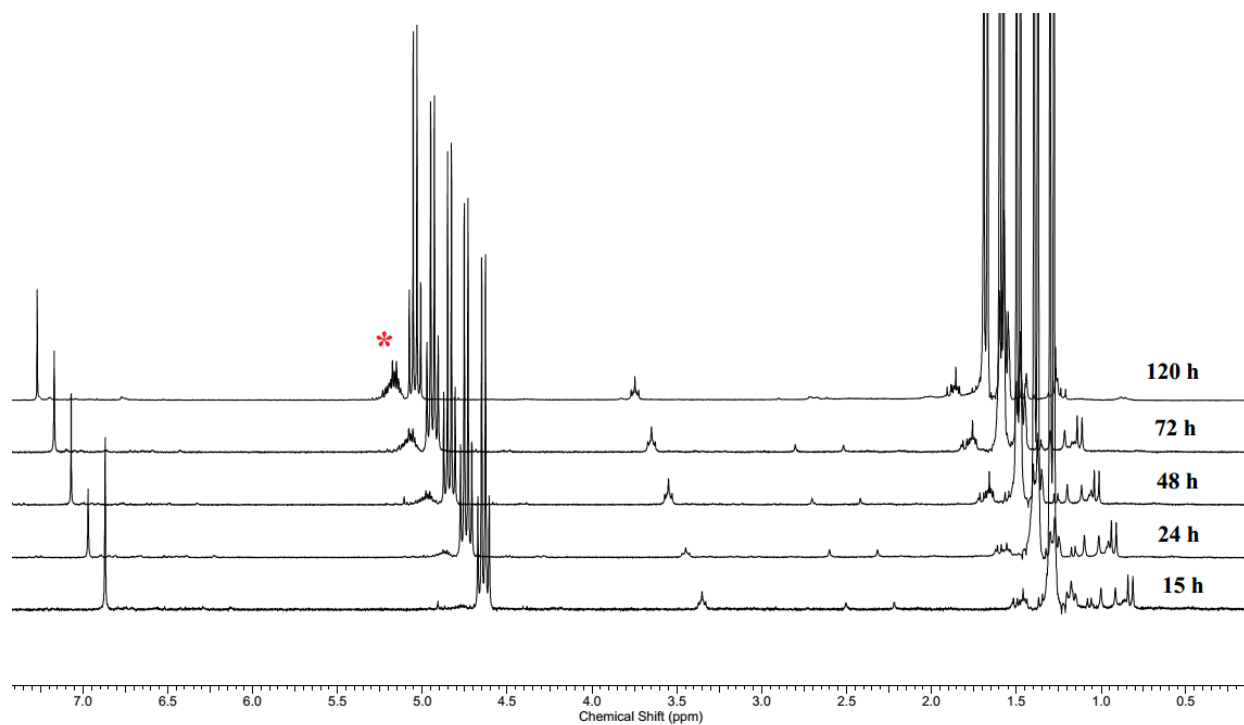
Figure 4.28 ^{1}H NMR (CDCl₃, 25 °C, 300 MHz) spectrum of polymerization [LA]:[**6**] = 110 in THF over 120 hours. Red star indicates the methylene protons on growing polymer.
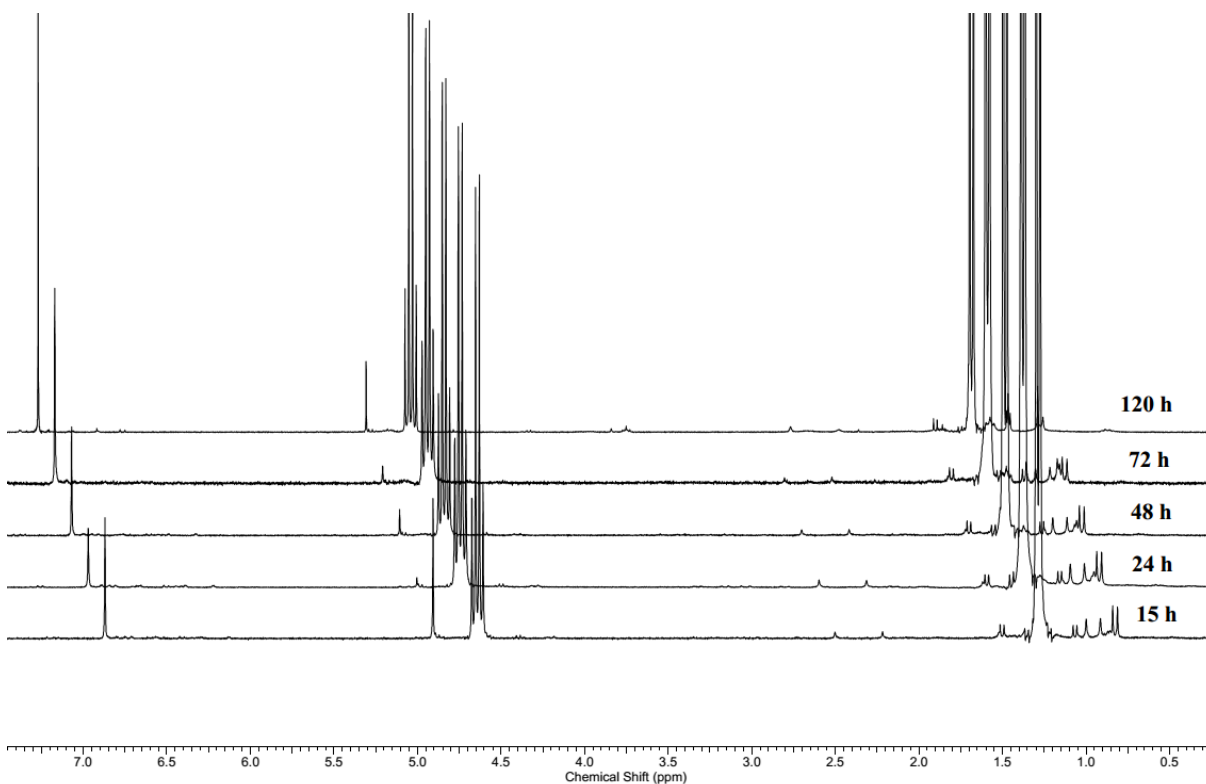
Figure 4.29 ^{1}H NMR (CDCl$_3$, 25 °C, 300 MHz) spectrum of polymerization [LA]:[**6**] = 110 in DCM over 120 hours.

4.3 Conclusions

We were interested in utilizing phenol rich bioproducts as chain transfer agents in catalytic reactions. In this chapter the role of phenols as initiators and as chain transfer agents in the polymerization of lactide catalyzed by diaminophenolate-supported indium complexes was explored. The correlation between electron deficiency of the bridging phenol for the aryloxide-bridged complexes **1-5**, and catalytic activity towards the living ring-opening polymerization of *rac*-lactide, was investigated. *In situ* studies showed that increasing electron deficiency of the bridging phenol leads to an associated increase in the initiation period and decrease in the rate of propagation. This effect is attributed to the lower nucleophilicity of the phenolic oxygen, which hinders the initial insertion into the monomer ester C-O bond and reduces the concentration of

140

active catalyst in solution, leading to higher-than-expected molecular weights. Although this effect is not surprising, the electron rich aryloxy species showed reaction rates only half that of the ethoxy catalysts, showing that these moieties have the potential to be active in catalysis.

Phenols were also used in tandem with ethoxy-bridged complex **A** to investigate the use of aromatic alcohols as chain transfer agents in the immortal ring-opening polymerization of lactide. Aromatic diols shut down polymerization by chelating one indium centre to form a stable metal complex; however, in coordinating solvents the formation chelating metal complexes is disrupted and polymerization can proceed. Immortal ROP was successful when using phenol and 1,5-naphthalenediol. Polymers with well-controlled molecular weights and molecular weight distributions were generated, and the aryl chain ends were confirmed using ^{1}H NMR spectroscopy, MALDI-ToF mass spectrometry and UV-Vis spectroscopy.

These results show that both alkyl and electron rich aryl alcohols can be active chain transfer agents with this family of dinuclear indium complexes. Future efforts will be focused on expanding this fundamental work to complex arylated molecules such as lignin.

4.4 Experimental

General Methods. All the air and moisture sensitive manipulations were carried out in an MBraun glovebox or using standard Schlenk line techniques. A Bruker Avance 300 or 400 MHz spectrometer was used to record ^{1}H spectra. ^{1}H NMR chemical shifts are given in ppm versus residual protons in deuterated solvents as follows: δ 7.27 CDCl$_3$, δ 5.31 CD$_2$Cl$_2$. Molecular weights, hydrodynamic radii and intrinsic viscosities were determined by GPC-MALS-RI-Viscometer using an Agilent liquid chromatograph equipped with a Agilent 1200 series pump and

autosampler, three Phenogel 5 μm Narrow Bore columns (4.6 × 300 mm with 500 Å, 10^3 Å and 10^4 Å pore size), a Wyatt Optilab differential refractometer, Wyatt tristar miniDAWN (laser light scattering detector) and a Wyatt ViscoStar viscometer. The column temperature was set at 40 °C. A flow rate of 0.5 mL/min was used and samples were dissolved in THF (*ca*. 4 mg/mL). The measurements were carried out at laser wavelength of 690 nm at 25 °C. Data were processed by ASTRA software (Wyatt Technology). Molecular masses were determined using a Bruker Autoflex time-of-flight mass (TOF) spectrometer equipped with MALDI ion source.

Materials. THF, toluene and diethyl ether was taken from an IT Inc. solvent purification system with activated alumina columns and degassed before use. HPLC grade DCM was purchased from Fisher Chemicals and was dried over CaH_2, transferred under vacuum and degassed before use. $CDCl_3$ was purchased from Cambridge Isotope Laboratories Inc. and dried over CaH_2, transferred under vacuum and degassed through three freeze−pump−thaw cycles before use. Pentane, acetonitrile and, CD_2Cl_2 were purchased from Sigma-Aldrich and dried over CaH_2, transferred under vacuum and degassed before use. Indium (III) trichloride, 1,5-naphthalenediol, 1,8-naphthalenediol, *para*-methoxyphenol, *para*-bromophenol, *para*-nitrophenol, and *para*-methylphenol were purchased from Sigma-Aldrich and were used as received. Phenol was purchased from Fisher Chemicals and used as received. 2,2-Methylenebis(4-chlorophenol) (95%) (dichlorophene) was purchased from Alfa Aesar and recrystallized from hot toluene before use. 2,2'-biphenol was purchased from ACOS and used as received. Racemic lactide was purchased from PURAC America Inc. and was recrystallized three times from hot dried toluene prior to use. The racemic proligand 2,4-di(t-butyl)-6-(((2-(dimethylamino)cyclohexyl)amino)methyl)phenol (±)-H(NNO), dichloro complex (NNO)InCl$_2$

and [(NNO)InCl]$_2$(μ-Cl)(μ-OEt) (**A**) were synthesized according to previously reported methods.[40]

Representative synthesis of phenolic potassium salts. Inside a glovebox, a suspension of potassium *tert*-butoxide (7.9 mg, 0.070 mmol) in 3 mL of Et$_2$O was added to a solution of *para*-nitrophenol in 3 mL of Et$_2$O (97.5 mg, 0.701 mmol). This was stirred at room temperature for one hour. After this time, a yellow solid precipitated and was filtered off, washed with acetonitrile and dried under vacuum.

Synthesis of [(NNO)InCl]$_2$(μ-Cl)(μ-OPh$_{OMe}$) (1) *via* salt metathesis. To a suspension of (NNO)InCl$_2$ (15.0 mg, 0.278 mmol) in toluene (5 mL) was added a suspension of potassium *para*-methoxyphenoxide (57.3 mg, 0.353 mmol) in toluene (2 mL) under N$_2$. The solution was made up to 8 mL and stirred at ambient temperature for 18 h. After this time the solution was a cloudy yellow colour and was concentrated to give a pale yellow solid. The solid was the dissolved in 2 mL of CHCl$_3$ and filtered through Celite. The solution was concentrated to give an off-white solid which was then stirred in acetonitrile. The crude product was then isolated by filtration and finally recrystallized twice from a 2:3 mixture of CHCl$_3$:pentane to give a white solid (45.0 mg, 28%). ^{1}H NMR (400 MHz, CDCl$_3$): δ 7.45 (d, $^3J_{H-H}$ = 8.8 Hz, 2H, Ph-*H*), 7.08 (d, $^4J_{H-H}$ = 2.4 Hz, 2H, Ar-*H*), 6.60 (d, $^4J_{H-H}$ = 2.4 Hz, 2H, Ar-*H*), 6.47 (d, $^3J_{H-H}$ = 8.8 Hz, 2H, Ph-*H*), 4.68 (d, $^2J_{H-H}$ = 11.7 Hz, 2H, Ar-C*H*$_2$-N), 3.54 (s, 3H, Ph-OC*H*$_3$), 3.54 (dd, 2H, $^3J_{H-H}$ = 1.76, Ar-C*H*$_2$-N), 3.17 (d, $^4J_{H-H}$ = 7.6 Hz, 2H, N*H*), 2.98 (td, $^3J_{H-H}$ = 10.0, $^3J_{H-H}$ = 1.8 Hz, 2H, DACH), 2.69 (s, 6H, N(C*H*$_3$)$_2$), 2.59-2.38 (m, 4H, DAC*H*), 1.93 − 1.85 (br m, 2H, DAC*H*), 1.813(s, 6H, N(C*H*$_3$)$_2$), 1.34 (s, 9H, C(C*H*$_3$)$_3$), 1.22 (s, 9H, C(C*H*$_3$)$_3$), 1.17 − 0.86 (m, 2H, DAC*H*). ^{13}C{^{1}H} NMR (151 MHz, CDCl$_3$): δ 162.4, 153.9, 152.8, 138.2, 135.9, 129.0, 128.2, 125.9, 125.2, 123.9, 118.8, 113.3, 64.4, 55.1, 53.0, 44.2, 37.8, 35.1, 35.1, 33.7, 30.7, 29.9, 29.7, 24.9, 24.8, 21.8. Elemental analysis calculated

for $C_{53}H_{85}Cl_3In_2N_4O_4$: C, 54.03; H, 7.27; Cl, 9.03; In, 19.49; N, 4.76; O, 5.43; found: C, 53.95, H, 7.09.

Synthesis of [(NNO)InCl]$_2$(μ-Cl)(μ-OPh$_{Me}$) (2) *via* salt metathesis. To a suspension of (NNO)InCl$_2$ (153 mg, 0.280 mmol) in toluene (5 mL) was added a suspension of potassium *para*-methoxyphenoxide (61.0 mg, 0.417 mmol) in toluene (2 mL) under N$_2$. The solution was made up to 8 mL and stirred at ambient temperature for 18 h. After this time the solution was a cloudy yellow colour and was concentrated to give a pale yellow solid. The solid was the dissolved in 2 mL of CHCl$_3$ and filtered through Celite. The solution was concentrated to give an off-white solid which was then stirred in acetonitrile. The crude product was then isolated by filtration and finally recrystallized from a 2:3 mixture of CHCl$_3$:pentane to give a white solid (34.1 mg, 21%). X-ray quality crystals were grown *via* slow evaporation of a toluene solution. ^{1}H NMR (400 MHz, CDCl$_3$): δ 7.40 (d, $^3J_{H-H}$ = 8.2 Hz, 2H, Ph-*H*), 7.10 (d, $^4J_{H-H}$ = 2.4 Hz, 2H, Ar-*H*), 6.69 (d, $^3J_{H-H}$ = 8.2 Hz, 2H, Ph-*H*), 6.60 (d, $^4J_{H-H}$ = 2.4 Hz, 2H, Ph-*H*), 4.66 (d, $^2J_{H-H}$ = 12.3 Hz, 2H, Ar-C*H$_2$*-N), 3.54 (d, 3H, $^2J_{H-H}$ = 12.3 Hz, 2H, Ar-C*H$_2$*-N), 3.20 (d, $^4J_{H-H}$ = 10.6 Hz, 2H, N*H*), 3.00 (td, $^3J_{H-H}$ = 11.4, $^3J_{H-H}$ = 3.5 Hz, 2H, DAC*H*), 2.68 (s, 6H, N(C*H$_3$*)$_2$), 2.58-2.40 (m, 4H, DACH), 1.92 – 1.80 (br m, 2H, DAC*H*), 1.80 (s, 6H N(C*H$_3$*)$_2$), 1.34 (s, 9H, C(C*H$_3$*)$_3$), 1.22 (s, 9H, C(C*H$_3$*)$_3$), 1.17 – 0.86 (m, 2H, DAC*H*). ^{13}C{^{1}H} NMR (151 MHz, CDCl$_3$): δ 162.5, 157.6, 138.3, 135.8, 128.8, 125.9, 123.8, 122.4, 118.9, 64.4, 53.2., 50.7, 44.3, 37.9, 35.1, 33.7, 31.7, 30.8, 29.9, 24.9, 24.8, 21.9, 20.6. Elemental analysis calculated for $C_{53}H_{85}Cl_3In_2N_4O_3$: C, 54.77; H, 7.37; Cl, 9.15; In, 19.76; N, 4.82; O, 4.13; found: C, 55.05; H, 7.34.

Synthesis of [(NNO)InCl]$_2$(μ-Cl)(μ-OPh$_H$) (3) *via* salt methathesis. To a suspension of (NNO)InCl$_2$ (111 mg, 0.204 mmol) in toluene (5 mL) was added a suspension of potassium phenoxide (39.6 mg, 0.300 mmol) in toluene (2 mL) under N$_2$. The solution was made up to 8 mL

and stirred at ambient temperature for 18 h. After this time the solution was a cloudy yellow colour and was concentrated to give a pale yellow solid. The solid was the dissolved in 2 mL of CHCl$_3$ and filtered through Celite. The solution was concentrated to give an off-white solid which was then stirred in acetonitrile. The crude product was then isolated by filtration and finally recrystallized from a 2:3 mixture of CHCl$_3$:pentane to give a white solid (66.6 mg, 57%). X-ray quality crystals were grown *via* slow evaporation of a toluene solution. ^{1}H NMR (400 MHz, CDCl$_3$): δ 7.54 (d, $^3J_{\text{H-H}}$ = 7.6 Hz, 2H, Ph-*H*), 7.08 (d, $^4J_{\text{H-H}}$ = 2.4 Hz, 2H, Ar-*H*), 6.93 (t, $^3J_{\text{H-H}}$ = 8.2, Ph-*H*) 6.59 (d, $^4J_{\text{H-H}}$ = 2.4 Hz, 2H, Ar-*H*), 6.54 (t, $^3J_{\text{H-H}}$ = 7.6 Hz, 2H, Ph-*H*), 4.66 (d, $^2J_{\text{H-H}}$ = 11.7 Hz, 2H, Ar-C*H$_2$*-N), 3.55 (d, 3H, $^2J_{\text{H-H}}$ = 10.0 Hz, 2H, Ar-C*H$_2$*-N), 3.20 (d, $^4J_{\text{H-H}}$ = 10.6 Hz, 2H, N*H*), 3.00 (td, $^3J_{\text{H-H}}$ = 11.1, $^3J_{\text{H-H}}$ = 2.4 Hz, 2H, DAC*H*), 2.70 (s, 6H, N(C*H$_3$*)$_2$), 2.59-2.39 (m, 4H, DAC*H*), 1.93 – 1.84 (br m, 2H, DAC*H*), 1.83 (s, 6H N(C*H$_3$*)$_2$), 1.34 (s, 9H, C(C*H$_3$*)$_3$), 1.20 (s, 9H, C(C*H$_3$*)$_3$), 1.16 – 0.86 (m, 2H, DAC*H*). ^{13}C{^{1}H} NMR (100 MHz, CDCl$_3$): δ 162.4, 160.0, 138.2, 137.9, 129.0, 128.2, 125.9, 125.2, 123.9, 122.9, 120.2, 118.8, 64.4, 53.1, 50.6, 44.2, 37.8, 35.1, 33.7, 31.7, 30.7, 29.9, 24.9, 24.8, 12.8, 21.4.

Synthesis of [(NNO)InCl]$_2$(μ-Cl)(μ-OPh$_{Br}$) (4) *via* alkoxide-phenoxide exchange. To a solution of **A** (115 mg, 0.112 mmol) in toluene (5 mL) was added *p*-bromophenol (59.2 mg, 0.342 mmol) under N$_2$. The solution was stirred for 18h. White precipitate slowly appeared as the reaction progressed. After stirring, the solution was concentrated to yield a white solid, which was washed with ACN (3 × 2 mL) and consequently dried under vacuum. The crude white product was recrystallized from 3:2 pentane/CH$_3$Cl at −30°C to afford product as long white crystalline needles (60.2 mg, 47%). Suitable crystals for x-ray crystallography were grown from slow evaporation of toluene. ^{1}H NMR (600 MHz, CDCl$_3$): δ 7.43 (d, $^3J_{\text{H-H}}$ = 8.7 Hz, 2H, Ph-*H*), 7.11 (d, $^4J_{\text{H-H}}$ = 2.6 Hz, 2H, Ar-*H*), 7.01 (t, $^3J_{\text{H-H}}$ = 8.7, Ph-*H*) 6.61 (d, $^4J_{\text{H-H}}$ = 2.6 Hz, 2H, Ar-*H*), 4.60 (d, $^2J_{\text{H-H}}$ = 12.8

145

Hz, 2H, Ar-CH_2-N), 3.56 (d, 3H, $^2J_{\text{H-H}}$ = 12.8 Hz, 2H, Ar-CH_2-N), 3.17 (d, $^4J_{\text{H-H}}$ = 10.2 Hz, 2H, NH), 2.98 (td, $^3J_{\text{H-H}}$ = 11.8, $^3J_{\text{H-H}}$ = 3.1 Hz, 2H, DACH), 2.84 (s, 6H, N(CH_3)$_2$), 2.57-2.43 (m, 4H, DACH), 1.92 – 1.83 (br m, 2H, DACH), 1.82 (s, 6H N(CH_3)$_2$), 1.34 (s, 9H, C(CH_3)$_3$), 1.23 (s, 9H, C(CH_3)$_3$), 1.16 – 0.92 (m, 2H, DACH). ^{13}C{^{1}H} NMR (151 MHz, CDCl$_3$): δ 162.2, 159.3, 138.2, 136.2, 131.0, 126.0, 124.8, 124.0, 118.7, 112.6, 64.4, 53.1, 50.7, 44.2, 37.8, 35.1, 33.7, 31.7, 30.8, 29.9, 24.9, 24.8, 21.8. Elemental analysis calculated for C$_{52}$H$_{82}$BrCl$_3$In2N$_4$O$_3$: C, 50.90; H, 6.74; Br, 6.51; Cl, 8.67; In, 18.71; N, 4.57; O, 3.91; found: C, 51.07, H, 6.70.

Synthesis of [(NNO)InCl]$_2$(μ-Cl)(μ-OPh$_{\text{Br}}$) (4) *via* salt methathesis. To a suspension of (NNO)InCl$_2$ (148 mg, 0.272 mmol) in toluene (5 mL) was added a suspension of potassium *para*-methoxyphenoxide (107 mg, 0.6200 mmol) in toluene (2 mL) under N$_2$. The solution was made up to 8 mL and stirred at ambient temperature for 18 h. After this time the solution was a cloudy yellow colour and was concentrated to give a pale yellow solid. The solid was the dissolved in 2 mL of CHCl$_3$ and filtered through Celite. The solution was concentrated to give an off-white solid which was then stirred in acetonitrile. The crude product was then isolated by filtration and finally recrystallized from a 2:3 mixture of CHCl$_3$:pentane to give a white solid. All characterization data was consistent with the previous description.

Synthesis of [(NNO)InCl]$_2$(μ-Cl)(μ-OPh$_{\text{NO2}}$) (5) *via* alkoxide-phenoxide exchange. To a solution of **A** (50.0 mg, 0.049 mmol) in toluene (4 mL) was added *p*-nitrophenol (24.1 mg, 0.173 mmol) under N$_2$. The solution was stirred for 18 h. Yellow precipitate appeared in the solution as the reaction progressed. The solution was concentrated to yield a dark yellow solid, which was washed with ACN (3 × 2 mL) and consequently dried under vacuum. The crude product was recrystallized from 3:2 pentane/CH$_3$Cl at −30 °C to yield product as short yellow crystalline needles (23.2 mg, 43%). X-ray quality crystals were grown *via* slow diffusion of pentane into

CHCl$_3$. ^{1}H NMR (400 MHz, CDCl$_3$) δ 7.85 (d, $^3J_{\text{H-H}}$= 8.9 Hz, 2H, Ph-*H*), 7.60 (d, $^3J_{\text{H-H}}$ = 9.0 Hz, 2H, Ph-*H*), 7.09 (s, 2H, Ar-*H*), 6.59 (s, 2H, Ar-*H*), 4.53 (d, $^2J_{\text{H-H}}$ = 12.6 Hz, 2H, Ar-C*H$_2$*-N), 3.56 (d, $^2J_{\text{H-H}}$ = 12.4 Hz, 2H, Ar-C*H$_2$*-N), 3.17 (d, $^4J_{\text{H-H}}$ = 9.4 Hz, 2H, N*H*), 2.96 (t, $^3J_{\text{H-H}}$ = 10.6 Hz, 2H, DAC*H*), 2.69 (s, 6H, N(C*H$_3$*)$_2$), 2.58 – 2.38 (m, 6H, N(C*H$_3$*)$_2$), 1.35 – 1.27 (m, 22H), 1.20 (s, 18H, C(C*H$_3$*)$_3$). ^{13}C{^{1}H} NMR (151 MHz, CDCl$_3$): δ 166.9, 161.9, 138.3, 136.7, 129.0, 128.2, 126.0, 124.7, 124.2, 123.5, 118.5, 64.6, 53.2, 50.7, 44.3, 37.9, 35.1, 34.6, 33.8, 31.7, 30.8, 30.0, 29.9, 24.7, 21.8. Elemental analysis calculated for C$_{52}$H$_{82}$Cl$_3$In$_2$N$_5$O$_5$: C, 52.34; H, 6.93; Cl, 8.91; In, 19.24; N, 5.87; O, 6.70; found: C, 52.66, H, 6.97.

Synthesis of [(NNO)InCl]$_2$(μ-Cl)(μ-OPh$_{\text{NO2}}$) (5) *via* salt metathesis. To a suspension of (NNO)InCl$_2$ (148 mg, 0.272 mmol) in toluene (5 mL) was added a suspension of potassium *para*-methoxyphenoxide (73.8 mg, 0.417 mmol) in toluene (2 mL) under N$_2$. The solution was made up to 8 mL and stirred at ambient temperature for 18 h. After this time the solution was a cloudy yellow colour and was concentrated to give a pale yellow solid. The solid was the dissolved in 2 mL of CHCl$_3$ and filtered through Celite. The solution was concentrated to give a yellow solid which was then stirred in acetonitrile. The crude product was then isolated by filtration and finally recrystallized from a 2:3 mixture of CHCl$_3$:pentane to give a yellow solid (90.9 mg, 56%). All characterization data was consistent with the previous description.

Synthesis of [(NNO)InCl]$_2$(μ-Cl)(κ^2,μ-diClPh) (6). To a solution of **A** (83.3 mg, 0.076 mmol) in toluene (4 mL) was added dichlorophene (40.8 mg, 0.151 mmol) under N$_2$. The solution was stirred for 18 h. White precipitate appeared in the solution as the reaction progressed. The solution was concentrated to yield an off-white solid, which dissolved in CHCl$_3$ and filtered through Celite. The solvent was again removed and the white solid washed with ACN (3 × 2 mL) and consequently dried under vacuum. The crude product was recrystallized from 3:2

pentane/CH$_3$Cl at –30 °C to yield product as a white powder needles (50.8 mg, 52%). X-ray quality crystals were grown *via* slow evaporation of toluene solution. ^{1}H NMR (400 MHz, CDCl$_3$) δ 7.58 (d, $^3J_{\text{H-H}}$ = 8.8 Hz, 1H, diClPh-*H*), 7.21 (d, $^4J_{\text{H-H}}$ = 2.3 Hz, 1H, Ar-*H*), 7.12 (d, $^4J_{\text{H-H}}$ = 2.3 Hz, 1H, Ar-*H*), 7.02 (d, $^3J_{\text{H-H}}$ = 2.9 Hz, 1H, diClPh-*H*), 7.01 (d, $^3J_{\text{H-H}}$ = 2.9 Hz, 1H, diClPh-*H*), 6.97 (d, $^3J_{\text{H-H}}$ = 8.5 Hz, 1H, diClPh-*H*), 6.83 (d, $^3J_{\text{H-H}}$ = 2.7 Hz, 1H, diClPh-*H*), 6.76 (d, $^3J_{\text{H-H}}$ = 2.6 Hz, 1H, diClPh-*H*), 6.74 (d, $^3J_{\text{H-H}}$ = 2.6 Hz, 1H, diClPh-*H*), 6.70 (d, $^4J_{\text{H-H}}$ = 2.3 Hz, 1H, Ar-*H*), 6.54 (d, $^4J_{\text{H-H}}$ = 2.3 Hz, 1H, Ar-*H*), 5.41 (d, $^2J_{\text{H-H}}$ = 15.2 Hz, 1H, diClPh-C*H$_2$*-PhCl), 4.63 (d, $^2J_{\text{H-H}}$ = 11.6 Hz, 2H, Ar-C*H$_2$*-N), 3.65 (dd, $^3J_{\text{H-H}}$ = 13.2 Hz, $^3J_{\text{H-H}}$ =2.9 Hz, 2H, C*H*), 3.49 (d, $^2J_{\text{H-H}}$ = 12.6 Hz, 2H, Ar-C*H$_2$*-N), 3.37 (d, $^2J_{\text{H-H}}$ = 15.8 Hz, 1H, diClPh-C*H$_2$*-PhCl), 3.13 (dd, $^3J_{\text{H-H}}$ = 13.2 Hz, $^3J_{\text{H-H}}$ =2.6 Hz, 2H, C*H*), 2.91 (s, 3H, N(C*H$_3$*)), 2.89 (m, 1H,), 2.62 (s, 3H, N(C*H$_3$*)), 2.61(m, 1H), 2.59 (m, 3H), 2.29 (m, 3H), 1.93 (s, 3H, N(C*H$_3$*)), 1.88 (m, 5H), 1.72 (s, 3H, N(C*H$_3$*)), 1.41 (s, 9H, C(C*H$_3$*)$_3$), 1.32 (s, 9H, C(C*H$_3$*)$_3$), 1.25 (s, 9H, C(C*H$_3$*)$_3$), 1.22 (s, 9H, C(C*H$_3$*)$_3$), 1.17 – 0.85 (m, 5H), 0.7 (d, J = 9.7 Hz, 1H). ^{13}C{^{1}H} NMR (151 MHz, CDCl$_3$): δ 162.63, 157.8, 137.9, 135.4, 133.2, 132.7, 131.2, 130.6, 127.2, 126.8, 126.0, 124.7, 124.1, 121.7, 120.5, 99.9, 65.0, 64.2, 53.3, 44.8, 44.2, 37.7, 35.9, 33.6, 31.7, 30.1, 29.7, 25.1, 24.9.

Representative living ring-opening polymerization. Inside a glovebox under nitrogen, appropriate volumes of a standard solution of catalyst in DCM (20 mg into 1 mL) were added to a solution of *rac*-lactide in DCM. The solutions were stirred at room temperature for at least 18 hours before the solvent was evaporated. A small sample of crude polymer was taken for ^{1}H NMR spectroscopic analysis, the remaining polymer was dissolved in minimal DCM (~2 mL) and precipitated with cold methanol. The methanol was decanted off and the precipitation repeated twice. The isolated polymer was then dried under vacuum for at least 24 hours before further analysis.

Representative immortal ring-opening polymerization. Inside a glovebox under nitrogen, appropriate amounts of *rac*-lactide were dissolved in DCM. Appropriate volumes of a standard solution of chain transfer agent in DCM were added and the solution stirred until homogenous. A standard solution of catalyst **A** in DCM (10 mg into 1 mL) was the added the reaction mixtures were stirred at room temperature for at least 18 hours before the solvent was evaporated. A small sample of crude polymer was taken for ^{1}H NMR spectroscopic analysis, the remaining polymer was dissolved in minimal DCM (~2 mL) and precipitated with cold MeOH. The MeOH was decanted off and the precipitation repeated twice. The isolated polymer was then dried under vacuum for at least 24 hours before further analysis.

Representative *in situ* living ring-opening polymerization. Inside a glovebox under nitrogen, 0.25 mL of a standard solution of catalyst in CD_2Cl_2 (20 mg, 0.004 M) was added to a J-Young tube. This was frozen in liquid nitrogen before 0.25 mL of CD_2Cl_2 was added then frozen. Finally, 0.5 mL of a standard solution of *rac*-lactide and TMB (internal standard) in CD_2Cl_2 (123 mg, 0.21 M) was added and frozen. The J-Young tube was evacuated and thawed before insertion into the NMR probe.

Representative *in situ* phenoxy-ethoxy exchange. Inside a glovebox under nitrogen, 0.50 mL of a standard solution of catalyst in CD_2Cl_2 (20 mg, 0.005 M) was added to a J-Young tube. This was frozen in liquid nitrogen before 0.25 mL of CD_2Cl_2 was added then frozen. Finally, 0.25 mL of a standard solution of phenol and TMB (internal standard) in CD_2Cl_2 (2.5 mg, 0.005 M) was added and frozen. The J-Young tube was evacuated and thawed before insertion into the NMR probe.

Living ring-opening polymerization with complex 6. Inside a glovebox under nitrogen, *rac*-lactide (31 mg, 0.215 mmol) was dissolved in THF (~2 mL). Catalyst **6** (2.5 mg, 0.002 mmol) in

149

1 mL of THF was then added. The reaction mixtures were stirred at room temperature. At regular intervals, a 0.5 mL aliquot was taken to check conversion.

Chapter 5: Thermorheological investigation of aromatic interactions in aryl-capped polylactides.[****]

5.1 Introduction

The previous chapter described the use of immortal ring-opening polymerization (iROP) as a trivial route to end-functionalized poly(lactide)s. This synthetic methodology is further utilized in the following sections to yield a variety of aryl-capped poly(lactide)s. Structure-property relationships are then studied with the goal of probing the properties of these potentially useful materials.

5.1.1 Network structures in polymeric materials.

Polymer networks can be divided into three main classes, characterized by their specific rheological properties.[240,241] The mechanical response of thermoset rubbery solids depends on crosslink density and molecular mass and due to the strong covalent bonds between chains, when a stress is applied, these materials display elastic response over a large deformation frequency range (G' > G").

Thermoplastic polymers have mechanical response which depends on entanglement molecular weight, chain alignment and degree of crystallinity. The melt rheological behaviour of thermoplastics are very distinctive whereby at very low deformation frequencies in the terminal zone (< 10^{-2} s^{-1}), thermoplastics behave as highly viscous liquids. As the frequency increases

viscoelastic response is given by the following relationships: $G' \propto \omega^2$ and $G'' \propto \omega^1$. At a certain cross-over frequency, the G' surpasses G'' and the material begins to display more elastic response.

Elastomers can contain non-covalent interactions and display intermediate behaviour between that of a thermoset and a thermoplastic. These materials are often healable because after deformation or breakage the secondary interactions between polymer chains can reform the network structure, restoring the material's mechanical properties.

5.1.2 Non-ionic secondary interactions to modify polymer properties.

Deliberate inclusion of moieties capable of secondary interactions in polymeric structures has become established in the field of functional and stimuli responsive materials.[242,243] The influence of non-covalent bonds, specifically hydrogen bonding and aromatic-aromatic electrostatic interactions, have been applied to achieve a variety of supramolecular structures including hydrogels and supramolecular polymers. The non-covalent bonds in these materials can lead to enhanced properties (elasticity and strength) as well as imparting self-healing capabilities[244] by altering the way in which polymer chains interact.[245,246]

The literature holds only a few examples of researchers using these secondary interactions to alter the properties of biodegradable polyesters.[188,207,247,248] Sijbesma and co-workers synthesized functionalized poly(caprolactone) (PCL), end-capped with a self-complimentary quadrupole hydrogen-bonding group, ureidopyrimidinone (UPy) (Figure 5.1).[249] The UPy groups were found to form aggregate dimers which remained present in the polymer melt (at $T > T_m$), giving rise to a physical network. The presence of this network influenced the melt rheological properties of the polymers and rheological analysis in the linear viscoelastic regime showed a plateau in the storage

modulus, G', at low deformation frequencies similar to that observed in covalently cross-linked systems.

Recently, the same UPy hydrogen-bonding unit was incorporated in PLA (UPy-PLA) using iROP by Brzeziński and Biela who showed that stereocomplexation in between PLLA and PDLA in dilute solutions was promoted by UPy aggregation.[250] To further these results, Pan *et al.* studied the crystallization rate of UPy-PLA polymers.[251] The UPy aggregation led to an increase in the melting temperature of the end-functionalized PLLAs and homocrystallization was faster when compared to the non-functionalized counterpart. In addition, when UPy-PDLA was blended with its enantiomer, the stereocomplex PLA formed showed significantly elevated melting temperatures, indicating the strength and efficacy of tailored hydrogen-bonding interactions on modifying polymer properties.
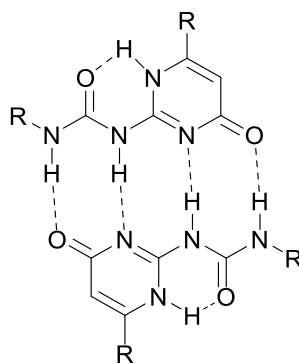
ureidopyrimidinone (Upy)

Figure 5.1 Self complimentary hydrogen-bonding unit, ureidopyrimidinone (UPy).

A healable polymer blend was reported by Colquhoun and Hayes in 2010 which utilized an electron deficient bis(diimide) capable of forming complimentary π-π interactions with π-electron rich species such as pyrene (Figure 5.2). These blends showed improved elasticity and toughness

153

(plastic deformation) and could maintain at least 90% of these properties after breaking and healing. The pyrene-capped polymer controls in this study did not display any re-healing character.[252]

Dubois and co-workers utilized iROP to synthesize pyrene-capped PLAs (pyr-PLA) and explored the effect on stereocomplexation of PDLA and PLLA units. When investigating the transport properties of pyr-PLA, slower diffusion of the end-capped polymers was observed, attributed to aromatic-aromatic interactions between pyrene chain-ends.[206] With the addition of carbon nanotubes, this aggregation was prevented and diffusion of the polymer chains was promoted leading to another report in 2015 on the use of pyr-PLAs as dispersion agents in PLA/multi-wall nanotube composites.[253]

electron poor
bis(diimide)

electron rich
pyrene
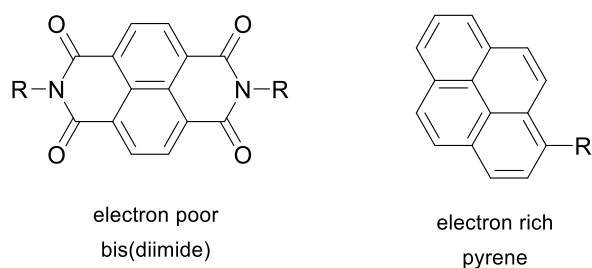
Figure 5.2 Bis(diimide) capable of forming complimentary π-π interactions with π-electron rich species such as pyrene.[206,253]

The following sections further the exploration of aromatic-aromatic electronic interactions as a method to modify and control polymer properties. In particular, the synthesis of a family of aryl-terminated PLAs *via* immortal ROP using aromatic alcohols is described and thermorheological techniques are used to understand the effects of aromatic interactions (*i.e.* extent of molecular associations) on bulk PLA properties.

5.2 Results and discussion

5.2.1 Synthesis of aryl-capped PLAs *via* immortal ring-opening polymerization.

A series of PLAs with bulky aromatic chain ends were synthesized through the immortal ring-opening polymerization (iROP) of *rac*-LA with dinuclear indium catalyst [(NNO)InCl]$_2$(μ-Cl)(μ-OEt) (**A**) using phenol (HOPh), 1-naphthol (Nap), hydroxymethylpyrene (HOMePyr), and hydroxymethylanthracene (HOMeAnth) as chain transfer agents (CTA) (Scheme 5.1 and Chart 5.1). Under an N$_2$ atmosphere in a glove box, solutions of *rac*-LA and CTA in DCM were prepared. After a homogenous solution had been obtained, appropriate amounts of complex **A** were added and the resulting reaction mixtures were stirred at room temperature. Catalyst to CTA ratios were kept constant at 1:20, while catalyst to monomer ratios were varied from 1050 to 21000 to generate polymer chains from 50 to 1000 units in length. The polymer samples were designated labels based on their end group and GPC molecular weight. For example, PLA-Ph$_{34}$ is a polymer with a phenol chain-end and $M_n = 34$ kg mol^{-1} (Table 5.1).

Scheme 5.1 Synthesis of end-functionalized PLA *via* immortal ring-opening polymerization with dinuclear indium catalyst [(NNO)InCl]$_2$(μ-Cl)(μ-OEt) (**A**).

[(NNO)InCl]$_2$(μ-Cl)(μ-OEt) (**A**)
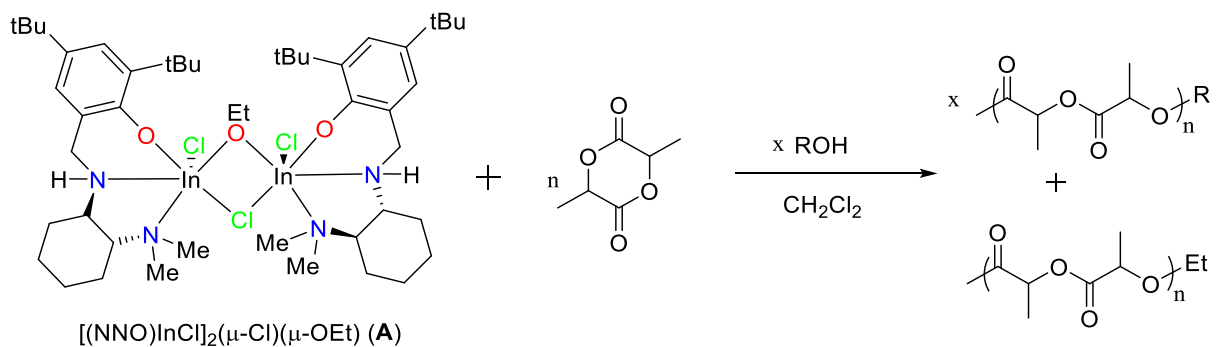
Chart 5.1 Alcohols used as chain transfer agents (CTAs) for the immortal ROP of *rac*-LA.

CH$_3$CH$_2$OH

ethanol
(EtOH)

phenol
(PhOH)

1-naphthol
(NapOH)

hydroxymethylpyrene
(HOMePyr)

hydroxymethylanthracene
(HOMeAnth)
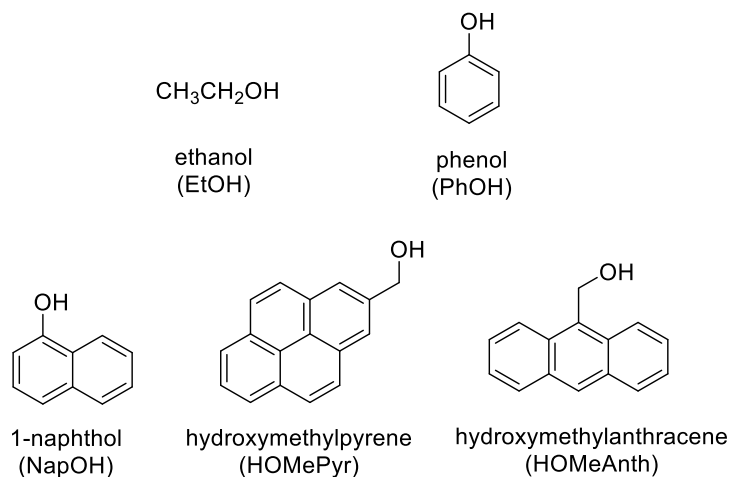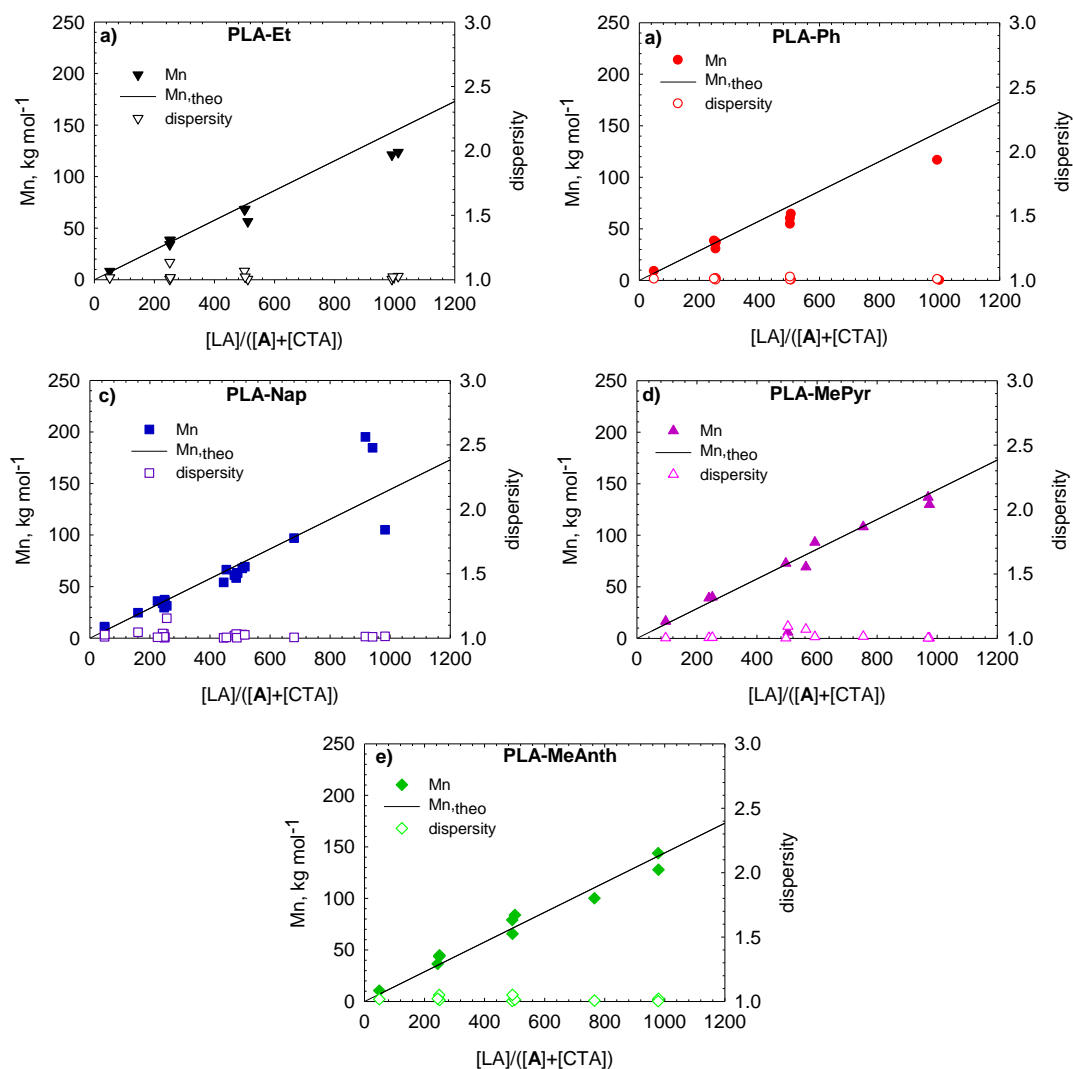
Figure 5.3 Plots of observed PLA number averaged molecular weight, M_n, (closed symbols) and dispersity, Đ, (open symbols) as functions of [LA]:([**A**]+[CTA]) for (a) CTA = ethanol (PLA-EtOH), (b) CTA = phenol (PLA-Ph), (c) CTA = naphthol (PLA-Nap), (d) CTA = hydroxymethylpyrene (PLA-MePyr) and (e) hydroxymethylanthracene (PLA-MeAnth). The black lines represent theoretical M_n values based on the [LA]:([**A**]+[CTA]) ratio at 100% conversion. All reactions were carried out room temperature in DCM.

Figure 5.3 shows the excellent agreement between the expected (black line on plots) and experimental molecular weights and low dispersity values achieved from iROP. The ^{1}H NMR spectra of low molecular weight PLAs (3 – 5 kg mol^{-1}) show peaks in the aromatic region corresponding to the aryl-chain ends (Figure 5.4 - Figure 5.6). In addition, the integrations of the

aromatic peaks and the polymer methylene proton signals (5.10-5.25 ppm) are in agreement with the calculated molar ratios of [LA]:([**A**]+[CTA]).

UV-Vis spectroscopic analysis of PLA solutions in $CHCl_3$ showed absorbance patterns similar to those of the free alcohols as well as showing the PLA absorbance signal at 240 nm (Figure 5.7 – Figure 5.10). Examination of the $^1H\{^1H\}$ NMR spectra of the aryl-capped PLA were all comparable to that of polymers produced by **A** alone, with P_m values around 0.6 implying low levels of isotacticity.

Table 5.1 Molecular weight data for immortal ring-opening polymerization of *rac*-LA with various aryl chain transfer agents.

Entry	CTA	sample[a]	Conv. (%)[b]	[LA]/([A]+[CTA])	$M_{n,theo}$ (g mol^{-1})[c]	$M_{n,GPC}$ (g mol^{-1})[d]	$Đ^d$
1		PLA-Ph$_9$	99	49.8	7080	8750	1.01
2	PhOH	PLA-Ph$_{30}$	92	255	33800	30400	1.00
3		PLA-Ph$_{54}$	97	503	70300	54400	1.00
4		PLA-Ph$_{117}$	98	993	140000	117000	1.01
5		PLA-Nap$_{11}$	94	52.0	7050	11200	1.01
6		PLA-Nap$_{63}$	99	497	70900	63100	1.03
7	NapOH	PLA-Nap$_{68}$	98	518	73300	67600	1.03
8		PLA-Nap$_{105}$	99	993	142000	105000	1.01
9		PLA-Nap$_{185}$	92	1020	136000	185000	1.01
10		PLA-MePyr$_{17}$	99	96	13700	16500	1.00
11	HOMePyr	PLA-MePyr$_{73}$	99	496	70800	72800	1.00
12		PLA-MePyr$_{137}$	98	970	137000	137000	1.00
13		PLA-MePyr$_{153}$	70	1530	154000	153000	1.00
14		PLA-MeAnth$_{11}$	98	49.5	6990	10500	1.02
15		PLA-MeAnth$_{44}$	99	249	35500	43700	1.05
16	HOMeAnth	PLA-MeAnth$_{79}$	99	492	70200	79200	1.00
17		PLA-MeAnth$_{128}$	99	979	140000	129000	1.02
18		PLA-MeAnth$_{144}$	93	978	131000	144000	1.00
19		PLA-MeAnth$_{181}$	98	1400	197000	181000	1.01
20		PLA-Et$_8$	97	51.5	7220	8200	1.02
21		PLA-Et$_{38}$	99	251	35800	38500	1.14
22	EtOH	PLA-Et6$_8$	98	500	70600	68000	1.07
23		PLA-Et$_{121}$	98	991	140000	121000	1.00
24		PLA-Et$_{124}$	99	1010	144000	124000	1.03

Reactions were carried out in DCM at 25 °C for 18 h. [a] PLA-MePyr$_{73}$ denotes a polymer with a molecular weight of 73 kg mol^{-1} and a hydroxymethylpyrene chain-end (Chart 5.1). [b] Monomer conversions determined by ^{1}H NMR spectroscopy. [c] Calculated from $M_{n,theo}$ = (144 g mol^{-1} × conversion × [LA]/([A]+[CTA])) + M_{OR}. Absolute molecular weights were determined by triple detector GPC (gel permeation chromatography) *via* Universal Calibration (THF 4 mg mL^{-1}, flow rate = 0.5 mL min^{-1}, dn/dc = 0.044 mL g^{-1}).
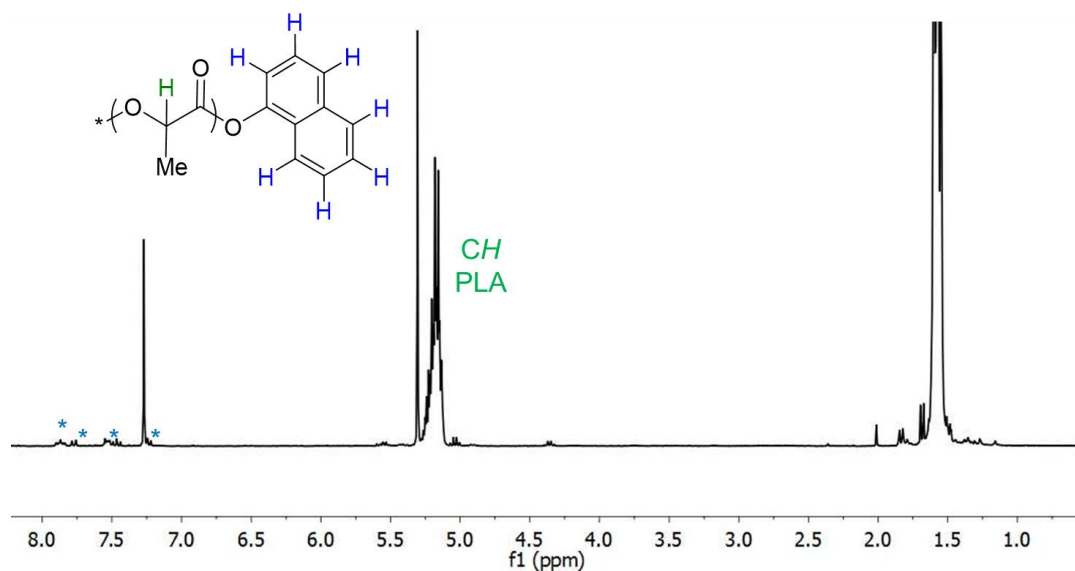
Figure 5.4 ^{1}H NMR (CDCl$_3$, 25 °C, 300 MHz) spectrum of PLA isolated from polymerization of [LA]:[**A**]:[NapOH] ratios of 1050:1:20 (Table 5.1, entry 5).
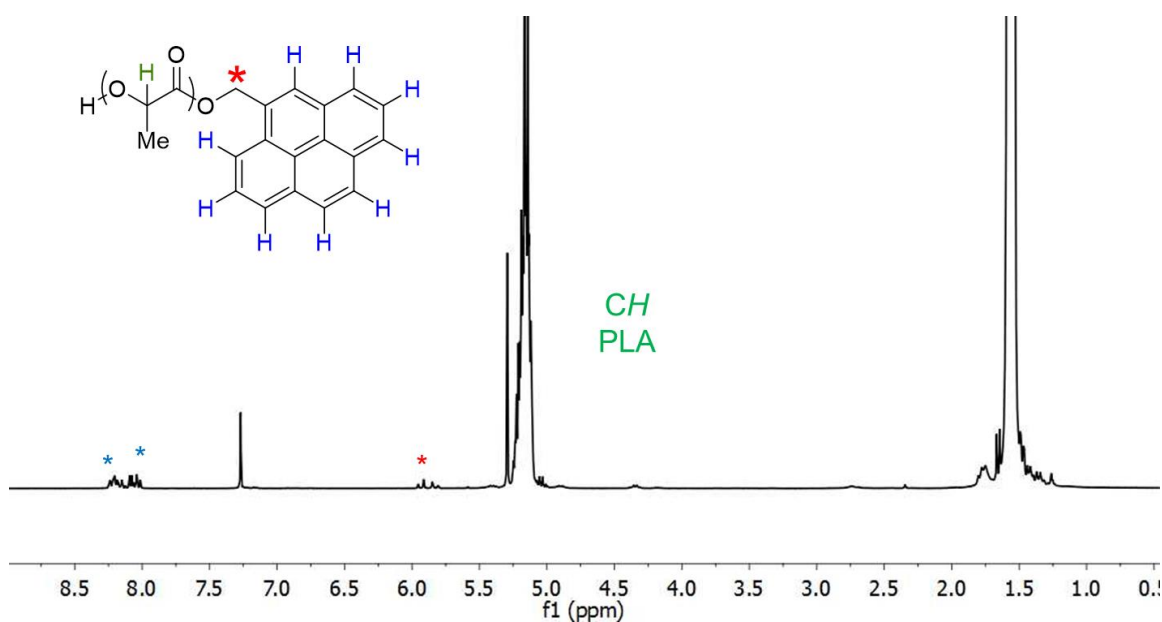
Figure 5.5 ^{1}H NMR (CDCl$_3$, 25 °C, 300 MHz) spectrum of PLA isolated from polymerization of [LA]:[**A**]:[PyrMeOH] ratios of 1050:1:20 (Table 5.1, entry 10).
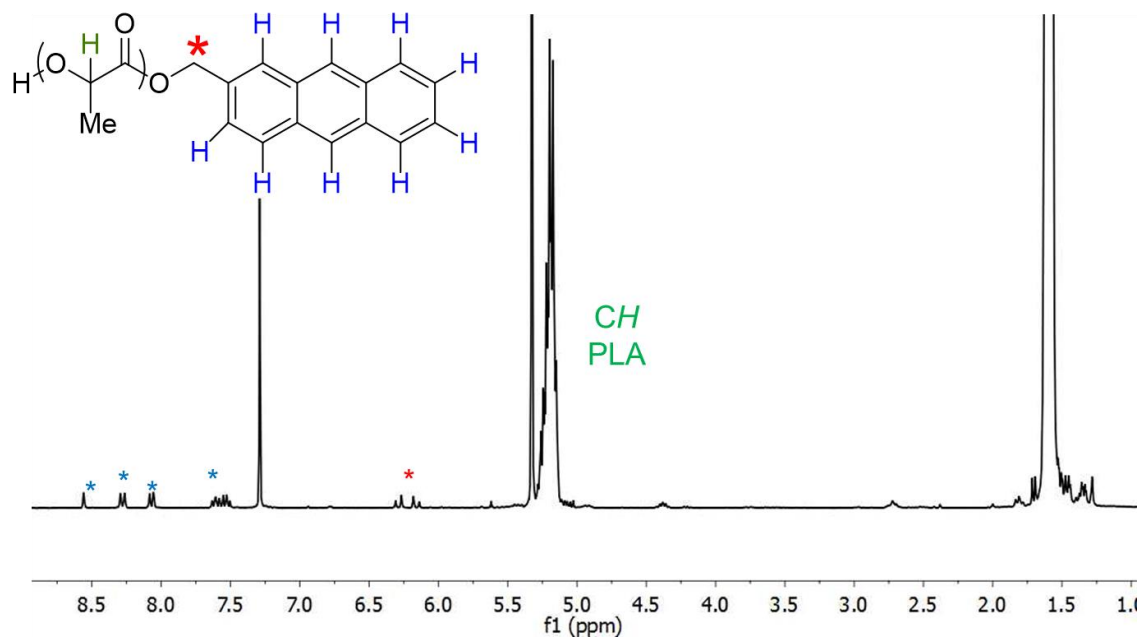
Figure 5.6 ^{1}H NMR (CDCl$_3$, 25 °C, 300 MHz) spectrum of PLA isolated from polymerization of [LA]:[**A**]:[AnthMeOH] ratios of 1050:1:20 (Table 5.1, entry 14).
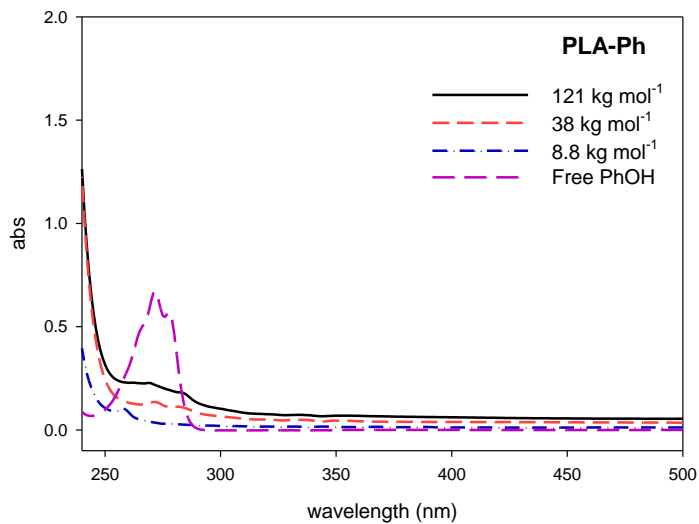
Figure 5.7 Solution UV-Vis spectra for phenol (purple line), PLA-Ph$_9$ (blue line), PLA-Ph$_{38}$ (red line) and PLA-Ph$_{121}$ (black line). Polymer solutions were in CHCl$_3$ with a concentration of 1×10^{-4} M.
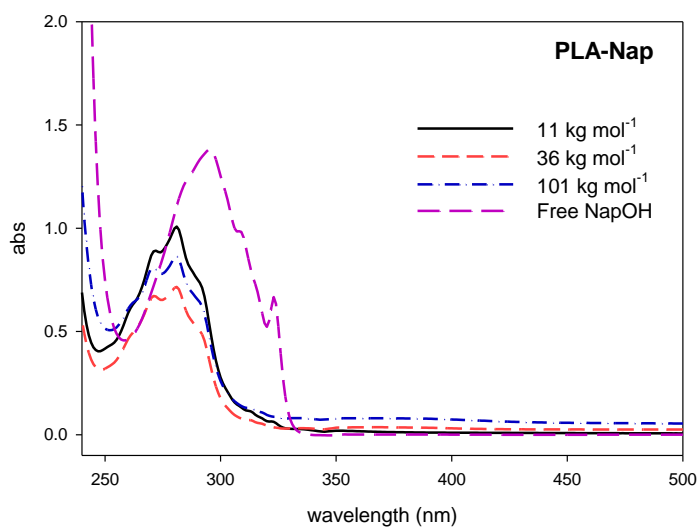
Figure 5.8 Solution UV-Vis spectra for naphthol (purple line), PLA-Nap$_{11}$ (black line), PLA-Nap$_{36}$ (red line) and PLA-Nap$_{101}$ (blue line). Polymer solutions were in CHCl$_3$ with a concentration of 1×10^{-4} M.
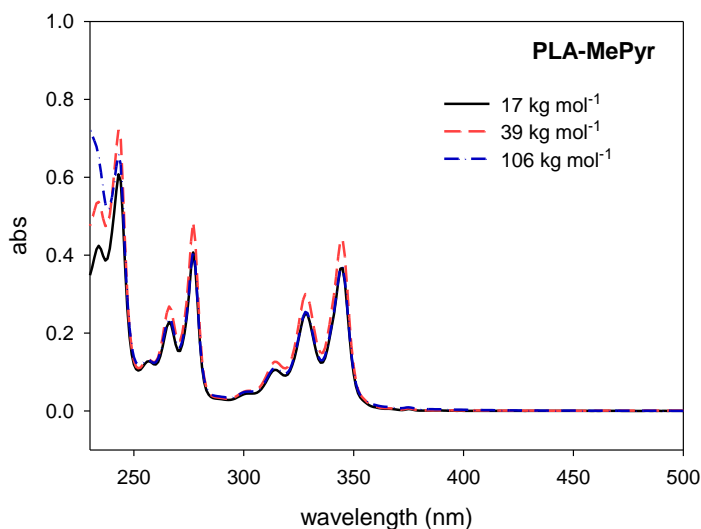
Figure 5.9 Solution UV-Vis spectra for PLA-MePyr$_{17}$ (black line), PLA-MePyr$_{39}$ (red line) and PLA-MePyr$_{106}$ (blue line). Polymer solutions were in CHCl$_3$ with a concentration of 1×10^{-5} M.
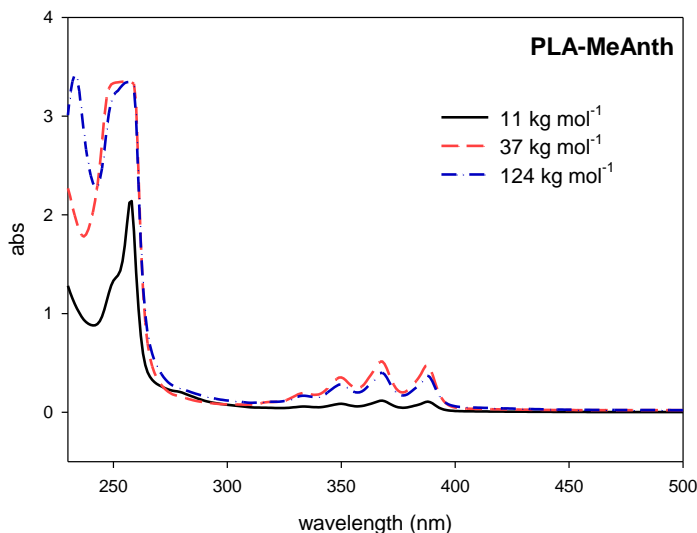
Figure 5.10 Solution UV-Vis spectra for PLA-MeAnth$_{11}$ (black line), PLA-MeAnth$_{37}$ (red line) and PLA-MeAnth$_{124}$ (blue line). Polymer solutions were in CHCl$_3$ with a concentration of 1×10^{-4} M.

5.2.2 Thermal studies of aryl-capped PLAs.

To identify an end-group effect on the thermal transitions, thermogravimetric analysis (TGA) and differential scanning calorimetery (DSC) were used to determine the thermal properties of the various aryl-capped PLAs in this study (Table 5.2).

Polymeric samples were heated at 20 °C/min from 25 °C to 500 °C, and the onset and total degradation temperatures, were calculated from the first derivative of the resulting thermographs (Figure 5.11). The aryl-capped polymers were thermally stable up to ~300 °C where they began their degradation. All the polymers including the native ethoxy-capped PLA, showed total degradation at ~ 395 °C. These observations indicate that the chain-end does not affect the overall thermal degradation pathways of PLA (Table 5.2). The most advantageous property of PLA is its biodegradability. The most advantageous property of PLA is its degradability. These results show that these potentially useful chain-end modifications will only affect melt or bulk properties while allowing for the same thermal degradation pathway as the corresponding native polymer.

Table 5.2 Thermal properties for various end-capped PLAs in this study (all values in °C).

Entry	Material	$T_g{}^a$	$T_{onset}{}^b$	$T_{total}{}^b$
1	PLA-Et	49.2 (6.7)	345(12)	400 (5)
2	PLA-Ph	47.9 (2.1)	340 (3)	391 (7)
3	PLA-Nap	43.3 (4.4)	341 (9)	396 (5)
4	PLA-MePyr	48.0 (5.4)	351 (8)	398 (5)
5	PLA-MeAnth	48.1 (7.5)	349 (8)	398 (9)

[a] Thermal analysis of samples was performed by using a differential scanning calorimeter (DSC) with ca. 5 mg of sample. Samples heated to 275 °C at 10 °C/min and cooled to 25 °C at 5 °C/min to determine T_g and T_m. Glass transitions and melting temperatures calculated from the second heating scans. [b] Thermogravimetric analysis was performed on approximately 20 mg of material. Samples were heated to 500 °C at a rate of 20 °C/min to determine the degradation onset temperature (temperature at which there is 5% weight loss, T_{onset}). Calculated standard errors given in parentheses.
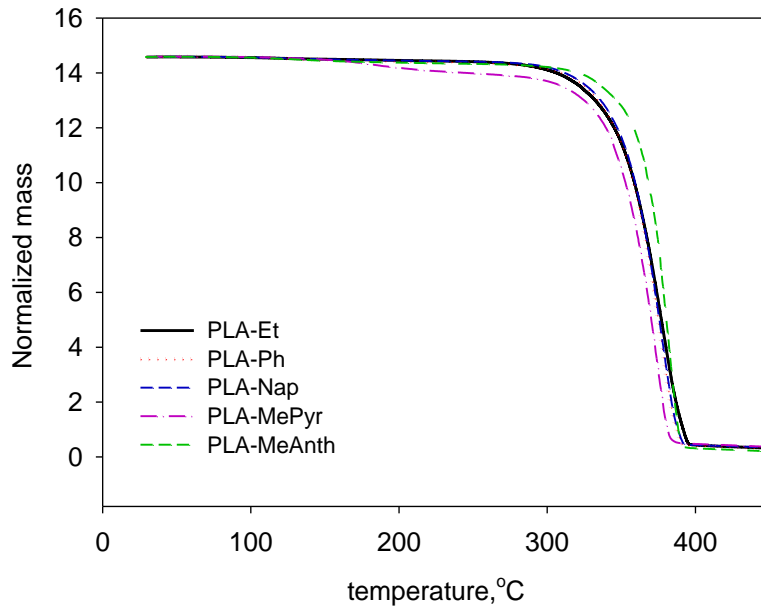
Figure 5.11 TGA heating traces for the various aryl-capped PLAs. Thermogravimetric analysis was performed on approximately 15 mg of material. Samples were heated to 500 °C at a rate of 20 °C/min.
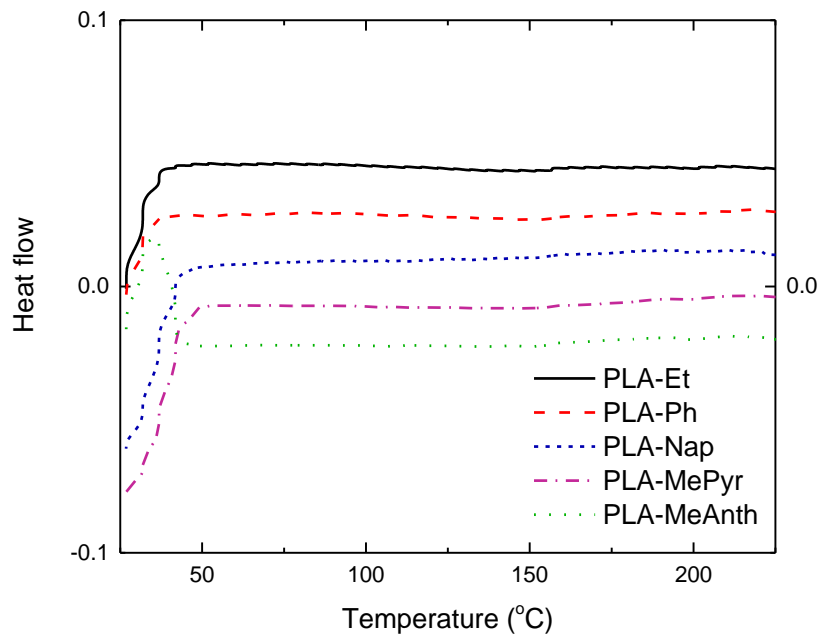
Figure 5.12 DSC traces for the various end-capped PLAs studied. Samples heated to 250 °C at 10 °C/min and cooled to 25 °C at 5 °C/min under a nitrogen atmosphere to reduce sample degradation. Glass transition and melting temperatures calculated from second cooling scans. *ca*. 5 mg of sample used. Plots shifted vertically for clarity.

In the DSC analysis of the aryl-capped PLAs, samples were heated from 25 °C to 275 °C at 10 °C/min and then cooled at 5 °C/min (Figure 5.12). To eliminate the influence of thermal history, glass transition temperatures were calculated from the second heating scans and averaged over all the molecular weights of polymers in the same family. All the PLAs were amorphous, displaying no crystallization peaks. The glass transition temperatures were comparable for all the end-capped PLAs and the enhancement in crystallization seen in studies by Yang[207] and Dubois[206,253] on isotactic PLA homopolymers capable of forming of π–π aggregates was not observed. The absence of this effect could be due to insufficient chain packing from the mostly atactic microstructure of the PLAs ($P_m \sim 0.6$), and thus the chain-end interactions are not sufficient to drive chain ordering between the small regions of isotacticity on the polymer chains.

5.2.3 Solution viscosity of aryl-capped PLAs.

Chain aggregation is expected to form physical networks which change the linear structure of the polymer chains thus influencing mobility of the polymer chains and their viscosity.[250] To investigate this effect in solution intrinsic viscosities of the aryl-capped PLAs were obtained from the GPC analysis (in THF) and are plotted versus weight-averaged molecular weight, M_w in Figure 5.13. The data for aryl-capped PLAs fall on a single line (consistent with the Mark-Houwink equation with slopes between 0.76 and 0.80). This is in agreement with the relationship determined by Dorgan[163] and Othman,[166] indicating random coil behaviour of linear polymers in a good solvent. More specifically, the intrinsic viscosities for all aryl-capped polymers follow the same behaviour suggesting the absence of any particular interaction to form aggregates through the various aryl groups in dilute solution. Similarly, the calculated hydrodynamic radii for the aryl-capped polymers also show comparable trends with respect to molecular weight as previously

166

reported[166] for other PLAs and the exponent implies linear microstructure and thus minimal chain aggregation in dilute solution (Figure 5.14).
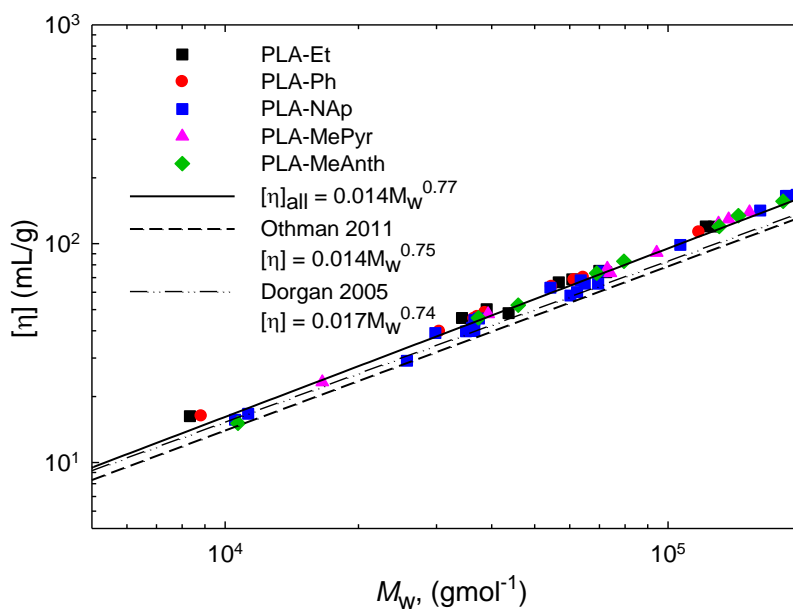
Figure 5.13 A log−log plot of intrinsic viscosity of various aryl-capped PLAs as a function of the molecular weight.
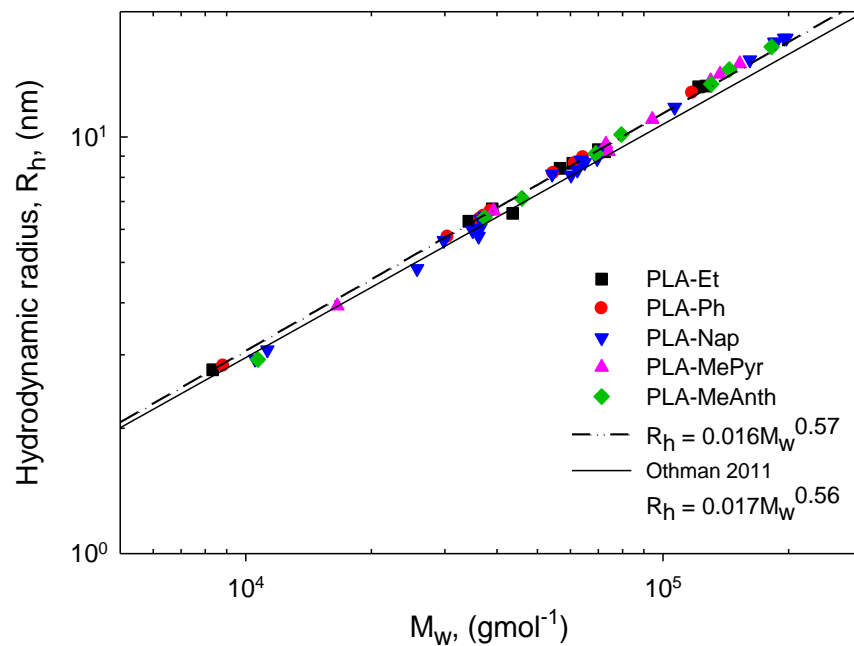
Figure 5.14 Characteristic hydrodynamic radius (R_h) as a function of molecular weight.

5.2.4 Melt Rheology - Linear viscoelasticity.

To determine the thermal stabilities of aryl-capped PLAs, time sweep experiments were conducted using a parallel plate rotational rheometer at 180 °C with constant angular frequency of 3.14 rad/s over 120 minutes. Data collection was started immediately after polymer samples were loaded onto the rheometer. The complex modulus $|G^*|$, a measure of resistance to deformation sensitive to structural changes, was monitored over the experimental time frame. To accurately compare the structural changes occurring within the aryl-capped polymer samples, the normalized complex modulus, $G^*(t)/G^*(t=0)$, is plotted against time in Figure 5.15a. Native ethoxy-capped polymers showed a steady complex modulus for much of the experiment, decreasing by ~10% as a result of thermal degradation. In contrast, aryl-capped polymers display a significant increase in

their complex moduli over the experimental time frame, with the modulus for pyrene capped PLAs showing the largest increase of ~450%. To further examine how these structural changes can be induced, similar experiments were conducted on PLA-Nap36 at 70 and 120 °C (Figure 5.15b) indicating similar increases. The increase in the normalized complex modulus appears to be temperature dependent as this effect is nearly absent at low temperatures (Figure 5.15b). Chains have greater mobility at higher temperatures, and as such end associations tend to occur more readily. Figure 5.15c shows the frequency dependence of these associations. At high deformation frequencies, segmental motion is prevalent and chain-ends cannot move to form aggregates therefore no enhancement of the complex modulus is seen, indicating that the observed increase in modulus can be attributed to the gradual aromatic electrostatic association of the aryl-groups under an oscillatory shearing force. [252,254]

At lower temperatures, the change in complex modulus diminishes and is absent at 70 °C. The upturn in the complex modulus is attributed to chain association through the aryl groups. At high temperature, due to higher chain mobility, the associations occur faster. Therefore, the observed upturn in modulus can be ascribed to the gradual $\pi-\pi$ aromatic electrostatic association of the aryl-groups under a constant shearing force. shows the frequency dependence of these associations. Increasing the frequency of oscillation causes a reduction in chain aggregation due to the application of a higher shearing force that can disrupt these weak associations. These results further demonstrate that increased chain mobility is needed for these associations to occur which is the case at high temperatures.
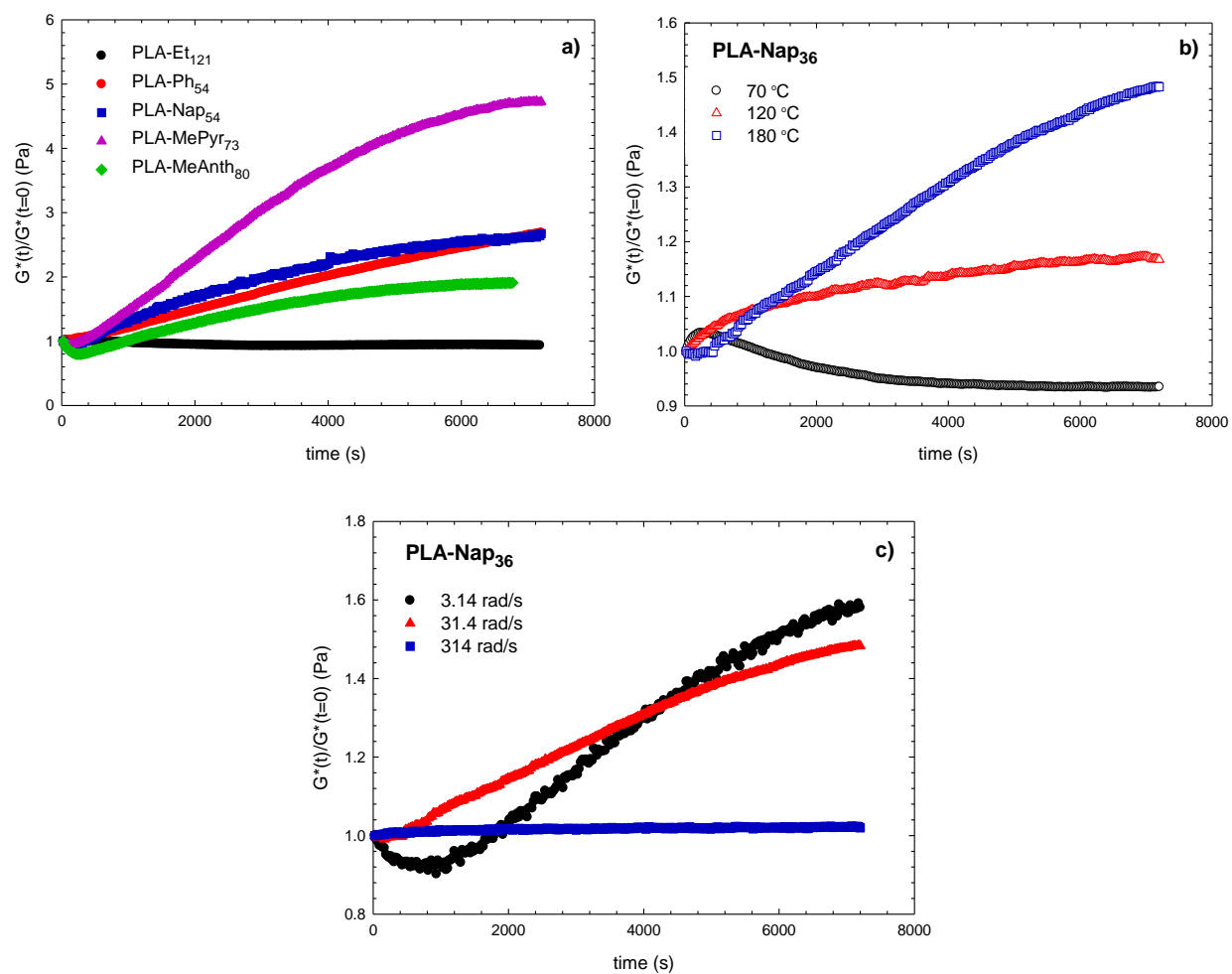
Figure 5.15 a) Normalized complex modulus, $G^*(t)/G^*(t=0)$, vs. time at 180 °C for end-capped PLAs in this study. b) Normalized complex modulus, $G^*(t)/G^*(t=0)$, vs. time at 70, 120 and 180 °C for PLA-Nap$_{36}$. c) Normalized complex modulus, $G^*(t)/G^*(t=0)$ vs. time at 3.14, 31.4 and 314 rad/s for PLA-Nap$_{36}$.

Small amplitude oscillatory shear (SAOS) experiments in the linear viscoelastic regime were performed to study the structure-property relationships of the aryl-capped materials in order to identify subtle differences between the microstructure of the various polymers. A parallel plate rotational rheometer was used at a constant strain amplitude of 2% over frequencies ranging from 0.01 to 100 Hz. Time-temperature superposition was applied to isothermal experiments in the temperature range of 70-170 °C to generate master curves of the viscoelastic moduli, G' and G" as well as the complex viscosity at the reference temperature of 150 °C. Figure 5.20a-b plots the master curves of the viscoelastic moduli as well as its complex viscosity at the reference temperature of 150 °C of two PLA-MePyr polymers of different molecular weights, 72 and 135 kg mol^{-1}. The high molecular weight aryl-capped PLA behaves similarly to the ethoxy-capped PLA whereby the storage moduli exhibit a clear plateau at high frequencies and the loss moduli increase with frequency, going through a maximum and reaching a minimum value at higher frequencies.[20] Deviations from the expected rheological behaviour of monodisperse linear polymers is observed as the molecular weight decreases where the aromatic groups begin to have a relatively larger effect on the rheological properties (note that there is only one aryl group per chain) (Figure 5.17). In the terminal region, at small deformation frequencies, the storage and loss moduli usually display characteristic slopes of 1 and 2, respectively. However, in the low molecular weight aryl-capped PLAs the slope of G' becomes closer to 1 showing increase in elasticity due to associations at small frequencies. As a result, the complex viscosity also exhibits an upturn at small frequencies, deviating from its Newtonian steady value (Figure 5.17). (Additional SAOS data for all aryl-capped PLAs are presented in appendix C and show similar results.)

The plots for the lower molecular weight polymer PLA-MePyr$_{72}$ (Figure 5.16a), show good superposition at medium to high frequencies (10-10^6 rad/s) due to the absence of associations at

171

these high frequencies, however, it clearly fails in the low frequency range. This indicates that the

microstructure of the material is different at each temperature due to the presence of associations.

These associations depend on both temperature and frequency as stated in the discussion of the

thermal stability experiments above (Figure 5.15).
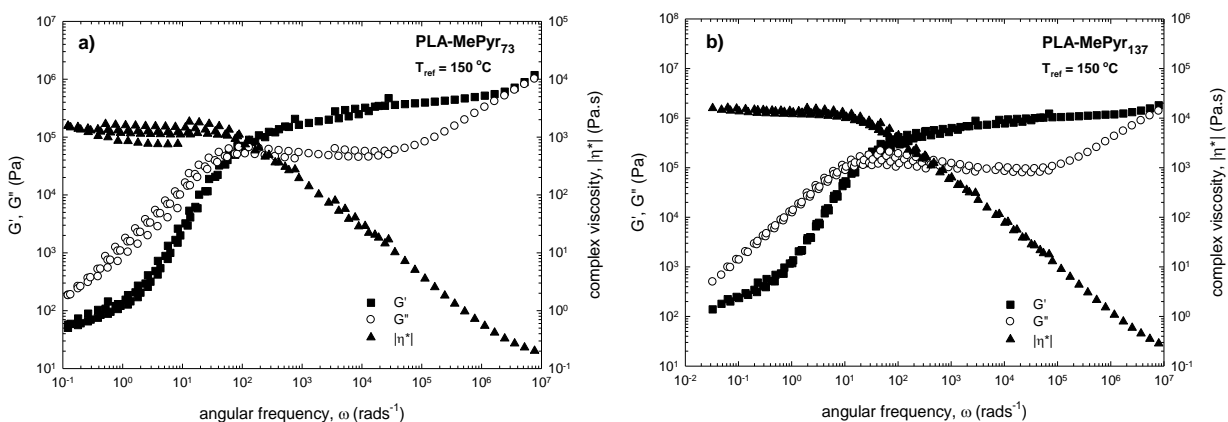
Figure 5.16 Thermorheologcial characterization of PLA-MePyrene polymers. a) Master curve of the linear viscoelastic moduli, G' and G" and |η*| complex viscosity for PLA-MePyr$_{72}$ at T$_{ref}$ = 150 °C. b) Master curve of the linear viscoelastic moduli, G' and G" and |η*| complex viscosity for PLA-MePyr$_{135}$ at T_{ref} = 150 °C.
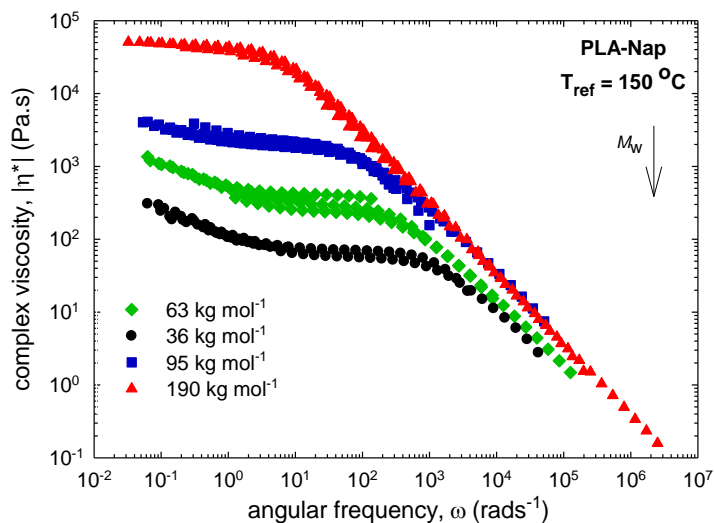
Figure 5.17 Master curve of the complex viscosity vs. angular frequency (T_{ref} = 150 °C) for naphthol-capped PLAs (Nap-PLA) to show the molecular weight dependence on the upturn in complex viscosity.

To further show that these aggregates are induced under low frequency oscillations, successive frequency sweep experiments were conducted on PLA-Nap$_{36}$ and PLA-Et$_{34}$ polymers (Figure 5.18). The G' increases in the low frequency region successively after each experiment, however, it remains the same at the high frequency region (Figure 5.18a). The native polymer, on the other hand, shows no change in the storage modulus over the time period of the three tests (Figure 5.18b). These results indicate that only under low shear do the aromatic chain-ends have enough time to associate and these associations do not seem to be disrupted at high shear rates.
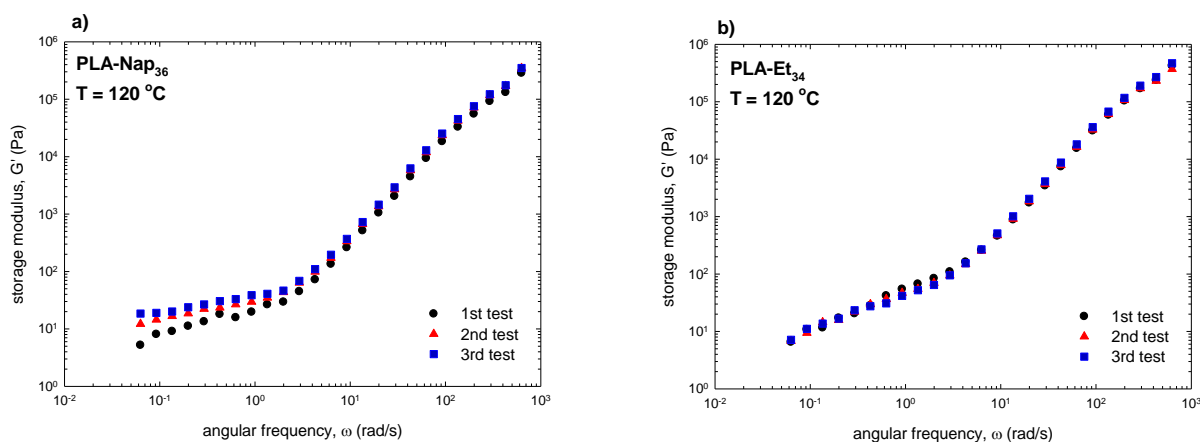
Figure 5.18 Successive frequency sweep experiments for a) PLA-Nap$_{36}$ and b) PLA-Et$_{34}$ polymers. $T = 120$ °C, $\omega = 0.063$-630 rad/s, strain $= 2\%$.

Time sweep experiments were conducted to show if the aromatic-aromatic associations can be disrupted (break) by high frequency deformations. The time sweep test started with an angular frequency of 3.14 rad/s for 60 minutes at 120 °C, and after this time the angular frequency was increased to 314 rad/s for another 60 minutes. After this a final test at 3.14 rad/s was then conducted for another 60 min. Figure 5.19 depicts the changes in the complex modulus over time. The G* at the high frequency is not shown on the plot in order to keep the vertical scale linear and to show the changes at small frequencies shown more clearly. It is noted that at high frequency only a very

173

minor increase in G* was observed within experimental error (see also Figure 5.15c for the effect of high frequency on G*). However, the onset of aggregation seems to have been restored when the lower frequency has been resumed and continues nearly from the point left at the end of in the first low frequency test (a small increase of 3% from the end of low frequency test one to the beginning of the low frequency test two after 60 min).
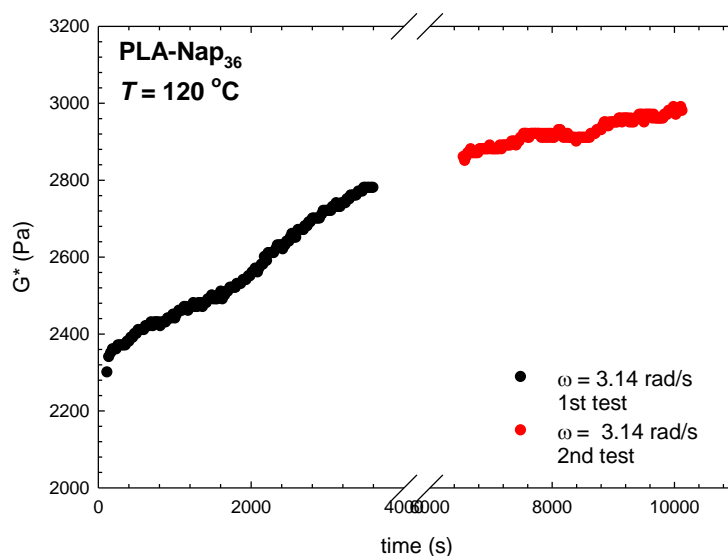
Figure 5.19 Successive time sweep experiments for PLA-Nap$_{36}$. T = 120 °C, ω = 3.14 rad/s, strain = 2%.

This temperature dependence can be further seen in the plots of the horizontal shift factor, a_T vs. the inverse temperature that we determined by shifting the data in Figure 5.20a-b to obtain the master curves plotted in Figure 5.16a-b. The shift factors in Figure 5.20c show two different slopes for the high and low temperature data. Similarly, the plot of the storage vs. loss modulus for the different isothermal experiments in Figure 5.20d. For linear PLAs isothermal experiments all collapse onto the same curve, however, the PLA-MePyr polymer plots show a temperature dependence on phase transitions in the aryl-capped polymers. This explains the failure of the time-

temperature superposition at low deformation frequencies where low shear cannot easily break the

chain-end associations.
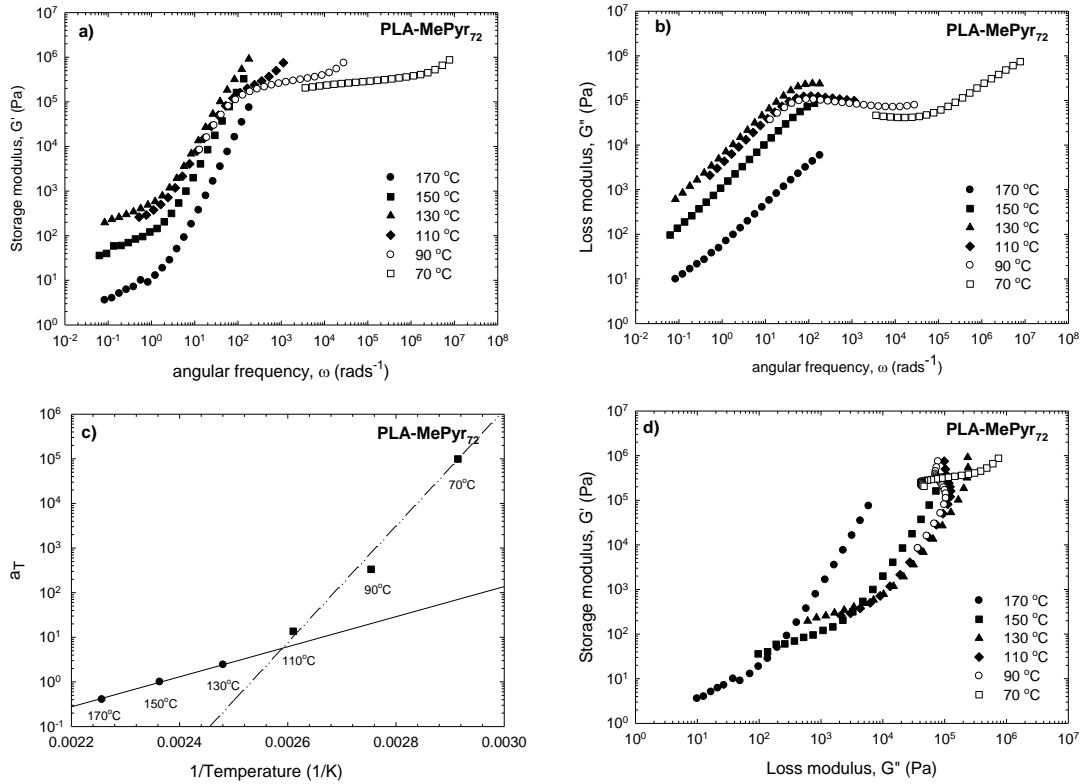
Figure 5.20 a) Storage modulus vs. frequency, b) loss modulus vs. frequency for the isothermal frequency sweep experiments for PLA-MePyr$_{72}$, to show the failure of the time-Temperature superposition principle. c) Horizontal shift factors, a$_T$ at 150 °C. d) Plot of G' vs. G" at various temperatures for PLA-MePyr$_{72}$ to check for possible thermal transitions.

The observed deviations from expected melt rheology for linear polymers are comparable to those seen in associating polymers which utilize secondary interactions to form network structures.[249,255-259] In this case, the network structure is developed under oscillatory shear conditions through the formation of extended aggregate structures, though because these aggregates are transient and slow in their onset, the exact morphology of the structures is difficult to probe.

Similar master curves for two lower molecular weight PLA-Nap polymers are shown in Figure 5.21. Analogous to the pyrene capped PLAs, the moduli at different temperatures do not form smooth master curves at low frequencies (displaying thermorheological complexity) mainly due to the temperature dependence of the aromatic associations in the low frequency regime. However, because these aggregates are transient and fast in their onset, the exact morphology of the structures are difficult to probe.
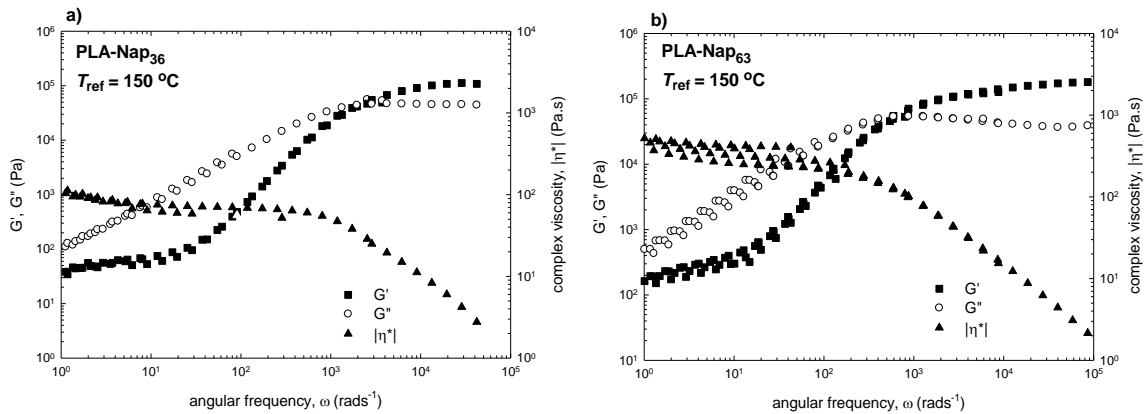
Figure 5.21 Master curve of the linear viscoelastic moduli, G′ and G″, and complex viscosity, $|\eta^*|$ (T_{ref} = 150 °C), for a) PLA-Nap$_{36}$ b) PLA-Nap$_{63}$ polymers.

As the formation of these network structures is observable by an increase (upturn) in the complex viscosity in the low frequency region (Figure 5.17), the strength of association can be

176

probed by defining an "index of association" based on their increase in viscosity at low frequencies (Equation 5.1).

$$\text{Index of association} = [(\eta_0 - \eta_{0.01})/ \eta_0] \times 100$$

Equation 5.1 where η_0 is the plateau (Newtonian) complex viscosity or zero-shear viscosity, and $\eta_{0.01}$ is the complex viscosity at 0.01 Hz (chosen arbitrarily).

The index of association is plotted against molecular weight in Figure 5.22. At high molecular weight, all the polymers show very low association factors, implying that the associations at this length scale do not affect the overall behaviours of the polymers (note that there is one aryl-group per chain). As the molecular weight decreases all the aryl-capped polymers show an increase in their aggregation due to assembling of their chain-ends. There is a rough correlation between the index of association with molecular weight as expected. Important to note is that the native polymer does not show this increase in association over all the molecular weights studied.

The favourable aggregation of aromatic systems usually occurs through off centre parallel or edge-to-face stacking.[260] The index of association may be related to the bulkiness of the end-group moiety and thus how well it can move through the polymer matrix, as well as its ability to form one of the preferred stacked structures. However, it is difficult to know how significant these trends are as we have no information about the initial aggregation present within the polymer samples.
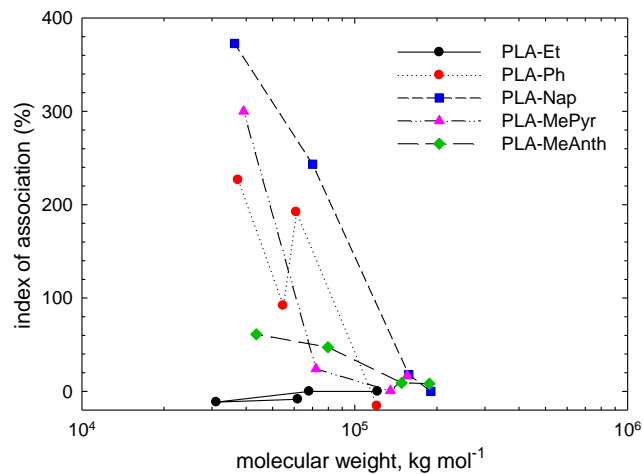
Figure 5.22 Index of association vs. molecular weight for aryl-capped PLAs in this study.

The reptation time, λ_c, is defined as the time it takes for the polymer chains to respond to a sudden applied force in order to fully relax after completing its diffusion out of its constrained tube. This parameter can be roughly calculated from the cross-over point between the storage and loss moduli in the frequency sweep experiments and is plotted against molecular weight in Figure 5.23. Reptation behaviour of linear microstructured PLA chains follow the relation, $\lambda_{c\,(PLA\text{-}Et)} = 1.512 \times 10^{-20}\,M_w^{3.4}$ (indicated by the black line on the plot). Higher molecular weights polymers follow the expected trend for linear PLAs but as the molecular weight decreases the reptation times tend to be higher than expected (Figure 5.23). The presence of chain associations and the formation of a weak network is expected to increase polymer reptation time, as the "apparent" molecular weight increases, therefore, chains will need more time to respond to applied strains. As discussed

above, these weak associations are only significant in low molecular weight polymers, which start to show deviation from linear behaviour, the threshold being around 100 kg mol^{-1}.
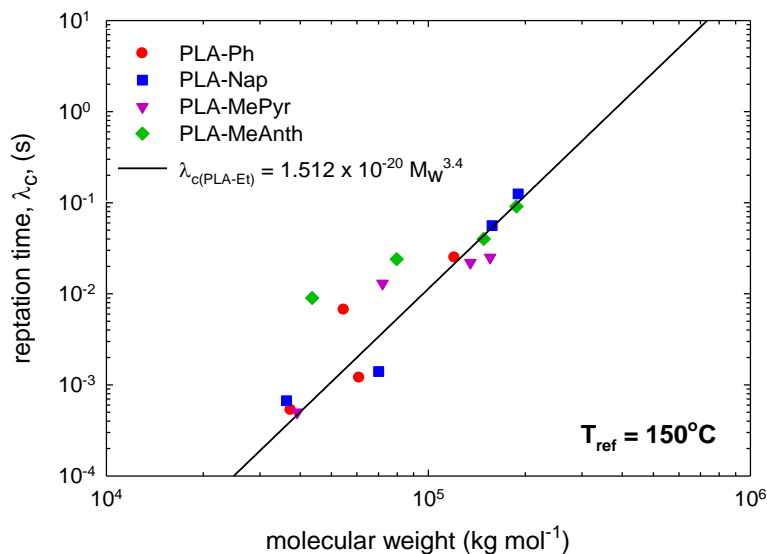
Figure 5.23 Reptation time versus molecular weight for aryl-capped PLAs in this study.

5.2.5 Uniaxial Extensional Rheology.

Chain interactions can be probed by measuring the extensional viscosity of polymeric materials. Strain hardening occurs when the deformation time exceeds the terminal relaxation time for relaxation of the polymer chains. Recently our group reported that high molecular weight PLAs do show this strain hardening effect at temperatures below 110 °C.[1,22] This technique was further utilized to explore the influence of the aryl end-groups on chain interactions within PLA. Uniaxial extensional tests were carried out at 90 °C at Hencky strain rates of 0.01 to 10 s^{-1} (appendix C). Figure 5.24a shows that all the materials studied display strain hardening at 10 s^{-1} strain rates, but this effect is lost at lower strains (Figure 5.24b). Reports of polymers with moieties capable of

secondary interactions show that these associations lead to extensive strain hardening.[261,262] The functionality in those reported polymers were dispersed throughout the polymer backbone leading to a large number of possible associations. The aryl-capped polymers in this study however, have functionality at only the chain end, and the observed strain hardening is more likely a product of PLA microstructure than the interactions of the chain-ends. To enhance the strain hardening, higher temperatures would impart more chain mobility to allow extensional stress to align the chains. Unfortunately, tests at high temperature were not possible as the materials became too viscous under these conditions.
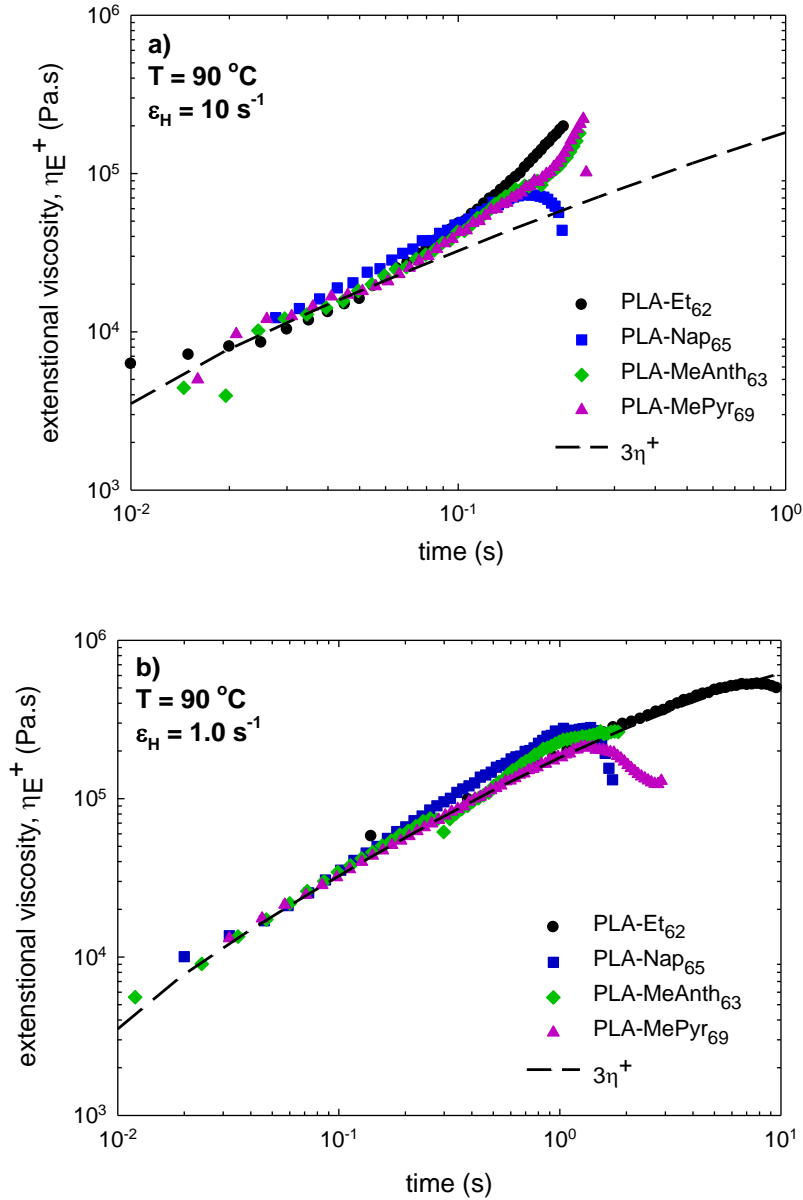
Figure 5.24 Comparison of tensile stress growth coefficients for selected aryl-capped PLAs (measure of elongational viscosity) at 90 °C as a function of time at Hencky strain rate of a) 10 s^{-1} and b) 1.0 s^{-1}.

5.2.6 Mechanical properties.

Tensile strength tests were performed on compression moulded samples with a thickness of 0.3-0.5 mm. The results are shown in Figure 5.25 to Figure 5.27. These aromatic electrostatic

interactions are very weak (section 5.2.4) thus we did not expect a large difference in the mechanical properties of the aryl-capped PLAs and within error there does not seem to be an enhancement or depreciation of the tensile properties with the incorporation of aryl groups to the chain end of the polymers. These results give more evidence that chain mobility is the determining factor for the onset of aggregation, therefore, at room temperature all the PLAs display comparable mechanical properties. This could be a beneficial property of these materials as the onset of aggregation during extrusion could improve the melt strength of PLA during processing.
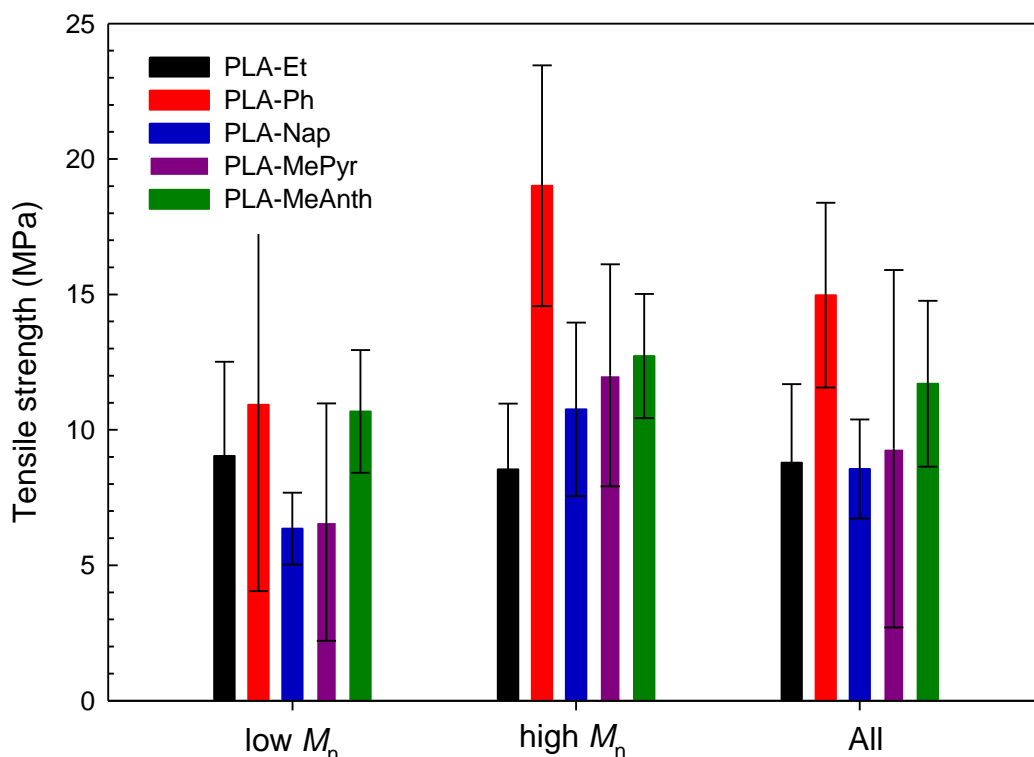
Figure 5.25 Tensile strength for aryl-capped PLAs in this study. Low molecular weight polymers had M_n between 25 and 35 kg mol^{-1}. High molecular weight polymers had M_n between 110 and 130 kg mol^{-1}. "All" combines data for all polymers of the same family.
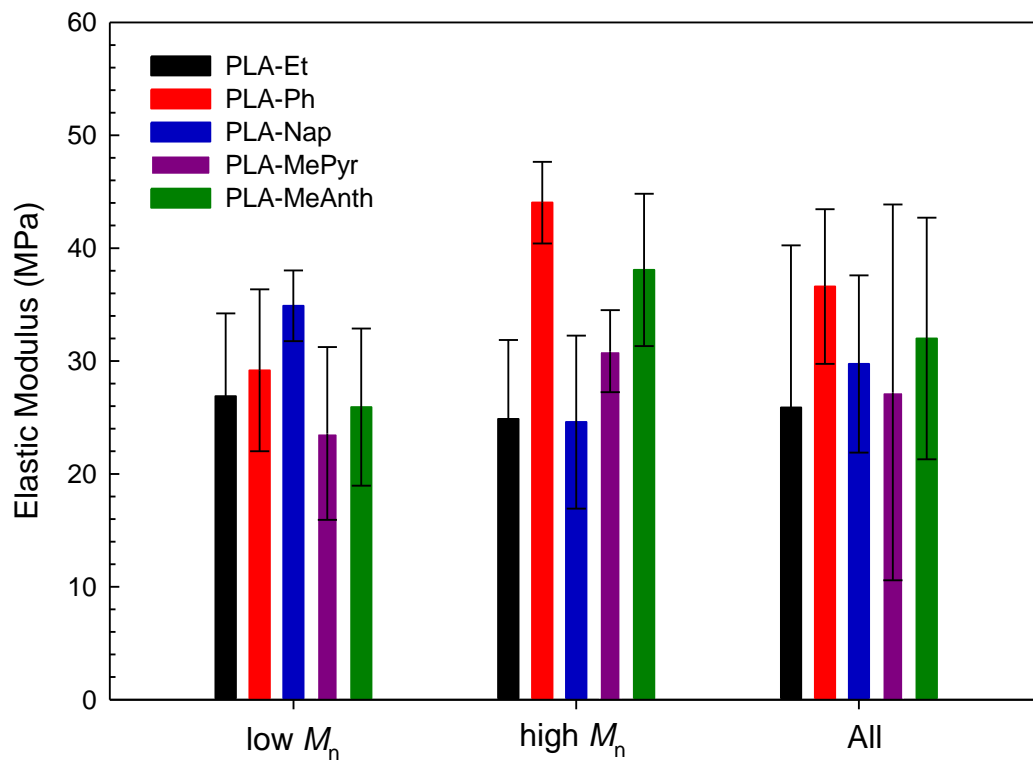
Figure 5.26 Elastic Modulus for aryl-capped PLAs in this study. Low molecular weight polymers had M_n between 25 and 35 kg mol^{-1}. High molecular weight polymers had M_n between 110 and 130 kg mol^{-1} "All" combines data for all polymers of the same family.
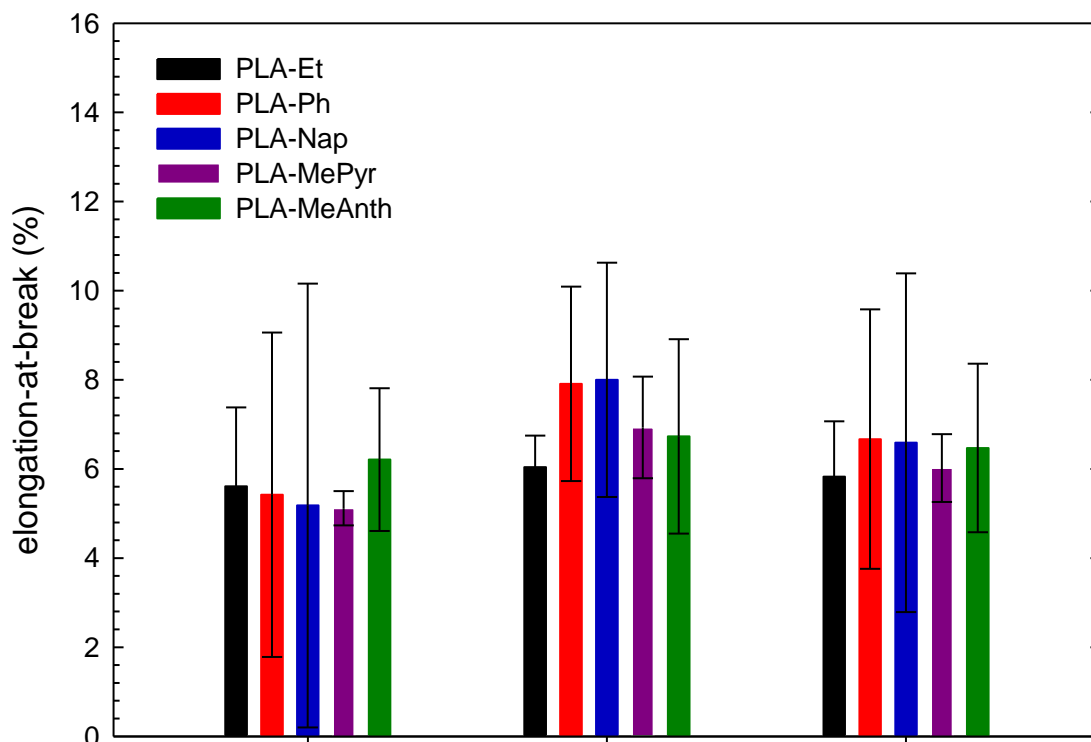
Figure 5.27 Elongation at break (%) for aryl-capped PLAs in this study. Low molecular weight polymers had M_n between 25 and 35 kg mol^{-1}. High molecular weight polymers had M_n between 110 and 130 kg mol^{-1}. "All" combines data for all polymers of the same family.

5.3 Conclusions

Immortal ROP was successful in generating aryl-capped PLAs with well-defined molecular weights and low molecular weight distributions. Aryl chain ends fidelity was confirmed using ^{1}H NMR, MALDI-ToF and UV-Vis spectroscopy. Thermal analysis of these PLAs show that end-group association *via* aromatic-aromatic π-π interactions are not strong enough to induce crystallization at room temperature. All polymers are amorphous, displaying similar degradation pathways. Rheological results presented give evidence that aggregation of the chain-ends manifest

their presence by an increase of viscosity at small frequencies in oscillatory shear due to an increase on the "apparent" molecular weight through chain association. A temperature and frequency dependence on the formation of these associated structures was shown as well as a dependence on the molecular weight of the polymer. There was no indication of a difference between the thermal and mechanical properties of the aryl-capped polymers compared to the native PLA-Et indicating that chain mobility is necessary when forming the aggregated structures within the polymer melt.

5.4 Experimental

General Methods. All the air and moisture sensitive manipulations were carried out in an MBraun glovebox or using standard Schlenk line techniques. A Bruker Avance 300 or 400 MHz spectrometer was used to record ^{1}H NMR spectra. ^{1}H NMR chemical shifts are given in ppm versus residual protons in CDCl$_3$ (δ 7.27). Molecular weights, hydrodynamic radii and intrinsic viscosities were determined by GPC-RI using an Agilent liquid chromatograph equipped with an Agilant 1200 series pump and autosampler, three Phenogel 5 μm Narrow Bore columns (4.6 × 300 mm with 500 Å, 10^3 Å and 10^4 Å pore size), a Wyatt Optilab differential refractometer, Wyatt tristar miniDAWN (laser light scattering detector) and a Wyatt ViscoStar viscometer. The column temperature was set at 40 °C. A flow rate of 0.5 mL/min was used and samples were dissolved in THF (*ca.* 4 mg/mL). The measurements were carried out at laser wavelength of 690 nm, at 25 °C. The data were processed using the Astra software provided by Wyatt Technology Corp. Molecular masses were determined using a Bruker Autoflex time-of-flight mass (ToF) spectrometer equipped with MALDI ion source. A differential scanning calorimeter (DSC) Q1000 (TA Instruments) was employed to measure the glass transition (T_g) and melting (T_m) temperatures of the synthesized

samples. Approximately 2-3 mg of the samples were weighed and sealed in an aluminium pan. The samples were heated at a rate of 10 °C/min from 25 to 275 °C, then held isothermally for 5 min to destroy any residual nuclei before cooling at 5 °C/min. The transition and melting temperatures were obtained from a second heating sequence, performed at 10 °C/min. Thermogravimetric analysis (TGA) traces were collected on a PerkinElmer Pyris 6 TGA with a nitrogen flow rate of 20 mL/min. Approximately 15 mg of the samples were weighed into a ceramic crucible. The samples were heated at a rate of 20 °C/min from 30 to 500 °C, and the total degradation and degradation onset temperatures were directly determined from the thermographs. Shear measurements were performed using the MCR 501 rheometer (Anton Paar), equipped with parallel plates, 8 mm in diameter. The dynamic linear viscoelastic measurements were carried out within the linear viscoelastic regime at temperatures in the range from 70 to 190 °C. The dynamic measurements were conducted in the range of 0.01-100 Hz at a strain of 2%. A gap of 0.5 mm was used to minimize edge effects and ensure a reasonable aspect ratio of plate radius and gap. The samples were melted at 150 °C for at least 3 min to eliminate the residual thermal histories. Uniaxial extensional measurements were performed using the SER-2 extensional fixture attached to an Anton Paar MCR 502 rheometer. Samples with diameters of 16−50 mm and thickness 0.4−0.6 mm were prepared by the same procedure used for shear samples. Individual polymer specimens were then cut to a width of 1.5−3.5 mm. Measurements were conducted at 90 °C at Hencky shear rates of 0.01, 0.1, 1.0, and 10 s^{-1}. Tensile tests were performed using COM-TEN 95 series tensile testing equipment (COM-TEN Industries) at ambient conditions. The films were compressed in a hot press at 160 °C for 15 min before being cooled. Tensile specimens were cut from compression-moulded films. Specimens were cut from the middle portion of the compressed films to avoid edge effects and edge imperfections. A gage length of 40 mm, crosshead speed of

186

25 mm/min and a 40 pound (178 N) capacity of load cell was used for testing all samples. To eliminate specimen slippage from the grips, double adhesive masking tape was used to wrap around the top and bottom portions of the sample. Five tests were run for each sample. The average modulus, tensile stress and elongation at break were calculated from the resultant stress-strain measurements and these are reported below along with standard deviations shown by the plotted error bars.

Materials. THF, toluene, and diethyl ether was taken from an IT Inc. solvent purification system with activated alumina columns and degassed before use. HPLC grade DCM was purchased from Fisher Chemicals and was dried over CaH_2, transferred under vacuum and degassed before use. Indium (III) trichloride, 1-naphthol, hydroxymethylanthracene and 1-pyrenemethlaldehyde, were purchased from Sigma-Aldrich and were used as received. Phenol was purchased from Fisher Chemicals and used as received. Racemic lactide was purchased from PURAC America Inc. and was recrystallized thrice from hot dried toluene prior to use. The catalyst $[(NNO)InCl]_2(\mu\text{-Cl})(\mu\text{-OEt})$ (**A**) can synthesized according to previously reported methods.[40]

Synthesis of hydroxymethylpyrene. 1-Pyrenemethlaldehyde (0.25 g, 0.001 mol) was stirred in 5 mL of ethanol at 80 °C. Sodium borohydride (0.22g, 0.006 mol) was added slowly. This off-white solution was then stirred at 80 °C for one hour. The reaction mixture was then cooled to room temperature and extracted three times with DCM, washed with brine and dried over magnesium sulphate. After concentration under vacuum the product was recrystallized from hot ethanol (0.18 g, 71%). %). ^{1}H NMR (400 MHz, CDCl$_3$): δ 8.42 (d, 1H, Pyr-*H*), 8.20 (m, 4H, Pyr-*H*), 8.06 (m 4H, Pyr-*H*), 5.44 (s, 2H, C*H*$_2$).

Representative immortal ring-opening polymerization. Inside a N_2 filled glovebox, appropriate amounts of *rac*-lactide were dissolved in DCM. Appropriate volumes of a standard solution of chain transfer agent in DCM was added and the solution stirred until homogenous. A standard solution of catalyst **A** in DCM (10 mg into 1 mL) was the added the reaction mixtures were stirred at room temperature for at least 18 hours before the solvent was evaporated. A small sample of crude polymer was taken for ^{1}H NMR spectroscopic analysis, the remaining polymer was dissolved in minimal DCM (~2 mL) and precipitated with cold methanol. The methanol was decanted off and the precipitation repeated twice. The isolated polymer was then dried under vacuum for at least 24 hours before further analysis.

Chapter 6: Synthesis and themorheological analysis of lignin-*graft*-poly(lactide) copolymers and their blends.

6.1 Introduction

After cellulose, lignin is the second most abundant polymer found in biomass, and is produced on the millions of tons scale as a by-product of the pulp and paper industry.[84,263] The surge of interest to increase the value of this cheap and renewable source of polymeric material[69,75,76] has prompted the use of lignin as a filler in a variety of green composites.[16,65] This chapter further explores potential modifications to poly(lactide) with the aim of improve processing properties by investigating lignin-*graft*-poly(lactide) copolymers and their blends; first, by assessing the various synthetic routes to these materials, followed by an analysis of their structure-property relationships.

6.1.1 Lignin-polymer materials

Unmodified lignin/polymer blends and their polymer properties have been a significant field of investigation.[81,82,85,193,264,265] In 2000 Alexy *et al.* prepared a family of blends comprised from low-density poly(ethylene) (LDPE) and up to 30 wt% of lignin. Mechanical tests of these materials showed a 55% decrease in tensile strength as lignin incorporation increased to 30 wt%.[83] A similar effect was noted by Doherty *et al.* who investigated poly(hydroxybutyrate) (PHB)/lignin blends. At lower than 30 wt%, lignin behaved as a plasticizer forming a single phase with PHB and increasing the fluidity of the materials under shears stress. At higher lignin loading, phase separation was observed which decreased the ability to dissipate applied stress leading to an increase in storage modulus, G', and complex viscosity, $|\eta^*|$.[86] Torkelson and co-workers

improved lignin dispersion in poly(ethylene) (PE) by using a solid-state shear pulveriser to synthesize their blends. These materials exhibited a greater elongation-at-break and tensile strength compared to previous lignin/PE blends.[266]

In general, lignin-polymer blends have shown greater thermal stability at high lignin loading, however the overall mechanical properties are often diminished or remain unchanged compared to neat PLA. This depreciation of composite properties has been attributed to poor stress transfer as a result of insufficient compatibilization between lignin and the polymer matrix.[65,75-77,263]

6.1.2 Lignin graft copolymers

Graft copolymerization is one technique to improve the dispersion of two immiscible polymers. Covalently bonding two polymers improves adhesion of the incompatible phases which can be confirmed by the presence of an intermediate glass transition temperature, T_g. Researchers have successfully grafted many synthetic[201,203,267-271] and bio-derived polymers to lignin.[198,272]

There are two major strategies to synthesize graft copolymers from lignin: grafting-*to* and grafting-*from.* In graft-to processes, discrete polymers are synthesized and are covalently bound to lignin in a second step, often utilizing the abundant hydroxyl functionality in the lignin structure (Scheme 6.1). Grafting-from requires the use of lignin (or modified lignin) as a macro-initiator for the polymerization of monomer to form the copolymer in one step (Scheme 6.2).

Scheme 6.1 Graft-to synthesis for lignin graft copolymers. Distinct polymers are synthesized and through a second step are covalently bound to lignin.
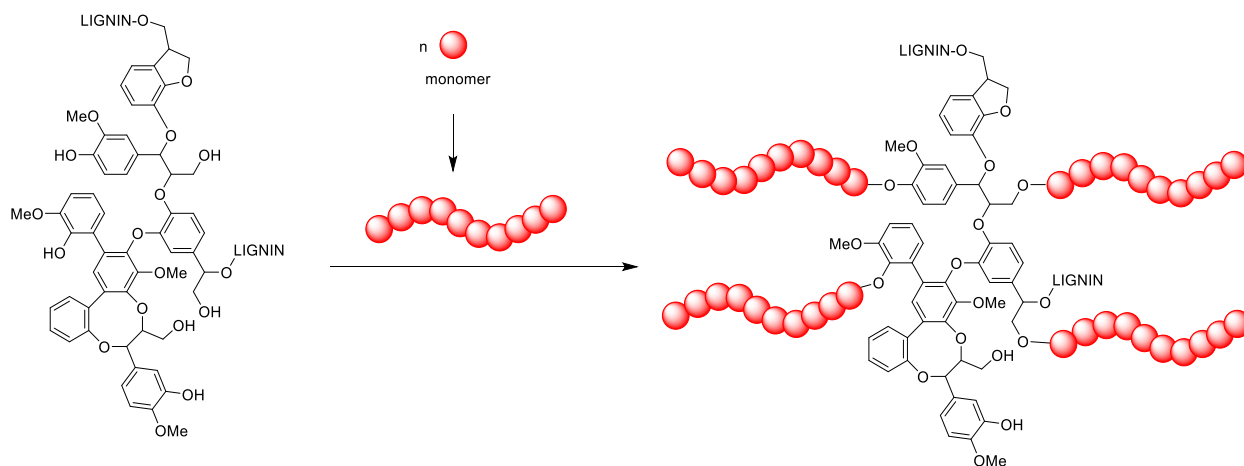
Scheme 6.2 Graft-from synthesis for lignin graft copolymers where lignin is used as a macro-initiator for polymerization.
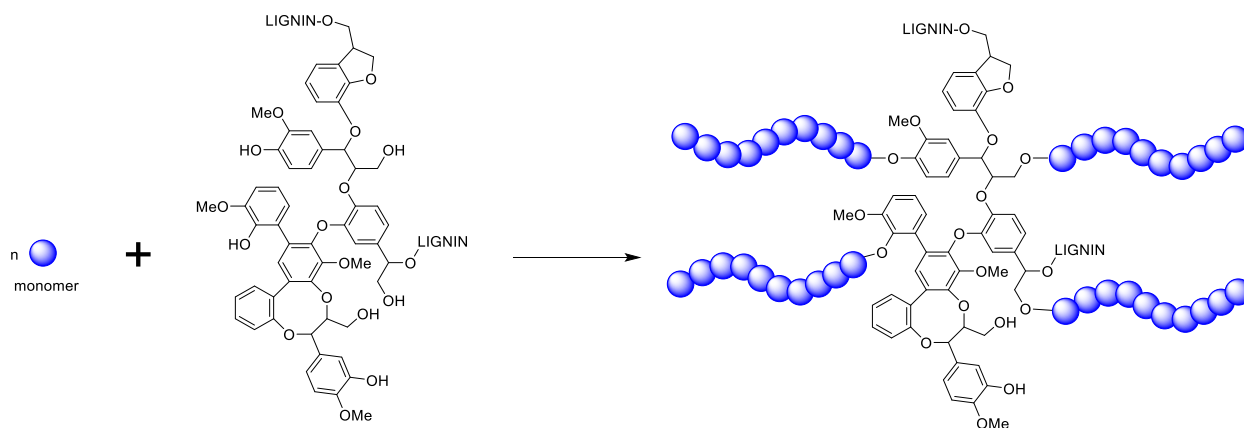
Using a grafting-to strategy to modify lignin with low molecular weight PLA, Park *et al.* showed increased dispersion of lignin within the PLA matrix. However, composites displayed diminished mechanical properties compared to neat PLA.[273] In a similar approach, Kim and co-workers synthesized lignin-*graft*-PLA using methanol-soluble lignin and low molecular weight chloro-terminated PLAs (PLA-Cl). The resulting graft copolymers displayed the highest molecular

weights reported for this type of polymer, ranging from 160 – 900 kg mol^{-1}. Analysis of the ash content after thermogravimetric experiments showed high incorporation of lignin and mechanical tests indicated that the grafts had increased tensile strength and modulus compared to the neat polymer.[274]

This method is advantageous as synthesis begins with well-defined polymers whose properties can be optimized before formation of copolymers. Grafting-to reactions, however, often require harsh reagents which could hinder the widespread industrial application. A more atom-economic synthesis has been adopted by many researchers in this field.

Grafting-from approaches were used by Kai and Loh who polymerized methyl methacrylate with ATRP-modified lignin, generating lignin-*graft*-PMMA copolymers. These were blended with poly(ε-caprolactone) (PCL) and electrospun into threads that displayed improved tensile strength and storage modulus compared to native polymers.[275]

In a leading report, Sattely and co-workers describe the synthesis of well-defined lignin-*graft*-PLA copolymers through organocatalyzed ROP of lactide. They show that the graft arm length could be controlled by pre-acetylation of lignin and by varying the lignin content in the reaction mixture.[194] Other organocatalytic systems were explored to synthesize PCL[267] and PLA-lignin[276] composites with UV-resistant and antioxidant properties. Most notable was a recent report by Liu *et al.* who recognized that the high concentration of hydroxy groups constrained the chain lengths of grafted PLA. Selectively alkylating 100% of phenolic hydroxy (OH) and 70% of carboxylic OH (COOH) groups allowed for the synthesis of graft copolymers with the longest reported PLA arm lengths (up to 28 kg mol^{-1}).[277]

In 2013, Averous and co-workers synthesized lignin-*graft*-PCL copolymers using a simple metal complex, SnOct$_2$. By controlling the CL/OH ratio a variety of copolymers with varying arm lengths were achieved. The copolymer with the shortest arm length contained 50 wt% lignin (M_n = 1.1 kg mol^{-1}).[203] High dispersities were observed in the copolymers ($Đ$ = 6.1 - 41.9) and were attributed to highly polydisperse lignin at the core of the grafts. The authors went on to investigate the grafts chain topology using differential scanning calorimetry (DSC) and melt rheological analyses. They concluded that the grafts were highly branched amorphous copolymers from the observed high T_g and G' values for copolymers with high lignin content.[270] Melt rheological analysis of the grafts highlighted the correlation between arm length and rheological response, whereby copolymers with shorter arms and high lignin content displayed elastomeric response and copolymers with longer arms showed thermoplastic response.[203] Yu and co-workers also reported structural analysis for a class of lignin-*graft*-poly(methyl methacrylate-*co*-butyl acrylate) (lignin-*graft*-P(MMA-*co*-BA)) composites. Although thermogravimetric analysis (TGA) results indicated that only 0.2 wt% of lignin had been incorporated into the copolymer, the lower slope for the graft copolymers in the Mark-Houwink plots ([η] vs. M_w) implied that the grafts were forming star-like shapes in solution. The grafts also displayed a lower zero-shear viscosity, η$_0$ (2.4 MPa.s vs. 3.4 MPa.s), supporting the solution viscosity results. Mechanical tests demonstrated a 2-fold enhancement in the elongation-at-break compared to the native copolymer.[267]

He *et al.* fabricated (PLA)–lignin composites by blending lignin-*graft*-(PCL-*co*-PLA)-*g*-poly(D-lactide) copolymer particles with commercial poly(L-lactide) (PLLA). Light scattering and small angle x-ray scattering (SAXS) studies showed enhanced dispersion of the graft copolymer in the PLLA matrix through stereo-complexation interactions between PLLA and PDLA units.

These composites exhibited a staggering 700% increase in their plastic deformation (toughness) as well as associated increases in tensile strength and modulus.[198]

Though there has been a large focus on this field in the recent years, and an exciting variety of bioderived and compostable materials have been synthesized, many of the recent reports of these lignin graft copolymers focus on determining mechanical response of composites [194,275] or on characterizing specific behaviour (*e.g.* wettability[269] or anti-oxidant behaviour).[198] There are many key questions which still need to be addressed, including the influence of unreacted lignin on polymer properties, accurate determination of lignin integration and the structure of graft copolymers. The following sections describe a systematic study of lignin-*graft*-PLA copolymers, their structure and viscoelastic properties. We focus on fundamental studies of the polymerization behaviour under various conditions by comparing metal catalyzed graft-from, organocatalyzed graft-from and graft-to synthetic routes to these copolymers; and fully characterize the polymers generated as star or cyclic PLAs. The lignin incorporation and melt rheology of the graft copolymers are explored, and finally, a variety of blends are prepared to further understand how the interaction between lignin and the matrix impact blend properties.

6.2 Results and discussion

6.2.1 Synthesis and characterization of lignin-*graft*-PLAs.

A series of lignin-*graft*-PLA copolymers were synthesized *via* a graft-from approach using the simple salt system reported by Hillmyer and Tolman.[120,121] *Rac*-lactide was stirred with 0.2 mol% $InCl_3$, 0.5 mol% NEt_3 and 1-35 mol% of lignin[††††] in toluene. The resulting mixture was

---

[††††] $[OH]_{lig}$ = 23 mmol g^{-1} determined *via* ^{31}P NMR spectroscopy (see section 6.4).

heated to 120 °C for 48 hours (Scheme 6.3). Graft copolymers were further purified to elucidate the way in which unreacted lignin influences polymer characterization and properties. Crude reaction mixtures were diluted with DCM and subjected to multiple centrifugation cycles. Polymer containing supernant was collected and the solvent removed under reduced pressure. Copolymers were isolated by precipitation from DCM with MeOH before drying under vacuum for 24 hours (Table 6.1). The polymers were characterized by ^{1}H, ^{1}H-^{1}H COSY (CDCl$_3$, 25 °C) and ^{31}P NMR spectroscopy (CHCl$_3$:pyridine, 25 °C) as well as by IR spectroscopy and gel permeation chromatography (GPC).

Scheme 6.3 Synthesis of lignin-*graft*-poly(lactide)s *via* ring-opening polymerization using InCl$_3$ and NEt$_3$.
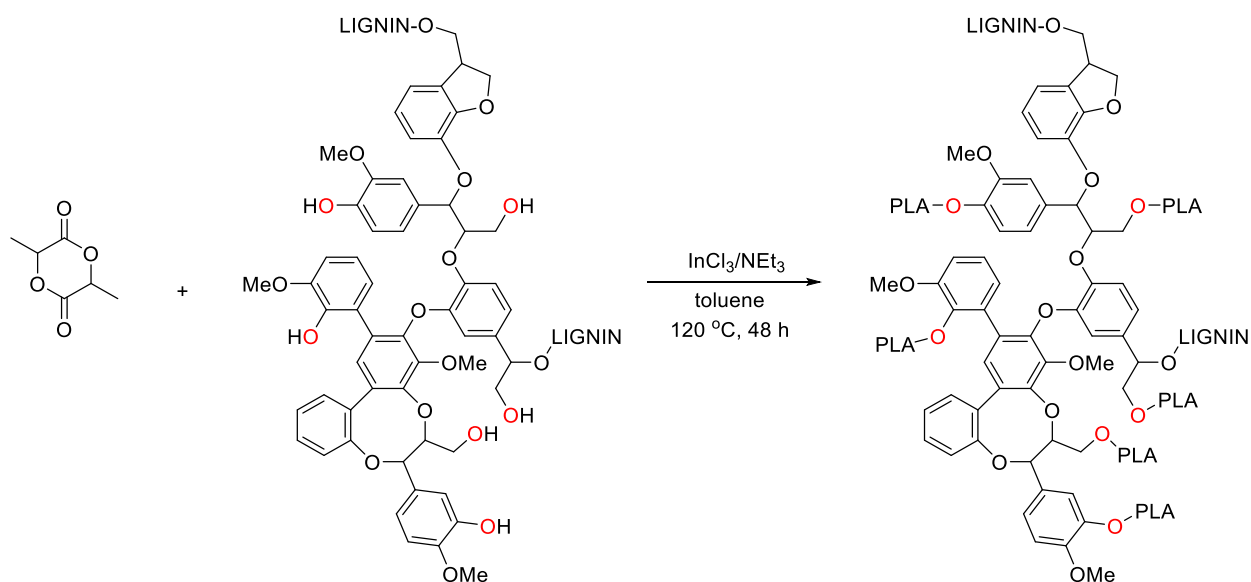
The formation of PLA is confirmed by the appearance of peaks in the ^{1}H NMR spectrum assigned to the methine proton (~5.20 ppm) and the methyl protons (~1.5 ppm) of the polymer (Figure 6.1). Peaks associated with the polymer chain end are distinguishable from the ^{1}H-^{1}H COSY NMR spectrum. A quartet at ~4.20 ppm was assigned to the methine proton closest to the

chain end, as this correlated to the signal for methyl protons of the polymer (Figure 6.2). Arm lengths were calculated from the ratio of polymer to chain-end peaks and we confirmed the literature supposition that changing the LA:OH ratio gives variable arm lengths (Figure 6.3).[194,203,277] It should be noted that the size of the PLA arms do not match the theoretical length calculated from the LA:OH ratio (Table 6.1), the observed arm lengths were longer than expected indicating incomplete activation of OH moieties on lignin (see Chapter 4). The PLA arms solubilize grafted lignin, as such more features belonging to lignin can be seen on the ^{1}H NMR spectra. Specifically, the broad aryl peaks around 7 ppm and the methoxy peaks at ~4 ppm (Figure 6.3).[194,267,268,273]

Table 6.1 Polymerization data from lignin-*graft*-poly(lactide)s formed *via* ring-opening polymerization using $InCl_3$ and NEt_3.

entry	mol% lignin-OH	[LA]:[OH]$_{lig}$[a]	conversion (%)[b]	arm length (g mol^{-1})[c]	$M_{n, GPC}$ (g mol^{-1})[d]	$M_{w, GPC}$ (g mol^{-1})[d]	$Đ$[d]
1	0	0	98	31500	115000	133000	1.15
2	5	7.7	96	7370	46600	56300	1.21
3	9	3.9	94	3390	444000	701500	1.66
4	21	1.5	90	1370	199000	450000	2.11
5	33	0.78	90	613	85200	110000	1.30

Reactions were carried out in toluene at 120 °C for 48 hours. [a][OH]$_{lig}$ = 23 mmol g^{-1} determined *via* ^{31}P NMR spectroscopy.[67,194] [b] Monomer conversions determined by ^{1}H NMR spectroscopy. [c] Calculated from integration of the polymer and chain end methine protons multiplied by the molecular weight of lactide. [d] Absolute molecular weights were determined by GPC−MALS−RI (gel permeation chromatography−multi-angle light scattering−refractive index) *via* Universal Calibration (THF 4 mg mL^{-1}, flow rate = 0.5 mL min^{-1}, dn/dc = 0.040 mL g^{-1} (calculated from 100% mass recovery, see appendix E)).
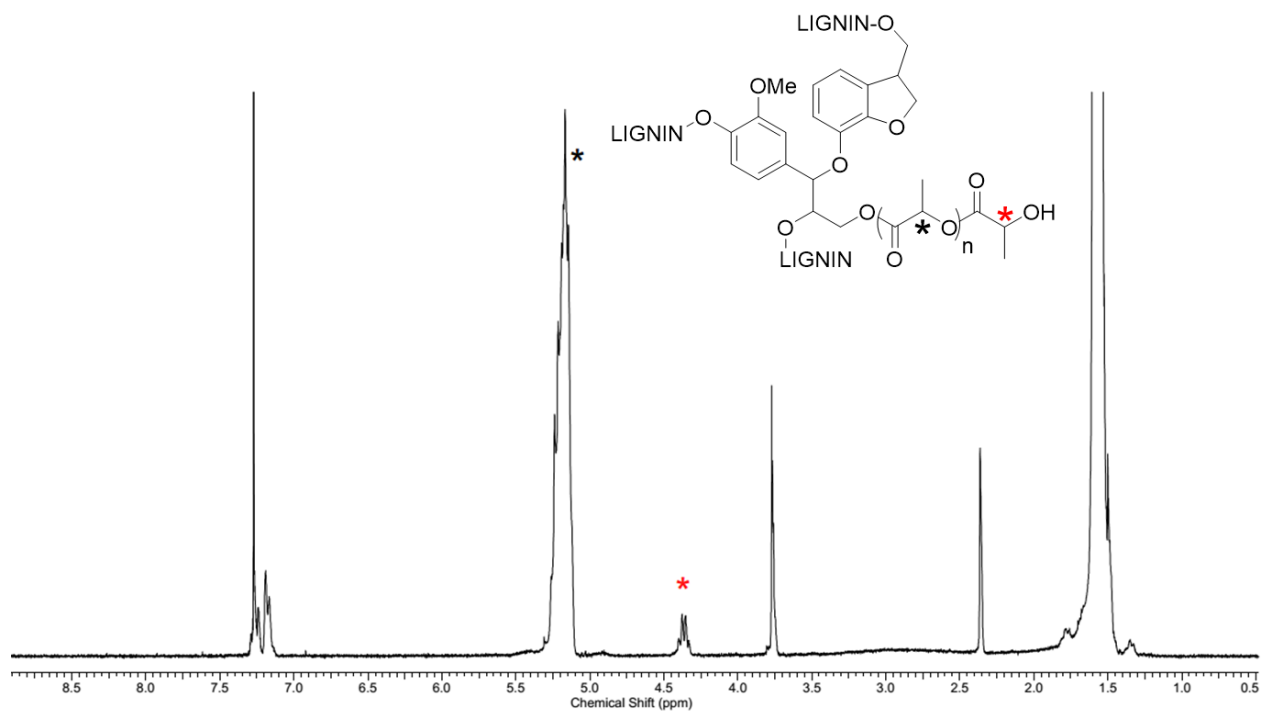
Figure 6.1 ^{1}H NMR spectrum (CDCl$_3$, 25 °C, 400 MHz) for polymer generated from metal-catalyzed system (arm length = 3.2 kg mol^{-1}).
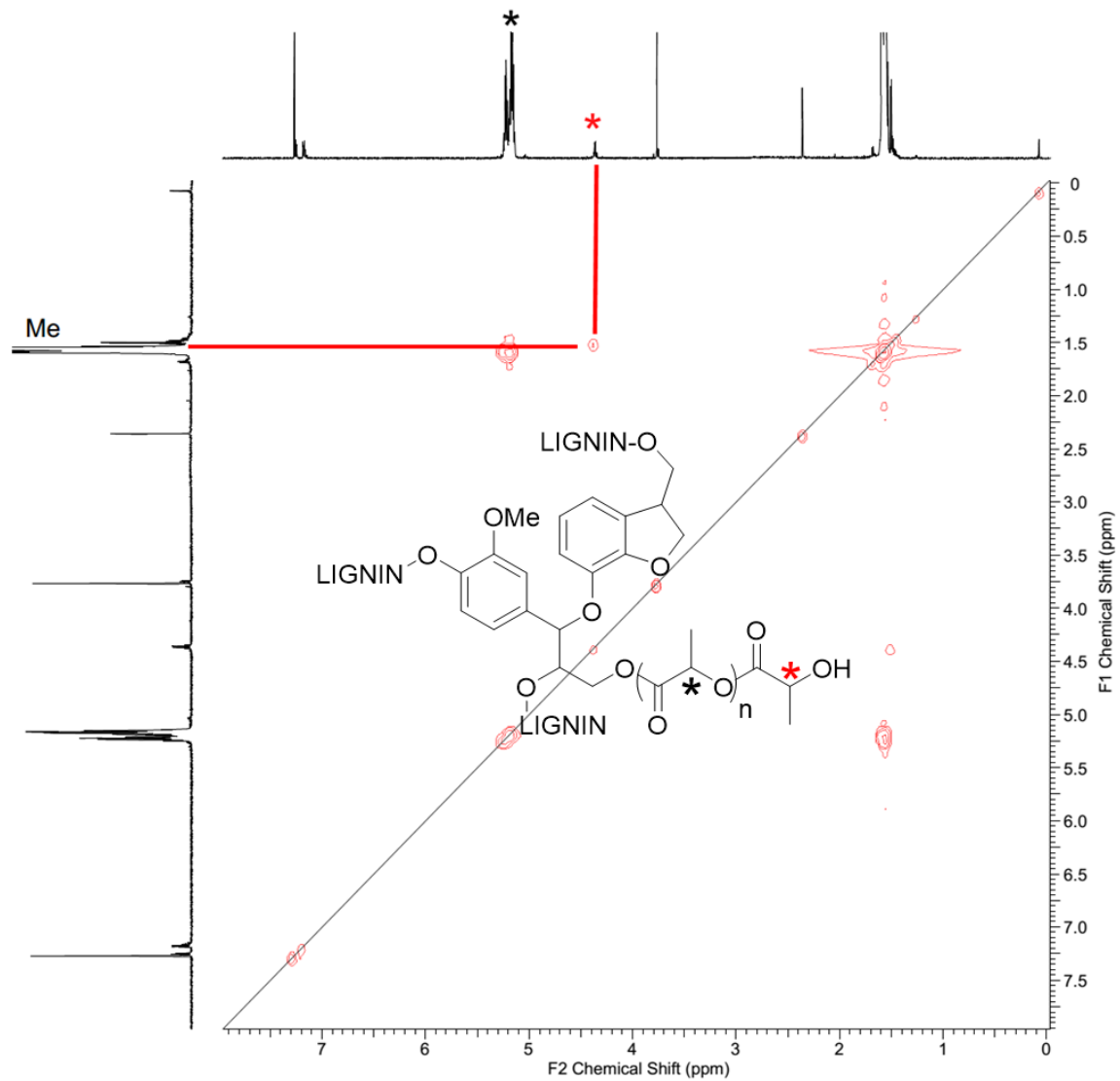
Figure 6.2 ^1H-^1H COSY NMR spectrum (CDCl$_3$, 25 °C, 600 MHz) for lignin-*graft*-PLA generated from metal-catalysed system (arm length = 13 kg mol^{-1}).

198
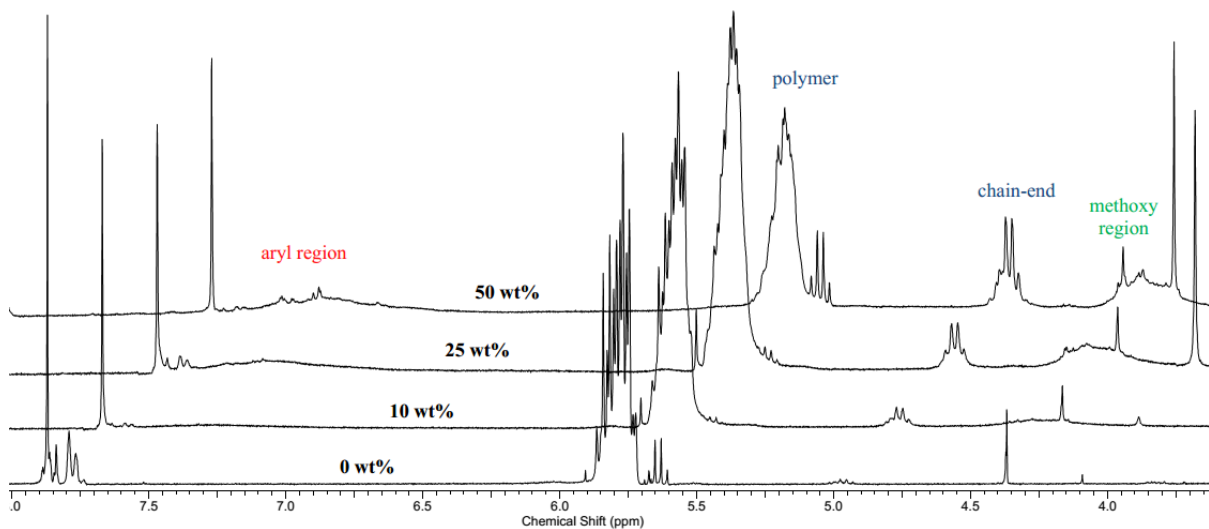
Figure 6.3 ^{1}H NMR spectra (CDCl$_3$, 25 °C, 400 MHz) for polymers with different wt% of lignin, generated from metal-catalyzed system.

^{31}P NMR spectroscopy was employed to further elucidate the types of hydroxy (OH) functionality present in the polymer.[67,194] Phosphitylation of the polymer produces various phosphate moieties with distinctive signals on the ^{31}P NMR spectrum (see section 1.1.2). Spectral analysis of polymer samples containing unreacted lignin showed the presence of alkyl and carboxylic OH groups indicative of the formation of PLA (Figure 6.4). A significant concentration of phenolic OH groups, likely from the unreacted lignin, is also observed. The ^{31}P NMR spectra obtained from graft copolymers is absent of phenolic moieties, implying little lignin is actually being incorporated into the copolymers (Figure 6.5).
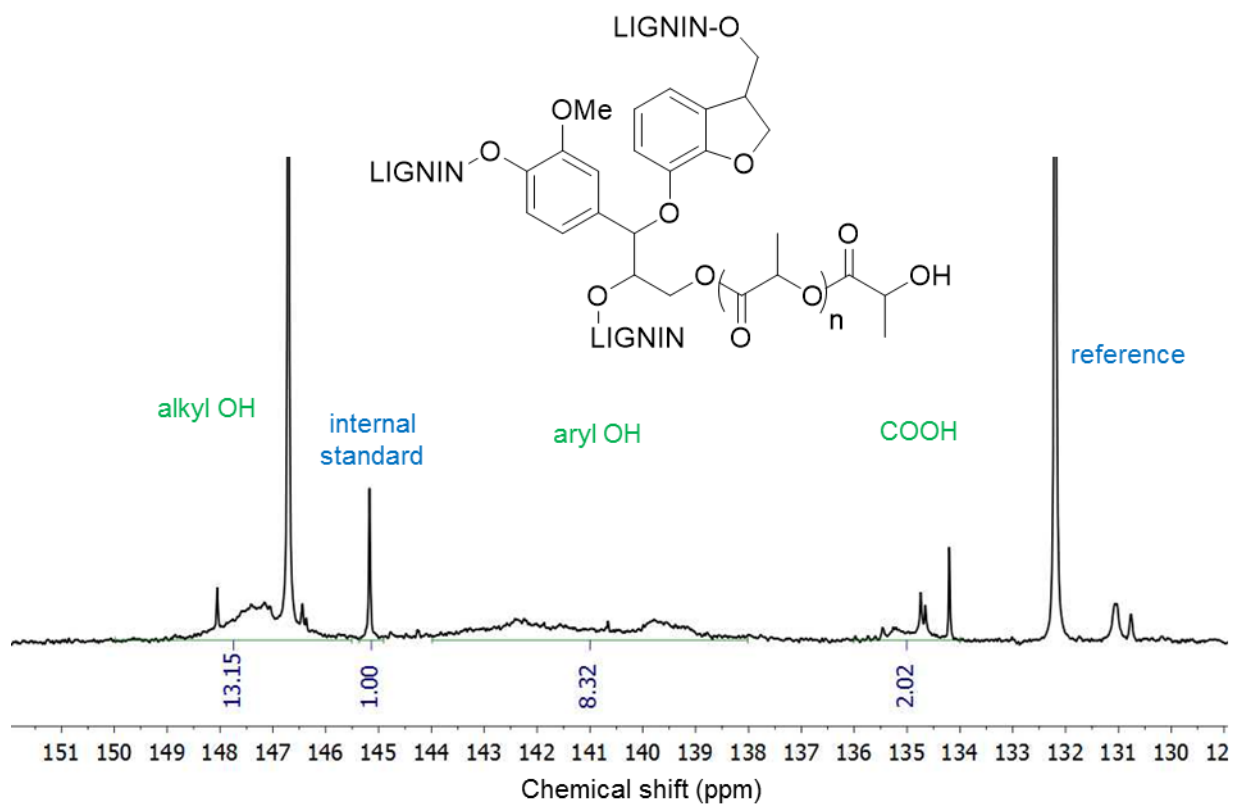
Figure 6.4 ^{31}P NMR spectrum (CHCl$_3$/pyridine, 25 °C, 121 MHz) of polymer containing unreacted lignin (arm length = 5 kg mol^{-1}). Derivatized by 2-chloro-4,4,5,5-tetramethyl-1,3,2-dioxaphospholane. Internal standard at 145.16 ppm (cyclohexanol).
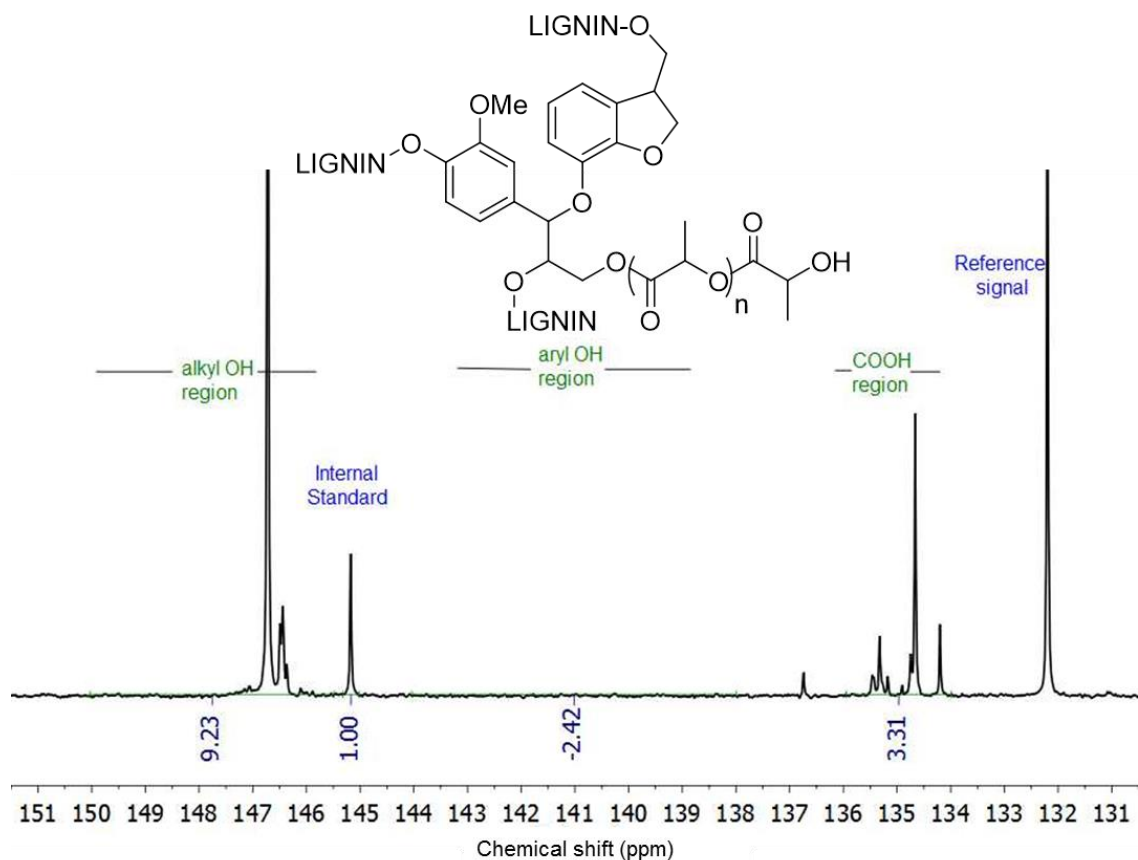
Figure 6.5 ^{31}P NMR spectrum (CHCl₃/pyridine, 25 °C, 121 MHz) of polymer generated from metal catalyzed system (arm length = 5 kg mol⁻¹). Derivatized by 2-chloro-4,4,5,5-tetramethyl-1,3,2-dioxaphospholane. Internal standard at 145.16 ppm (cyclohexanol).

Polymers were also characterized by GPC in THF at room temperature. Broadly, increasing the [LA]:[OH]$_{lig}$ gives polymers whose peaks elute at longer retention times indicating lower molecular weight polymers (Figure 6.6). Samples with low lignin loading (high [LA]:[OH]$_{lig}$) gave peaks with long low molecular weight tails, whereas polymerizations at higher lignin loading (low [LA]:[OH]$_{lig}$) gave peaks with high molecular weight shoulders. Similar multimodal peak shapes have been reported for both lignin-*graft*-PMMA[23,267] and lignin-*graft*-PCL[203] copolymers. The graft copolymers were also seen to elute out slower than linear chains of similar M_w indicative of polymers with different chain architectures (Figure 6.7).

201
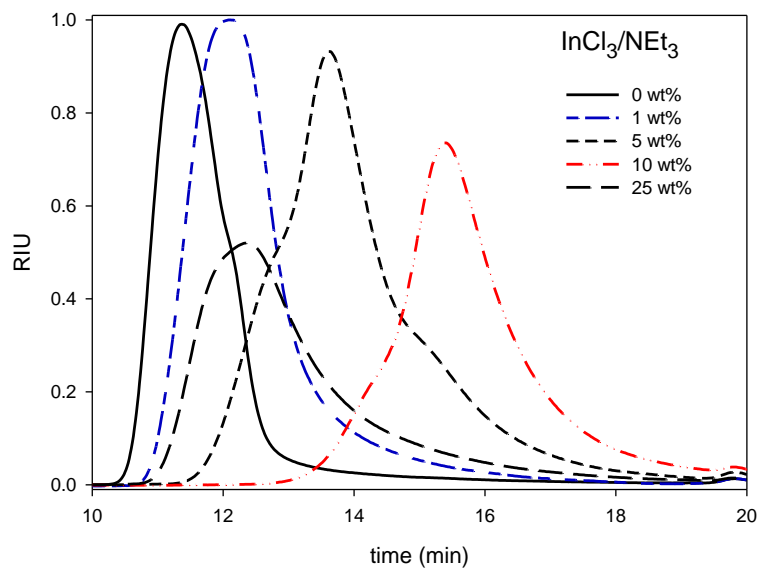
Figure 6.6 GPC traces for a series of lignin-*graft*-PLAs generated from the metal catalyzed graft-from approach.
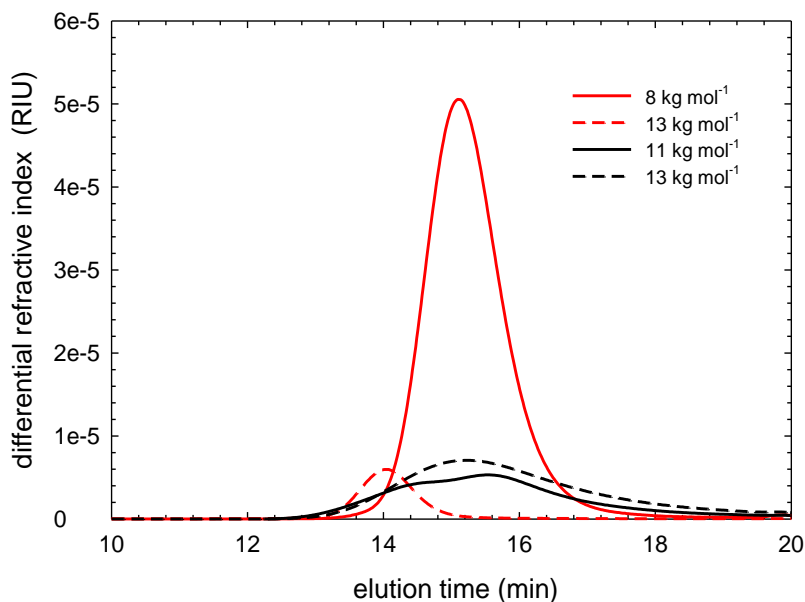
Figure 6.7 GPC traces for linear PLA (red lines) and lignin-*graft*-PLAs (black lines).

The IR spectra for lignin, PLA, and a representative lignin-*graft*-PLA copolymer are shown in Figure 6.8. The most diagnostic peak in lignin is the broad OH stretch at around 3300 cm^{-1} resulting from the large number of phenolic and alkyl OH groups within the lignin framework.

PLA has a characteristic carbonyl stretch at 1738 cm^{-1} as well as C-H stretches at 2959 and 3001 cm^{-1}. The spectrum for the graft copolymer shows a carbonyl peak at 1744 cm^{-1} which has shifted to higher wavenumber compared to native PLA. Averous and co-workers also observed this bathochromic shift which they attributed to hydrogen-bonding between PCL and phenolic moieties on lignin.[203] The small OH band at 3542 cm^{-1} implies the loss of the hydroxyl groups through the grafting process and gives further evidence that a low percentage of lignin is incorporated into the copolymer.
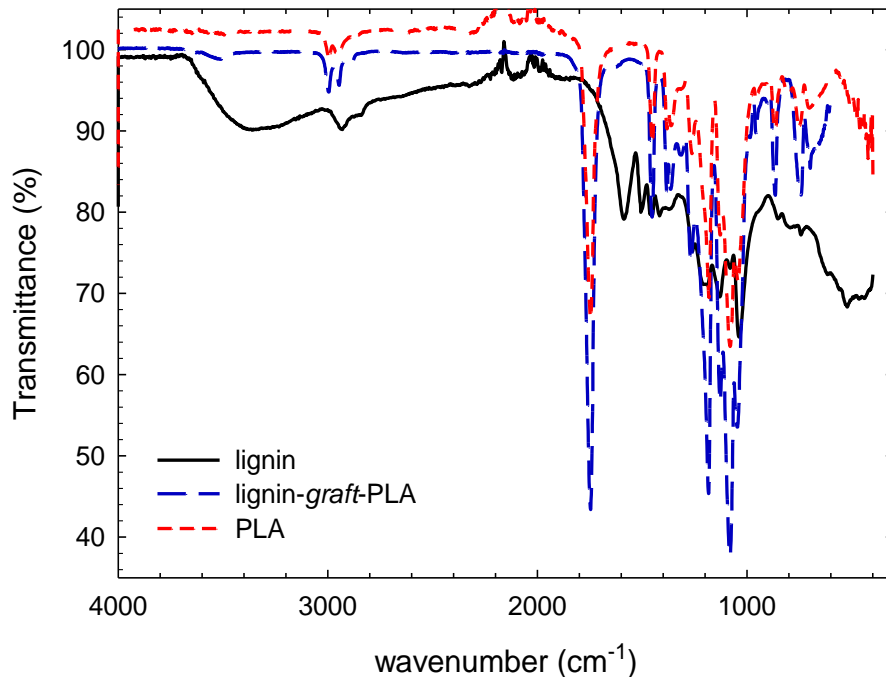
Figure 6.8 IR spectra of lignin-*graft*-PLA (long blue dashes), lignin (black line) and PLA (short red dashes).

6.2.2 Effect of lignin source on copolymerization.

A vast array of lignin is currently available on the market, each with different chemical compositions and the potential to generate polymers with different architectures (see section 1.1.2).

To determine the robustness of this system, a series of polymerizations were attempted with two commercially available lignins: Indulin AT kraft lignin (IAK) from ingevity™, and alkali kraft lignin (AK) from Sigma Aldrich.

Graft copolymerization was successful with both lignin sources (Table 6.2). Polymers generated with IAK lignin had higher dispersities implying higher lignin incorporation.[203] These polymers also followed the trends discussed above where changing the [LA]:[OH]$_{lig}$ ratio generated polymers with varying arm length (Table 6.2, entries 5 to 9). On the other hand, arm lengths for copolymers generated with AK seemed to have less dependence on [LA]:[OH]$_{lig}$ ratio, though this lignin source gave much longer arms then the IAK variant (Table 6.2, entries 3 vs. 9). These observations can be rationalized by inspecting the ^{31}P NMR spectra of the lignin after phosphitylation (Table 6.3). IAK has a higher concentration of hydroxy groups than AK suggesting there are more active sites from which PLA can grow, leading to higher lignin content and shorter PLA arms. The lower OH concentration in AK has the complimentary effect of giving longer polymer chains due to fewer reactive groups. This is an interesting observation, which indicates that these materials can be further optimized and modified by tailoring the specific lignin source.

Table 6.2 Polymerization data from lignin-*graft*-poly(lactide)s formed using two commercially available lignin sources.

entry	Lignin	mol% lignin-OH	[LA]:[OH]$_{lig}$ [a]	conversion (%)[b]	arm length (g mol^{-1}) [c]	$M_{n, GPC}$ (g mol^{-1})[d]	$M_{w, GPC}$ (g mol^{-1})[d]	$Đ$[d]
1	IAK[e]	5	7.7	96	7370	46600	56300	1.21
2	IAK	9	3.9	94	3390	444000	701500	1.66
3	IAK	21	1.5	90	1370	199000	450000	2.11
4	IAK	33	0.78	90	613	85200	110000	1.30
5	AK[f]	1	32	86	38200	74000	91200	1.26
6	AK	5	7.5	78	17700	52200	60400	1.16
7	AK	9	4.0	73	13900	9090	10100	1.12
8	AK	11	3.1	82	12700	30500	38500	1.28
9	AK	21	1.4	70	5900	32300	36300	1.11

Reactions were carried out using InCl$_3$/NEt$_3$ in toluene at 120 °C for 48 hours. [a][OH]$_{lig}$ in mmol g^{-1} determined *via* ^{31}P NMR spectroscopy.[67,194] [b] Monomer conversions determined by ^{1}H NMR spectroscopy. [c]Calculated from integration of the polymer and chain end methine protons multiplied by the molecular weight of lactide. [d] Absolute molecular weights were determined by triple detector GPC (gel permeation chromatography) *via* Universal Calibration (THF 4 mg mL^{-1}, flow rate = 0.5 mL min^{-1}, dn/dc = 0.040 mL g^{-1} (calculated from 100% mass recovery, see appendix E)). [e] IAK Indulin AT kraft lignin [f] AK = alkali kraft lignin.

Table 6.3 Hydroxy group content for Indulin AT kraft lignin (IAK) and alkali kraft lignin (AK).

Type of OH	Indulin AT kraft lignin (IAK)	alkali kraft lignin (AK)
alkyl OH (150 -146 ppm)[a]	7.5(0.9)	5.0(0.9)
phenolic OH (144 -138 ppm)[a]	14(1)	9.1(0.7)
COOH (136 - 134 ppm)[a]	1.5(2)	2.3(0.2)
Total OH[a]	23(3)	16(1)

Calculated from ^{31}P NMR spectra of 2-chloro-4,4,5,5-tetramethyl-1,3,2-dioxaphospholane derivatized lignin in CHCl$_3$/pyridine. Internal standard at 145.16 ppm (cyclohexanol). [a]Hydroxyl (OH) group content in units of mmol g^{-1}.

Polymerization was also attempted using lignin sludge obtained from an industrial source. Lignin with a final H$_2$O content of 3.8% was obtained after drying at high temperatures under vacuum (Figure 6.9). This lignin was successfully used as a macro-initiator for the ROP of lactide, showing the versatility of this catalyst system to form industrially relevant polymers.

Figure 6.9 Lignin sludge obtained from industrial sources was boiled at 140 °C for 4 h and further dried under high vacuum for 24 h. Gravimetric analysis showed 77% decrease in H_2O content with a final H_2O content of 3.8%.

6.2.3 Other synthetic routes to lignin-*graft*-PLAs.

A review of the literature does not reveal any reports of the chain architecture of lignin-*graft*-PLA copolymers. The literature also contains a variety of synthetic routes to these copolymers, each potentially producing materials with different chain topologies. It was thus of interest to generate more families of these copolymers and to characterize and compare their structures and properties.

Triazabicyclodecene (TBD) was used as an organocatalyst to produce a second family of copolymers using a graft-from approach.[194] A reaction flask was charged with PLA, TBD and 1-30 mol% of lignin (Scheme 6.4). The reaction mixtures were stirred at 130 °C for 3-4 hours before quenching with 5% acetic acid in DCM, precipitating from cold MeOH and drying under vacuum for 24 hours (Table 6.4).

The polymers generated from this reaction showed the expected arm-length dependence on [LA]:[OH]$_{lig}$ ratio, whereby at low lignin loading long arms were observed (Table 6.4, entry 2 vs. 5). All the polymers showed high dispersities, indicative of lignin incorporation.

Scheme 6.4 Synthesis of lignin-*graft*-poly(lactide)s *via* ring-opening polymerization using TBD.
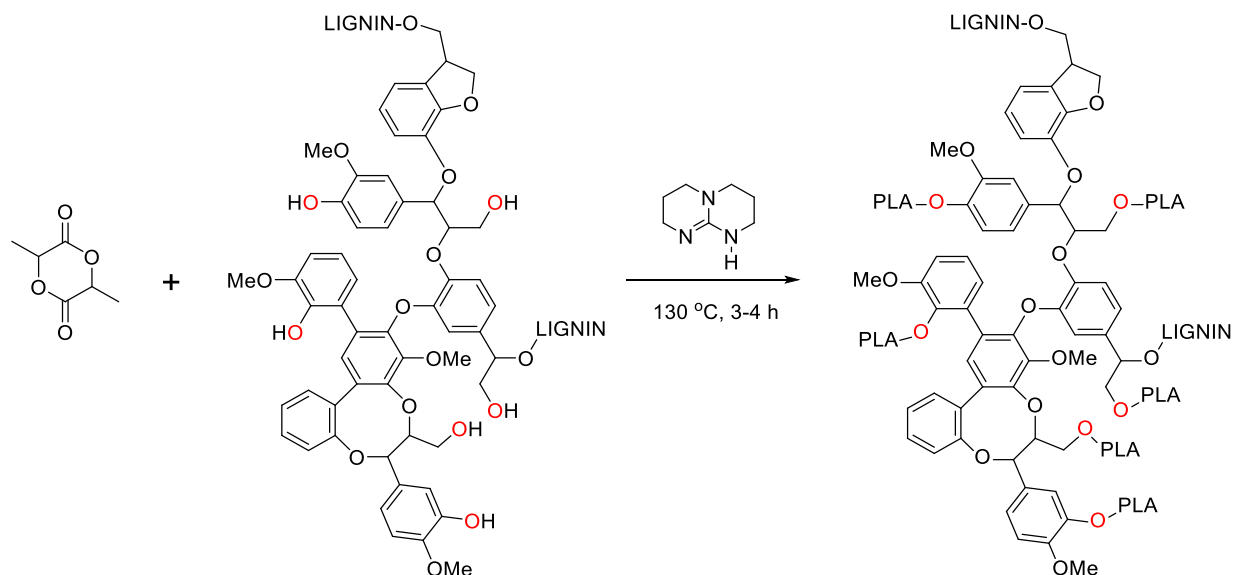
Table 6.4 Polymerization data from lignin-*graft*-poly(lactide)s formed *via* ring-opening polymerization using TBD.

entry	mol% lignin-OH	[LA]:[OH]$_{lig}$ [a]	conversion (%)[b]	arm length (g mol^{-1}) [c]	$M_{n, GPC}$ (g mol^{-1}) [d]	$M_{w, GPC}$ (g mol^{-1}) [d]	$Đ^d$
1	0	0.0	83	19300	38300	51700	1.32
2	4.8	7.6	97	31900	45700	55500	1.22
3	9.0	3.9	70	19500	87000	173000	2.33
4	20	1.5	74	8160	88100	131000	1.48
5	33	0.8	72	9390	70700	96600	1.33

Reactions were carried out in the melt at 130 °C for 3-4 h. [a] [OH]$_{lig}$ = 23 mmol g^{-1} determined *via* ^{31}P NMR spectroscopy.[67,194] [b] Monomer conversions determined by ^{1}H NMR spectroscopy. [c] Calculated from integration of the polymer and chain end methine protons multiplied by the molecular weight of lactide. [d] Absolute molecular weights were determined by triple detector GPC (gel permeation chromatography) *via* Universal Calibration (THF 4 mg mL^{-1}, flow rate = 0.5 mL min^{-1}, dn/dc = 0.040 mL g^{-1} (calculated from 100% mass recovery, see appendix E)).

A graft-to synthetic strategy, adapted from a 2016 report from Kim and co-workers,[274] was used to synthesize a final family of lignin-*graft*-PLA copolymers (Scheme 6.5). Linear PLAs were synthesized *via* the immortal ROP of lactide using dinuclear indium complex [(NNO)InCl]$_2$(μ-Cl)(μ-OEt) (**A**) and MeOH. These polymers were reacted with oxalyl chloride producing chloro-terminated PLA (PLA-Cl). Finally, lignin was stirred with K$_2$CO$_3$ in dry DMF for 30 minutes before a solution of PLA-Cl in DMF was added dropwise. The resulting mixture was heated to 50 °C and stirred for one hour before being cooled to room temperature and precipitated from DCM and MeOH (Table 6.5).

Table 6.5 Polymerization data from lignin-*graft*-poly(lactide)s formed *via* a graft-to strategy.

entry	PLA-Cl M_w (g mol^{-1})	[K$_2$CO$_3$]:[OH]$_{lig}$[a]	mol% lignin	arm length (g mol^{-1})[b]	$M_{n, GPC}$ (g mol^{-1})[c]	$M_{w, GPC}$ (g mol^{-1})[c]	$Đ$[c]
1	18200	0.158	19	7273	27700	30880	1.11
2	18200	1.01	21	6303	19300	21178	1.10
3	46400	0.988	20	290	30200	33400	1.11
4	46400	0.158	4	268	32700	113000	3.44
5	46400	0.158	8	2460	82500	483000	5.86
6	154000	<0.005	5	NA[d]	152000	184000	1.21
7	154000	<0.005	9	NA[d]	153000	172000	1.12
8	154000	0.095	5	NA[d]	99900	112000	1.19
9	32300	0.768	5	22300	116000	1100000	9.45

Grafting reactions were carried out in DMF, at 50 °C for 60 mins. [a][OH]$_{lig}$ in mmol g^{-1} determined *via* ^{31}P NMR spectroscopy.[67,194] [b] Calculated from integration of the polymer and chain end methine protons multiplied by the molecular weight of lactide. [c] Absolute molecular weights were determined by triple detector GPC (gel permeation chromatography) *via* Universal Calibration (THF 4 mg mL^{-1}, flow rate = 0.5 mL min^{-1}, dn/dc = 0.040 mL g^{-1} (calculated from 100% mass recovery, see appendix E)). [d]No chain end peaks were detected in the ^{1}H NMR spectra.

Scheme 6.5 Graft-to synthesis of lignin-*graft*-poly(lactide)s employed in this study.
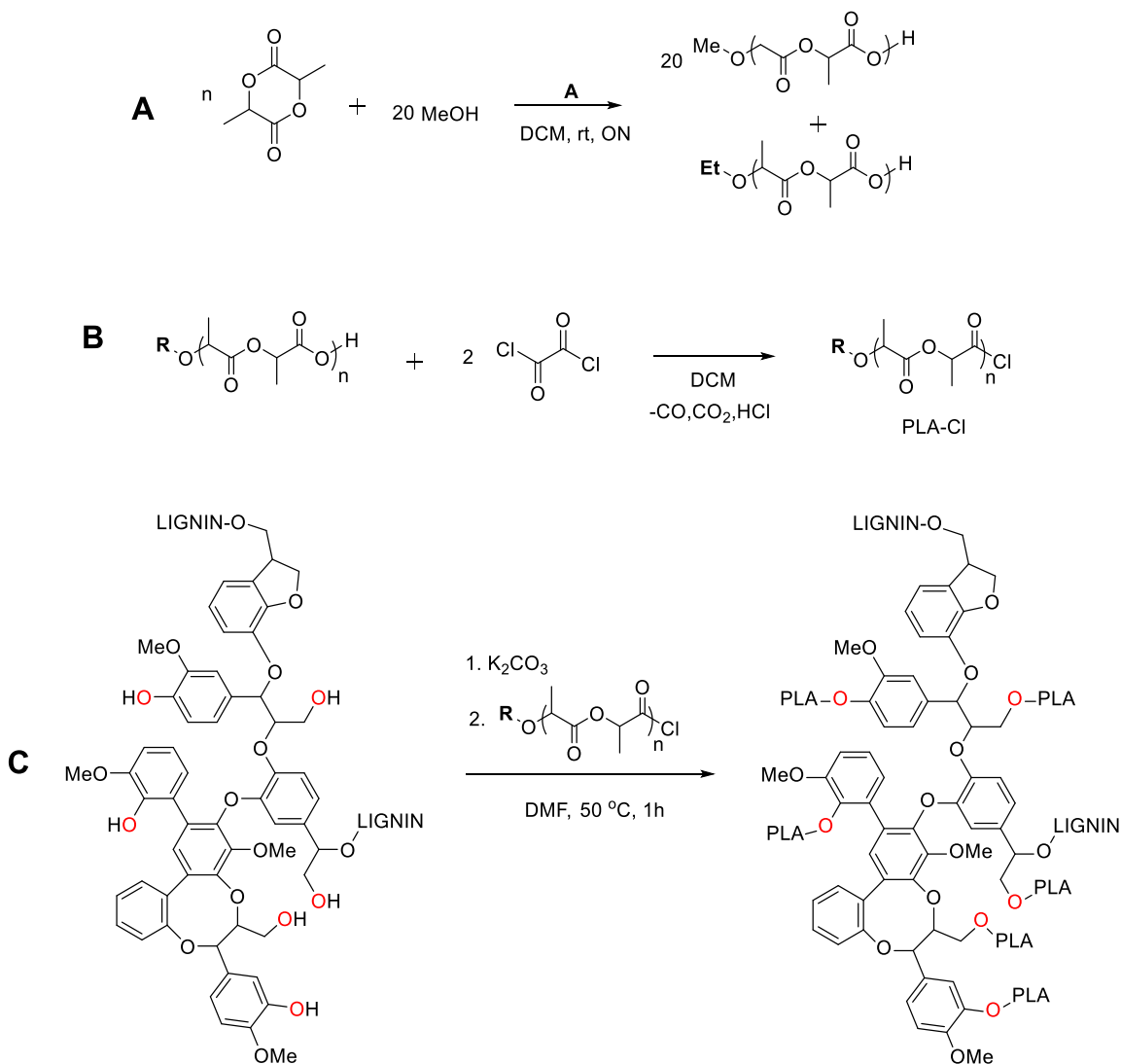
The K$_2$CO$_3$:lignin-OH ratio does not appear to have an impact on the formation of graft copolymers. Reactions with 10 fold difference in [K$_2$CO$_3$]:[OH]$_{lig}$ gave polymers with comparable arm lengths (Table 6.5, entries 1 and 2). The molecular weight of the pre-polymer (PLA-Cl) may have more of a significant impact on graft formation, where the ideal molecular weight of the pre-polymer is between 20 and 50 kg mol^{-1} (Table 6.5, entries 2 and 3). Graft copolymerization attempted with higher molecular weight pre-polymers do not show a significant difference in their

$M_{w,GPC}$ and display low dispersity values before and after reaction implying unsuccessful grafting to lignin (Table 6.5, entries 6 to 8). Graft-to reactions utilizing an excess K_2CO_3 compared to $[OH]_{lig}$, and 5-10 mol% lignin-OH gave the best lignin incorporation (Table 6.5, entries 4, 5 and 9).

6.2.4 Characterization and comparison of polymers generated from the three synthetic methodologies.

The three families of copolymer were further characterized by $^1H\{^1H\}$ NMR spectroscopy and thermogravimetric analysis (TGA). Chain tacticity for the various graft copolymers were determined by analysis of the $^1H\{^1H\}$ NMR spectra. Polymers generated from the $InCl_3/NEt_3$ system displayed diminished heterotactic enrichment than that reported for linear chains, $P_r = 0.67$ (Figure 6.10).[1,120] The organocatalyst gave polymers which were mostly atactic, $P_m = 0.56$ (Figure 6.11). The tacticity was determined for the two pre-polymers and final copolymer in the graft-to synthesis. There was no observed change in tacticity going from PLA to the graft copolymers, each being isotactically enriched with a P_m value of 0.60 (Figure 6.12). By tailoring the synthetic route, researchers may be able to access multiple chain microstructures giving more avenues to applications for these materials.
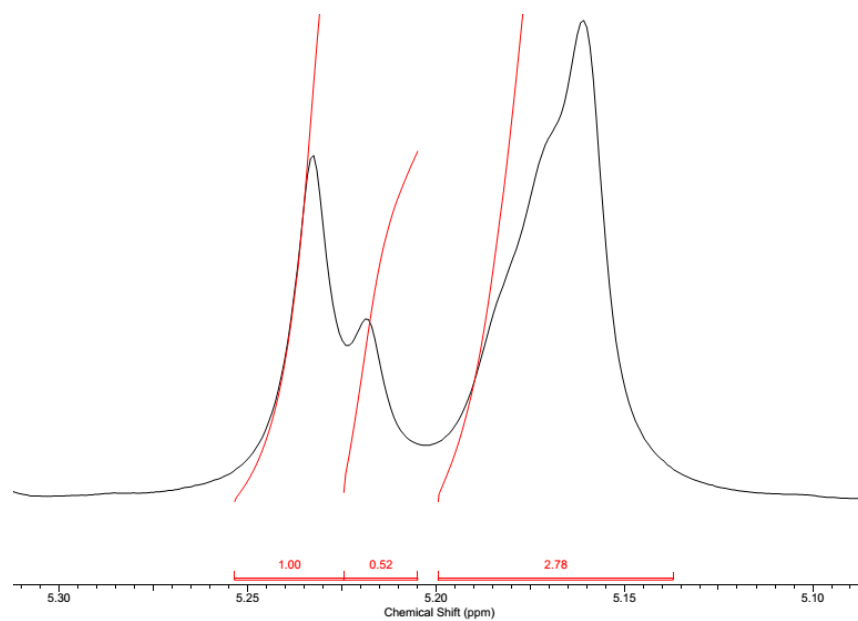
Figure 6.10 ^{1}H{^{1}H} NMR spectra (CDCl$_3$, 25 °C, 600 MHz) for polymer generated from the metal catalyst. $P_r = 0.67$.
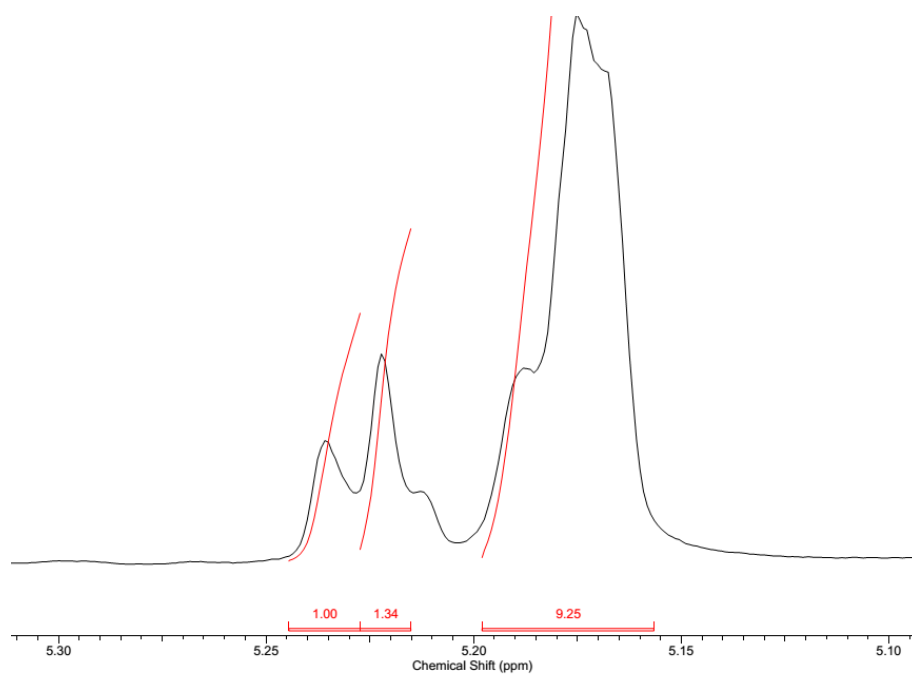
Figure 6.11 ^{1}H{^{1}H} NMR spectra (CDCl$_3$, 25 °C, 600 MHz) for polymer generated from the organocatalyst. $P_m = 0.56$.
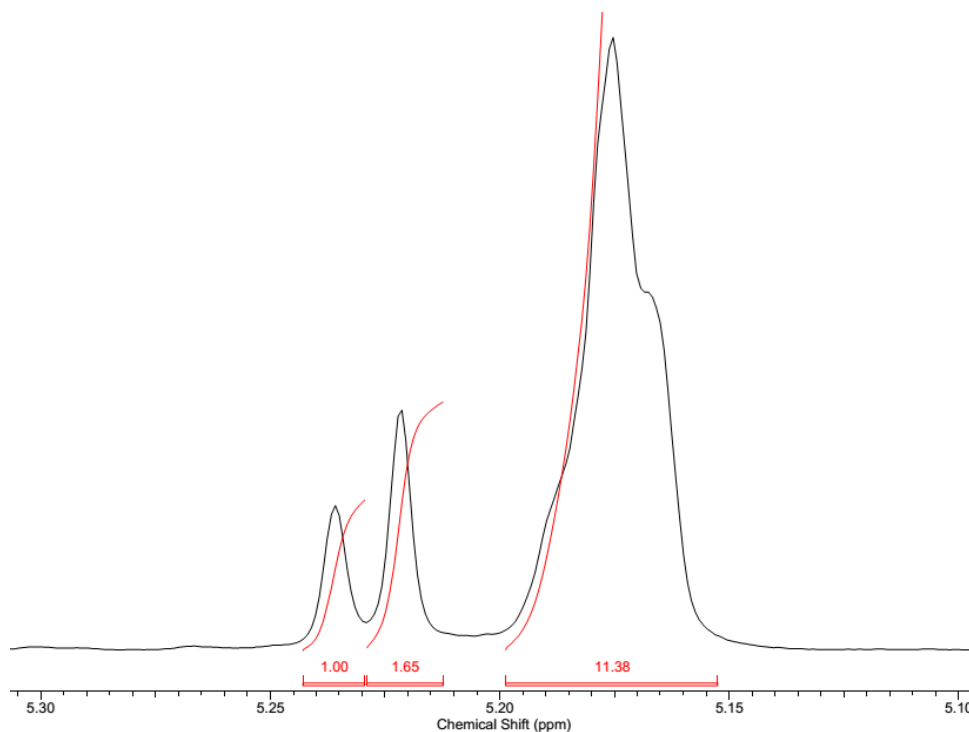
Figure 6.12 ^{1}H{^{1}H} NMR spectra (CDCl$_3$, 25 °C, 600 MHz) for polymer generated by a graft-to synthesis. $P_m = 0.60$.

Lignin has a distinctive thermal degradation profile but does not fully degrade below 500 °C. Thus, the lignin content of the copolymers can be estimated by examining the ash content after thermal exposure.[274] Polymers generated from the graft-to synthesis show the highest lignin incorporation, averaging 24% lignin content across the whole family. Of the graft-from catalysts, TBD gave the highest lignin incorporation albeit only averaging 2.9% (Figure 6.13). This was an expected difficulty using lignin as a macro-initiator for ROP of lactide. Chapter 4 described the living and immortal ROP of lactide using aryl initiators, which are less active than alkyl initiators due to lower nucleophilicity. ^{31}P NMR spectroscopic analysis of phosphorus-derivatized lignin shows an abundance of phenolic OH groups (Figure 6.14). The previous study of aryl initiators showed that not all the phenolic OH groups are likely to be activated and thus once a few have initiated polymerization, ring-opening is expected to occur more predominantly in those positions, giving copolymers with low lignin incorporation and fewer arms than expected. Alkylation[197] and

212

pre-acylation[194] have been used to improve polymer growth however extra steps in the synthesis reduce industrial feasibility of the materials.

TGA was performed on copolymer samples that had been purified from unreacted lignin and those which had not. Figure 6.15 clearly shows that the unreacted lignin erroneously shows higher lignin content in the copolymer, when actually a copolymer/lignin blend is being formed. The melt rheology of lignin-contaminated samples had higher storage moduli and complex viscosity compared to the pure copolymer indicating that lignin is acting as filler and further modifying the properties of the copolymer (Figure 6.16). Awareness of this contamination is important during preliminary studies of these materials as they have a strong impact on flow properties.
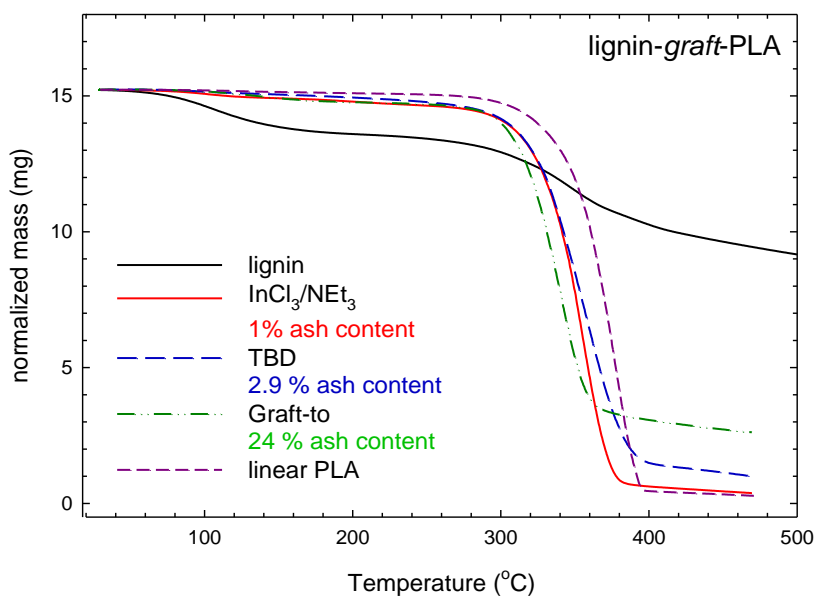
Figure 6.13 Thermogravimetric analysis traces for lignin-*graft*-PLA copolymers from the various synthetic routes, after removal of excess lignin.
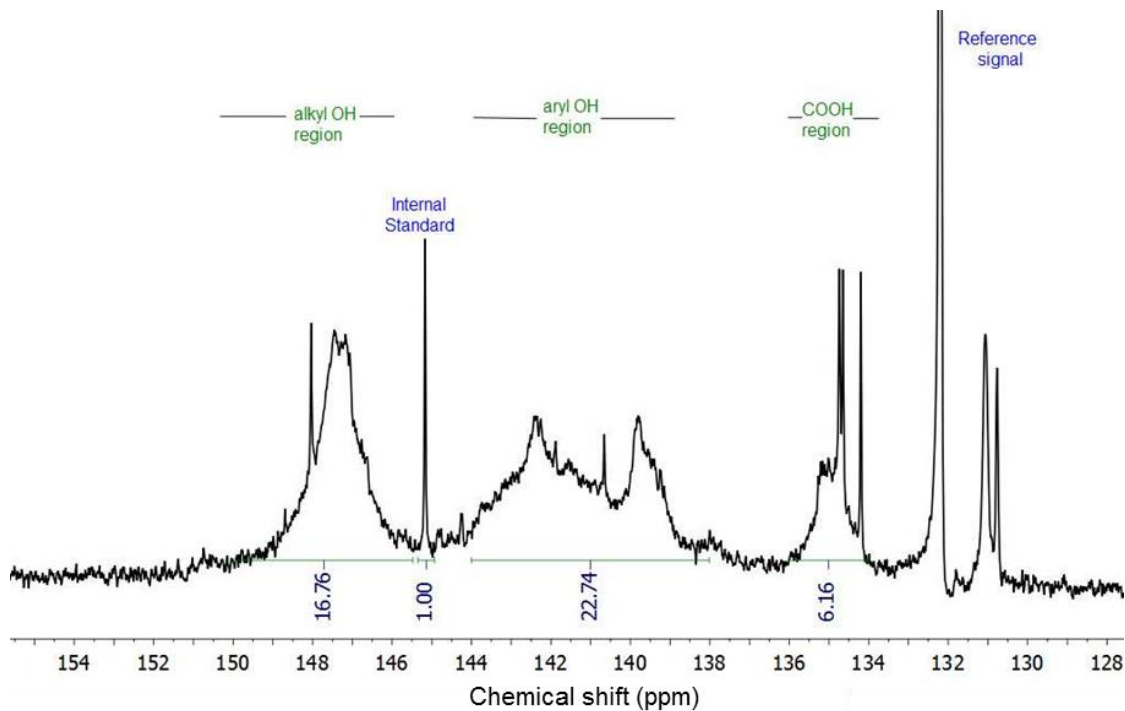
Figure 6.14 ^{31}P NMR spectrum (CHCl$_3$/pyridine, 25 °C, 121 MHz) of Indulin AT kraft lignin. Derivatized by 2-chloro-4,4,5,5-tetramethyl-1,3,2-dioxaphospholane. Internal standard at 145.16 ppm (cyclohexanol).
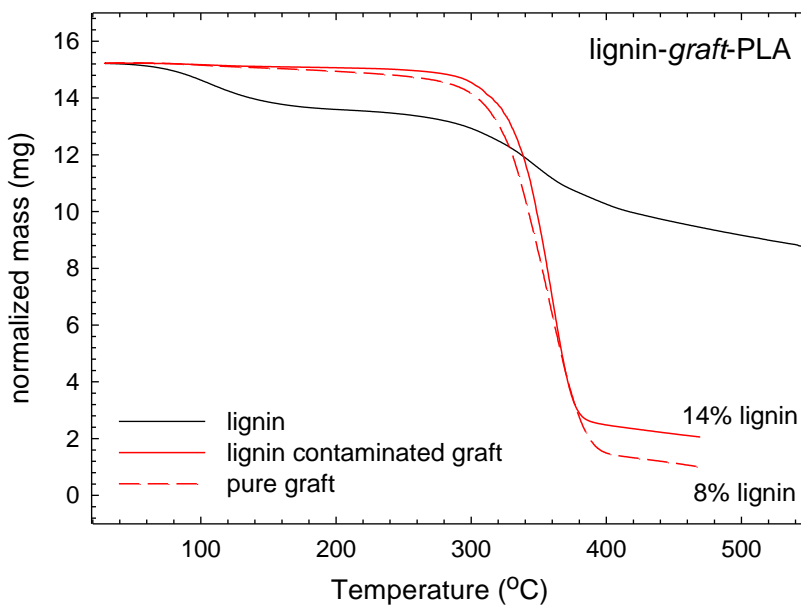
Figure 6.15 Thermogravimetric analysis traces for pure lignin-*graft*-PLA and that contaminated with lignin.
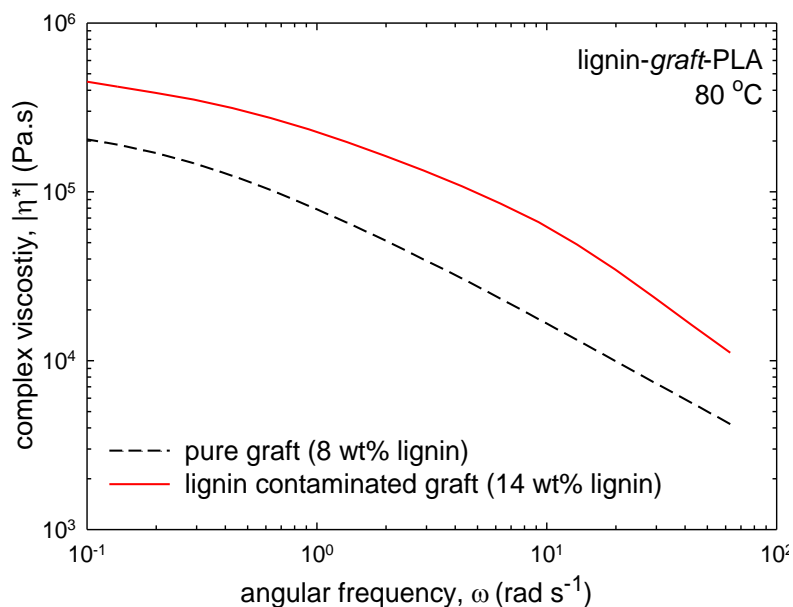
Figure 6.16 Complex viscosity, |η*| vs. angular frequency at 80 °C for pure lignin-*graft*-PLA copolymers and that lignin contaminated copolymers.

6.2.5 Determining lignin-*graft*-PLA copolymer topology.

Lignin graft copolymers have been reported to have different chain structures. Glasser[278] and Yu[267] both showed evidence for the formation of star-like copolymers, whereas Averous reported their lignin-*graft*-PCL polymers to be branched, forming 3-dimensional hydrogen-bonding networks at high lignin incorporation.[203] An overlooked aspect of these graft copolymerizations is that under normal conditions, both InCl$_3$/NEt$_3$ and TBD catalyst systems require an external alcohol additive to generate linear polymers in a controlled manner (usually benzyl alcohol (BnOH)).[120,121,279] Under alcohol-free conditions, analogous systems to those used in this study have been shown to form cyclic PLAs.[280-282] Graft-to synthesis can also generate cyclic polymers *via* the self-condensation of PLA-Cl pre-polymers under basic conditions (Scheme 6.6). As such, there are a variety of possible chain structures which could be present in the final polymer, impacting polymer properties. Thus, to determine the extent of cyclic-PLA formation during graft

215

copolymerization, lignin-free control reactions were performed under the same conditions as described in sections 6.2.1 and 6.2.3 above (Table 6.6).

Only PLAs generated from well-defined dinuclear indium complex, [(NNO)InCl]$_2$(μ-Cl)(μ-OEt) (**A**), showed good agreement between theoretical and GPC molecular weights (Table 6.6, entries 11 to 14). Polymers generated from lignin-free reactions with InCl$_3$/NEt$_3$ and TBD were less controlled, giving higher-than-expected molecular weights in most cases (Table 6.6, entries 1 to 10).

Scheme 6.6 Formation of cyclic-PLAs from the self-condensation of chloro-terminated PLA (PLA-Cl).
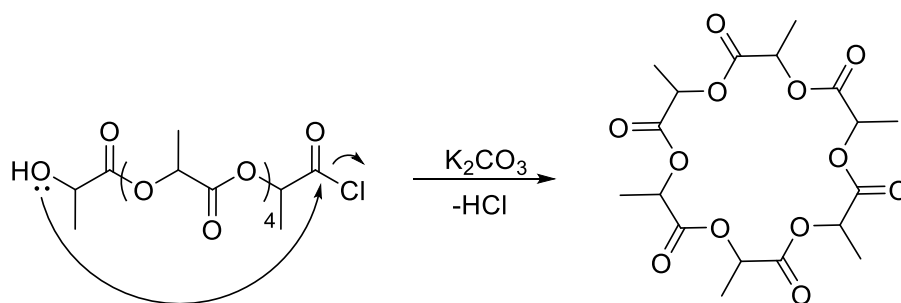
Table 6.6 Polymerization data for control reactions in the absence of lignin.

entry	catalyst	conversion (%)^a	$M_{n,theo}$ (g mol^{-1})^b	arm length (g mol^{-1})^c	$M_{n, GPC}$ (g mol^{-1})^d	$M_{w, GPC}$ (g mol^{-1})^d	$Đ^d$
1^e	InCl$_3$/NEt$_3$	93	118000	20300	44500	62600	1.41
2^e	InCl$_3$/NEt$_3$	91	111000	NA^h	27600	28900	1.05
3^e	InCl$_3$/NEt$_3$	96	76800	NA^h	166000	181000	1.09
4^e	InCl$_3$/NEt$_3$	98	81100	21500	71300	80600	1.13
5^e	InCl$_3$/NEt$_3$	97	77800	41600	158000	186000	1.18
6^f	TBD	88	13700	NA^h	56100	66500	1.19
7^f	TBD	76	13300	21400	31800	50200	1.58
8^f	TBD	83	12800	22900	35900	57400	1.60
9^f	TBD	89	12800	14400	19200	20300	1.05
10^g	TBD	84	12700	20600	59900	77600	1.29
11^g	A	99	7200	7300	10300	10400	1.01
12^g	A	98	14400	20000	18500	18600	1.01
13^g	A	99	37400	NA^h	46400	47000	1.01
14^g	A	98	73400	NA^h	81700	82800	1.01

^{a} Monomer conversions determined by ^{1}H NMR spectroscopy. ^{b} Calculated from: [LA]/[cat] × $M_{n,LA}$. ^{c} Calculated from integration of the polymer and chain end methine protons multiplied by the molecular weight of lactide. ^{d} Absolute molecular weights were determined by triple detector GPC (gel permeation chromatography) *via* Universal Calibration (THF 4 mg mL^{-1}, flow rate = 0.5 mL min^{-1}, dn/dc = 0.040 mL g^{-1} (calculated from 100% mass recovery, see appendix E)). ^{e} Reactions were carried out in toluene at 120 °C for 48 h. ^{f} Reactions were carried out in the melt at 130 °C for 3-4 h. ^{g} Reactions were carried out in the DCM at room temperature for 16 h. ^{h} No chain end peaks were detected in the ^{1}H NMR spectra.

Lower intrinsic viscosity compared to linear polymers has been observed in studies of both star-like[267,278,283] and cyclic[284,285] polymers. The intrinsic viscosities for PLAs generated from lignin-free control polymerizations are plotted in Figure 6.17. Polymers from control polymerizations with complex **A** are seen to fall on a trend line higher than that of all the polymers studied, and have a Mark-Houwink slope of 0.75, which is in agreement with reports of other linear PLAs.[1,163,166,286] Lignin-free reactions using InCl$_3$/NEt$_3$ and TBD, on the other hand, produce polymers which fall into second trend of PLAs with lower intrinsic viscosity than that of linear PLAs (Figure 6.17, red circles).
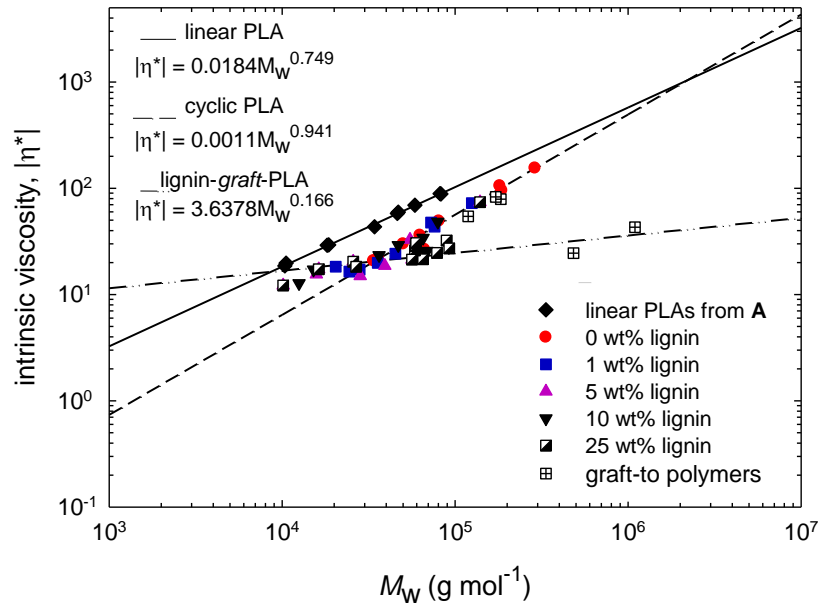
Figure 6.17 Intrinsic viscosity vs. molecular weight for products from the three synthetic strategies routes to the graft copolymers.

Figure 6.17 shows that there are two species generated from graft co-polymerization reactions, each with lower intrinsic viscosity than linear PLAs. These results support our hypothesis that the copolymerization conditions can generate PLAs with two possible structures, stars and cycles; however, their formation seems to be independent of synthetic route. Also evident from the data is that cyclic PLAs are preferentially generated at low lignin loading ($\leq$ 5wt% lignin) and star-graft copolymers generated at high lignin loading ($\geq$ 10 wt%). At intermediate lignin loading, it is assumed that an indistinguishable mixture of cyclic PLAs and star-graft copolymers are being generated. Analysis of the GPC traces for cyclic and star-graft copolymers show both species elute at longer times than linear polymers (Figure 6.18).
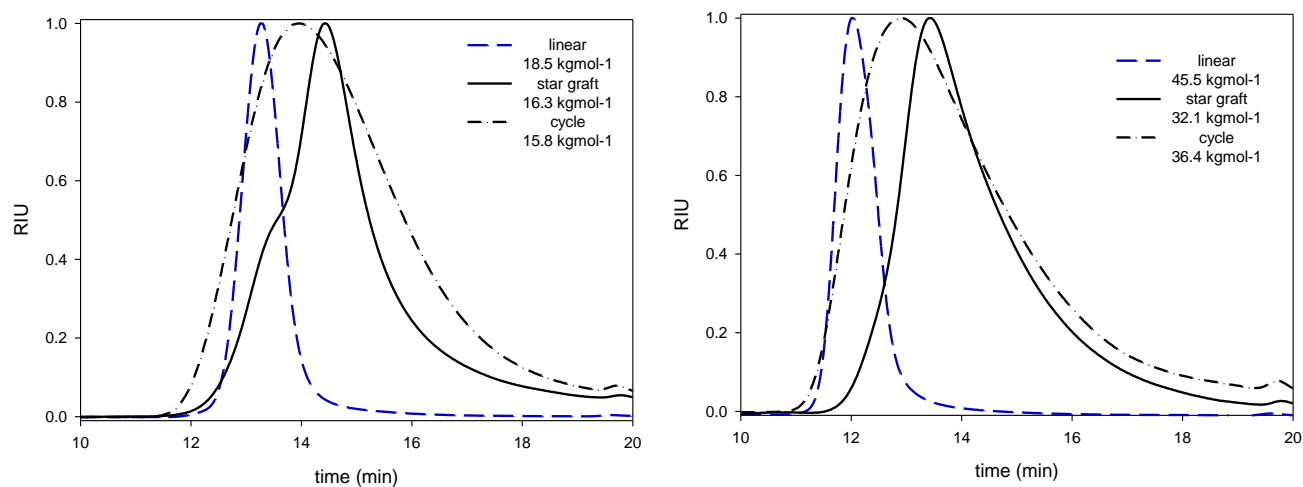
Figure 6.18 GPC traces (THF 4 mg mL^{-1}, flow rate = 0.5 mL min^{-1}, dn/dc = 0.040 mL g $^{-1}$) for linear PLA (blue dashed lines), cyclic PLA (black dash-dot line) and lignin-*graft*-PLAs (black line).

To further explore the cause of the variable chain structures, MALDI-ToF mass spectral analysis of the polymers generated from control polymerizations with no lignin was conducted (Figure 6.19). A major set of peaks separated by 72 mass units with no calculated chain end was observed, indicative of the formation of cyclic species. A second distribution is calculated to have a methoxy (OMe) chain end, possibly resulting from ring-opening of the cyclic polymers when precipitating with MeOH during work-up. Inspection of the MALDI-ToF spectra of polymers produced at low [OH]$_{lig}$ reveal similar cyclic polymer distributions (Figure 6.20). Whereas mass spectra for polymers generated from reactions using higher [OH]$_{lig}$, show distributions that correspond to polymers with chain-end masses of greater than 59 *m/z*, which could be from fragmentation of the lignin core during ionization (Figure 6.21). However, because lignin is highly disordered and fragments in a variety of ways,[287] it is difficult to determine exactly what these ends groups are. Regardless, these results allowed us to assign the three trends seen on the intrinsic viscosity vs. M_w plots to linear PLAs, cyclic PLAs and star-shaped lignin-*graft*-PLAs.
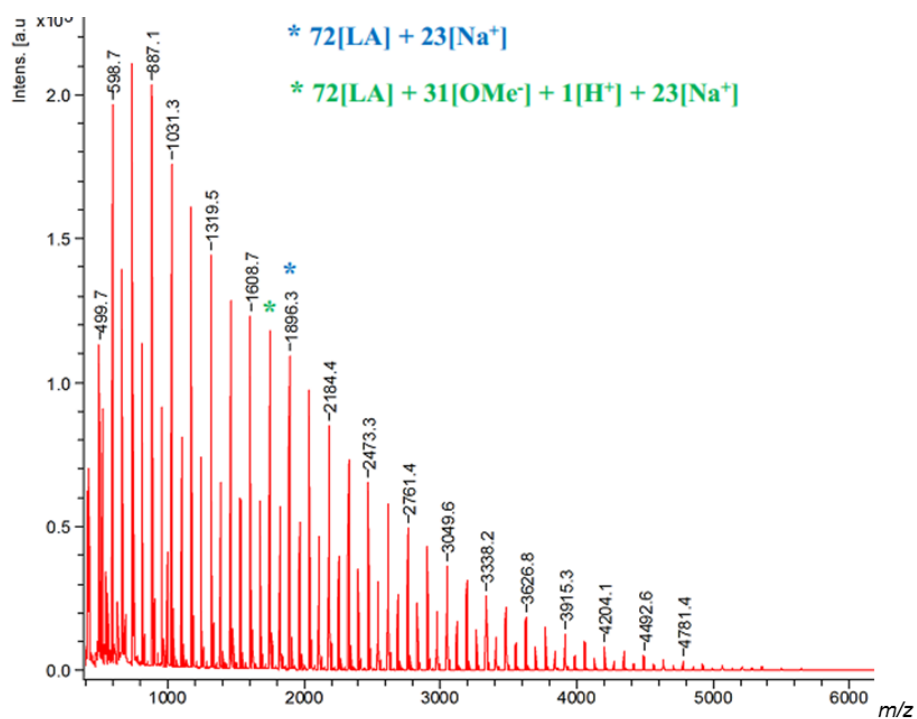
Figure 6.19 MALDI-ToF mass spectrum for polymer generated from a control graft-from polymerization ($M_{w,GPC}$ = 63 kg mol^{-1}).
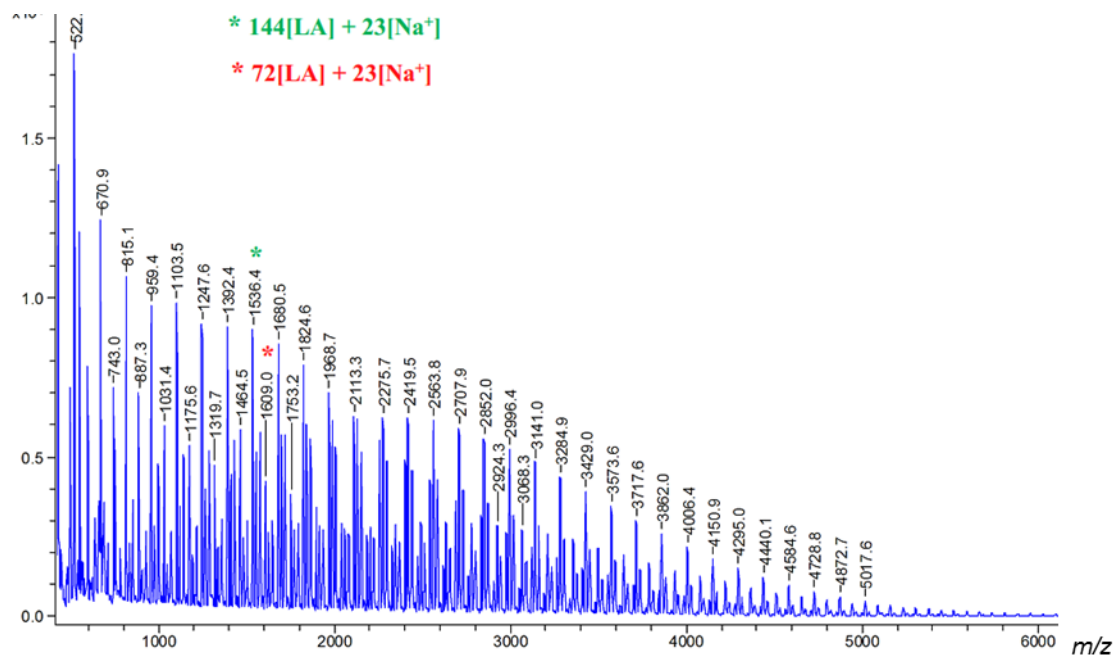
Figure 6.20 MALDI-ToF mass spectrum for polymer generated from a graft-from polymerization with low [OH]$_{lig}$ ($M_{w,GPC}$ = 78 kg mol^{-1}).
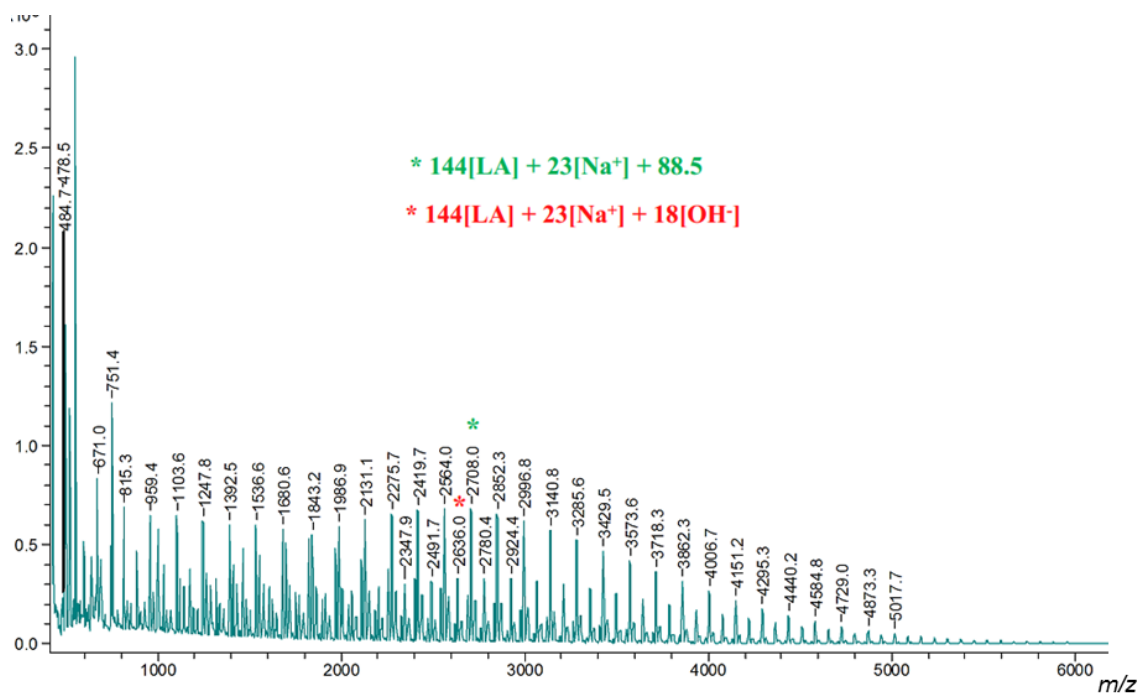
Figure 6.21 MALDI-ToF mass spectrum for polymer generated from a graft-from polymerization with high [OH]$_{lig}$ ($M_{w,GPC}$ = 18 kg mol^{-1}).

Rheological analysis was employed to compare of the linear viscoelastic moduli for the chain topologies generated from these reactions. Isothermal small-angle oscillatory shear (SAOS) experiments at angular frequencies from 0.01 to 100 Hz were conducted on the three classes of polymers. Both cyclic[285,288-290] and star[283,291] polymers have access to more relaxation modes giving them higher fluidity compared to linear polymers. The deviation of the slopes in the high frequency region of the complex viscosity, $|\eta^*|$ vs. angular frequency, ω plot indicate more shear thinning behaviour for the graft copolymers and cycles compared to linear PLA (Figure 6.22). Recent simulation studies by Li *et al.* showed that although both loops and the dense core of stars can retard deformation, cycles have a larger restoring force, making them less deformable than stars.[292] This effect is also seen in the melt rheology of PLA cycles and star grafts whereby cycles have a higher viscosity compared to the star-graft copolymers. Zero-shear viscosities for linear PLAs are one order of magnitude higher those that of cyclic polymers and two orders of magnitude higher than those of graft copolymers (Table 6.7 and Figure 6.23). These results are in line with a report by Schäler and Saawächter, which showed that cyclic PCLs have 2-fold lower viscosity than linear PCLs,[284] and Yu *et al.* who show a 5-fold decrease in the intrinsic viscosities of their lignin-*graft*-PMMA star copolymers.[267]
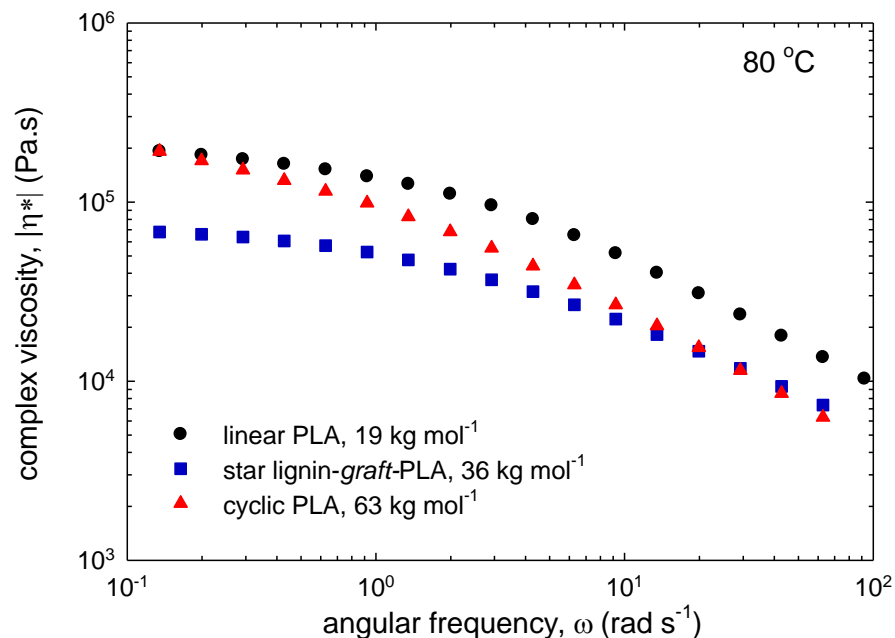
Figure 6.22 Complex viscosity, $|\eta^*|$ (Pa.s) vs. angular frequency, ω, (rad s^{-1}) for linear PLA ($M_w = 19$ kg mol^{-1}), star lignin-*graft*-PLA ($M_w = 36$ kg mol^{-1}) and cyclic PLA ($M_w = 63$ kg mol^{-1}).
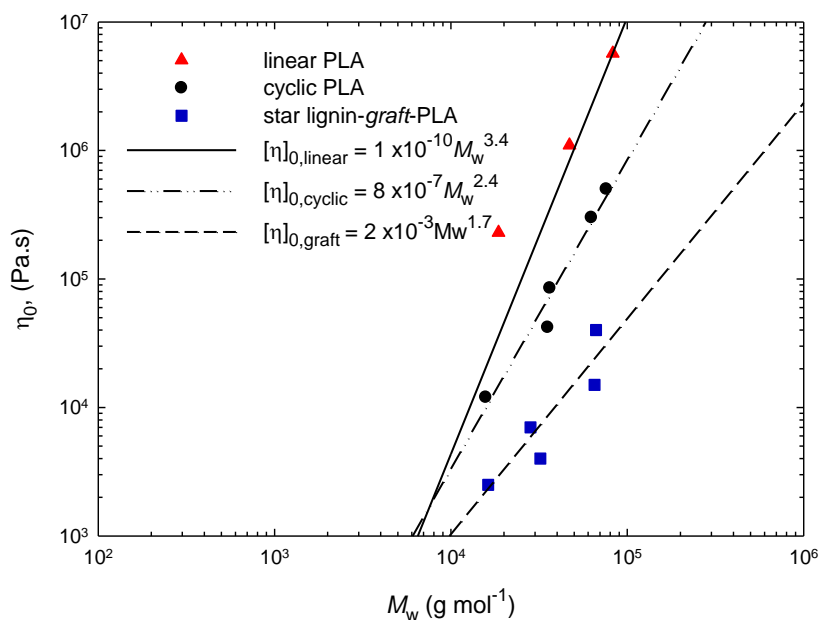
Figure 6.23 Zero-shear viscosity, η_0 vs. weight-averaged molecular weight, M_w, for linear PLAs (red triangles), cyclic PLAs (black circles) and star lignin-*graft*-PLA copolymers (blue squares**).**

Table 6.7 Polymerization data for linear PLA, cyclic PLA and star lignin-*graft*-PLAs used in rheological analyses.

entry	type	catalyst	lignin	mol% lignin-OH	ash content [a]	arm length (g mol^{-1})[b]	$M_{w, \text{ GPC}}$ (g mol^{-1}) [c]	Đ [c]	η_0 (× 10^5 Pa.s)[d]
1[e]	linear	**A**	--	--	--	20000	18600	1.01	2.3
2[e]	linear	**A**	--	--	--	NA[h]	47000	1.01	11
3[e]	linear	**A**	--	--	--	NA[h]	82800	1.01	57
4[f]	cyclic	InCl$_3$/NEt$_3$	--	0	0.9	20300	62600	1.41	3.0
5[g]	cyclic	TBD	--	0	0.6	26900	35400	1.32	0.42
6[f]	cyclic	InCl$_3$/NEt$_3$	AK	1	1.4	15200	76000	1.44	5.0
7[g]	cyclic	TBD	AK	5	2.3	19500	15800	1.26	0.12
8[g]	cyclic	TBD	AK	9	1.8	27300	36400	1.68	0.85
9[f]	star graft	InCl$_3$/NEt$_3$	AK	4	2.7	17300	16300	1.13	0.025
10[g]	star graft	TBD	IAK	5	4.7	20300	28300	1.46	0.70
11[g]	star graft	InCl$_3$/NEt$_3$	AK	13	5.5	1750	32200	1.17	0.040
12[g]	star graft	TBD	IAK	26	3.0	6270	65200	1.30	0.15

[a] Ash content calculated from mass of residue after thermal treatment to 450 °C. [b] Calculated from integration of the polymer and chain end methine protons multiplied by the molecular weight of lactide. [c] Absolute molecular weights were determined by triple detection GPC (gel permeation chromatography) *via* Universal Calibration (THF 4 mg mL^{-1}, flow rate = 0.5 mL min^{-1}, dn/dc = 0.040 mL g^{-1}). [d] Zero-shear viscosities obtained from the limits of master curves generated from isothermal frequency sweeps. [e] Reactions were carried out in the DCM at room temperature for 16 h. [f] Reactions were carried out in toluene at 120 °C for 48 h. [g] Reactions were carried out in the melt at 130 °C for 3-4 h.. [h] No chain end peaks were detected in the ^{1}H NMR spectra.

The results in this section confirm that the three polymerization methods do in fact generate both cyclic polymers and star-like graft copolymers. The different chain topologies can be determined from GPC analysis. The GPC traces of star grafts show that they seem to have high molecular weight shoulders which could be linear contaminates and cyclic PLAs have very broad traces with long tails. It is possible that the cycles could also be contaminated with linear chains (Figure 6.24). Polymerizations with little to no lignin loading generate cyclic PLAs. Under these conditions, the combined effect of low OH concentration, inactive phenolic moieties and added

base leads to the self-polymerization of lactide to form cyclic polymers.[281,282] The proposed mechanism for the formation of these cyclic PLAs is shown in Scheme 6.7 below. In the metal-catalyzed synthesis, $InCl_3$ activates the monomer to nucleophilic attack by the base additive which performs the initial ring opening event. This generates a zwitterion, which at low [OH], can go on to ring-open more lactide monomers. On the other hand, at higher lignin loading, there are enough OH groups present for transesterification to occur giving lignin-*graft*-PLAs which can go on to propagate ring-opening.
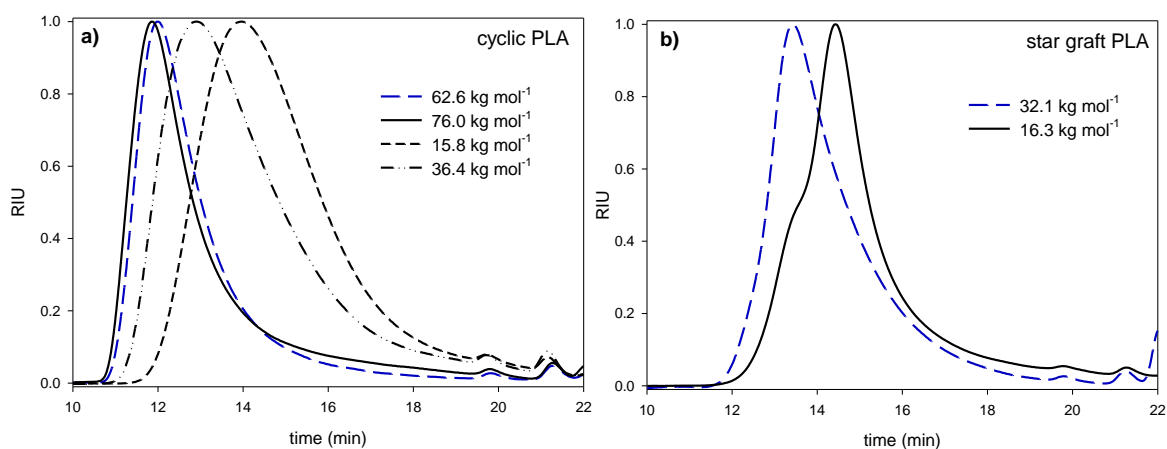
Figure 6.24. GPC traces for a) cyclic PLAs and b) star graft copolymers generated in this study.

Scheme 6.7 Proposed mechanism for the formation of cyclic PLAs in the absence lignin.[282]
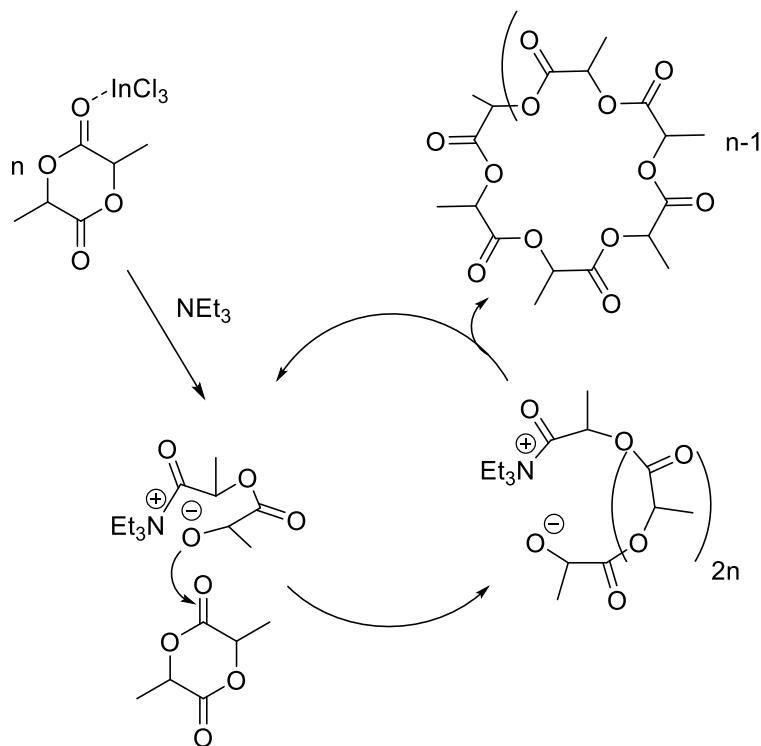
6.2.6 Rheological analysis of lignin-*graft*-poly(lactide)s.

Having confirmed the formation of various chain structures, further SAOS experiments were conducted on the cyclic and star-like graft copolymers. An 8-mm parallel plate rotational rheometer was used at a constant strain amplitude of 2% over frequencies ranging from 0.01 to 100 Hz. The time-temperature superposition principle was applied to isothermal experiments in the temperature range of 50-110 °C generating master curves of linear viscoelastic (LVE) moduli, G' and G", as well as the complex viscosity at the reference temperature of 80 °C.
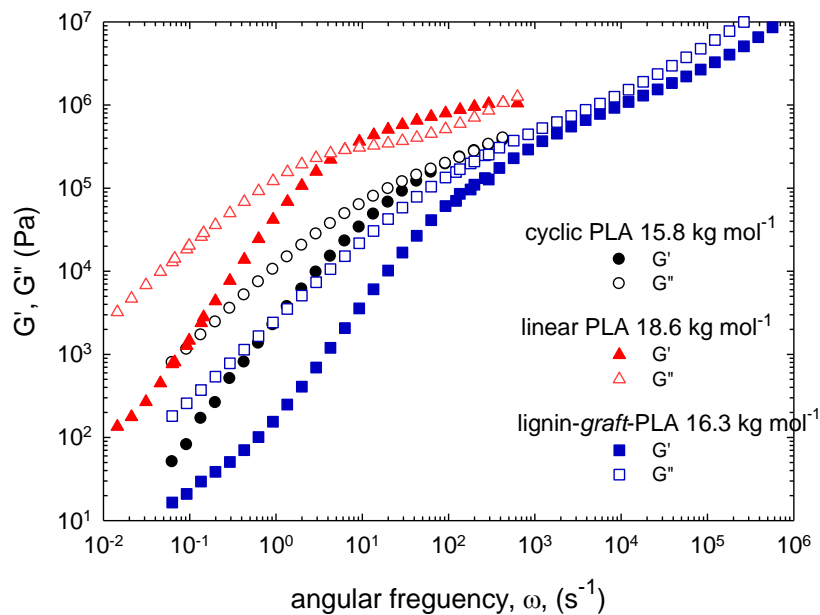
Figure 6.25. Viscoelastic moduli (G'-filled symbols, G"-open symbols) vs. angular frequency, ω (Pa.s) for linear PLA (red triangles, Table 6.7, entry 1), cyclic PLAs (black circles, Table 6.7, entry 7) and star lignin-*graft*-PLA copolymers (blue squares, Table 6.7, entry 9).
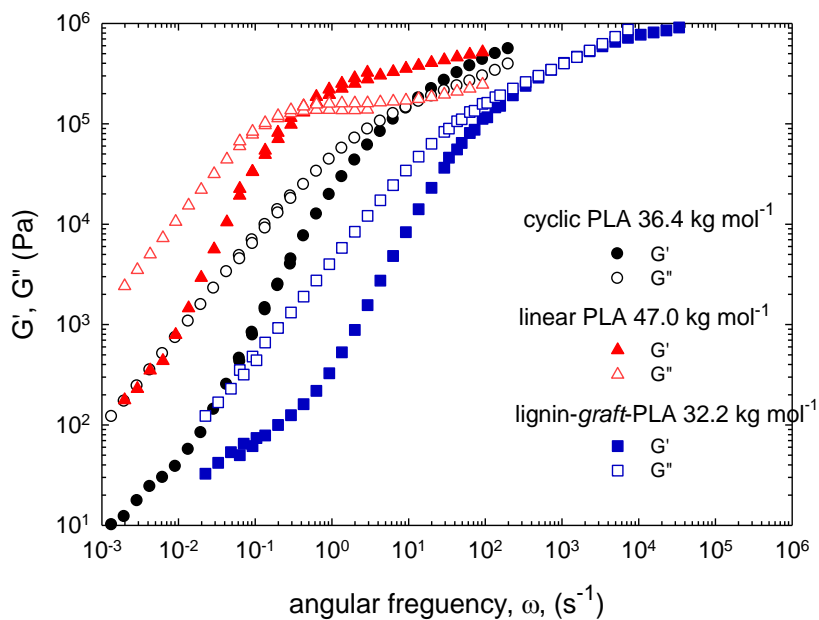
Figure 6.26. Viscoelastic moduli (G'-filled symbols, G"-open symbols) vs. angular frequency, ω (Pa.s) for linear PLA (red triangles, Table 6.7, entry 2), cyclic PLAs (black circles, Table 6.7, entry 8) and star lignin-*graft*-PLA copolymers (blue squares, Table 6.7entry 11).

227

Figure 6.25 and Figure 6.26 compare the LVE moduli for linear PLA, cyclic PLA and star lignin-*graft*-PLA copolymers in this study. Linear PLAs exhibit characteristic thermoplastic behaviour for a linear polymer above its entanglement molecular weight, whereby G' increases to an elastic plateau at intermediate deformation frequencies to then transition into the glassy zone at high frequencies. Comparing the LVE plots of cyclic and star graft PLAs with similar GPC molecular weights, it is clear that the frequency dependence on the loss and storage moduli are different to that of linear PLAs. Both cyclic PLAs and star graft PLAs show faster terminal relaxation for the whole molecular weight range studied. As discussed above cyclic polymers have a large restoring force, making them less deformable than stars.[292] Studies of ultra-pure cyclic poly(styrene)s (PS) also reported faster relaxation compared to linear counterparts and an extended relaxation regime.[293] Recently Matsushita and co-workers showed that even high molecular weight ring chains form few intermolecular entanglements leading to a lack of a rubbery plateau.[294] The cyclic PLAs in this study are likely to be contaminated with linear chains, either from thermal ring-opening during analysis[295] or as a by-product of polymerization. Linear chains have been shown to retard the relaxation of cyclic polymers through threading interactions leading to an enhancement in the rubbery plateau. As the molecular weight of the cyclic copolymers increases, the plateau becomes more defined, which may be attributed to more entanglement between the rings or the presence of higher molecular weight linear chain contaminates (Figure 6.27).
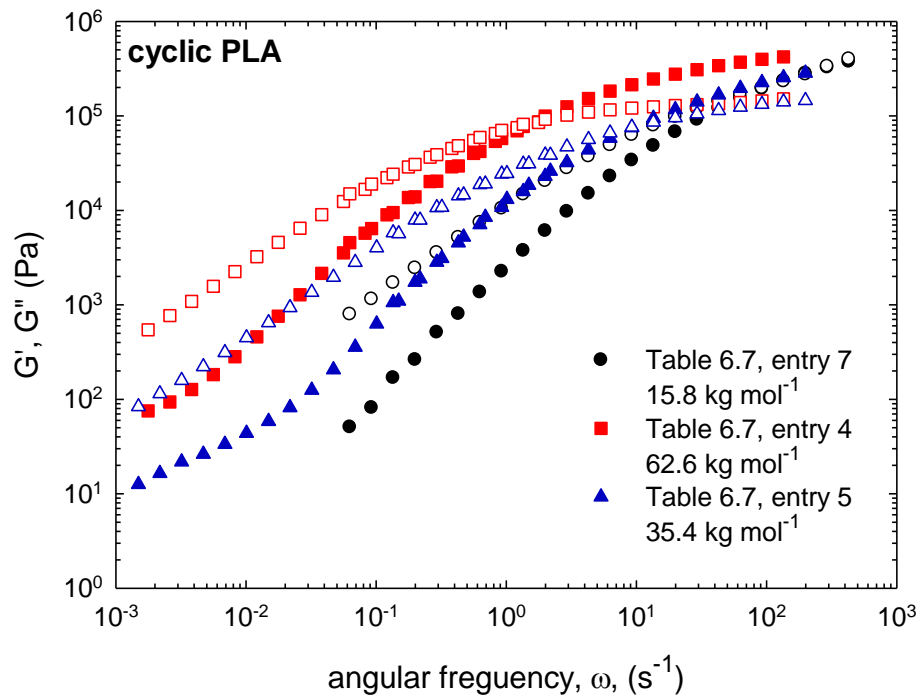
Figure 6.27. Viscoelastic moduli (G'- filled symbols, G"- open symbols) vs. angular frequency, ω (Pa.s) for cyclic PLAs in this study.

Master curves for star lignin-*graft*-PLA with GPC molecular weights of 16.2, 32.2 and 65.2 kg mol^{-1} all showed loss modulus dominating over the whole frequency range, G" > G' (Figure 6.28). At medium to high frequencies, the storage and loss moduli become almost equivalent, G' ≈ G", implying gel-like behaviour. The terminal zone was reached at very low frequencies, where LVE moduli display the characteristic slopes of $G' \propto \omega^2$ and $G'' \propto \omega$. Another interesting feature of the master curves are the lack of a rubber plateau in the storage modulus at high deformation frequencies. A similar result was observed for 3- and 6-arm PHBs which showed that increasing the arm length from 3 to 6 reduced the intensity of the rubber plateau.[283] The loss of the rubber plateau in the graft copolymers is likely due to the large number of shorts arms growing from the various hydroxyl groups in the lignin structure, which are densely packed with few chain

entanglements, thus reducing the ability of the polymer to form a rubbery network. It is hypothesized that by increasing the PLA graft arm length would allow for thermoplastic behaviour, however there are currently very few reports of lignin-graft-PLA copolymers with arm lengths greater than 30 kg mol^{-1}.[277]
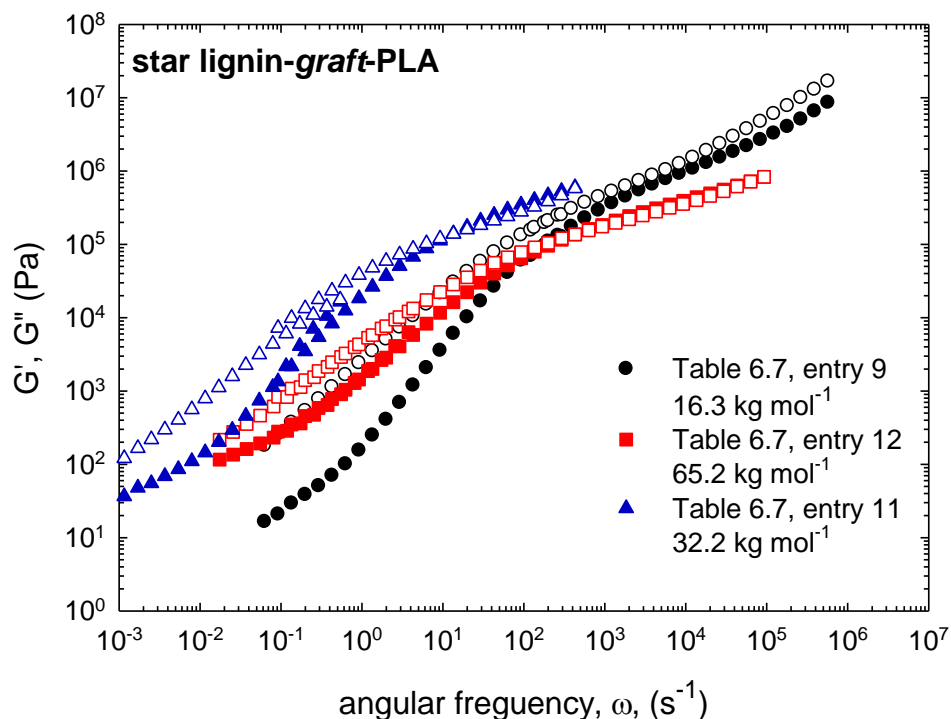
Figure 6.28. Viscoelastic moduli (G'-filled symbols, G"-open symbols) vs. angular frequency, ω (Pa.s) for star lignin-*graft*-PLA copolymers in this study.

The dynamics of star and ring blends are currently under-explored in the literature., though some assumptions can be made from studies of cyclic/linear[284,293,294,296] and star/linear blends.[23,291,292,295,297-301] If the graft copolymer has short chains then it is likely to have lower viscosity if contaminated with cyclic PLAs as they will not entangle with each other. Graft copolymers with long chain stairs could have retardation from threading but this could be balanced

by arm retraction relaxation modes. From the result presented in this study we estimate these graft copolymers to be likely have dense cores with short PLA arms.

Thermal transitions were probed using temperature ramp experiments at constant deformation strain (2%) and frequency (0.5 Hz). Both cyclic and star lignin-*graft*-PLAs showed glass transitions at ~45 °C. At lower temperatures, the G' dominates and thus copolymers display glassy behaviour. Above 45 °C the polymers display gel-like behaviours up to ~ 65 °C after which fluid response dominates (Figure 6.29).
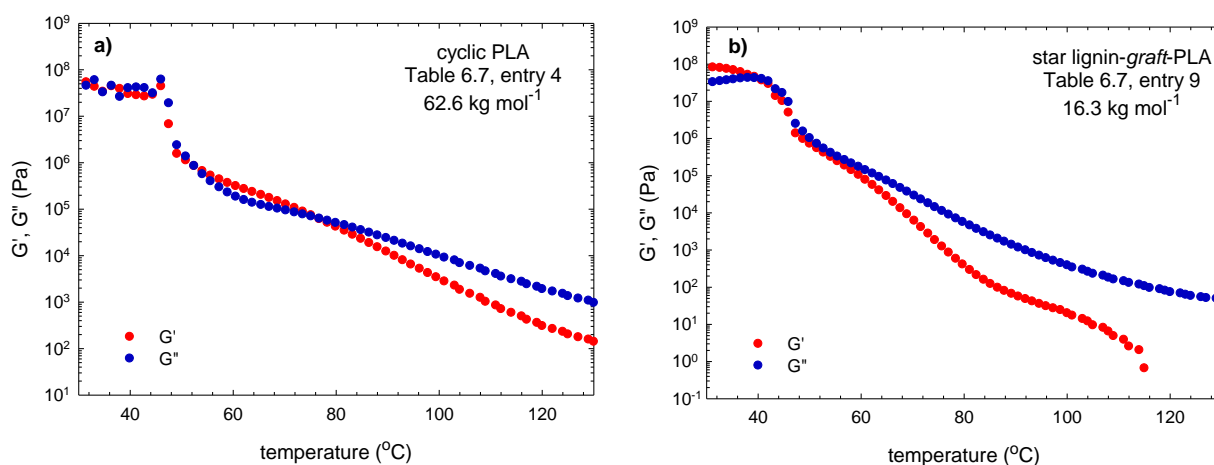
Figure 6.29 Temperature ramp experiments from 30 – 130 °C for a) cyclic PLA (Table 6, entry 4) and b) lignin-*graft*-PLA copolymers (Table 6, entry 10).

6.2.7 Lignin-*graft*-PLLA/PLLA blends.‡‡‡‡

A graft-from strategy was used to synthesize lignin-*graft*-PLLA with arm lengths of 12 kg mol^{-1} and 14 kg mol^{-1} (section 6.2.1). High molecular weight PLLA was also synthesized to use in blends. LLA (20 g) was stirred with InCl$_3$, NEt$_3$ and BnOH in toluene at 80 °C for 48 hours. After this time the reaction mixture was concentrated under reduced pressure and the polymer precipitated three times from cold MeOH before being dried for 48 hours under vacuum (Table 6.8).

Blends with varying compositions were made by dissolving the appropriate amounts of PLLA and lignin-*graft*-PLLA in DCM. Following solution casting and drying under vacuum at 40 °C for 8 h, the blends were compression molded at 165 °C to make discs for rheological and mechanical measurements (Table 6.8).

Table 6.8 Results for graft-from copolymerizations of 90% L-lactide with InCl$_3$/NEt$_3$.

entry	conversion^a (%)	arm length (g mol^{-1})^b	$M_{n,\ GPC}$ (g mol^{-1})^c	$M_{w,\ GPC}$ (g mol^{-1})^c	$Đ^c$
1^d	80	NA^e	210000	214000	1.02
2	92	14200	33900	40300	1.19
3	77	12300	18900	22700	1.20

Standard conditions: InCl$_3$/NEt$_3$ and 5 wt% lignin stirred with 90% L-LA at 120 °C. ^{a} Monomer conversion determined by ^{1}H NMR spectroscopy. ^{b} Calculated from integration of the polymer and chain end methine protons multiplied by the molecular weight of lactide. ^{c} Absolute molecular weights were determined by triple detector GPC (gel permeation chromatography) *via* Universal Calibration (THF 4 mg mL^{-1}, flow rate = 0.5 mL min^{-1}, dn/dc = 0.040 mL g^{-1} (calculated from 100% mass recovery)). ^{d} 2 eq. BnOH used as co-initiator, reaction stirred at 80 °C for 2 days. ^{e} No chain end peaks were detected in the ^{1}H NMR spectra.

---

‡‡‡‡ To model commercially available PLAs while maintaining solubility for characterization purposes, 90% L-LA was used as a monomer for the following experiments.

To determine the thermal stability of the lignin-*graft*-PLLA/PLLA blends under shearing conditions, experiments were conducted over 60 minutes at a constant temperature and angular frequency of 180 °C and 0.5 Hz, respectively. The complex modulus, |G*| is plotted against time in Figure 6.30. Blends show similar or increased |G*| with up to 10 wt% incorporation of graft copolymer. Further increase of graft copolymer concentration in the blend causes a marked decrease in thermal stability. Blends containing graft copolymers with shorter arm lengths (12 kg mol^{-1}) also showed a decrease in thermal stability.

The time-Temperature superposition principle was applied to isothermal SAOS experiments performed at temperatures ranging from 80-180 °C to generate master curves of the complex viscosity at a reference temperature of 160 °C. Zero-shear viscosities obtained from these master curves and are shown in Table 6.9. The viscosity of blends was observed to decrease with increasing graft copolymer content, though this decrease is less distinct with the 10 wt% blend. Interestingly, decreasing the copolymer arm length does not seem to impact viscosity compared to the neat polymer. Under oscillatory-shear flow conditions, star-shaped lignin-*graft*-PLLA copolymers act mainly as a plasticizer to the PLLA matrix, decreasing the modulus and viscosity of the blends.
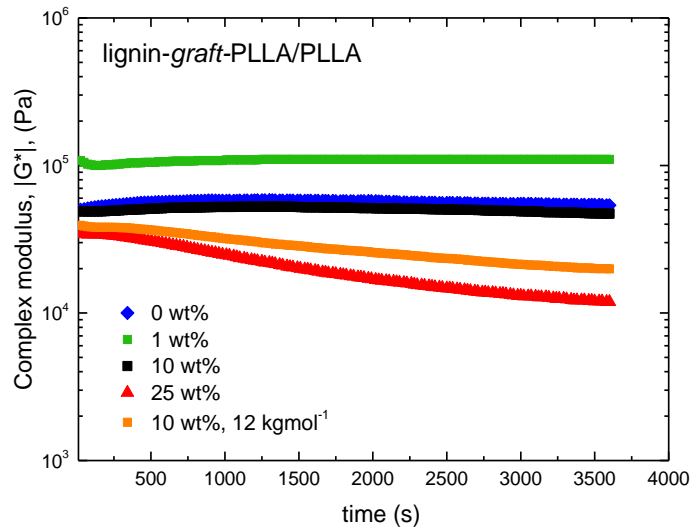
Figure 6.30 Complex modulus, |G*| vs. time at 180 °C for 60 minutes for lignin-*graft*-PLLA/PLLA blends.

Table 6.9 Lignin-*graft*-PLLA/PLLA blend properties.

entry	wt% graft	graft arm length (g mol⁻¹)ᵃ	$\eta_{\omega \to 0}$ (160 °C) (kPa.s)ᵇ	Tensile strength (MPa)	Elastic modulus (MPa)	Elongation at break (%)
1	0	*NA*ᵉ	133	10.9 ±1.9	305 ±50	8.0 ± 0.5
2	1	14200	42.1	19.7 ±1.0	328±50	9.1±1.5
3	10	14200	80.0	36.4 ±6.7	754 ±99	6.6 ± 0.7
4	25	14200	39.0	13.8±2.4	291±42	7.5±1.8
5	10	12300	139	17.6±2.2	357±61	8.5±1.3

ᵃ Calculated from integration of the polymer and chain end methine protons multiplied by the molecular weight of lactide. ᵇ Determined from isothermal SAOS experiments at 160 °C.

Mechanical tests were performed on compression-molded samples, and the results are shown in Figure 6.31 to Figure 6.33. Similar to melt rheology results, incorporation of graft copolymer up 10 wt% improves the tensile strength and elastic modulus of the resulting blends. Undesirably, increases in tensile strength are associated with a decrease in elongation-at-break. Blend of grafts

with shorter arms do not show significant improvement to the mechanical properties of the resulting blends.
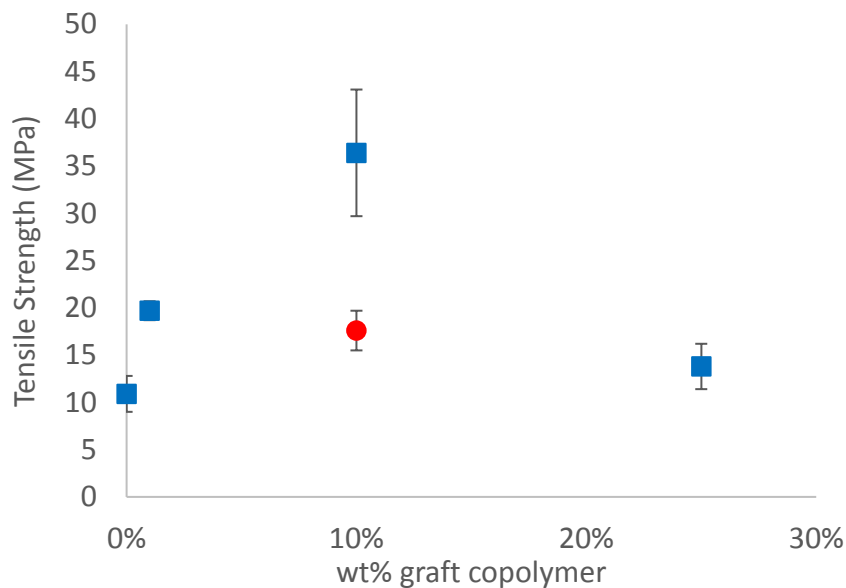
Figure 6.31 Tensile strength of lignin-*graft*-PLLA/PLLA blends. Blends with graft arm length = 14 kg mol^{-1} (■) and Blends with graft arm length = 12 kg mol^{-1}(●).
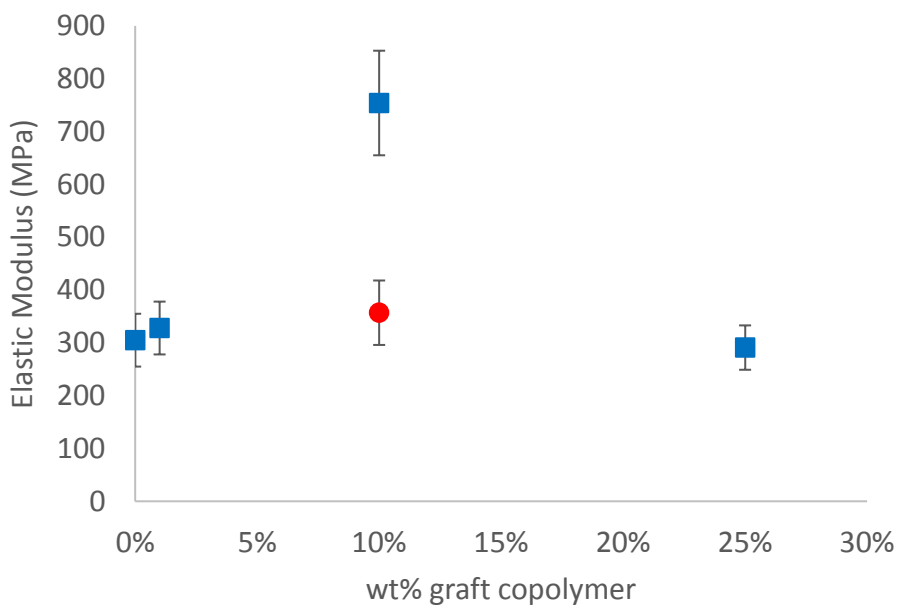
Figure 6.32 Elastic moduli of lignin-*graft*-PLLA/PLLA blends. Blends with graft arm length = 14 kg mol^{-1} (■) and Blends with graft arm length = 12 kg mol^{-1}(●).
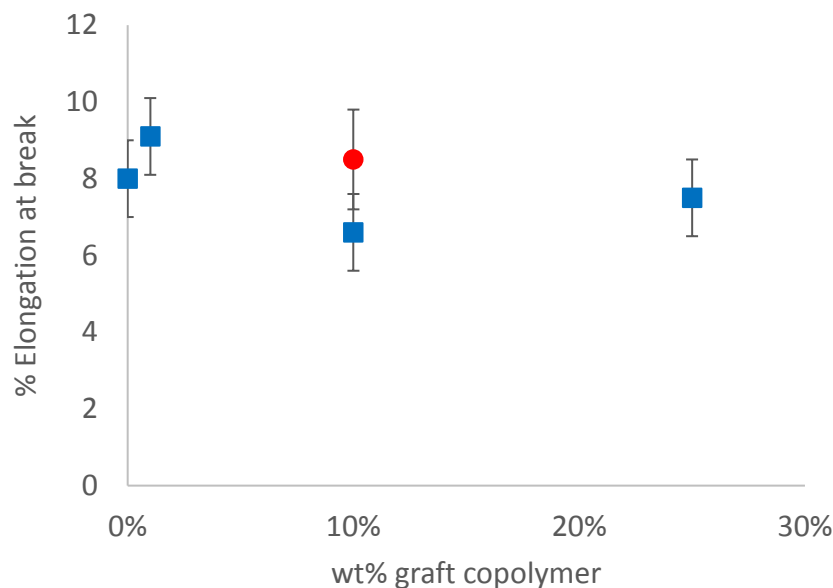
Figure 6.33 Percent elongation at break for lignin-*graft*-PLLA/PLLA blends. Blends with graft arm length = 14 kg mol^{-1} (■) and Blends with graft arm length = 12 kg mol^{-1}(●).

6.3 Conclusions

Lignin-*graft*-PLAs were successfully synthesized *via* two synthetic strategies. The highest lignin incorporation was achieved using a graft-to approach. The organocatalyst, TBD, gave the highest lignin incorporation of the two graft-from syntheses. Graft arm length was found to depend on a variety of factors such as: lignin source and catalysis route and showed that determining $[OH]_{lig}$ is important when predicting the arm length. Avoiding very low $[OH]_{lig}$ was found to be particularly important, as cyclic PLAs can be formed as an unwanted by-product of polymerization. Cyclic PLAs can act as plasticizers, impacting polymer properties. The influence of unreacted lignin on copolymer rheology was also shown to cause errors when predicting melt properties.

We investigated the melt rheology of cyclic PLAs and star lignin-*graft*-PLAs. Both of these materials showed viscous behaviour at low deformation frequency followed by a region of gel-like behaviour at intermediate deformation frequencies. It is predicted that by further increasing the graft arm length, thermoplastic behaviour could be imparted to the material. However, this requires careful control of $[OH]_{lig}$, potentially through pre-alkylation of the lignin.

A family of lignin-*graft*-PLLA/PLA blends was formulated. It was shown that increasing the amount of graft copolymer up to 10 wt% in PLLA blends improves tensile strength and elastic modulus; however, increasing graft copolymer content past this point does not further improve these properties. Unfortunately, an associated decrease in percent elongation at break is also observed for the 10 wt% blend.

6.4 Experimental

General Methods. All the air and moisture sensitive manipulations were carried out in an MBraun glovebox or using standard Schlenk line techniques. A Bruker Avance 300 or 400 MHz spectrometer was used to record ^{1}H NMR spectra. ^{1}H NMR chemical shifts are given in ppm versus residual protons in deuterated $CDCl_3$ (δ 7.27). Molecular weights, hydrodynamic radii and intrinsic viscosities were determined by GPC-MALS-RI-Viscometer using an Agilent liquid chromatograph equipped with a Agilent 1200 series pump and autosampler, three Phenogel 5 µm Narrow Bore columns (4.6 × 300 mm with 500 Å, 10^3 Å and 10^4 Å pore size), a Wyatt Optilab differential refractometer, Wyatt tristar miniDAWN (laser light scattering detector) and a Wyatt ViscoStar viscometer. The column temperature was set at 40 °C. A flow rate of 0.5 mL/min was used and samples were dissolved in THF (*ca*. 4 mg/mL). The measurements were carried out at laser wavelength of 690 nm at 25 °C. The data were processed using the Astra™ software provided

by Wyatt Technology Corp. dn/dc values for cyclic and lignin-*graft*-PLA copolymers were calculated using 100% mass recovery program on the Astra 6.0™ software and an average value of 0.04 was used for molecular weight determination (see appendix E). Molecular masses were determined using a Bruker Autoflex time-of-flight (TOF) mass spectrometer equipped with MALDI ion source. Thermogravimetric analysis (TGA) traces were collected on a PerkinElmer Pyris 6 TGA with a nitrogen flow rate of 20 mL/min. Approximately 15 mg of the samples were weighed into a ceramic crucible. The samples were heated at a rate of 20 °C/min from 30 to 500 °C, and the degradation onset temperatures were directly determined from the thermographs. Shear measurements were performed using the MCR 501 rheometer (Anton Paar), equipped with parallel plates, 8 mm in diameter. The dynamic linear viscoelastic measurements were carried out within the linear viscoelastic regime at temperatures in the range from 50 to 190 °C. The dynamic measurements were conducted in the range of 0.01-100 Hz at a strain of 2%. A gap of 0.5 mm was used to minimize edge effects and ensure a reasonable aspect ratio of plate radius and gap. The samples were melted at 150 °C for at least 5 min to eliminate the residual thermal histories. Tensile tests were performed using COM-TEN 95 series tensile testing equipment (COM-TEN Industries) at ambient conditions. Tensile specimens were cut from compression-moulded films. Specimens were cut from the middle portion of the compressed films to avoid edge effects and edge imperfections. A gage length of 40 mm, crosshead speed of 25 mm/min and a 40 pound (178 N) capacity of load cell was used for testing all samples. To eliminate specimen slippage from the grips, double adhesive masking tape was used to wrap around the top and bottom portions of the sample. For each sample five tests were run. The average modulus, tensile stress and elongation at break were calculated from the resultant stress-strain measurements and these are reported below along with standard deviations shown by the plotted error bars.

238

Materials. Toluene was taken from an IT Inc. solvent purification system with activated alumina columns and degassed before use. DCM and DMF were purchased from Fisher Chemical and were dried over CaH_2, transferred under vacuum and degassed before use. $CDCl_3$ was purchased from Cambridge Isotope Laboratories Inc. and dried over CaH_2, transferred under vacuum and degassed through three freeze−pump−thaw cycles before use. MeOH and K_2CO_3 were purchased from Fisher Chemicals and were used as received. Alkali kraft lignin was purchased from Sigma-Aldrich and was dried at 60 °C under vacuum for 48 hours before use. Indulin AT kraft lignin was a gift from ingevity™ and was dried at 60 °C under vacuum for 48 hours before use. Indium (III) trichloride, NEt_3, and 2-chloro-4,4,5,5-tetramethyl-1,3,2-dioxaphospholane (TMDP) were purchased from Sigma-Aldrich and were used as received. Oxalyl chloride was purchased from Alfa Aesar and was used as received. Racemic and L-lactide were purchased from PURAC America Inc. and were recrystallized three times from hot dry toluene prior to use. $[(NNO)InCl]_2(\mu\text{-Cl})(\mu\text{-OEt})$ (**A**) was synthesized according to previously reported methods.[40]

Phosphitylation of lignin for ^{31}P NMR spectroscopic analysis. Phosphitylation of lignin and lignin-*graft*-PLA copolymers were performed based on modification of the method described by Sattely *et al.*[67,194] A solvent mixture composed of chloroform ($CHCl_3$) and pyridine (1.6:1.0 v/v) was prepared and dried over molecular sieves prior to use. This solution was used for the preparation of relaxation reagent and internal standard solution (chromium(III) acetylacetonate, 5.0 mg/mL and cyclohexanol, 10.0 mg/mL). A total of 30 mg of sample was dissolved in a $CHCl_3$-pyridine solvent (800 μL) followed by the addition of the relaxation reagent and internal standard solution (100 μL) and TMDP (100 μL). The resulting mixtures were left to stir for 24 hours to ensure complete derivatization prior to ^{31}P NMR analysis.

Representative graft-from copolymer synthesis using InCl₃/NEt₃. Under an N_2 atmosphere, a vacuum adapted flask was equipped with a magnetic stir bar and was charged with *rac*-lactide (1000 mg, 6.94 mmol) and stirred in 5 mL of toluene. Lignin ($[OH]_{lig} = 23$ mmol g^{-1}), InCl₃ (2.8 mg, 0.013 mmol), and triethylamine (3.4 μL, 0.025 mmol) were then added and the volume made up to 15 mL. The reaction mixture was stirred at 120 °C for 48 h under N_2. Solvent was removed under reduced pressure and the conversion was determined using ^{1}H NMR spectroscopy. The polymer was then dissolved in 15 mL of DCM and subjected to centrifugation. The supernant was collected and another 15 mL aliquot of DCM added to the solid. This was repeated at least three times. The supernant was combined and concentrated under reduced pressure. Polymers were then precipitated using an excess of cold methanol. The light brown copolymer was then dried under vacuum for 48 h.

Representative graft-from copolymer synthesis using TBD. Under an N_2 atmosphere, a vacuum adapted flask was equipped with a magnetic stir bar and was charged with *rac*-lactide (1000 mg, 6.94 mmol). Lignin ($[OH]_{lig} = 23$ mmol g^{-1}) and TBD (10.3 mg, 0.078 mmol) were then added and the reaction mixture were heated to 130 °C for 3-4 h under N_2. Solvent was removed under reduced pressure and the conversion was determined using ^{1}H NMR spectroscopy. The polymer was then dissolved in 15 mL of DCM and subjected to centrifuge. The supernant was collected and another 15 mL aliquot of DCM added to the solid. This was repeated at least three times. The supernant was combined and concentrated under reduced pressure. Polymers were then precipitated using an excess of cold methanol. The light brown copolymer sample was then dried under vacuum for 48 h.

Synthesis of linear PLA for graft-to copolymer formation. A 20 mL scintillation vial was equipped with a magnetic stir bar. *Rac*-lactide (1000 mg, 6.94 mmol) was dissolved in 2 mL of DCM and to this a solution of [(NNO)InCl]$_2$(μ-Cl)(μ-OEt) (**A**) (1.3 mg, 0.001 mmol) in 2 mL of DCM was added. The solution was stirred at room temperature for 16 h. Solvent was removed under reduced pressure and the conversion was determined using ^{1}H NMR spectroscopy. The polymer was then dissolved in minimal DCM and precipitated using excess of cold MeOH at least three times to remove residual catalyst. The polymer sample was then dried under vacuum overnight.

Synthesis of PLA-Cl for graft-to copolymer formation. PLA (500 mg, M_n = 81700 kg mol^{-1}, Đ = 1.01) was dissolved in 5 mL of DCM. To this, a solution of oxalyl chloride in DCM (0.204 M) was added and the mixture stirred at room temperature overnight. After this time the reaction mixture was concentrated under reduced pressure and the polymer precipitated with cold MeOH.

Representative graft-to copolymer synthesis. Lignin (5 wt% with respect to PLA-Cl) and K$_2$CO$_3$ (1 eq. with respect to PLA-Cl) were stirred in DMF for 30minutes. After this time, a solution of PLA-Cl (200 mg, M_n = 80900 kg mol^{-1}, Đ = 1.01) in 5 mL DMF was added dropwise. The resulting mixture was heated to 50 °C for 1 hour before being cooled to room temperature. The reaction mixture was then poured into a beaker containing 1:1 MeOH:H$_2$O to precipitate the graft copolymer. This was dissolved in minimal DCM and precipitated again with cold MeOH. The final brown copolymer was then dried under vacuum for 48 hours.

Synthesis of high molecular weight PLLA for blends. A vacuum adapted flask was equipped with a magnetic stir bar and was charged with *L*-lactide (20 000 mg, 139 mmol) and stirred in 50 mL of toluene. InCl$_3$ (17 mg, 0.077 mmol), benzyl alcohol (7.4 µL, 0.069 mmol) and

triethylamine (17.7 µL, 0.138 mmol) were then added and the volume made up to 60 mL. The reaction mixture was stirred at 80 °C for 48 h under N_2. Solvent was removed under reduced pressure and the conversion was determined using ^{1}H NMR spectroscopy. The polymer was then dissolved in minimal DCM and precipitated using excess of cold methanol at least three times to remove residual catalyst. The polymer was then dried under vacuum for 48 h.

Representative preparation of lignin-*graft*-PLLA/PLLA blend. To a homogeneous solution of PLLA (2700 mg) in 45 mL of DCM, was added lignin-*graft*-PLLA (300 mg in 15 mL of DCM) and the solution stirred for 30 mins. The solution was then poured into a petri dish and the solvent evaporated overnight. After this time, the films were removed from their dishes and dried under vacuum at 40 °C for 18 h. The blends were compression molded at 165 °C to make discs for rheological and mechanical measurements.

Chapter 7: Conclusion and future directions

The aim of this thesis was to probe catalysis and polymer synthesis in order to gain control over polymer properties. The polymerization behaviour of well-defined dinuclear indium complexes towards *meso*-LA was investigated in Chapter 2. From these studies, I gained insight into which stereocontrol mechanisms are acting in these systems. Attention was focused on catalyst family **A** and its related compounds, **1-6**. Defect peak analysis of polymers generated from both alkoxide and aryloxide initiators showed that ESC is the major mechanism affording stereoselectivity in this system. Interestingly, regardless of the nucleophilicity of the bridging species or the isomer of lactide, this family of complexes retains their dimeric structure during polymerization. Analysis of solid-state structures showed that these metal complexes are held together by an important hydrogen bonding interaction between the secondary amine of the ligand and the terminal chlorine on the metal centre. This result has continued to present itself throughout investigation of this catalyst system by the Mehrkhodavandi group and has prompted the exploration of new ligand architectures which can bind two metal centres. The formation of chelated complexes discussed in Chapter 4 indicates the limitations of using diols as co-initiators for polymerization; a surprising result as triols such as, 1,3,5-tris(hydroxymethyl)-benzene (THMB), have been successful co-initiators for this reaction.[283,300] The reactivity of aryl initiators also provides useful information for ligand design. Complexes with electron deficient initiators (**4** and **5**) were the least active towards lactide polymerization, giving an indication of the vitality of avoiding the use of electron rich phenols as ligands to ensure that the ligands do not participate or compete in polymerization with lactide.

To gain control of polymer properties, I targeted efficient catalyst systems which would yield PLAs with controllable M_w and Đ so we would be able to precisely relate structure to properties.

By exploiting the systems described in Chapters 2 and 4, the controlled synthesis of both stereoregular and end-functionalized PLAs was achieved. The field was lacking an accurate comparison of stereoregular PLAs. Most of the analysis of the material properties of PLAs was focused on highly isotactic or isotactic stereocomplex PLAs. In Chapter 3, the assumption that PLA tacticity has a similar effect on properties as observed with other polymers such as PP and PS was challenged and found to be false. PLA is unique in its physical properties due to strong dipole-dipole interactions between polymer chains. These interactions are magnified between regions of high isotacticity (and to a lesser extent heterotacticity). Moderately syndiotactic PLAs displayed diminished melt properties compared to PLA of other microstructures, albeit with greater thermal stability. There is a lot of potential for researchers to apply this information to the development of methods to further control and quantify PLAs during industrial production. Moreover, this information allows researchers to explore more rewarding directions when applying this material and opens the door to using combinations of stereoregular PLAs to act as internal fillers and plasticizers within the PLA matrix, generating interesting composites comprised of just one polymer family.

End-group aggregation of aryl-capped PLAs was shown to be induced under shearing conditions in Chapter 5. Though the onset of aggregation was slow, this effect could prove to be useful under creeping conditions. Experiments in the non-linear viscoelastic regime could further elucidate the benefits of these end-group associations. Another under-explored feature of these polymers was their absorption spectra. Even high molecular weight polymers with relatively low chromophore concentrations (as polymer chain-ends) were strongly absorbing. There is potential for these materials to be used as compostable coatings for novelty applications or devices. Further investigation of the spin- or drop-casting of these PLAs is needed as well as how annealing could

further align the chain-ends to enhance their photochemical properties. It would also be of importance to consider the bio-toxicity of the chromophore chain-ends.

It became of interest to extend my research and use other bio-sourced materials in order to bolster developing green industries by creating new materials with appealing properties. The last seven years has seen the emergence of researchers exploring lignin/PLA materials. From the reactivity studies described in Chapters 2 and 4, I recognized the value of understanding how catalytic systems are behaving in order to impart control of the materials generated. In Chapter 6, is it shown that proper analysis of polymerization products is vital, otherwise the resultant material properties will not be predictable. In the specific graft-from processes investigated, I show that under certain conditions, cyclic PLAs are generated instead of the desired graft copolymers. The impact of these cycles on material response is an area still in need of investigation. However, the melt rheological properties of lignin-*graft*-PLAs were analyzed and depend on the PLA arm length. Below 30 kg mol^{-1} viscous flow or gel-like behaviour dominates. Studies on the barrier properties of these materials of lignin-*graft*-PLAs have recently been reported.[267,276] Lignin composites have also been electrospun into fibers.[268,275] As these grafts can be processed at relatively low temperatures (< 60 °C), these composite materials may make valuable fibers, sheets or coatings for use in agricultural, biomedical or packaging applications. Thus, it would be of interest to explore the ability of these materials to be solution cast or spin coated onto different substrates. Depolymerization and pre-alkylation of lignin *in situ* could be performed to further increase lignin incorporation and potentially enhance barrier properties.

Preliminary studies were conducted in an attempt to synthesize thermally responsive lignin/PLA composites using Diels-Alder chemistry (Scheme 7.1). By using our established catalyst systems to end-functionalize PLA with furfural alcohol moieties and coupling these

polymers to maleimide-modified-lignin, these materials would have the potential to undergo a change in microstructure causing the polymer to go from a low T_g, viscous state to a high T_g rubbery solid state when placed in a thermal gradient. These would be fascinating materials which could change the way we envision processing these polymeric materials.

Scheme 7.1 Proposed synthesis of thermoresponsive lignin/PLA composites.
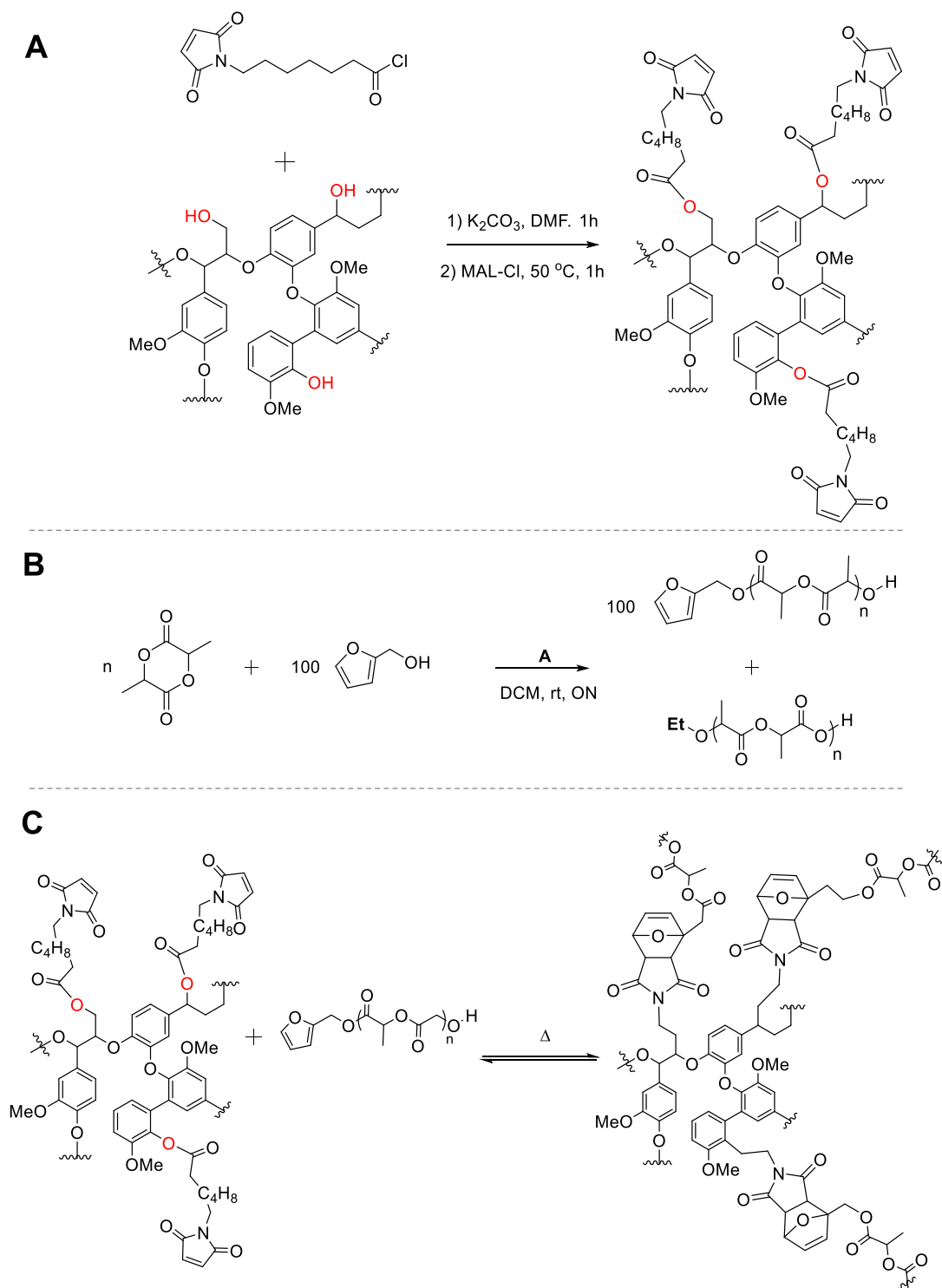
Bibliography

(1)   Chile, L.-E.; Mehrkhodavandi, P.; Hatzikiriakos, S. G.; *Macromolecules* **2016**, *49*, 909.

(2)   Chile, L.-E.; Ebrahimi, T.; Wong, A.; Aluthge, D. C.; Hatzikiriakos, S. G.; Mehrkhodavandi, P.; *Dalton Trans.* **2017**.

(3)   Thompson, R. C.; Moore, C. J.; vom Saal, F. S.; Swan, S. H.; *Philosophical Transactions of the Royal Society B: Biological Sciences* **2009**, *364*, 2153.

(4)   Andrady, A. L.; Neal, M. A.; *Philosophical Transactions of the Royal Society B: Biological Sciences* **2009**, *364*, 1977.

(5)   Barnes, D. K. A.; Galgani, F.; Thompson, R. C.; Barlaz, M.; *Philosophical Transactions of the Royal Society B: Biological Sciences* **2009**, *364*, 1985.

(6)   Eriksen, M.; Lebreton, L. C. M.; Carson, H. S.; Thiel, M.; Moore, C. J.; Borerro, J. C.; Galgani, F.; Ryan, P. G.; Reisser, J.; *PLoS ONE* **2014**, *9*, e111913.

(7)   Song, J. H.; Murphy, R. J.; Narayan, R.; Davies, G. B. H.; *Philosophical Transactions of the Royal Society B: Biological Sciences* **2009**, *364*, 2127.

(8)   Hopewell, J.; Dvorak, R.; Kosior, E.; *Philosophical Transactions of the Royal Society B: Biological Sciences* **2009**, *364*, 2115.

(9)   Koch, H. M.; Calafat, A. M.; *Philosophical Transactions of the Royal Society B: Biological Sciences* **2009**, *364*, 2063.

(10)   Teuten, E. L.; Saquing, J. M.; Knappe, D. R. U.; Barlaz, M. A.; Jonsson, S.; Björn, A.; Rowland, S. J.; Thompson, R. C.; Galloway, T. S.; Yamashita, R.; Ochi, D.; Watanuki, Y.; Moore, C.; Viet, P. H.; Tana, T. S.; Prudente, M.; Boonyatumanond, R.; Zakaria, M. P.; Akkhavong, K.; Ogata, Y.; Hirai, H.; Iwasa, S.; Mizukawa, K.; Hagino, Y.; Imamura, A.; Saha, M.; Takada, H.; *Philosophical Transactions of the Royal Society B: Biological Sciences* **2009**, *364*, 2027.

(11)   Williams, C.; Hillmyer, M.; *Polymer Reviews* **2008**, *48*, 1.

(12)   Gandini, A. In *Biocatalysis in Polymer Chemistry* Loos, K., Ed.; WILEY-VCH Verlag GmbH & Co. KGaA: Weinheim, 2011.

(13)   Foundation, E. M.; www.ellenmacarthurfoundation.org/; Vol. 2017 (Accessed May 27th, 2017).

(14)   Heijungs, R.; Huppes, G.; Guinée, J. B.; *Polymer Degradation and Stability* **2010**, *95*, 422.

(15)   Holmberg, A. L.; Reno, K. H.; Wool, R. P.; Epps, I. I. I. T. H.; *Soft Matter* **2014**, *10*, 7405.

(16)   Llevot, A.; Dannecker, P.-K.; von Czapiewski, M.; Over, L. C.; Söyler, Z.; Meier, M. A. R.; *Chemistry – A European Journal* **2016**, *22*, 11510.

(17)   Vroman, I.; Tighzert, L.; *Materials* **2009**, *2*, 307.

(18)   Mecking, S.; *Angew. Chem. Int. Ed.* **2004**, *43*, 1078.

(19)   Zhu, J.-B.; Chen, E. Y. X.; *J. Am. Chem. Soc.* **2015**, *137*, 12506.

(20)   Dorgan, J. R.; Williams, J. S.; Lewis, D. N.; *J. Rheol.* **1999**, *43*, 1141.

(21)   Palade, L.-I.; Lehermeier, H. J.; Dorgan, J. R.; *Macromolecules* **2001**, *34*, 1384.

(22)   Othman, N.; Acosta-Ramírez, A.; Mehrkhodavandi, P.; Dorgan, J. R.; Hatzikiriakos, S. G.; *J. Rheol.* **2011**, *55*, 987.

(23)   Nouri, S.; Dubois, C.; Lafleur, P. G.; *Journal of Polymer Science Part B: Polymer Physics* **2015**, *53*, 522.

(24)   Yamane, H.; Sasai, K.; Takano, M.; Takahashi, M.; *J. Rheol.* **2004**, *48*, 599.

(25)   Perego, G.; Cella, G. D.; Bastioli, C.; *J. Appl. Polym. Sci.* **1996**, *59*, 37.

(26)   Maharana, T.; Pattanaik, S.; Routaray, A.; Nath, N.; Sutar, A. K.; *Reactive and Functional Polymers* **2015**, *93*, 47.

(27)   Dechy-Cabaret, O.; Martin-Vaca, B.; Bourissou, D.; *Chem. Rev.* **2004**, *104*, 6147.

(28)   Jamshidian, M.; Tehrany, E. A.; Imran, M.; Jacquot, M.; Desobry, S.; *Compr. Rev. Food. Sci. Food. Saf.* **2010**, *9*, 552.

(29)   Garlotta, D.; *Journal of Polymers and the Environment* **2001**, *9*, 63.

(30)   Södergård, A.; Stolta, M.; *Prog. Polym. Sci.* **2002**, *27*, 1123.

(31)   Madhavan Nampoothiri, K.; Nair, N. R.; John, R. P.; *Bioresource Technology* **2010**, *101*, 8493.

(32)   Chisholm, M. H.; Eilerts, N. W.; Huffman, J. C.; Iyer, S. S.; Pacold, M.; Phomphrai, K.; *J. Am. Chem. Soc.* **2000**, *122*, 11845.

(33)   Kricheldorf, H. R.; Boettcher, C.; Tönnes, K.-U.; *Polymer* **1992**, *33*, 2817.

(34) Chabot, F.; Vert, M.; Chapelle, S.; Granger, P.; *Polymer* **1983**, *24*, 53.

(35) Auras, R.; Harte, B.; Selke, S.; *Macromol. Biosci.* **2004**, *4*, 835.

(36) Stanford, M. J.; Dove, A. P.; *Chem. Soc. Rev.* **2010**, *39*, 486.

(37) Buffet, J.-C.; Okuda, J.; *Polym. Chem.* **2011**, *2*, 2758.

(38) Dijkstra, P. J.; Du, H.; Feijen, J.; *Polym. Chem.* **2011**, *2*, 520.

(39) Spassky, N.; Wisniewski, M.; Pluta, C.; Le Borgne, A.; *Macromolecular Chemistry and Physics* **1996**, *197*, 2627.

(40) Yu, I.; Acosta-Ramirez, A.; Mehrkhodavandi, P.; *J. Am. Chem. Soc.* **2012**, *134*, 12758.

(41) Osten, K. M.; Aluthge, D. C.; Patrick, B. O.; Mehrkhodavandi, P.; *Inorg. Chem.* **2014**, *53*, 9897.

(42) Osten, K. M.; Aluthge, D. C.; Mehrkhodavandi, P.; *Dalton Trans.* **2015**, *44*, 6126.

(43) Thakur, K. A. M.; Kean, R. T.; Hall, E. S.; Kolstad, J. J.; Lindgren, T. A.; Doscotch, M. A.; Siepmann, J. I.; Munson, E. J.; *Macromolecules* **1997**, *30*, 2422.

(44) Thakur, K. A. M.; Kean, R. T.; Zell, M. T.; Padden, B. E.; Munson, E. J.; *Chem. Commun.* **1998**, 1913.

(45) Thakur, K. A. M.; Kean, R. T.; Hall, E. S.; Kolstad, J. J.; Munson, E. J.; *Macromolecules* **1998**, *31*, 1487.

(46) Zell, M. T.; Padden, B. E.; Paterick, A. J.; Thakur, K. A. M.; Kean, R. T.; Hillmyer, M. A.; Munson, E. J.; *Macromolecules* **2002**, *35*, 7700.

(47) Coates, G. W.; *J. Chem. Soc., Dalton Trans.* **2002**, 467.

(48) Buffet, J. C.; Okuda, J.; Arnold, P. L.; *Inorg. Chem.* **2010**, *49*, 419.

(49) Vainionpää, S.; Rokkanen, P.; Törmälä, P.; *Progress in Polymer Science* **1989**, *14*, 679.

(50) Codari, F.; Lazzari, S.; Soos, M.; Storti, G.; Morbidelli, M.; Moscatelli, D.; *Polymer Degradation and Stability* **2012**, *97*, 2460.

(51) Tokiwa, Y.; Jarerat, A.; *Biotechnology Letters* **2004**, *26*, 771.

(52) Rudeekit, Y.; Numnoi, J.; Tajan, M.; Chaiwutthian, P.; Leejarkpai, T.; *Journal of Metals, Materials and Minerals* **2008**, *18*, 83.

(53) Drumright, R. E.; Gruber, P. R.; Henton, D. E.; *Adv. Mater.* **2000**, *12*, 1841.

(54) Oh, J. K.; *Soft Matter* **2011**, *7*, 5096.

(55) Carrasco, F.; Pagès, P.; Gámez-Pérez, J.; Santana, O. O.; Maspoch, M. L.; *Polymer Degradation and Stability* **2010**, *95*, 116.

(56) Liu, H. Z.; Zhang, J. W.; *J. Polym. Sci. Part B: Polym. Phys.* **2011**, *49*, 1051.

(57) Rasal, R. M.; Janorkar, A. V.; Hirt, D. E.; *Prog. Polym. Sci.* **2010**, *35*, 338.

(58) Inkinen, S.; Hakkarainen, M.; Albertsson, A. C.; Sodergard, A.; *Biomacromolecules* **2011**, *12*, 523.

(59) Platel, R.; Hodgson, L.; Williams, C.; *Polymer Reviews* **2008**, *48*, 11.

(60) Whetten, R.; Sederoff, R.; *Plant Cell* **1995**, *7*, 1001.

(61) Lora, J. H.; Glasser, W. G.; *Journal of Polymers and the Environment* **2002**, *10*, 39.

(62) Dorrestijn, E.; Laarhoven, L. J. J.; Arends, I. W. C. E.; Mulder, P.; *Journal of Analytical and Applied Pyrolysis* **2000**, *54*, 153.

(63) Vanholme, R.; Demedts, B.; Morreel, K.; Ralph, J.; Boerjan, W.; *Plant Physiology* **2010**, *153*, 895.

(64) Laurichesse, S.; Avérous, L.; *Progress in Polymer Science* **2014**, *39*, 1266.

(65) Duval, A.; Lawoko, M.; *Reactive and Functional Polymers* **2014**, *85*, 78.

(66) Lochab, B.; Shukla, S.; Varma, I. K.; *RSC Advances* **2014**, *4*, 21712.

(67) Granata, A.; Argyropoulos, D. S.; *Journal of Agricultural and Food Chemistry* **1995**, *43*, 1538.

(68) Peelman, N.; Ragaert, P.; Ragaert, K.; De Meulenaer, B.; Devlieghere, F.; Cardon, L.; *J. Appl. Polym. Sci.* **2015**, *132*, n/a.

(69) Kai, D.; Tan, M. J.; Chee, P. L.; Chua, Y. K.; Yap, Y. L.; Loh, X. J.; *Gren Chem.* **2016**, *18*, 1175.

(70) Falade, A. O.; Nwodo, U. U.; Iweriebor, B. C.; Green, E.; Mabinya, L. V.; Okoh, A. I.; *MicrobiologyOpen* **2017**, *6*, e00394.

(71) Eggert, C.; Temp, U.; Eriksson, K. E.; *App. Environ. Microbiology* **1996**, *62*, 1151.

(72) Wan, C.; Li, Y.; *Biotechnology Advances* **2012**, *30*, 1447.

(73) Ruiz-Dueñas, F. J.; Martínez, Á. T.; *Microbial biotechnology* **2009**, *2*, 164.

(74) Hatakka, A.; *FEMS Microbiology Reviews* **1994**, *13*, 125.

(75) Ten, E.; Vermerris, W.; *Journal of Applied Polymer Science* **2015**, *132*, n/a.

(76) Norgren, M.; Edlund, H.; *Current Opinion in Colloid & Interface Science* **2014**, *19*, 409.

(77) Upton, B. M.; Kasko, A. M.; *Chem. Rev.* **2016**, *116*, 2275.

(78) Sen, S.; Patil, S.; Argyropoulos, D. S.; *Gren Chem.* **2015**, *17*, 4862.

(79) Kim, D. H.; Kang, H. J.; Song, Y. S.; *Carbohydrate Polymers* **2013**, *92*, 1006.

(80) Gordobil, O.; Egüés, I.; Llano-Ponte, R.; Labidi, J.; *Polymer Degradation and Stability* **2014**, *108*, 330.

(81) Gordobil, O.; Delucis, R.; Egüés, I.; Labidi, J.; *Industrial Crops and Products* **2015**, *72*, 46.

(82) Spiridon, I.; Leluk, K.; Resmerita, A. M.; Darie, R. N.; *Composites Part B: Engineering* **2015**, *69*, 342.

(83) Alexy, P.; Košíková, B.; Podstránska, G.; *Polymer* **2000**, *41*, 4901.

(84) Stewart, D.; *Industrial Crops and Products* **2008**, *27*, 202.

(85) Mousavioun, P.; Doherty, W. O. S.; George, G.; *Industrial Crops and Products* **2010**, *32*, 656.

(86) Mousavioun, P.; Halley, P. J.; Doherty, W. O. S.; *Industrial Crops and Products* **2013**, *50*, 270.

(87) Dealy, J. M. W., K. F. In *Melt Rheology and its Role in Plastic Processing: Theory and Applications*; Van Nostrand Reinhold: New York, 1990, p 1.

(88) Lim, L. T.; Auras, R.; Rubino, M.; *Prog. Polym. Sci.* **2008**, *33*, 820.

(89) Lipatov, Y.; *Polym. Chem.* **2005**, *26* 63.

(90) Dealy, J. M. W., K. F.; *Melt Rheology and its Role in Plastic Processing: Theory and Applications*; Van Nostrand Reinhold: New York, 1990.

(91) Munstedt, H.; *Soft Matter* **2011**, *7*, 2273.

(92) Tadmor, Z.; Gogos, C. G.; *Principles of Polymer Processing*; Wiley: New York, 1979.

(93) Rosenbaum, E. E.; Hatzikiriakos, S. G.; Stewart, C. W.; *International Polymer Processing* **1995**, *10*, 204.

(94) Mezger, T. G.; *Applied Rheology*; 1st ed.; Anton Paar GMbH: Austria, 2015.

(95) Sentmanat, M. L.; *Rheol. Acta.* **2004**, *43*, 657.

(96) Ikada, Y.; Jamshidi, K.; Tsuji, H.; Hyon, S. H.; *Macromolecules* **1987**, *20*, 904.

(97) Tsuji, H.; Ikada, Y.; *Polymer* **1995**, *36*, 2709.

(98) Tsuji, H.; Ikada, Y.; *Journal of Applied Polymer Science* **1995**, *58*, 1793.

(99) Tsuji, H.; Ikada, Y.; *Polymer* **1999**, *40*, 6699.

(100)   Opaprakasit, P.; Opaprakasit, M.; Tangboriboonrat, P.; *Appl. Spectrosc.* **2007**, *61*, 1352.

(101)   Rahman, N.; Kawai, T.; Matsuba, G.; Nishida, K.; Kanaya, T.; Watanabe, H.; Okamoto, H.; Kato, M.; Usuki, A.; Matsuda, M.; Nakajima, K.; Honma, N.; *Macromolecules* **2009**, *42*, 4739.

(102)   Tomotsu, N.; Ishihara, N.; Newman, T. H.; Malanga, M. T.; *Chemical. J. Mol. Catal.* **1998**, *128*, 167.

(103)   Ovitt, T. M.; Coates, G. W.; *J. Am. Chem. Soc.* **1999**, *121*, 4072.

(104)   Dove, A. P.; Li, H.; Pratt, R. C.; Lohmeijer, B. G. G.; Culkin, D. A.; Waymouth, R. M.; Hedrick, J. L.; *Chem. Commun.* **2006**, 2881.

(105)   Coudane, J.; Ustariz-Peyret, C.; Schwach, G.; Vert, M.; *J. Polym. Sci. A Polym. Chem.* **1997**, *35*, 1651.

(106)   Ovitt, T. M.; Coates, G. W.; *J. Am. Chem. Soc.* **2002**, *124*, 1316.

(107)   Zhong, Z. Y.; Dijkstra, P. J.; Feijen, J.; *J. Am. Chem. Soc.* **2003**, *125*, 11291.

(108)   Chisholm, M. H.; Gallucci, J. C.; Quisenberry, K. T.; Zhou, Z.; *Inorg. Chem.* **2008**, *47*, 2613.

(109)   Peckermann, I.; Kapelski, A.; Spaniol, T. P.; Okuda, J.; *Inorg. Chem.* **2009**, *48*, 5526.

(110)   Wang, L.; Ma, H.; *Dalton Trans.* **2010**, *39*, 7897.

(111)   Routaray, A.; Nath, N.; Maharana, T.; Sutar, A. k.; *J. Macromol. Sci. Part A* **2015**, *52*, 444.

(112)   McGuinness, D. S.; Marshall, E. L.; Gibson, V. C.; Steed, J. W.; *J. Polym. Sci. A Polym. Chem.* **2003**, *41*, 3798.

(113)   Biernesser, A. B.; Li, B.; Byers, J. A.; *J. Am. Chem. Soc.* **2013**, *135*, 16553.

(114)   Amgoune, A.; Thomas, C. M.; Roisnel, T.; Carpentier, J. F.; *Chem. Eur. J.* **2006**, *12*, 169.

(115)   Chamberlain, B. M.; Cheng, M.; Moore, D. R.; Ovitt, T. M.; Lobkovsky, E. B.; Coates, G. W.; *J. Am. Chem. Soc.* **2001**, *123*, 3229.

(116)   Buffet, J. C.; Kapelski, A.; Okuda, J.; *Macromolecules* **2010**, *43*, 10201.

(117)   Sauer, A.; Buffet, J. C.; Spaniol, T. P.; Nagae, H.; Mashima, K.; Okuda, J.; *Inorg. Chem.* **2012**, *51*, 5764.

(118)   Buffet, J.-C.; Davin, J. P.; Spaniol, T. P.; Okuda, J.; *New Journal of Chemistry* **2011**, *35*, 2253.

(119)   Amgoune, A.; Thomas, C. M.; Carpentier, J.-F.; *Macromol. Rapid Commun.* **2007**, *28*, 693.

(120)   Pietrangelo, A.; Hillmyer, M. A.; Tolman, W. B.; *Chem. Comm.* **2009**, 2736.

(121)   Pietrangelo, A.; Knight, S. C.; Gupta, A. K.; Yao, L. J.; Hillmyer, M. A.; Tolman, W. B.; *J. Am. Chem. Soc.* **2010**, *132*, 11649.

(122)   Amgoune, A.; Thomas, C. M.; Roisnel, T.; Carpentier, J. F.; *Chemistry* **2005**, *12*, 169.

(123)   Douglas, A. F.; Patrick, B. O.; Mehrkhodavandi, P.; *Angew. Chem. Int. Ed.* **2008**, *47*, 2290.

(124)   Acosta-Ramirez, A.; Douglas, A. F.; Yu, I.; Patrick, B. O.; Diaconescu, P. L.; Mehrkhodavandi, P.; *Inorg. Chem.* **2010**, *49*, 5444.
(125)   Aluthge, D. C.; Patrick, B. O.; Mehrkhodavandi, P.; *Chem. Commun.* **2013**, *49*, 4295.
(126)   Aluthge, D. C.; Yan, E. X.; Ahn, J. M.; Mehrkhodavandi, P.; *Inorg. Chem.* **2014**, *53*, 6828.
(127)   Aluthge, D. C.; Ahn, J. M.; Mehrkhodavandi, P.; *Chem. Sci.* **2015**, *6*, 5284.
(128)   Hummel, G. J. v. a. H., S. and Kohn, F.E. and Feijen, J; *Acta Crystallographica B* **1982**, *38*, 1679.
(129)   Fang, J.; Yu, I.; Mehrkhodavandi, P.; Maron, L.; *Organometallics* **2013**, *32*, 6950.
(130)   Hatada, K.; *J. Polym. Sci. A Polym. Chem.* **1999**, *37*, 245.
(131)   Chatani, Y.; Shimane, Y.; Inoue, Y.; Inagaki, T.; Ishioka, T.; Ijitsu, T.; Yukinari, T.; *Polymer* **1992**, *33*, 488.
(132)   Chatani, Y.; Shimane, Y.; Ijitsu, T.; Yukinari, T.; *Polymer* **1993**, *34*, 1625.
(133)   Chatani, Y.; Shimane, Y.; Inagaki, T.; Ijitsu, T.; Yukinari, T.; Shikuma, H.; *Polymer* **1993**, *34*, 1620.
(134)   De Rosa, C.; Corradini, P.; *Macromolecules* **1993**, *25*, 5711.
(135)   Jr., A. J. P.; Landes, B. G.; Karjala, P. J.; *Thermochimica Acta* **1991**, *177*, 187.
(136)   Sakata, Y.; Unwin, A. P.; Ward, I. M.; *Journal of Materials Science* **1995**, *30*, 5841.
(137)   Ebrahimi, T.; Aluthge, D. C.; Hatzikiriakos, S. G.; Mehrkhodavandi, P.; *Macromolecules* **2016**, *49*, 8812.
(138)   Karasz, F. E.; MacKnight, W. J.; *Macromolecules* **1968**, *1* 537.
(139)   Eckstein, A.; Friedrich, C.; Lobbrecht, A.; Mulhaupt, R.; *Acta Polym.* **1997**, *48*, 41.
(140)   Grohens, Y.; Brogly, M.; Labbe, C.; David, M.-O.; Schultz, J.; *Langmuir* **1998**, *14* 2929.
(141)   Chisholm, M. H.; Gallucci, J.; Phomphrai, K.; *Chem. Commun.* **2003**, 48.
(142)   Chisholm, M. H.; Gallucci, J. C.; Phomphrai, K.; *Inorg. Chem.* **2004**, *43*, 6717.
(143)   Hormnirun, P.; Marshall, E. L.; Gibson, V. C.; White, A. J. P.; Williams, D. J.; *J. Am. Chem. Soc.* **2004**, *126*, 2688.
(144)   Bonnet, F.; Cowley, A. R.; Mountford, P.; *Inorg. Chem.* **2005**, *44*, 9046.
(145)   Coulembier, O.; Mespouille, L.; Hedrick, J. L.; Waymouth, R. M.; Dubois, P.; *Macromolecules* **2006**, *39*, 4001.
(146)   Chmura, A. J.; Chuck, C. J.; Davidson, M. G.; Jones, M. D.; Lunn, M. D.; Bull, S. D.; Mahon, M. F.; *Angew. Chem. Int. Edit.* **2007**, *46*, 2280.
(147)   Buffet, J.-C.; Okuda, J.; *Chem. Commun.* **2011**, *47*, 4796.
(148)   Blake, M. P.; Schwarz, A. D.; Mountford, P.; *Organometallics* **2011**, *30*, 1202.
(149)   Bouyahyi, M.; Ajellal, N.; Kirillov, E.; Thomas, C. M.; Carpentier, J. F.; *Chem. Eur. J.* **2011**, *17*, 1872.
(150)   Romain, C.; Heinrich, B.; Laponnaz, S. B.; Dagorne, S.; *Chem. Commun.* **2012**, *48*, 2213.
(151)   Nayab, S.; Jeong, J. H.; *Polyhedron* **2013**, *59*, 138.
(152)   Klitzke, J. S.; Roisnel, T.; Kirillov, E.; Casagrande, O. L.; Carpentier, J.-F.; *Organometallics* **2014**, *33*, 309.
(153)   Kong, W. L.; Chai, Z. Y.; Wang, Z. X.; *Dalton Trans.* **2014**, *43*, 14470.
(154)   Yang, S.; Nie, K.; Zhang, Y.; Xue, M.; Yao, Y.; Shen, Q.; *Inorg. Chem.* **2014**, *53*, 105.
(155)   Pilone, A.; De Maio, N.; Press, K.; Venditto, V.; Pappalardo, D.; Mazzeo, M.; Pellecchia, C.; Kol, M.; Lamberti, M.; *Dalton Trans.* **2015**, *44*, 2157.
(156)   Fuoco, T.; Meduri, A.; Lamberti, M.; Venditto, V.; Pellecchia, C.; Pappalardo, D.; *Polym. Chem.* **2015**, *6*, 1727.
(157)   Fuchs, K.; Friedrich, C.; Weese, J.; *Macromolecules* **1996**, *29*, 5893.
(158)   Eckstein, A.; Suhm, J.; Friedrich, C.; Maier, R.-D.; Sassmannshausen, J.; Bochmann, M.; Mülhaupt, R.; *Macromolecules* **1998**, *31* 1335.
(159)   Huang, C.-L.; Chen, Y.-C.; Hsiao, T.-J.; Tsai, J.-C.; Wang, C.; *Macromolecules* **2011**, *44*, 6155.
(160)   Liu, C.; Yu, J.; He, J.; Liu, W.; Sun, C.; Jing, Z.; *Macromolecules* **2004**, *37*, 9279.
(161)   Fetters, L. J.; Lee, J. H.; Mathers, R. T.; Hustad, P. D.; Coates, G. W.; Archer, L. A.; Rucker, S. P.; Lohse, D. J.; *Macromolecules* **2005**, *38*, 10061.
(162)   Lyoo, W. S.; Kim, B. C.; Ha, W. S.; *Polym. Eng. Sci.* **1997**, *37*, 1259.
(163)   Dorgan, J. R.; Janzen, J.; Knauss, D. M.; Hait, S. B.; Limoges, B. R.; Hutchinson, M. H.; *J. Polym. Sci. Part B: Polym. Phys.* **2005**, *43*, 3100.
(164)   Dorgan, J. R.; Janzen, J.; Clayton, M. P.; Hait, S. B.; Knauss, D. M.; *J. Rheol.* **2005**, *49*, 607.
(165)   Hirata, M.; Kimura, Y.; *Polymer* **2008**, *49*, 2656.

(166)   Othman, N.; Xu, C.; Mehrkhodavandi, P.; Hatzikiriakos, S. G.; *Polymer* **2012**, *53*, 2443.
(167)   Chen, K.; Harris, K.; Vyazovkin, S.; *Macromolecular Chemistry and Physics* **2007**, *208*, 2525.
(168)   Burchard, W. In *Branched Polymers II*; Roovers, J., Ed.; Springer Berlin Heidelberg: 1999; Vol. 143, p 113.
(169)   Lehermeier, H. J.; Dorgan, J. R.; *Polym. Eng. Sci.* **2001**, *41*, 2172.
(170)   Eckstein, A.; Suhm, J.; Friedrich, C.; Maier, R. D.; Sassmannshausen, J.; Bochmann, M.; Mülhaupt, R.; *Macromolecules* **1998**, *31*, 1335.
(171)   Zirkel, A.; Urban, V.; Richter, D.; Fetters, L. J.; Huang, J. S.; Kampmann, R.; Hadjichristidis, N.; *Macromolecules* **1992**, *25*, 6148.
(172)   Green, M. S.; Tobolsky, A. V.; *J. Chem. Phys.* **1946**, *14*, 80.
(173)   Palade, L.; Lehermeier, H. J.; Dorgan, J. R.; *Macromolecules* **2001**, *34*, 1384.
(174)   Shimasaki, K.; Aida, T.; Inoue, S.; *Macromolecules* **1987**, *20*, 3076.
(175)   Barakat, I.; Dubois, P.; Jerome, R.; Teyssie, P.; *Macromolecules* **1991**, *24*, 6542.
(176)   Aluthge, D. C.; Xu, C.; Othman, N.; Noroozi, N.; Hatzikiriakos, S. G.; Mehrkhodavandi, P.; *Macromolecules* **2013**, *46*, 3965.
(177)   Kataoka, K.; Harada, A.; Nagasaki, Y.; *Adv. Drug Delivery Rev.* **2012**, *64*, 37.
(178)   Yao, K. J.; Tang, C. B.; *Macromolecules* **2013**, *46*, 1689.
(179)   Chen, G.-Q.; Patel, M. K.; *Chem. Rev.* **2012**, *112*, 2082.
(180)   Gupta, A. P.; Kumar, V.; *Eur. Polym. J.* **2007**, *43*, 4053.
(181)   Okada, M.; *Prog. Polym. Sci.* **2002**, *27*, 87.
(182)   Aida, T.; Inoue, S.; *Acc. Chem. Res.* **1996**, *29*, 39.
(183)   Guillaume, S. M.; Carpentier, J.-F.; *Catal. Sci.Technol.* **2012**, *2*, 898.
(184)   Ajellal, N.; Carpentier, J.-F.; Guillaume, C.; Guillaume, S. M.; Helou, M.; Poirier, V.; Sarazin, Y.; Trifonov, A.; *Dalton Trans.* **2010**, *39*, 8363.
(185)   Wang, L.; Poirier, V.; Ghiotto, F.; Bochmann, M.; Cannon, R. D.; Carpentier, J.-F.; Sarazin, Y.; *Macromolecules* **2014**, *47*, 2574.
(186)   Delgado, P. A.; Hillmyer, M. A.; *RSC Advances* **2014**, *4*, 13266.
(187)   Williams, C. K.; *Chem. Soc. Rev.* **2007**, *36*, 1573.
(188)   Biedroń, T.; Brzeziński, M.; Biela, T.; Kubisa, P.; *J. Polym. Sci. Part A: Polym. Chem.* **2012**, *50*, 4538.
(189)   Corneillie, S.; Smet, M.; *Polym. Chem.* **2015**, *6*, 850.
(190)   Liu, N.; Liu, B.; Yao, C.; Cui, D.; *Polymers* **2016**, *8*, 17.
(191)   FitzPatrick, M.; Champagne, P.; Cunningham, M. F.; Whitney, R. A.; *Bioresource Technology* **2010**, *101*, 8915.
(192)   Bozell, J. J.; Petersen, G. R.; *Gren Chem.* **2010**, *12*, 539.
(193)   Kubo, S.; Kadla, J. F.; *Macromolecules* **2004**, *37*, 6904.
(194)   Chung, Y.-L.; Olsson, J. V.; Li, R. J.; Frank, C. W.; Waymouth, R. M.; Billington, S. L.; Sattely, E. S.; *ACS Sus. Chem. Eng.* **2013**, *1*, 1231.
(195)   Rahman, M. A.; De Santis, D.; Spagnoli, G.; Ramorino, G.; Penco, M.; Phuong, V. T.; Lazzeri, A.; *Journal of Applied Polymer Science* **2013**, *129*, 202.
(196)   Anwer, M. A. S.; Naguib, H. E.; Celzard, A.; Fierro, V.; *Composites Part B: Engineering* **2015**, *82*, 92.
(197)   Ren, W.; Pan, X.; Wang, G.; Cheng, W.; Liu, Y.; *Gren Chem.* **2016**, *18*, 5008.
(198)   Sun, Y.; Yang, L.; Luc, X.; He, C.; *J. Mater. Chem. A.* **2015**, *3*, 3699.
(199)   Zhang, W.; Ma, Y.; Wang, C.; Li, S.; Zhang, M.; Chu, F.; *Industrial Crops and Products* **2013**, *43*, 326.
(200)   Hatakeyama, T.; Izuta, Y.; Hirose, S.; Hatakeyama, H.; *Polymer* **2002**, *43*, 1177.
(201)   Bonini, C.; D'Auria, M.; Ferri, R.; Pucciariello, R.; Sabia, A. R.; *Journal of Applied Polymer Science* **2003**, *90*, 1163.
(202)   Duong, L. D.; Luong, N. D.; Binh, N. T. T.; Park, I. K.; Lee, S. H.; Kim, D. S.; Lee, Y. S.; Lee, Y. K.; Kim, B. W.; Kim, K. H.; KyuYoon, H.; Yun, J. H.; Do Nam, J.; *Bioresources* **2013**, *8*, 4518.
(203)   Laurichesse, S.; Avérous, L.; *Polymer* **2013**, *54*, 3882.
(204)   Sun, Y.; Yang, L. P.; Lu, X. H.; He, C. B.; *J. Mater. Chem. A* **2015**, *3*, 3699.
(205)   Ge, F. J.; Huang, Y.; Luo, Y.; Jiang, L.; Dan, Y.; *RSC Advances* **2014**, *4*, 63118.
(206)   de Arenaza, I. M.; Sarasua, J. R.; Amestoy, H.; Lopez-Rodriguez, N.; Zuza, E.; Meaurio, E.; Meyer, F.; Santos, J. I.; Raquez, J. M.; Dubois, P.; *J. Appl. Polym. Sci.* **2013**, *130*, 4327.

(207)   Xie, H.; He, M. J.; Deng, X. Y.; Du, L.; Fan, C. J.; Yang, K. K.; Wang, Y. Z.; *ACS Appl. Mater. Interfaces* **2016**, *8*, 9431.

(208)   Manna, C. M.; Kaur, A.; Yablon, L. M.; Haeffner, F.; Li, B.; Byers, J. A.; *J. Am. Chem. Soc.* **2015**, *137*, 14232.

(209)   Biernesser, A. B.; Chiaie, K. R.; Curley, J. B.; Byers, J. A.; *Angew. Chem. Int. Ed.* **2016**, *55*, 5251.

(210)   Takashima, Y.; Nakayama, Y.; Watanabe, K.; Itono, T.; Ueyama, N.; Nkamura, A.; Yasuda, H.; Harada, A.; *Macromolecules* **2002**, 7538.

(211)   Coffindaffer, T. W.; Rothwell, I. P.; Huffman, J. C.; *Inorg. Chem.* **1983**, *22*, 2910.

(212)   Cayuela, J.; Bounor-Legare, V.; Cassagnau, P.; Michel, A.; *macromolecules* **2006**, *39*, 1338.

(213)   Platel, R. H.; White, A. J.; Williams, C. K.; *Inorg. Chem.* **2011**, *50*, 7718.

(214)   Walshe, A.; Fang, J.; Maron, L.; Baker, R. J.; *Inorg. Chem.* **2013**, *52*, 9077.

(215)   Ng, J. J.; Durr, C. B.; Lance, J. M.; Bunge, S. D.; *Eur. J. Inorg. Chem.* **2010**, *2010*, 1424.

(216)   Yang, S.; Nie, K.; Zhang, Y.; Xue, M.; Yao, Y.; Shen, Q.; *Inorg. Chem.* **2014**, *53*, 105.

(217)   Nishiura, M.; Hou, Z.; Koizumi, T.-a.; Imamoto, T.; Wakatsuki, Y.; *Macromolecules* **1999**, *32*, 8245.

(218)   Ling, J.; Shen, Z.; Huang, Q.; *Macromolecules* **2001**, *34*, 7613.

(219)   Schuetz, S. A.; Silvernail, C. M.; Incarvito, C. D.; Rheingold, A. L.; Clark, J. L.; Day, V. W.; Belot, J. A.; *Inorg. Chem.* **2004**, *43*, 6203.

(220)   Zhu, W.; Ling, J.; Shen, Z.; *Polymer Bulletin* **2004**, *52*, 185.

(221)   Hsieh, K. C.; Lee, W. Y.; Hsueh, L. F.; Lee, H. M.; Huang, J. H.; *Eur. J. Inorg. Chem.* **2006**, *2006*, 2306.

(222)   Pérez, Y.; del Hierro, I.; Sierra, I.; Gómez-Sal, P.; Fajardo, M.; Otero, A.; *Journal of Organometallic Chemistry* **2006**, *691*, 3053.

(223)   Bunge, S. D.; Lance, J. M.; Bertke, J. A.; *Organometallics* **2007**, *26*, 6320.

(224)   Clark, L.; Cushion, M. G.; Dyer, H. E.; Schwarz, A. D.; Duchateau, R.; Mountford, P.; *Chem. Commun.* **2010**, *46*, 273.

(225)   Ikram, M.; Baker, R. J.; *Journal of Fluorine Chemistry* **2012**, *139*, 58.

(226)   Yuan, C.; Xu, X.; Zhang, Y.; Ji, S.; *Chinese Journal of Chemistry* **2012**, *30*, 1474.

(227)   Turner, Z. R.; Buffet, J.-C.; O'Hare, D.; *Organometallics* **2014**, *33*, 3891.

(228)   Honrado, M.; Otero, A.; Fernández-Baeza, J.; Sánchez-Barba, L. F.; Garcés, A.; Lara-Sánchez, A.; Martínez-Ferrer, J.; Sobrino, S.; Rodríguez, A. M.; *Organometallics* **2015**, *34*, 3196.

(229)   Keuchguerian, A.; Mougang-Soume, B.; Schaper, F.; Zargarian, D.; *Canadian Journal of Chemistry* **2015**, *93*, 594.

(230)   Honrado, M.; Otero, A.; Fernández-Baeza, J.; Sánchez-Barba, L. F.; Garcés, A.; Lara-Sánchez, A.; Rodríguez, A. M.; *Organometallics* **2016**, *35*, 189.

(231)   Stevels, W. M.; Akone, M. J. K.; Dijkstra, P. J.; Feijen, J.; *Macromolecules* **1996**, 6132.

(232)   Manna, C. M.; Kaplan, H. Z.; Li, B.; Byers, J. A.; *Polyhedron* **2014**, *84*, 160.

(233)   Liao, T.-C.; Huang, Y.-L.; Huang, B.-H.; Lin, C.-C.; *Macromol. Chem. Phys.* **2003**, *204*, 885.

(234)   Monegan, J. D.; Bunge, S. D.; *Inorg. Chem.* **2009**, *48*, 3248.

(235)   Calvo, B.; Davidson, M. G.; García-Vivó, D.; *Inorg. Chem.* **2011**, *50*, 3589.

(236)   Castro-Osma, J. A.; Alonso-Moreno, C.; Marquez-Segovia, I.; Otero, A.; Lara-Sanchez, A.; Fernandez-Baeza, J.; Rodriguez, A. M.; Sanchez-Barba, L. F.; Garcia-Martinez, J. C.; *Dalton Trans.* **2013**, *42*, 9325.

(237)   Munoz, M. T.; Cuenca, T.; Mosquera, M. E. G.; *Dalton Trans.* **2014**, *43*, 14377.

(238)   Otero, A.; Lara-Sánchez, A.; Fernández-Baeza, J.; Alonso-Moreno, C.; Castro-Osma, J. A.; Márquez-Segovia, I.; Sánchez-Barba, L. F.; Rodríguez, A. M.; Garcia-Martinez, J. C.; *Organometallics* **2011**, *30*, 1507.

(239)   Osten, K. M.; Yu, I.; Duffy, I. R.; Lagaditis, P. O.; Yu, J. C.; Wallis, C. J.; Mehrkhodavandi, P.; *Dalton Trans.* **2012**, *26*, 8123.

(240)   Rossmurphy, S. B.; *Polym. Gels Netw.* **1994**, *2*, 229.

(241)   Kavanagh, G. M.; Ross-Murphy, S. B.; *Prog. Polym. Sci.* **1998**, *23*, 533.

(242)   Cretu, A.; Kipping, M.; Adler, H. J.; Kuckling, D.; *Polymer International* **2008**, *57*, 905.

(243)   Wei, M.; Gao, Y.; Li, X.; Serpe, M. J.; *Polym. Chem.* **2017**, *8*, 127.

(244)   Yang, Y.; Ding, X. C.; Urban, M. W.; *Prog. Polym. Sci.* **2015**, *49*, 34.

(245)   Annable, T.; Buscall, R.; Ettelaie, R.; Whittlestone, D.; *J. Rheol.* **1993**, *37*, 695.

(246)   Tanaka, F.; Edwards, S. F.; *Macromolecules* **1992**, *25* 1516.

(247)	Wietor, J. L.; van Beek, D. J. M.; Peters, G. W.; Mendes, E.; Sijbesmat, R. P.; *Macromolecules* **2011**, *44*, 1211.
(248)	Zhao, W.; Li, C.; Liu, B.; Wang, X.; Li, P.; Wang, Y.; Wu, C.; Yao, C.; Tang, T.; Liu, X.; Cui, D.; *Macromolecules* **2014**, *47*, 5586.
(249)	van Beek, D. J. M.; Spiering, A. J. H.; Peters, G. W. M.; te Nijenhuis, K.; Sijbesma, R. P.; *Macromolecules* **2007**, *40*, 8464.
(250)	Brzeziński, M.; Biela, T.; *Macromolecules* **2015**, *48*, 2994.
(251)	Bao, J.; Chang, R.; Shan, G.; Bao, Y.; Pan, P.; *Crystal Growth & Design* **2016**, *16*, 1502.
(252)	Burattini, S.; Greenland, B. W.; Merino, D. H.; Weng, W.; Seppala, J.; Colquhoun, H. M.; Hayes, W.; Mackay, M. E.; Hamley, I. W.; Rowan, S. J.; *J. Am. Chem. Soc.* **2010**, *132*, 12051.
(253)	Arenaza, I. M. d.; Obarzanek-Fojt, M.; Sarasua, J. R.; Meaurio, E.; Meyer, F.; Raquez, J. M.; Dubois, P.; Bruinink, A.; *Biomedical Materials* **2015**, *10*, 045003.
(254)	Woodward, P. J.; Hermida Merino, D.; Greenland, B. W.; Hamley, I. W.; Light, Z.; Slark, A. T.; Hayes, W.; *Macromolecules* **2010**, *43*, 2512.
(255)	Hu, G. J.; Zhao, C. G.; Zhang, S. M.; Yang, M. S.; Wang, Z. G.; *Polymer* **2006**, *47*, 480.
(256)	Krishnamoorti, R.; Giannelis, E. P.; *Macromolecules* **1997**, *30*, 4097.
(257)	Herbst, F.; Schroter, K.; Gunkel, I.; Groger, S.; Thurn-Albrecht, T.; Balbach, J.; Binder, W. H.; *Macromolecules* **2010**, *43*, 10006.
(258)	McNally, T.; Potschke, P.; Halley, P.; Murphy, M.; Martin, D.; Bell, S. E. J.; Brennan, G. P.; Bein, D.; Lemoine, P.; Quinn, J. P.; *Polymer* **2005**, *46*, 8222.
(259)	Wu, D.; Wu, L.; Sun, Y.; Zhang, M.; *J. Polym. Sci. Part B: Polym. Phys.* **2007**, *45*, 3137.
(260)	Martinez, C. R.; Iverson, B. L.; *Chem. Sci.* **2012**, *3*, 2191.
(261)	Shabbir, A.; Goldansaz, H.; Hassager, O.; van Ruymbeke, E.; Alvarez, N. J.; *Macromolecules* **2015**, *48*, 5988.
(262)	Li, Y.; Yao, Z.; Chen, Z.-h.; Qiu, S.-l.; Zeng, C.; Cao, K.; *Ind. Eng. Chem. Res.* **2013**, *52*, 7758.
(263)	Thakur, V. K.; Thakur, M. K.; Raghavan, P.; Kessler, M. R.; *ACS Sus. Chem. Eng.* **2014**, *2*, 1072.
(264)	Chunyu, M.; Liyuan, X.; Jun, Z.; Man, J.; Zuowan, Z.; *BioResources* **2014**, *9*, 5557.
(265)	Gordobil, O.; Egues, I.; Llano-Ponte, R.; Labidi, J.; *Polymer Degradation and Stability* **2014**, *108*, 330.
(266)	Iyer, K. A.; Torkelson, J. M.; *ACS Sus. Chem. Eng.* **2015**, *3*, 959.
(267)	Yu, J.; Wang, J.; Wang, C.; Liu, Y.; Xu, Y.; Tang, C.; Chu, F.; *Macromol. Rapid Commun.* **2015**, *36*, 398.
(268)	Wang, C.; Venditti, R. A.; *ACS Sus. Chem. Eng.* **2015**, *3*, 1839.
(269)	Liu, X.; Zong, E.; Jiang, J.; Fu, S.; Wang, J.; Xu, B.; Li, W.; Lin, X.; Xu, Y.; Wang, C.; Chu, F.; *International Journal of Biological Macromolecules* **2015**, *81*, 521.
(270)	Pérez–Camargo, R. A.; Saenz, G.; Laurichesse, S.; Casas, M. T.; Puiggalí, J.; Avérous, L.; Müller, A. J.; *Journal of Polymer Science Part B: Polymer Physics* **2015**, *53*, 1736.
(271)	Lin, X.; Zhou, M.; Wang, S.; Lou, H.; Yang, D.; Qiu, X.; *ACS Sus. Chem. Eng.* **2014**, *2*, 1902.
(272)	Luo, S.; Cao, J.; McDonald, A. G.; *ACS Sus. Chem. Eng.* **2016**, *4*, 3465.
(273)	Kim, S.; Oh, S.; Lee, J.; Ahn, N.; Roh, H.; Cho, J.; Chun, B.; Park, J.; *Fibers and Polymers* **2014**, *15*, 2458.
(274)	Kim, S. J.; Kim, Y. S.; Lee, O.-K.; Ahn, B.-J.; *Wood Science and Technology* **2016**, 1.
(275)	Kai, D.; Jiang, S.; Low, Z. W.; Loh, X. J.; *Journal of Materials Chemistry B* **2015**, *3*, 6194.
(276)	Kai, D.; Ren, W.; Tian, L.; Chee, P. L.; Liu, Y.; Ramakrishna, S.; Loh, X. J.; *ACS Sus. Chem. Eng.* **2016**.
(277)	Ren, W.; Pan, X. Y.; Wang, G.; Cheng, W. R.; Liu, Y.; *Gren Chem.* **2016**, *18*, 5008.
(278)	Vink, E. T. H.; Rábago, K. R.; Glassner, D. A.; Gruber, P. R.; *Polym. Degrad. Stab.* **2003**, *80*, 403.
(279)	Pratt, R. C.; Lohmeijer, B. G. G.; Long, D. A.; Waymouth, R. M.; Hedrick, J. L.; *J. Am. Chem. Soc.* **2006**, *128*, 4556.
(280)	Sherck, N. J.; Kim, H. C.; Won, Y.-Y.; *Macromolecules* **2016**, *49*, 4699.
(281)	Shin, E. J.; Jones, A. E.; Waymouth, R. M.; *Macromolecules* **2012**, *45*, 595.
(282)	Brown, H. A.; Waymouth, R. M.; *Acc. Chem. Res.* **2013**, *46*, 2585.
(283)	Ebrahimi, T.; Hatzikiriakos, S. G.; Mehrkhodavandi, P.; *Macromolecules* **2015**, *48*, 6672.
(284)	Schäler, K.; Ostas, E.; Schröter, K.; Thurn-Albrecht, T.; Binder, W. H.; Saalwächter, K.; *Macromolecules* **2011**, *44*, 2743.

(285)   Henke, S. F.; Shanbhag, S.; *Reactive and Functional Polymers* **2014**, *80*, 57.

(286)   Othman, N.; Acosta-Ramirez, A.; Mehrkhodavandi, P.; Dorgan, J. R.; Hatzikiriakos, S. G.; *J. Rheol.* **2011**, *55*, 987.

(287)   Liu, Q.; Li, P.; Liu, N.; Shen, D.; *Polymer Degradation and Stability* **2017**, *135*, 54.

(288)   Halverson, J. D.; Grest, G. S.; Grosberg, A. Y.; Kremer, K.; *Phys. Rev. Lett.* **2012**, *108*, 038301.

(289)   Pasquino, R.; Vasilakopoulos, T. C.; Jeong, Y. C.; Lee, H.; Rogers, S.; Sakellariou, G.; Allgaier, J.; Takano, A.; Brás, A. R.; Chang, T.; Gooßen, S.; Pyckhout-Hintzen, W.; Wischnewski, A.; Hadjichristidis, N.; Richter, D.; Rubinstein, M.; Vlassopoulos, D.; *ACS macro letters* **2013**, *2*, 874.

(290)   Pérez, R. A.; Córdova, M. E.; López, J. V.; Hoskins, J. N.; Zhang, B.; Grayson, S. M.; Müller, A. J.; *Reactive and Functional Polymers* **2014**, *80*, 71.

(291)   Kharchenko, S. B.; Kannan, R. M.; Cernohous, J. J.; Venkataramani, S.; *Macromolecules* **2003**, *36*, 399.

(292)   Chen, W.; Zhang, K.; Liu, L.; Chen, J.; Li, Y.; An, L.; *Macromolecules* **2017**, *50*, 1236.

(293)   Kapnistos, M.; Lang, M.; Vlassopoulos, D.; Pyckhout-Hintzen, W.; Richter, D.; Cho, D.; Chang, T.; Rubinstein, M.; *Nat Mater* **2008**, *7*, 997.

(294)   Doi, Y.; Matsubara, K.; Ohta, Y.; Nakano, T.; Kawaguchi, D.; Takahashi, Y.; Takano, A.; Matsushita, Y.; *Macromolecules* **2015**, *48*, 3140.

(295)   Schwenke, K.; Lang, M.; Sommer, J. U.; *Macromolecules* **2011**, *44*, 9464.

(296)   Kwon, Y.; Matsumiya, Y.; Watanabe, H.; *Macromolecules* **2016**, *49*, 3593.

(297)   de Oliveira, W.; Glasser, W. G.; *Macromolecules* **1994**, *27*, 5.

(298)   Hatzikiriakos, S. G.; Kapnistos, M.; Vlassopoulos, D.; Chevillard, C.; Winter, H. H.; Roovers, J.; *Rheol. Acta.* **2000**, *1*, 38.

(299)   Yu, J.; Wang, J.; Wang, C.; Liu, Y.; Xu, Y.; Tang, C.; Chu, F.; *Macromol Rapid Commun* **2015**, *36*, 398.

(300)   Yu, I.; Ebrahimi, T.; Hatzikiriakos, S. G.; Mehrkhodavandi, P.; *Dalton Trans.* **2015**, *44*, 14248.

(301)   Tang, S.; Habicht, A.; Li, S.; Seiffert, S.; Olsen, B. D.; *Macromolecules* **2016**.

Appendices

Appendix A

A.1 GC-MS analysis for *meso*-lactide purification
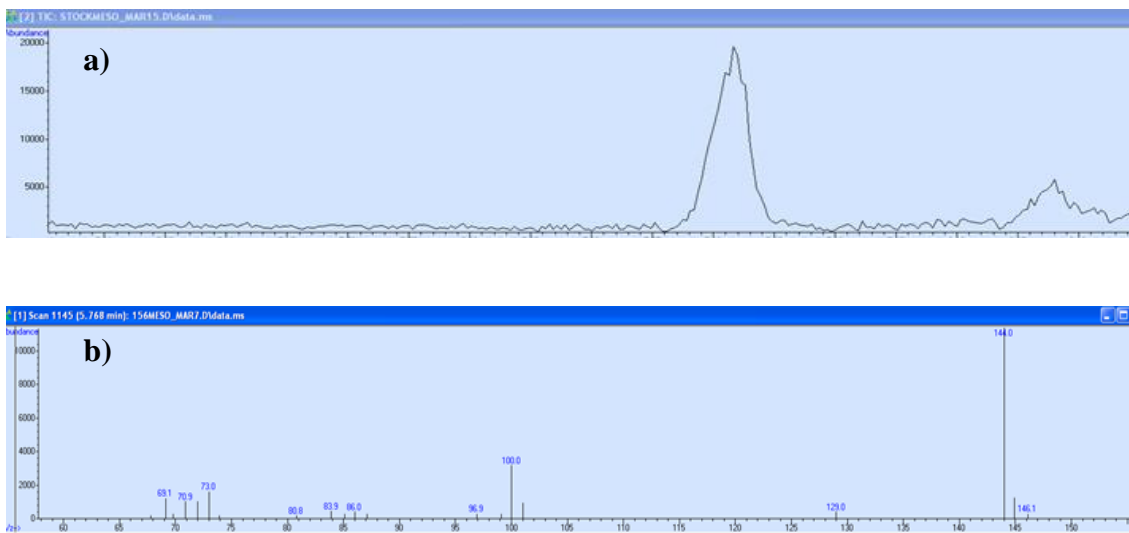
Figure A.1 a) GC-MS trace of *meso*-lactide before purification (26% *rac*-lactide) b) mass spectral data for peak eluting at 5.90 minutes.
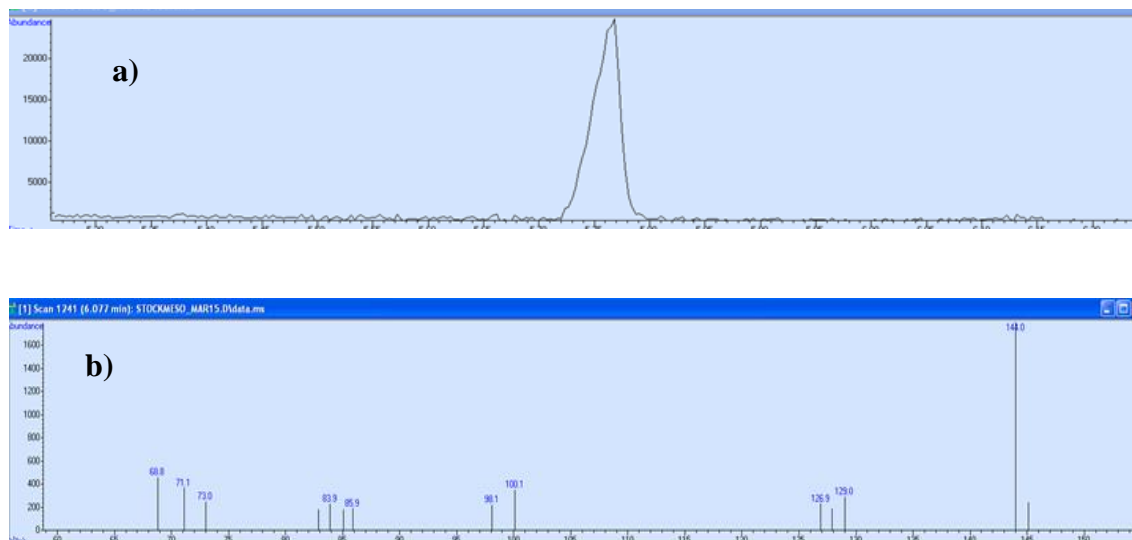
Figure A.2 a) GC-MS trace of *meso*-lactide after purification (<1% *rac*-lactide) b) mass spectral data for peak eluting at 5.75 minutes.

Appendix B

B.1 Isothermal time sweep experiments
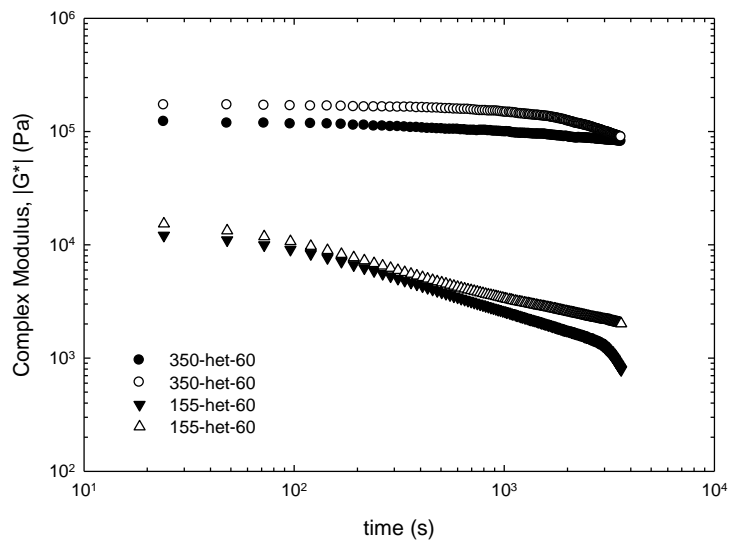
Figure B.1 Complex modulus, |G*| , vs. time for het-60 polymers of various molecular weights.
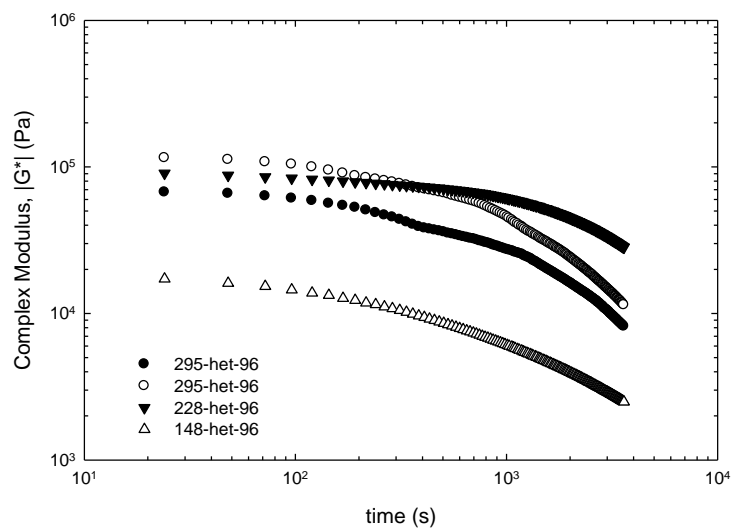
Figure B.2 Complex modulus, |G*| , vs. time for het-96 polymers of various molecular weights.
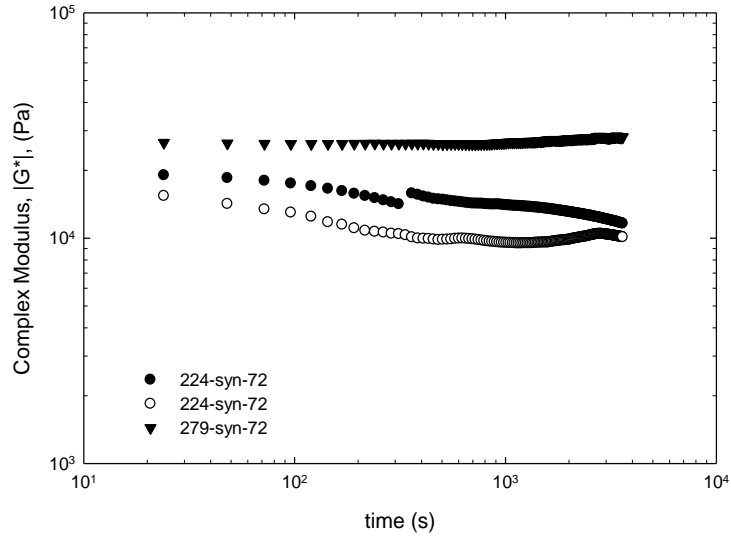
Figure B.3 Complex modulus, |G*| , vs. time for syn-72 polymers of various molecular weights.
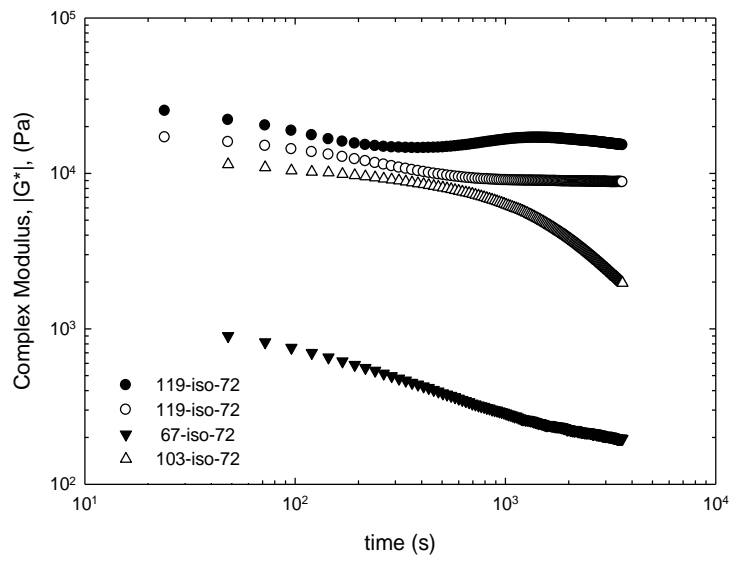
Figure B.4 Complex modulus, |G*| , vs. time for iso-72 polymers of various molecular weights

B.2 Van Gurp-Palmen plots
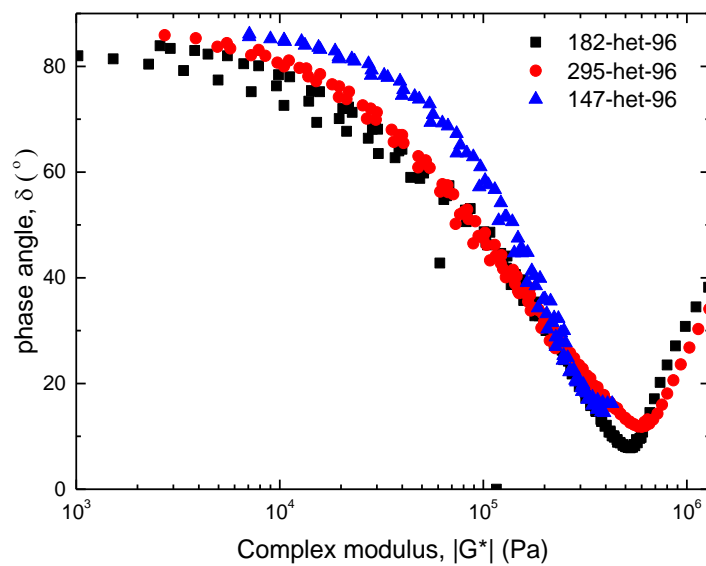
Figure B.5 Van Gurp-Palmen plots of het-96 polymers with varying molecular weights.
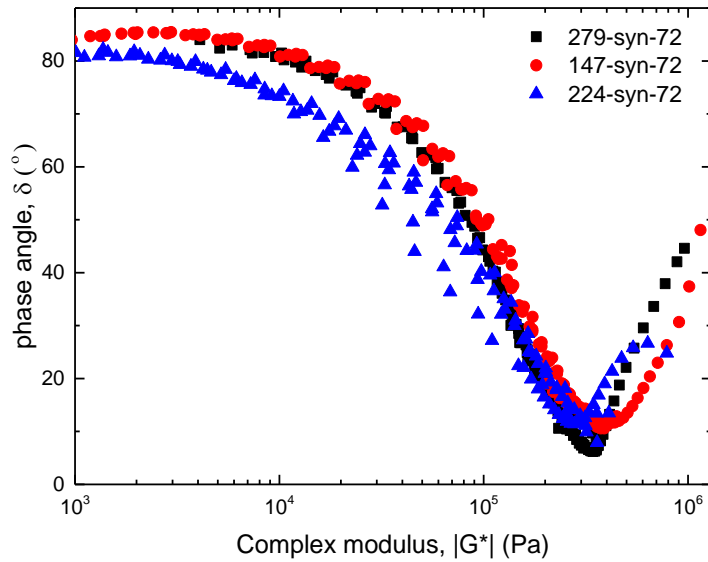
Figure B.6 Van Gurp-Palmen plots of syn-72 polymers with varying molecular weights.

B.3 Uniaxial extension experimental plots
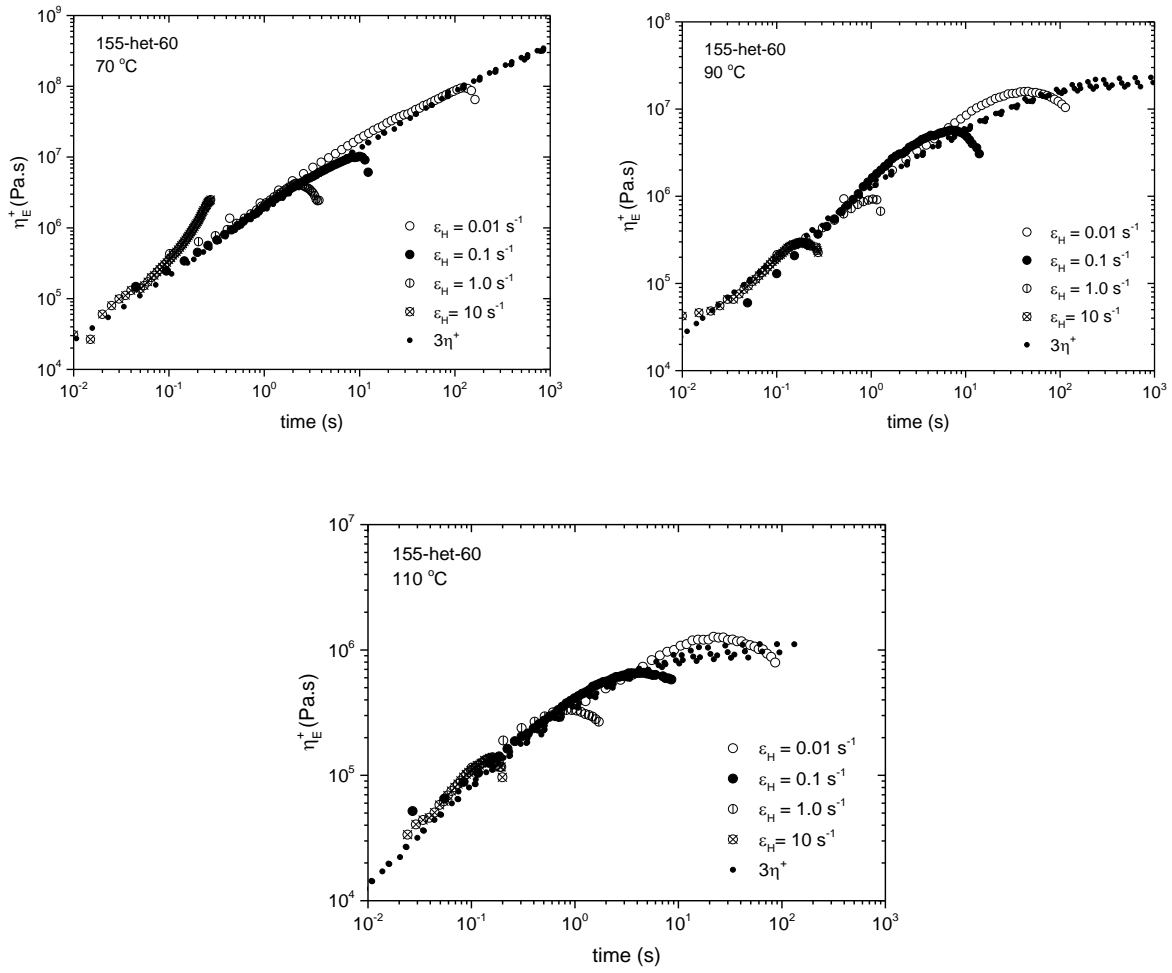
Figure B.7 Elongational viscosity as a function of time at Hencky strain rates from 0.01 to 10s[-1] for atactic PLA.
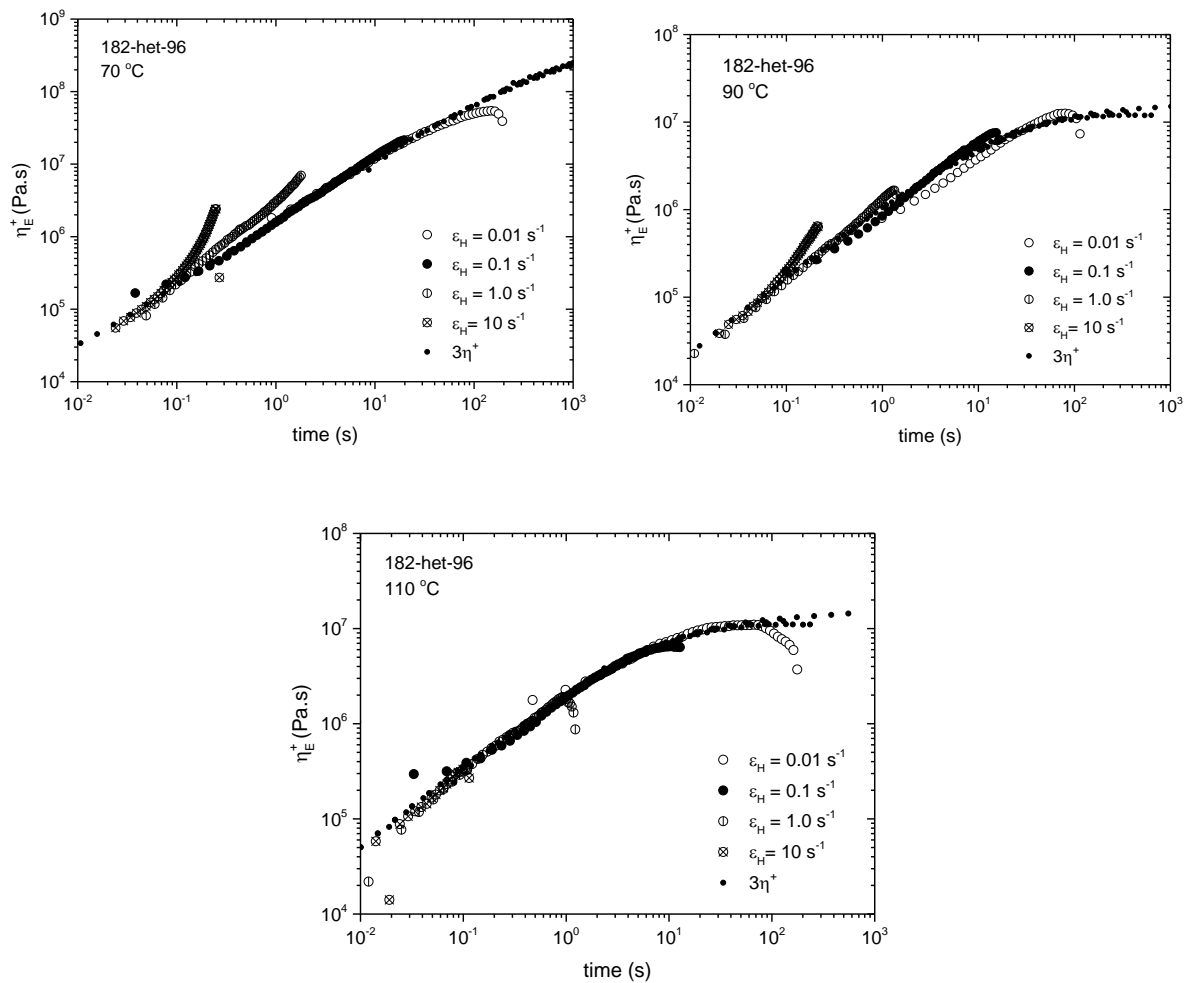
Figure B.8 Elongational viscosity as a function of time at Hencky strain rates from 0.01 to 10s[-1] for heterotactic PLA.
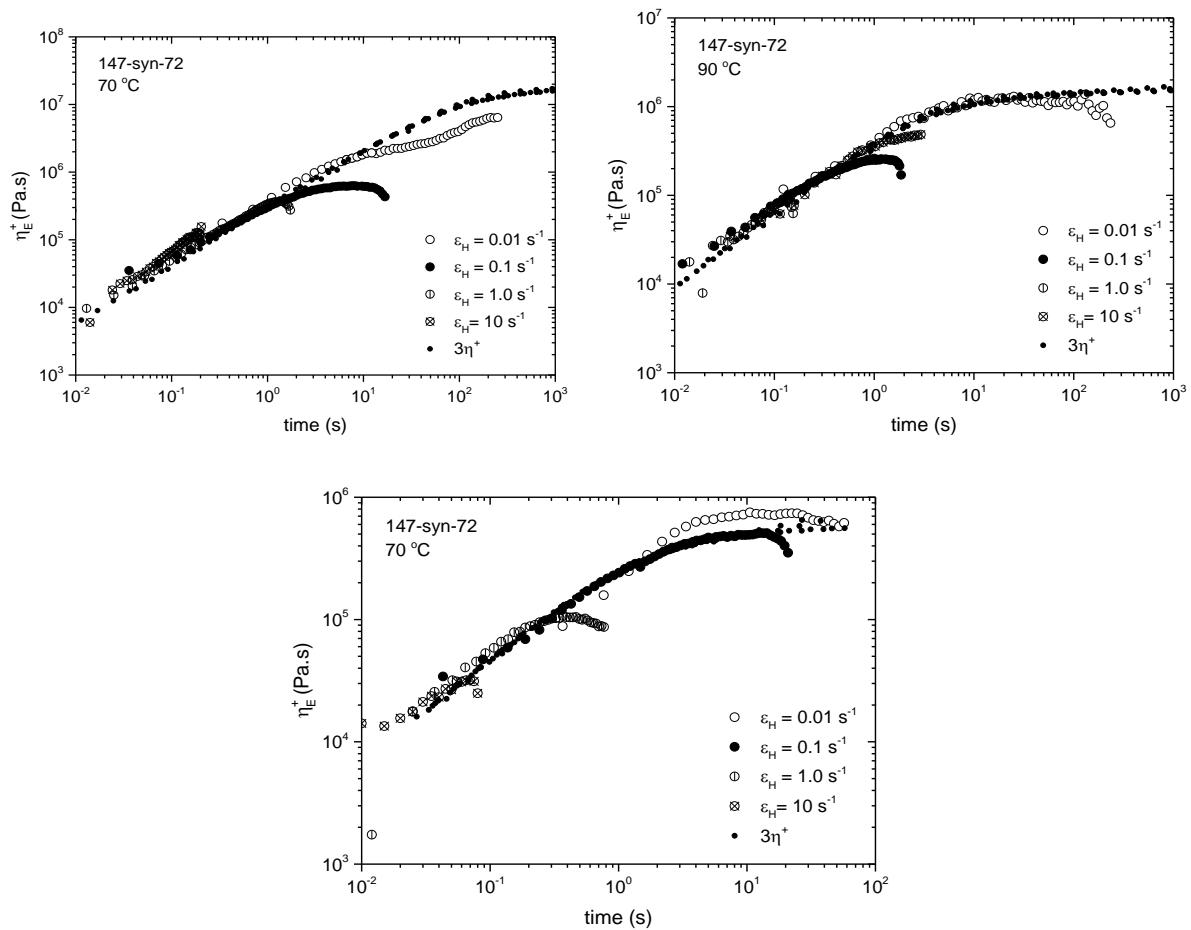
Figure B.9 Elongational viscosity as a function of time at Hencky strain rates from 0.01 to 10s[-1] for syndio-enriched PLA.
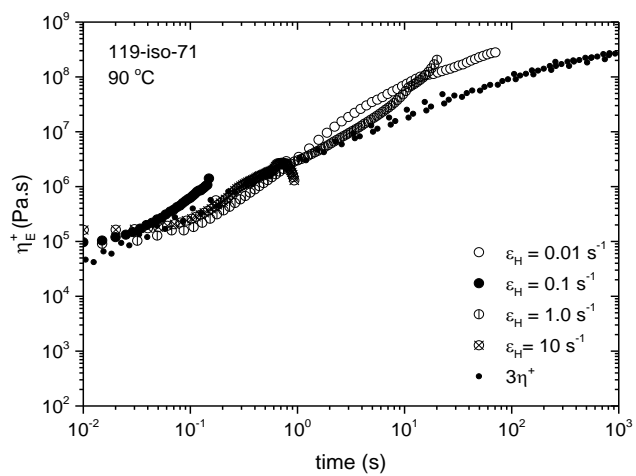
Figure B.10 Elongational viscosity as a function of time at Hencky strain rates from 0.01 to 10s^{-1} for isotactic stereo-gradient PLA.

Appendix C

C.1 Characterization of complexes 1-6 in the solution state
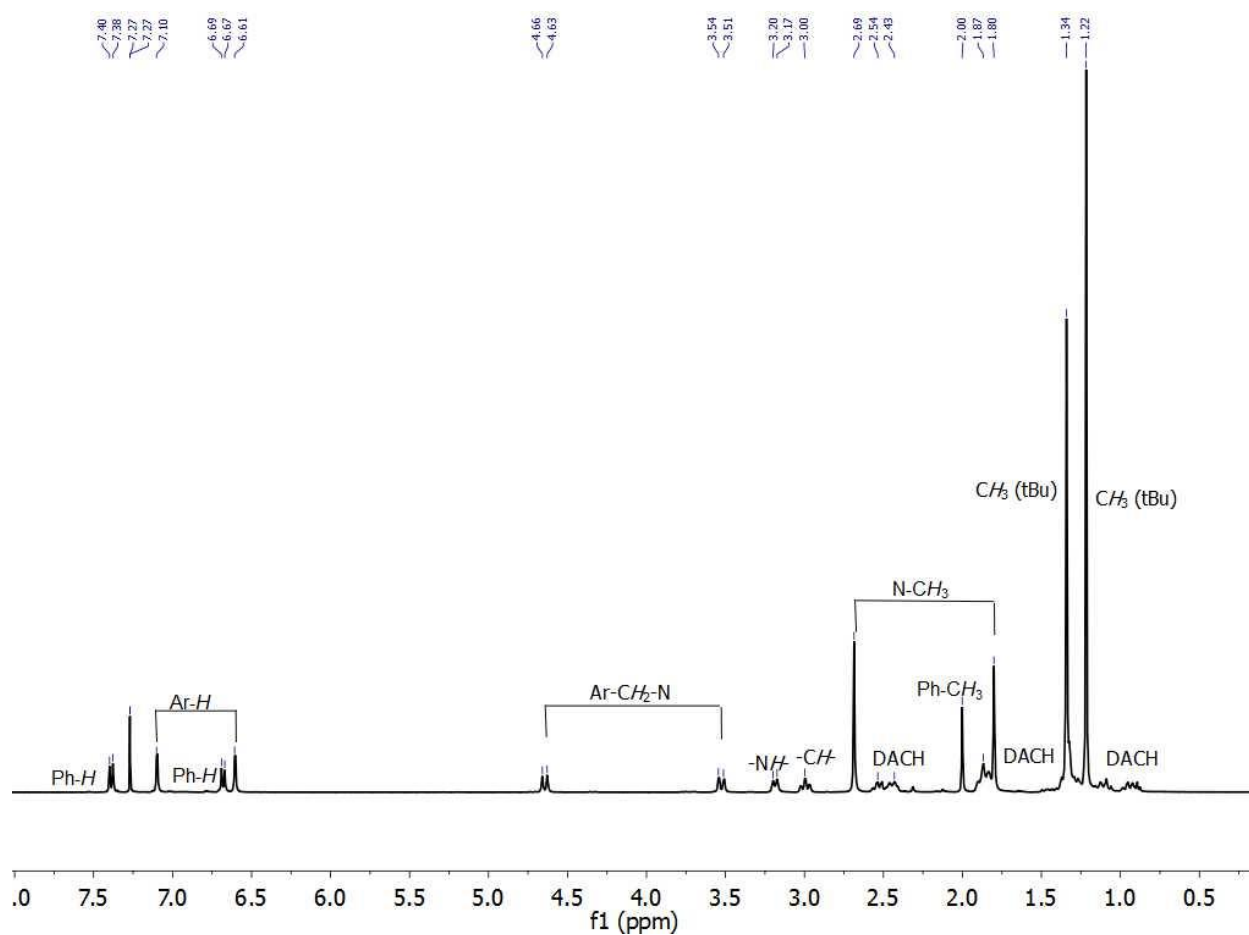
Figure C.1 ^{1}H NMR (CDCl$_3$, 25 °C, 400 MHz) spectrum of ($\pm$)-[(NNO)InCl]$_2$(μ-Cl)(μ-OPh$_{OMe}$) (**1**).
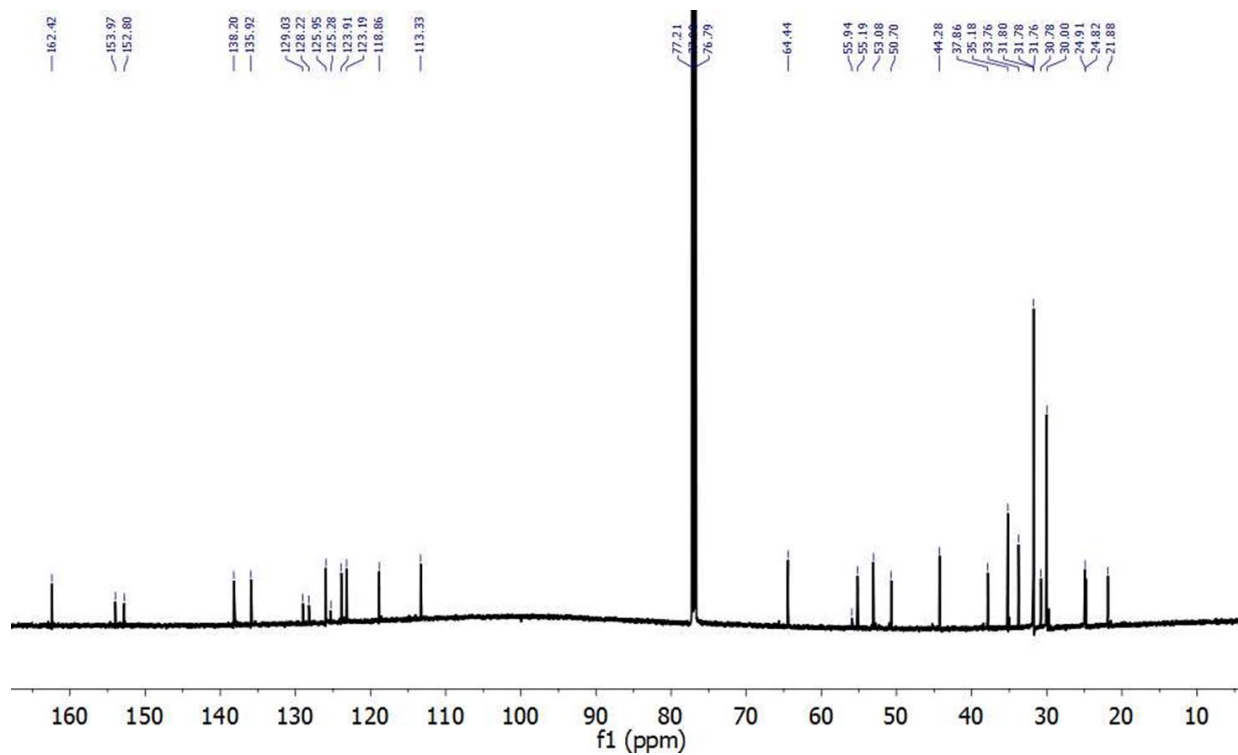
Figure C.2 $^{13}C\{^1H\}$ NMR (CDCl$_3$, 25 °C, 400 MHz) spectrum of (±)-[(NNO)InCl]$_2$(μ-Cl)(μ-OPh$_{OMe}$) (**1**).
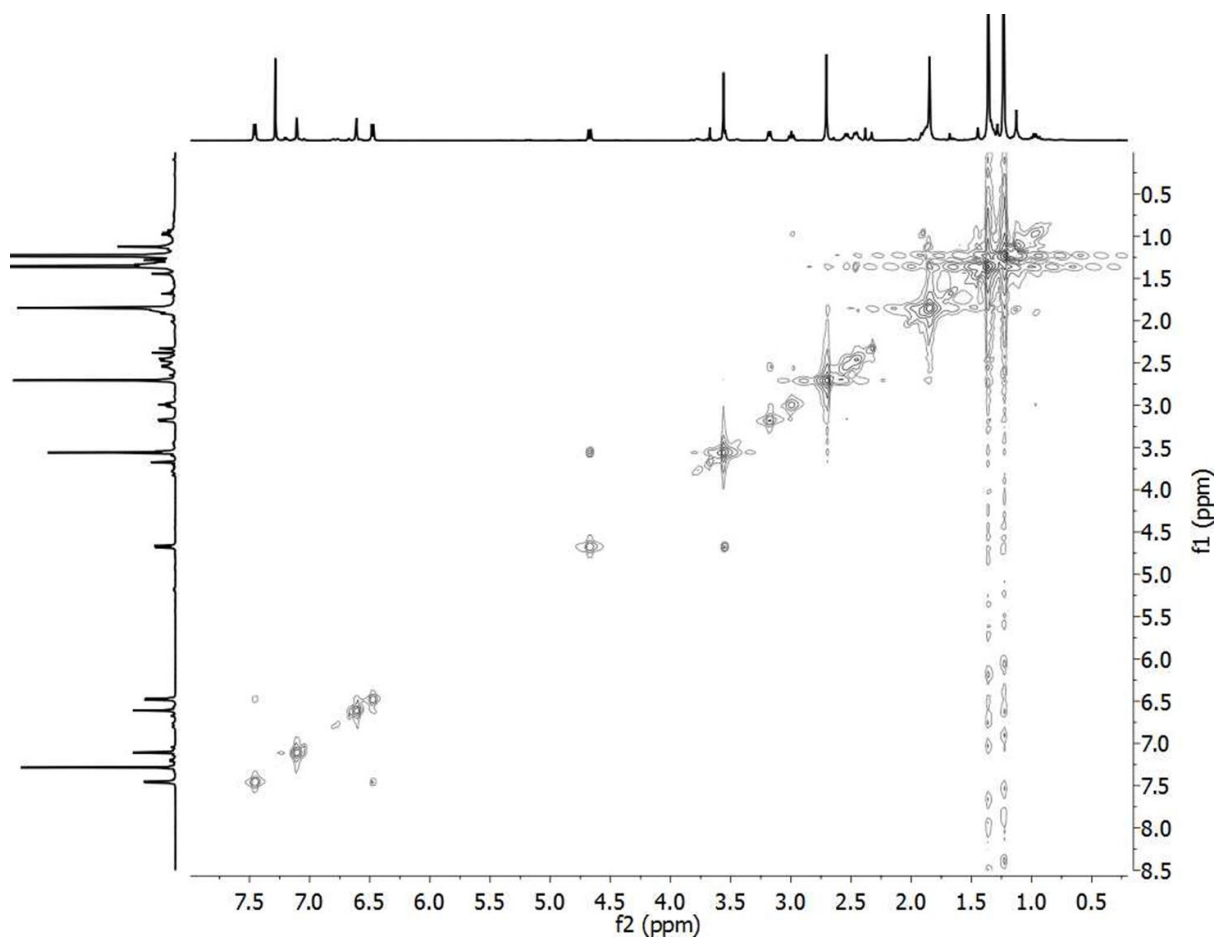
Figure C.3 ^{1}H – ^{1}H COSY (CDCl$_3$, 25 °C, 400 MHz) spectrum of (±)-[(NNO)InCl]$_2$(μ-Cl)(μ-OPh$_{OMe}$) (**1**).
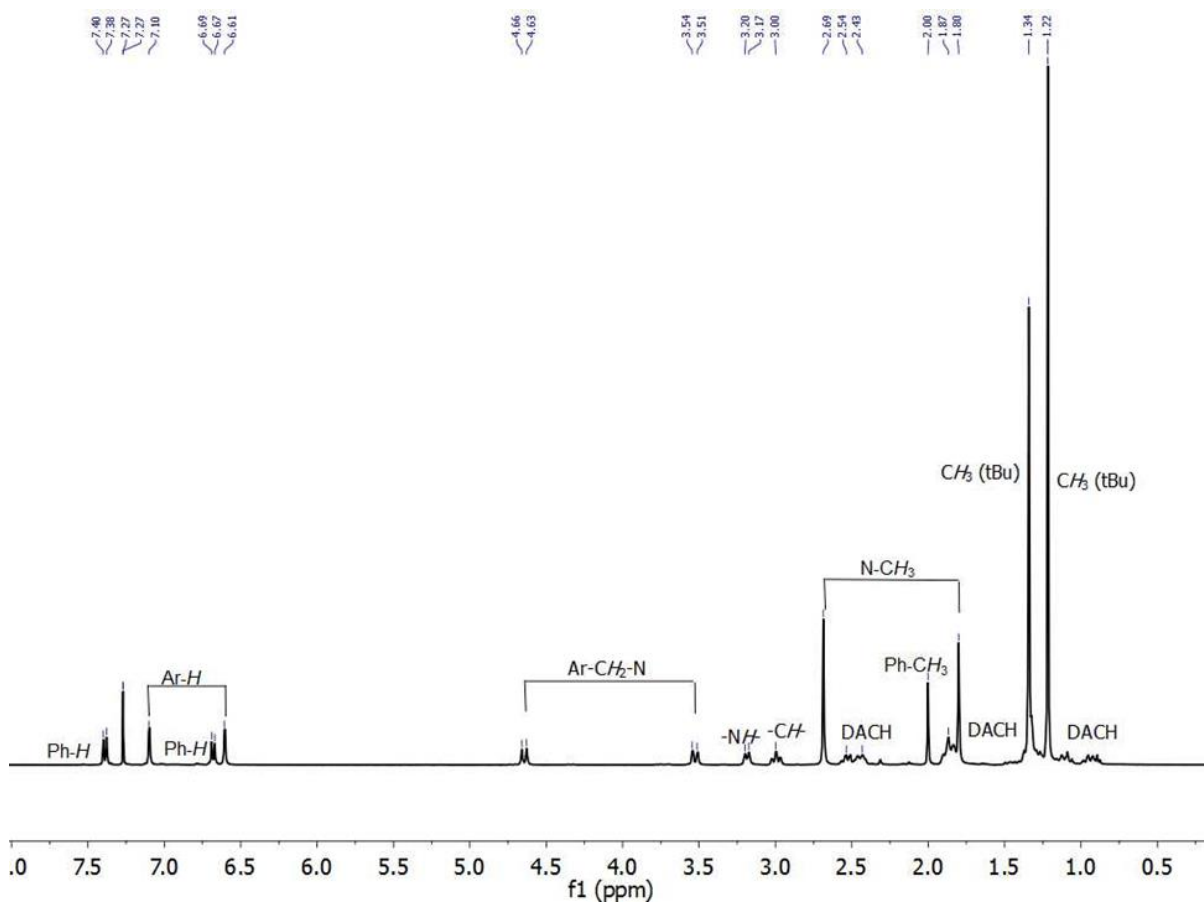
Figure C.4 ^{1}H NMR (CDCl$_3$, 25 °C, 400 MHz) spectrum of (±)-[(NNO)InCl]$_2$(μ-Cl)(μ-OPh$_{Me}$) (**2**).
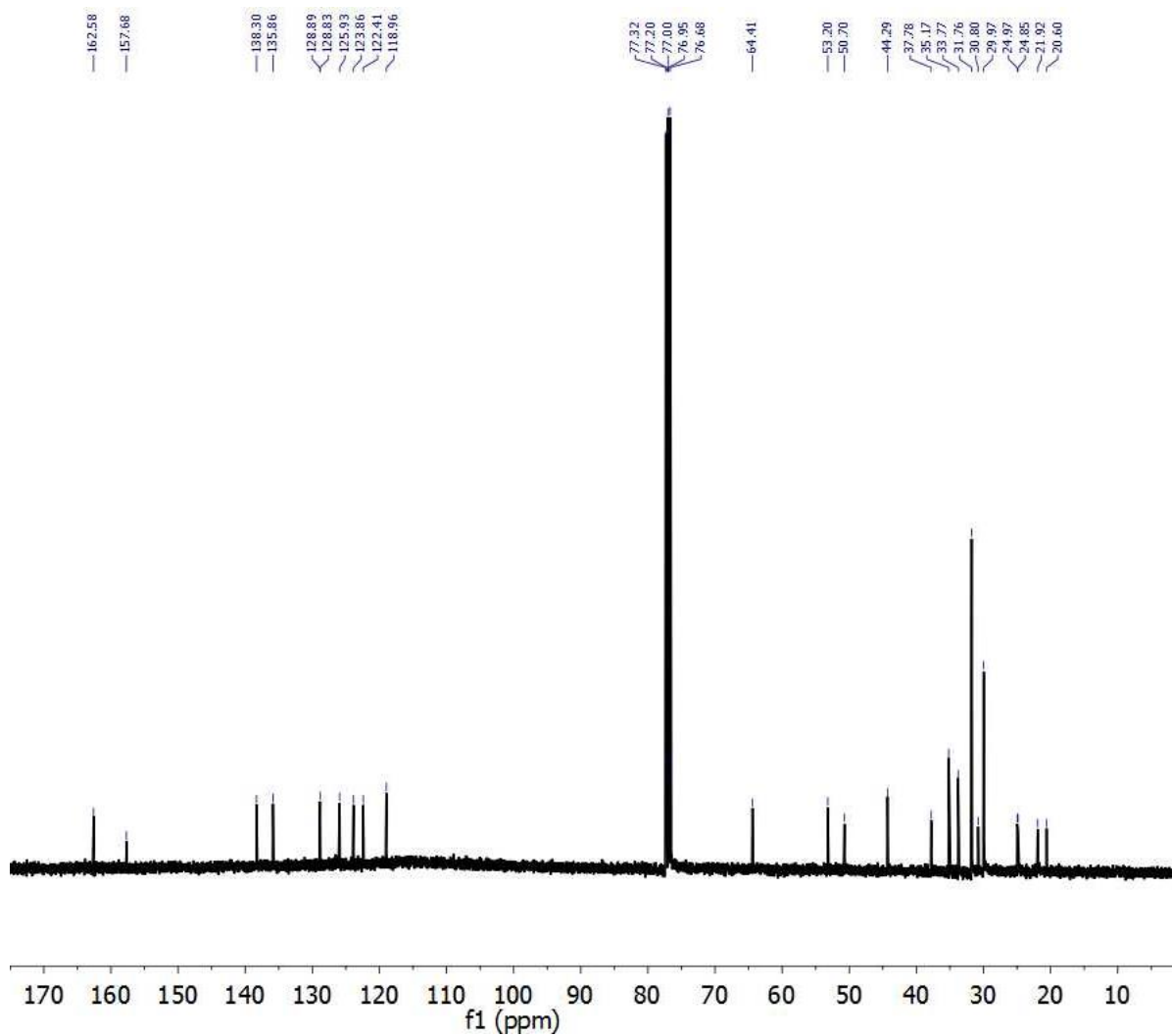
Figure C.5 ^{13}C{^{1}H} NMR (CDCl$_3$, 25 °C, 400 MHz) spectrum of (±)-[(NNO)InCl]$_2$(μ-Cl)(μ-OPh$_{Me}$) (**2**).
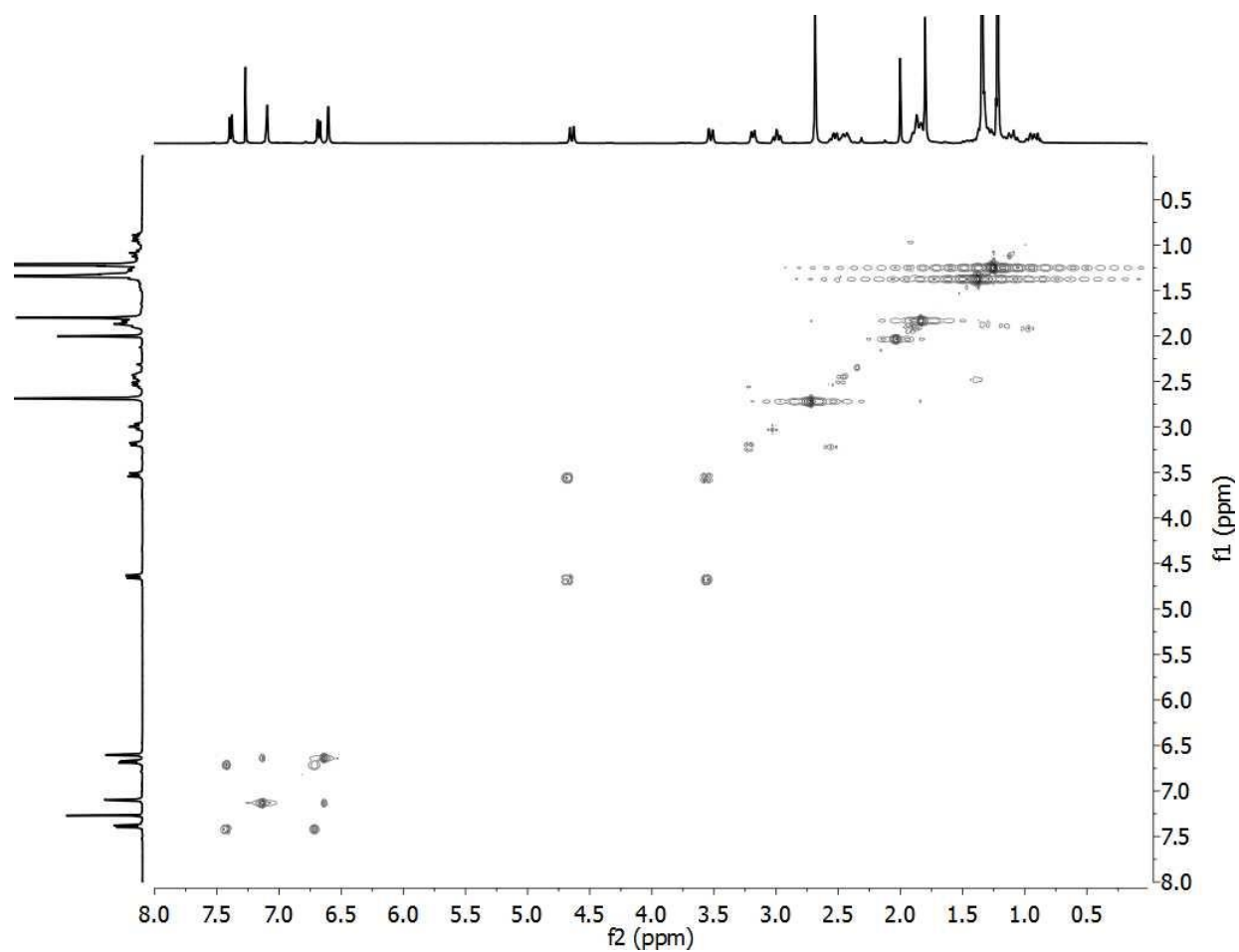
Figure C.6 ^{1}H – ^{1}H COSY (CDCl$_3$, 25 °C, 400 MHz) spectrum of (±)-[(NNO)InCl]$_2$(μ-Cl)(μ-OPh$_{Me}$) (**2**).
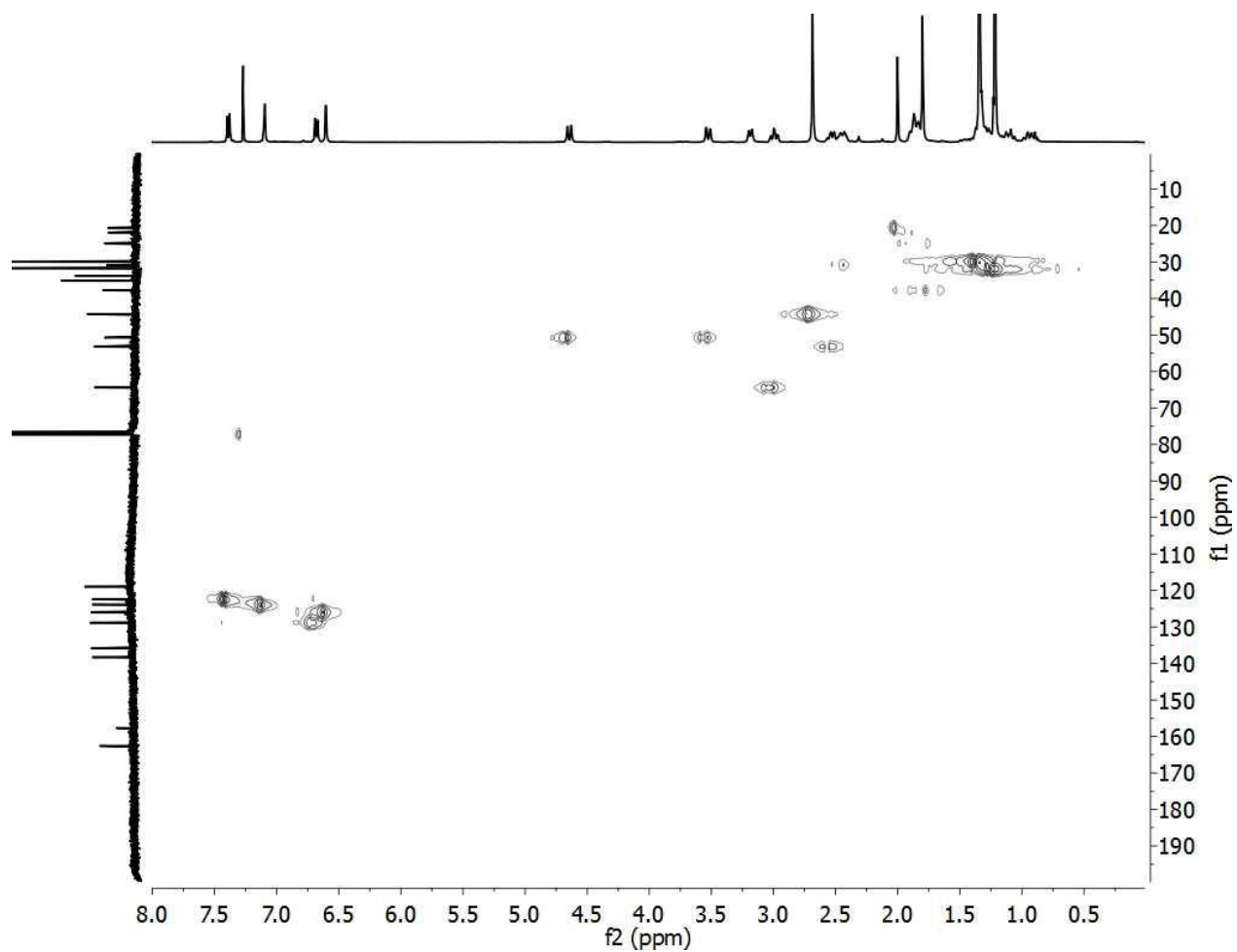
Figure C.7 ^1H – ^{13}C HMBC (CDCl$_3$, 25 °C, 40 MHz) spectrum of (±)-[(NNO)InCl]$_2$(μ-Cl)(μ-OPh$_{Me}$) (**2**).

270
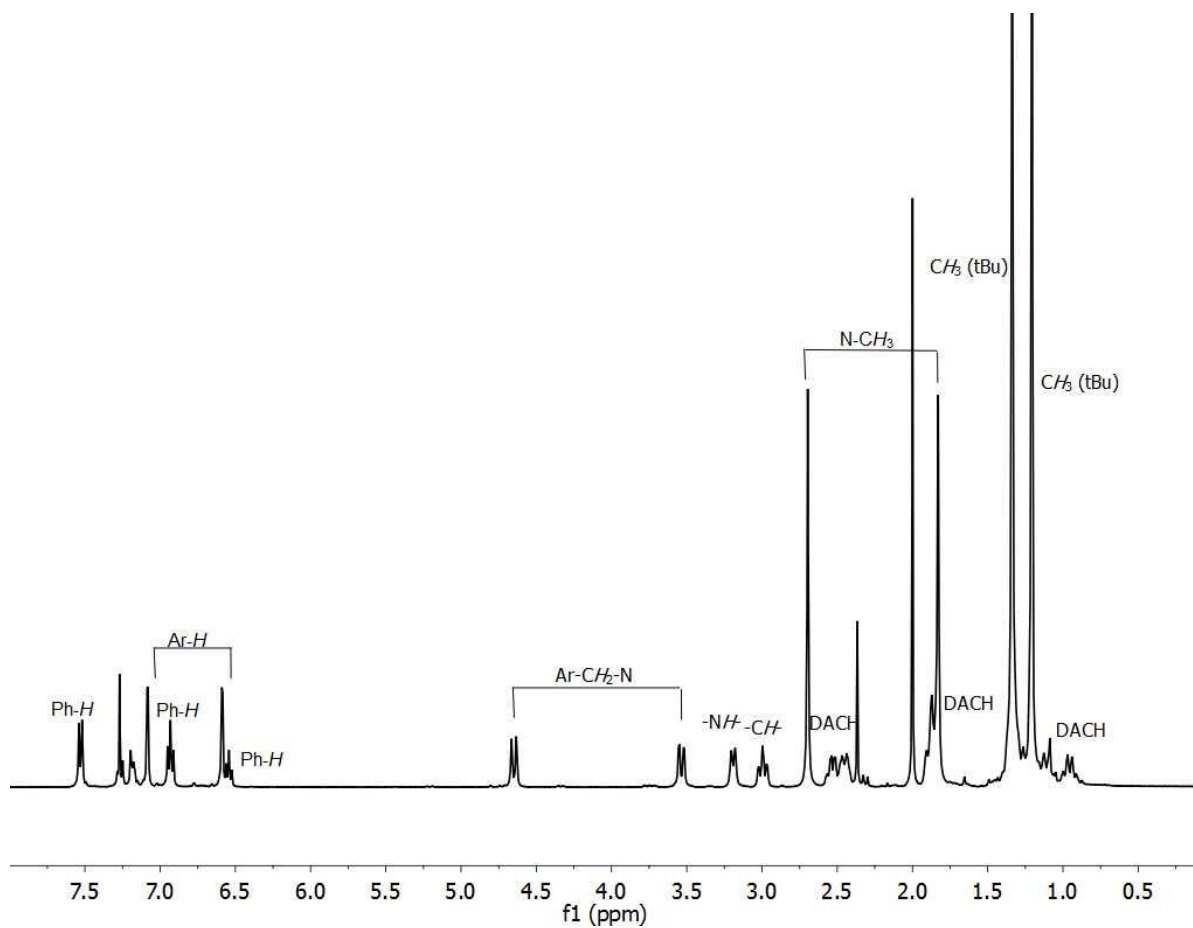
Figure C.8 ^{1}H NMR (CDCl$_3$, 25 °C, 400 MHz) spectrum of (±)-[(NNO)InCl]$_2$(μ-Cl)(μ-OPh$_H$) (**3**).
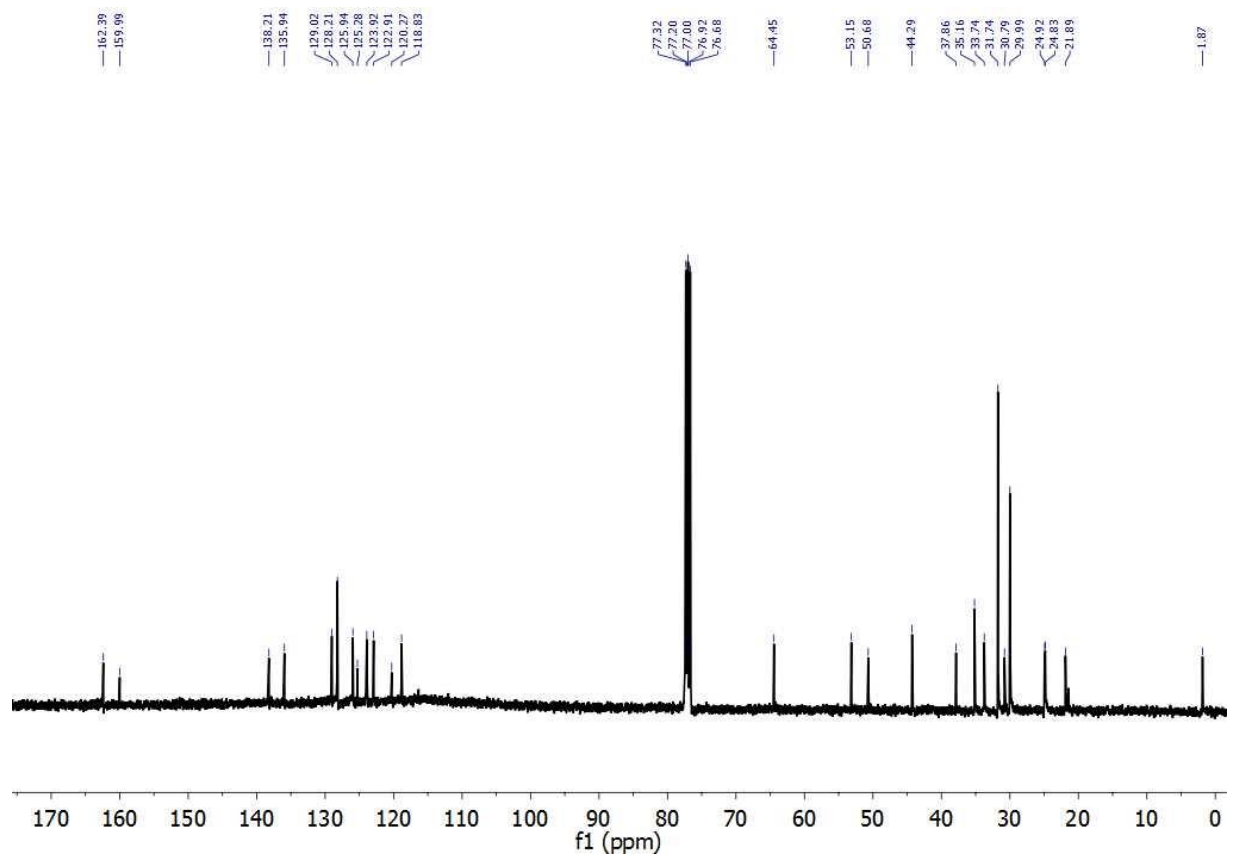
Figure C.9 $^{13}C\{^{1}H\}$ NMR (CDCl$_3$, 25 °C, 400 MHz) spectrum (±)-[(NNO)InCl]$_2$(μ-Cl)(μ-OPh$_H$) (**3**).
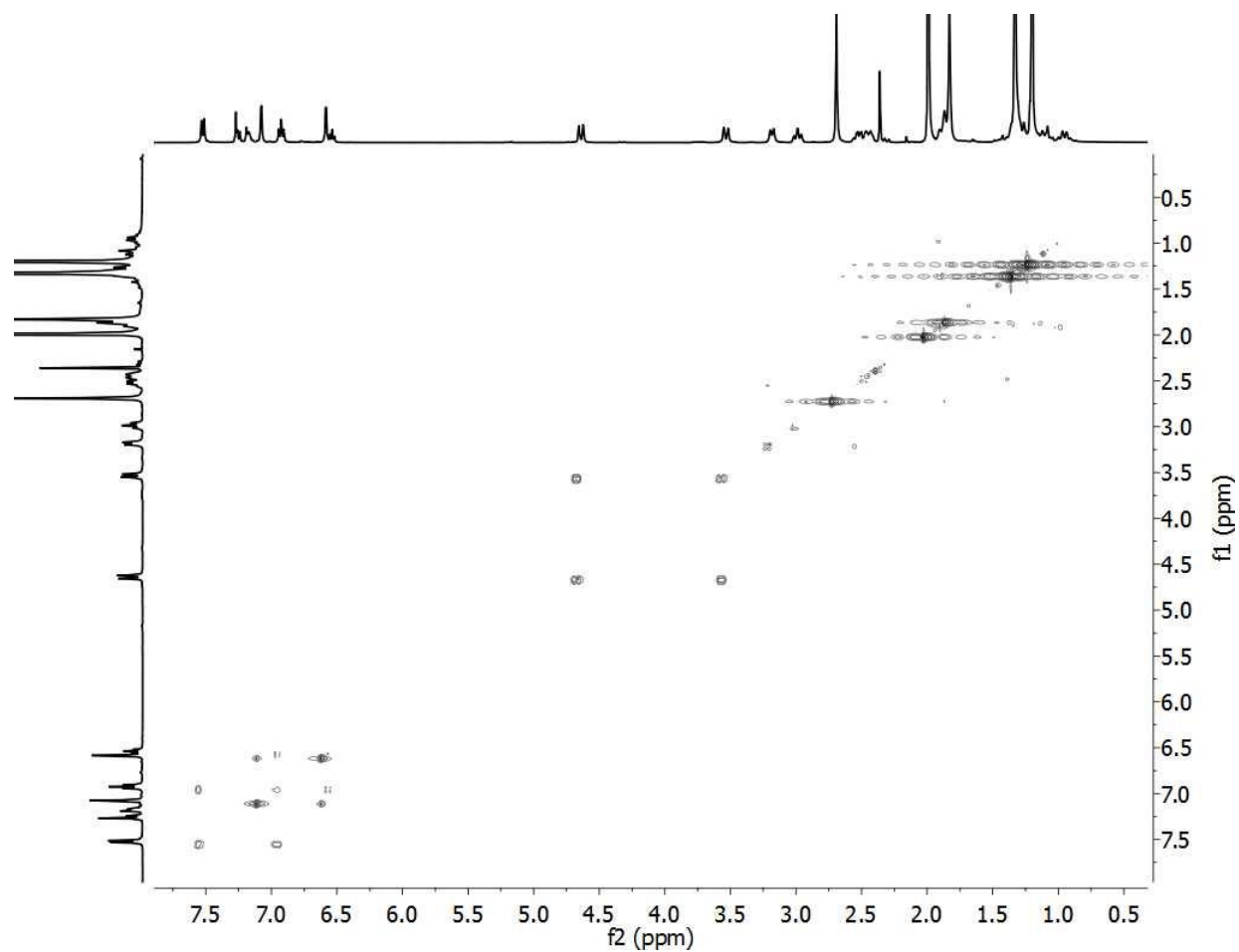
Figure C.10 ^1H – ^1H COSY (CDCl$_3$, 25 °C, 400 MHz) spectrum of (±)-[(NNO)InCl]$_2$(μ-Cl)(μ-OPh$_H$) (**3**).
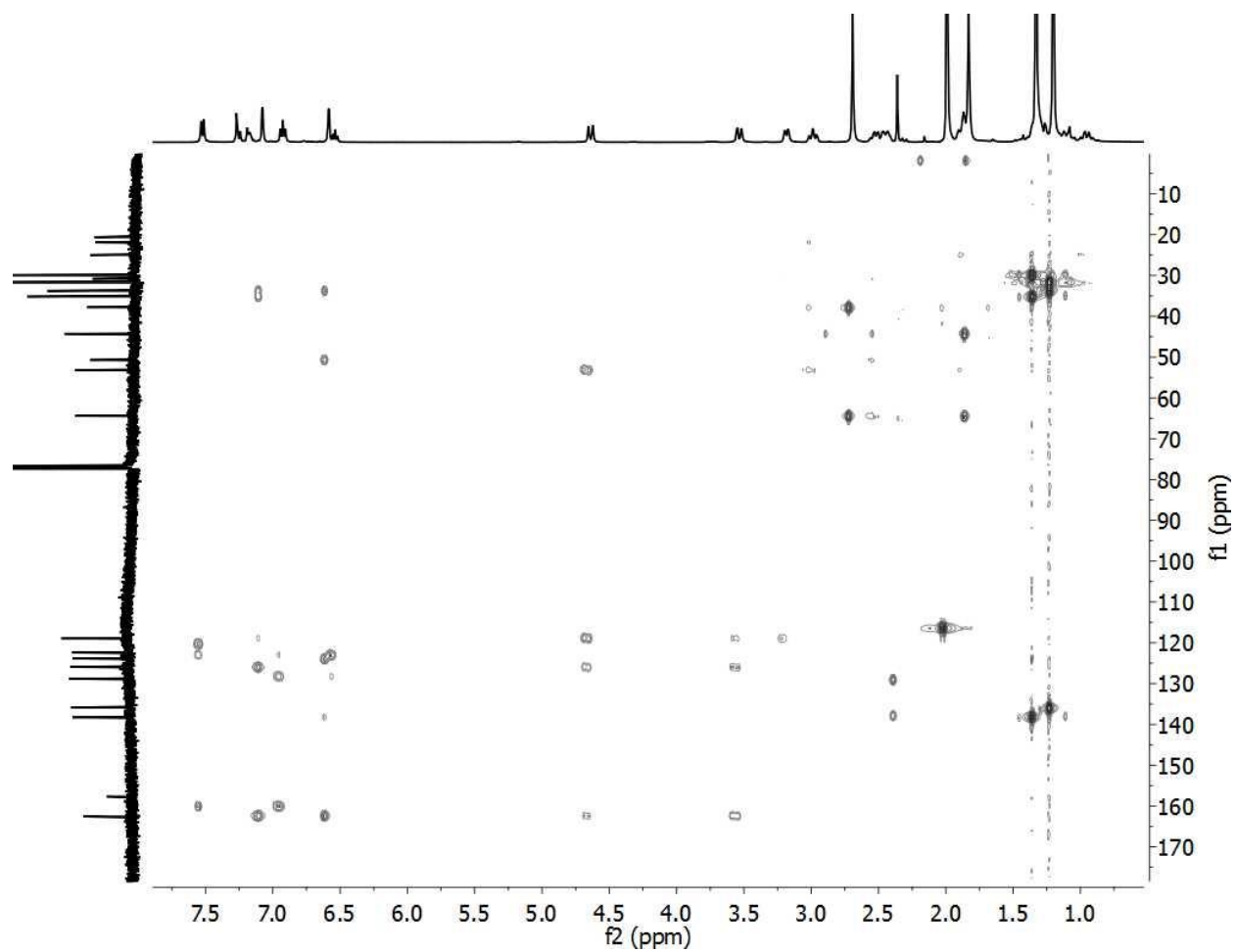
Figure C.11 ^{1}H – ^{13}C HMBC (CDCl$_3$, 25 °C, 400 MHz) spectrum (±)-[(NNO)InCl]$_2$(μ-Cl)(μ-OPh$_H$) (**3**).
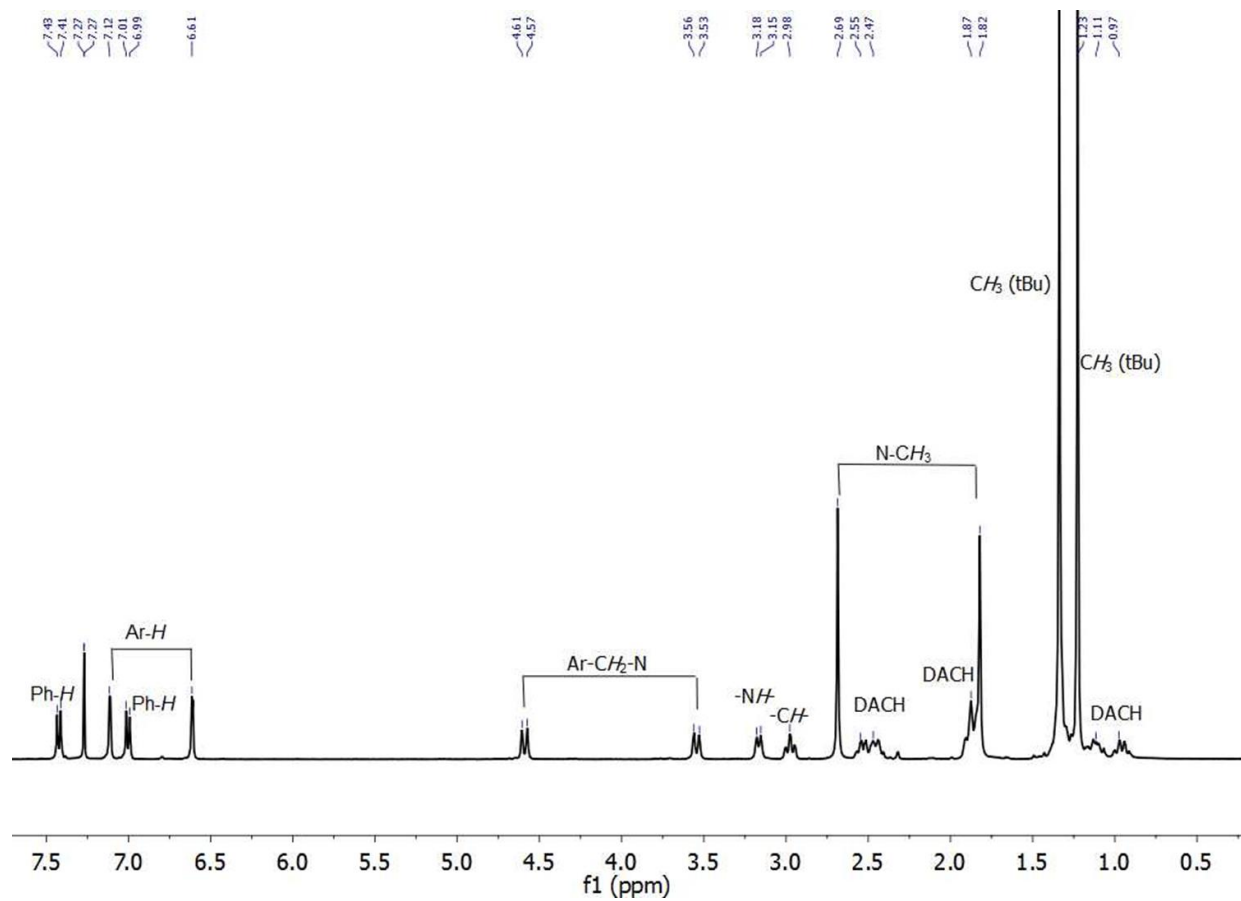
Figure C.12 ^{1}H NMR (CDCl$_3$, 25 °C, 400 MHz) spectrum of (±)-[(NNO)InCl]$_2$(μ-Cl)(μ-OPh$_{Br}$) (**4**).
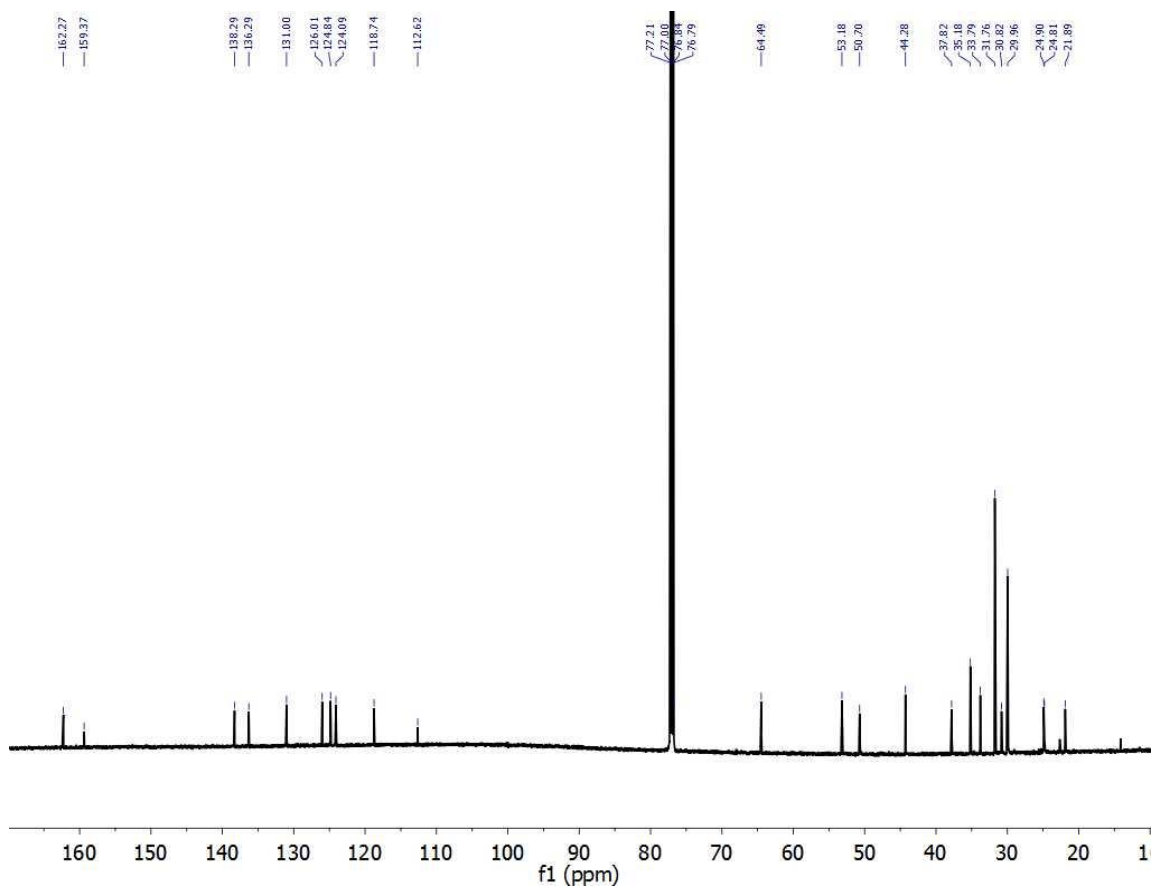
Figure C.13 $^{13}C\{^1H\}$ NMR (CDCl$_3$, 25 °C, 400 MHz) spectrum of (±)-[(NNO)InCl]$_2$(μ-Cl)(μ-OPh$_{Br}$) (**4**).
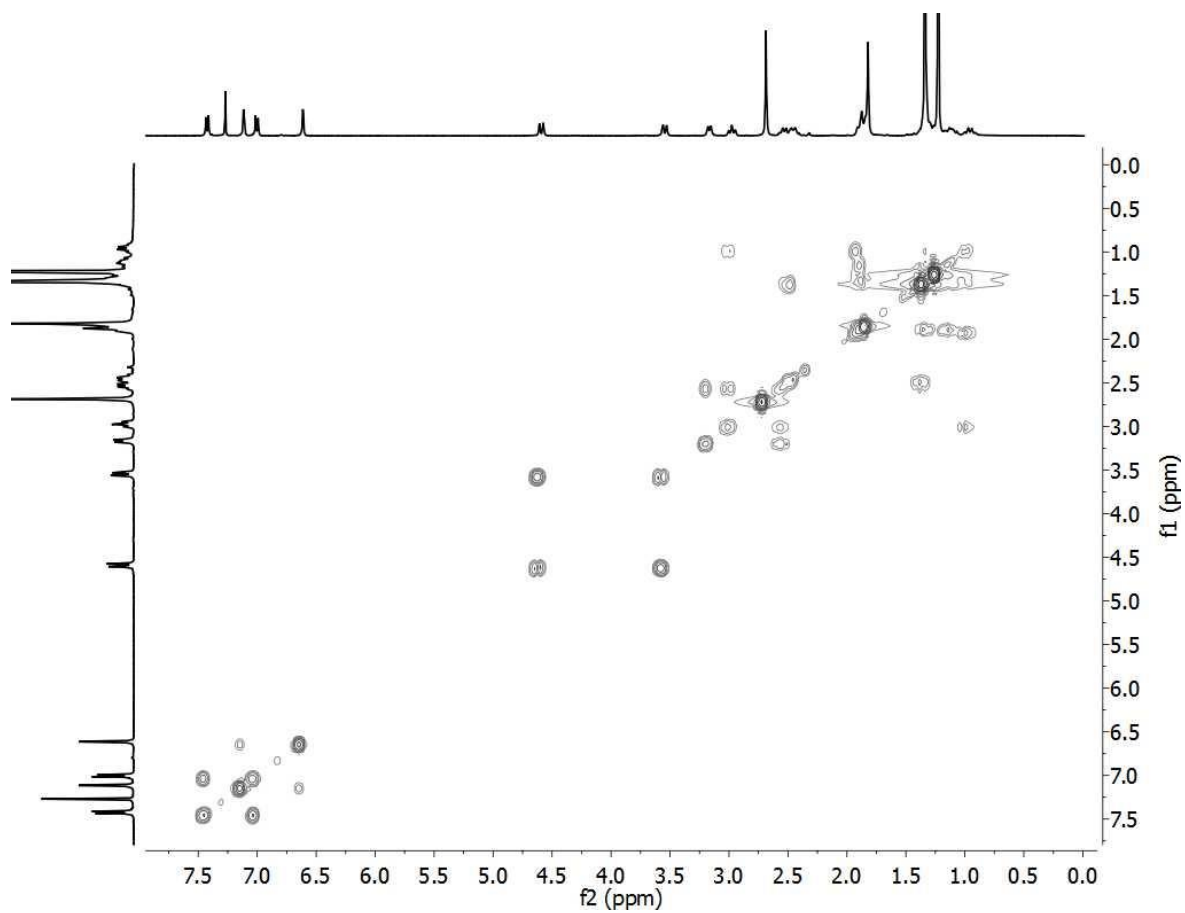
Figure C.14 ^{1}H – ^{1}H COSY (CDCl$_3$, 25 °C, 400MHz) spectrum of (±)-[(NNO)InCl]$_2$(μ-Cl)(μ-OPh$_{Br}$) (**4**).
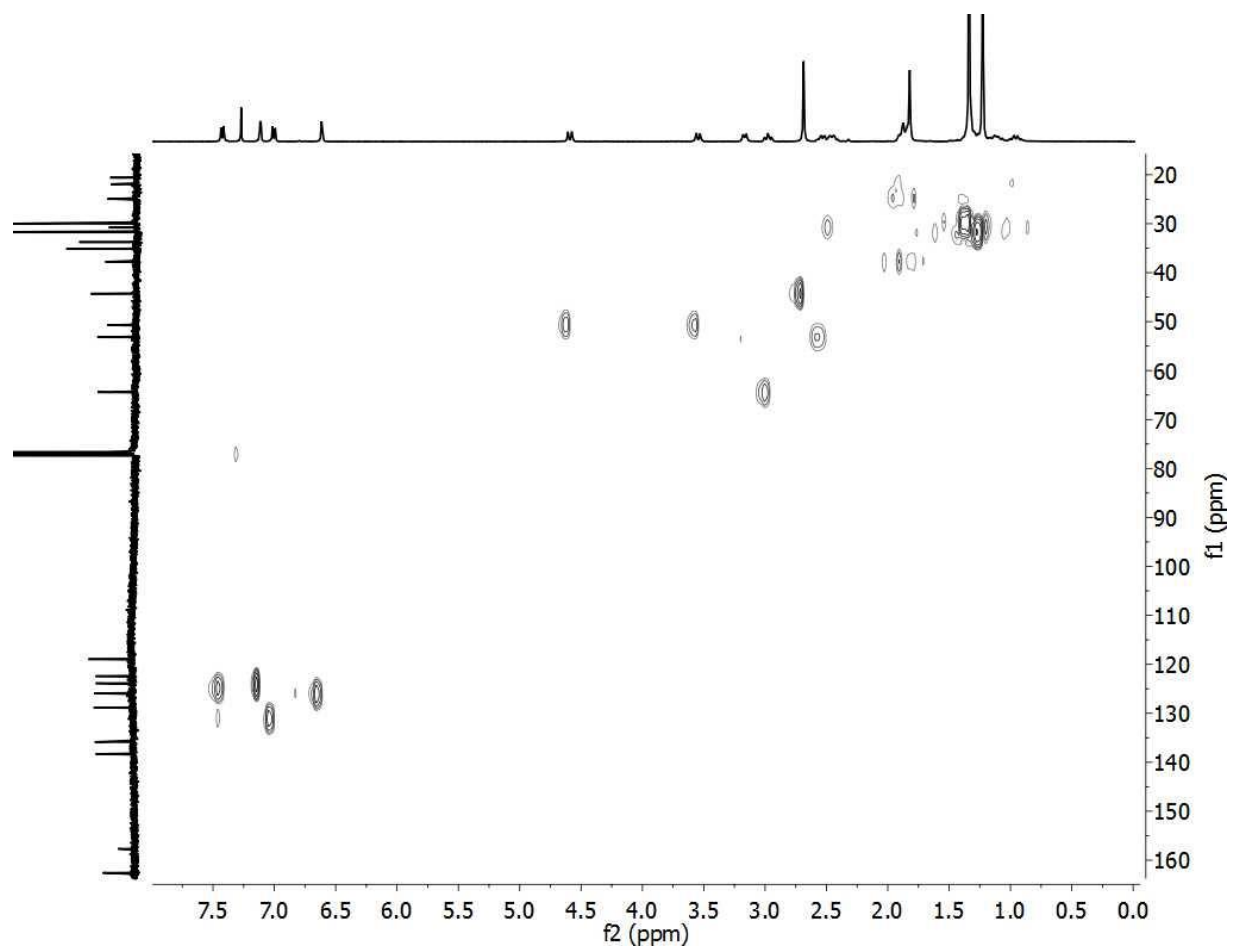
Figure C.15 ^1H – ^{13}C HMBC (CDCl$_3$, 25 °C, 400 MHz) spectrum of (±)-[(NNO)InCl]$_2$(μ-Cl)(μ-OPh$_{Br}$) (**4**).
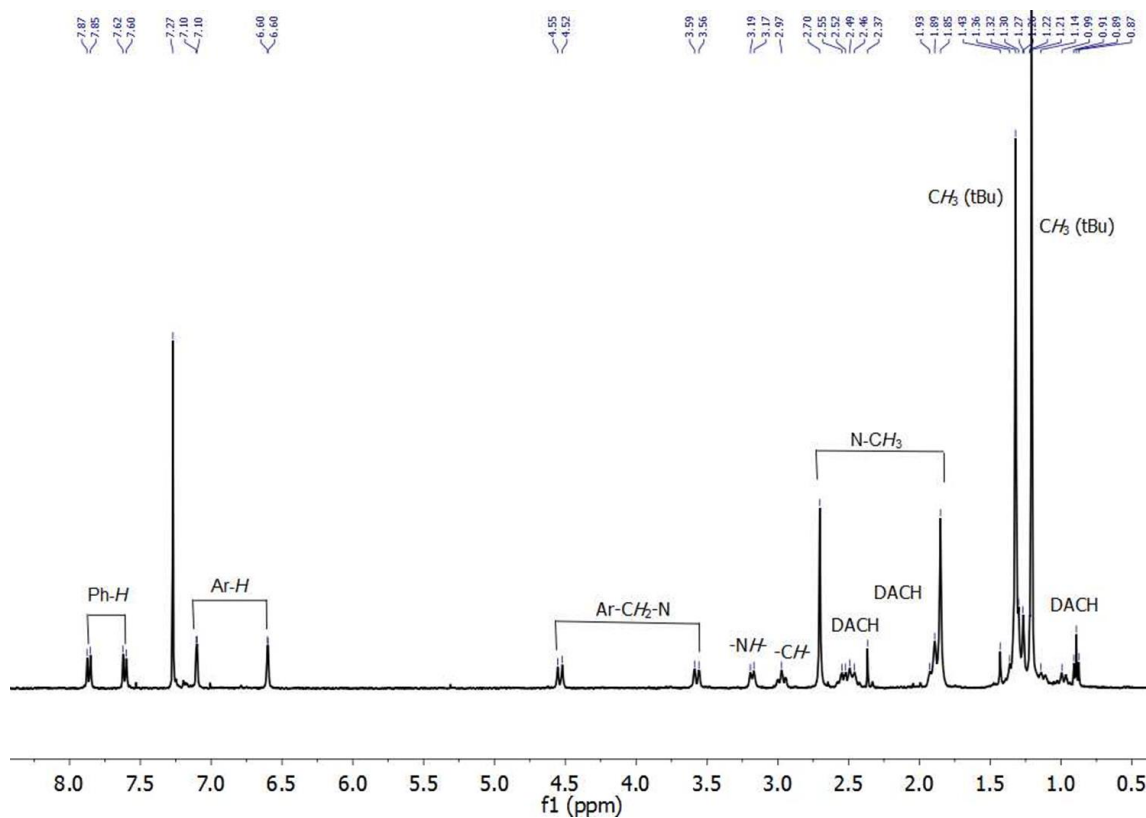
Figure C.16 ^{1}H NMR (CDCl$_3$, 25 °C, 400MHz) spectrum of (±)-[(NNO)InCl]$_2$(μ-Cl)(μ-OPh$_{NO2}$) (**5**).
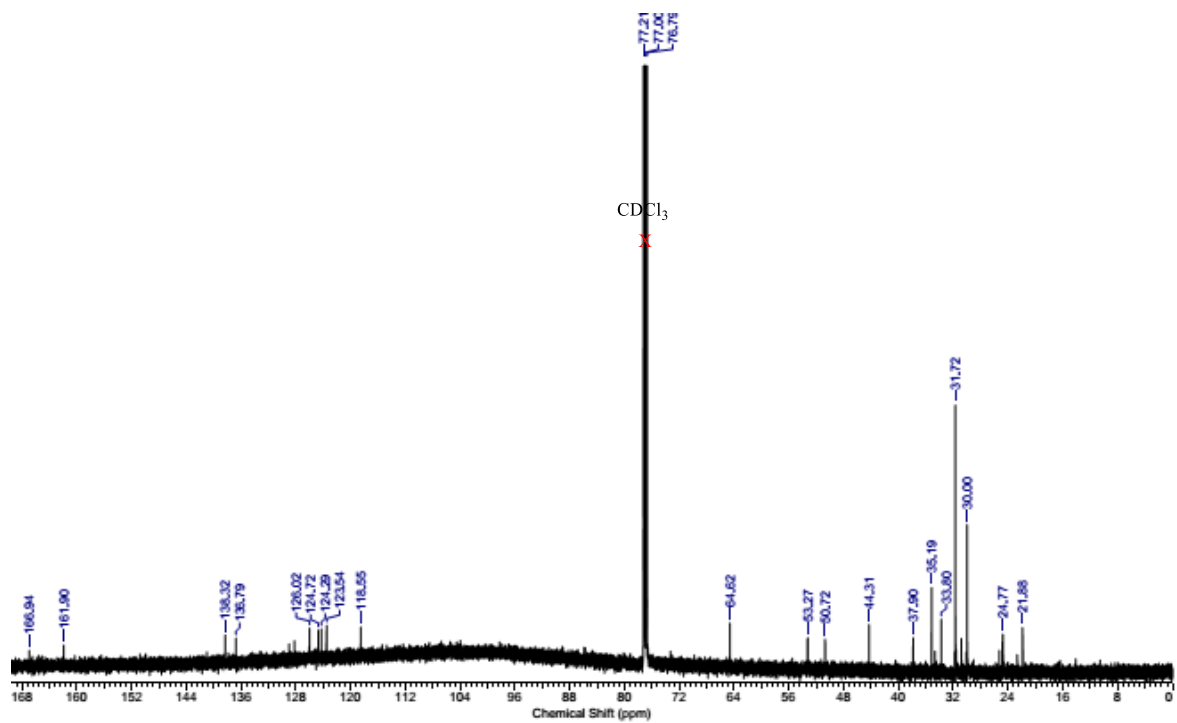
Figure C.17 ^{13}C{^{1}H} NMR (CDCl$_3$, 25 °C, 400MHz) spectrum of (±)-[(NNO)InCl]$_2$(μ-Cl)(μ-OPh$_{NO2}$) (**5**).
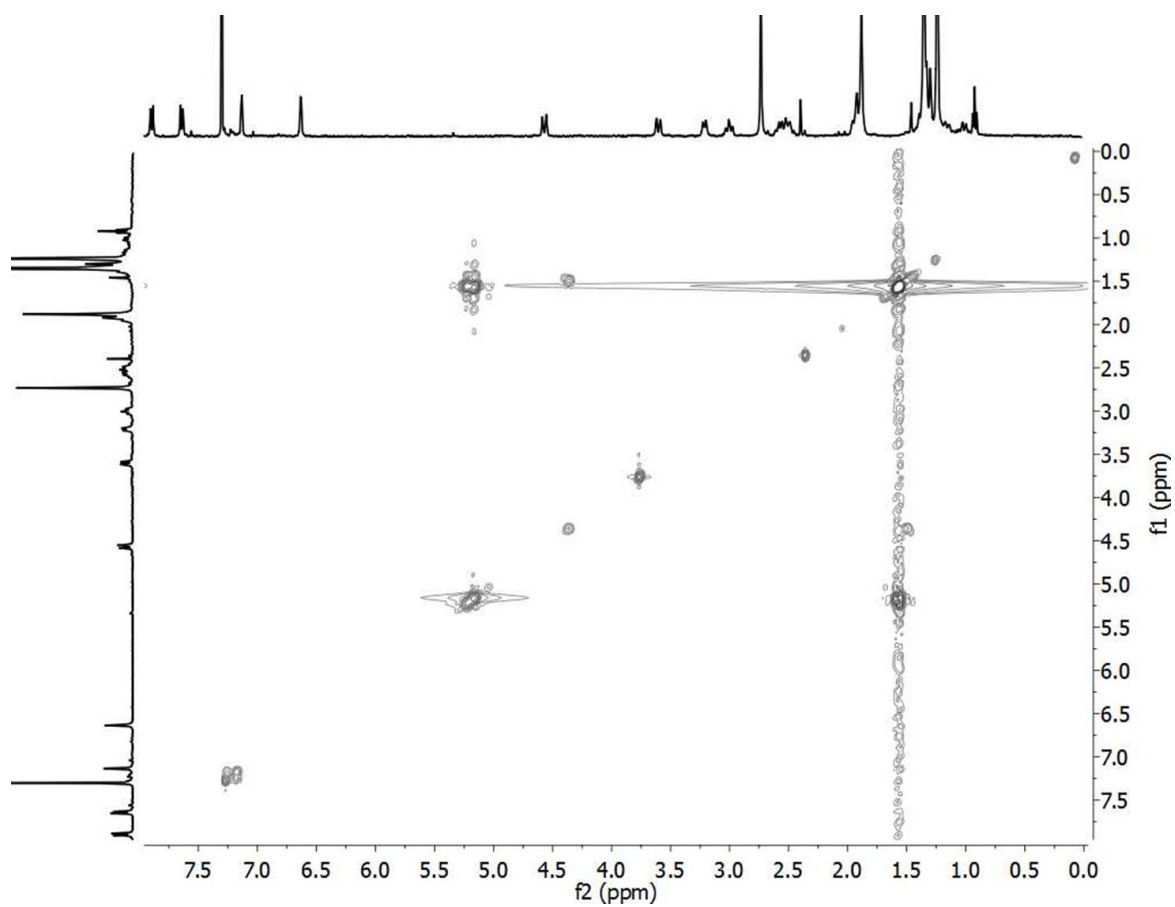
Figure C.18 ^1H – ^1H COSY (CDCl$_3$, 25 °C, 400 MHz) spectrum of (±)-[(NNO)InCl]$_2$(μ-Cl)(μ-OPh$_{NO2}$) (**5**).
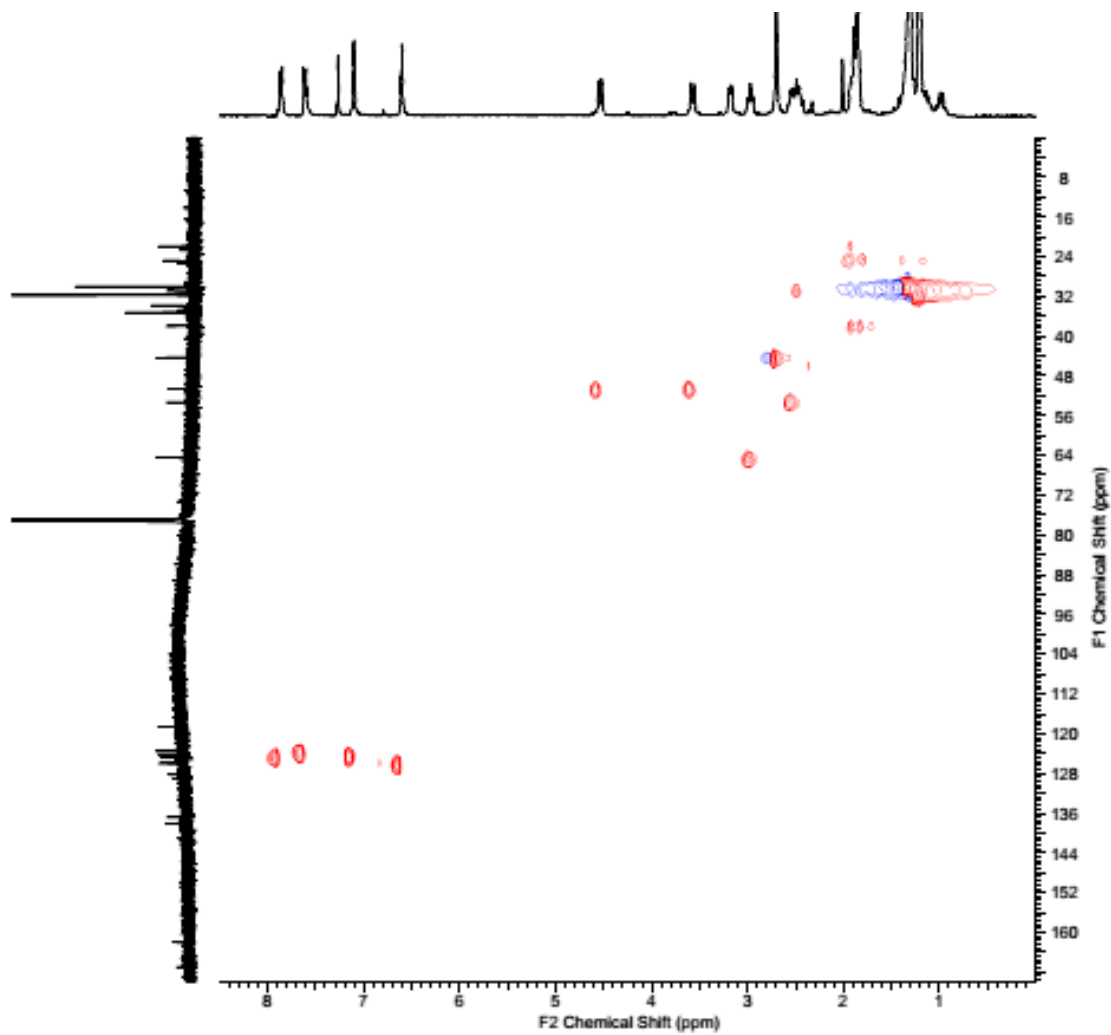
Figure C.19 ^{1}H – ^{13}C HMBC (CDCl$_3$, 25 °C, 400 MHz) spectrum of (±)-[(NNO)InCl]$_2$(µ-Cl)(µ-OPh$_{NO2}$) (**5**).
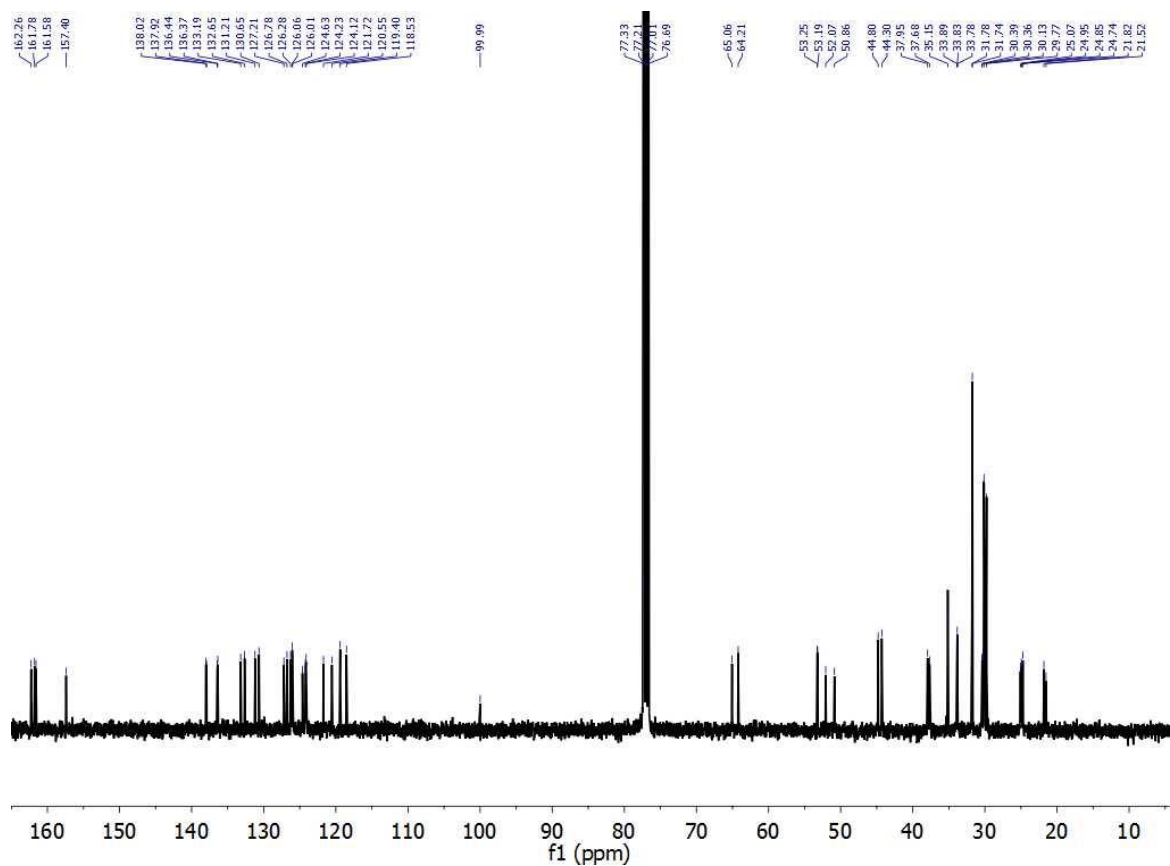
Figure C.20 $^{13}C\{^{1}H\}$ NMR (CDCl$_3$, 25 °C, 400 MHz) spectrum of (±)-[(NNO)InCl]$_2$(μ-Cl)(κ^2,μ-diClPh) (**6**).
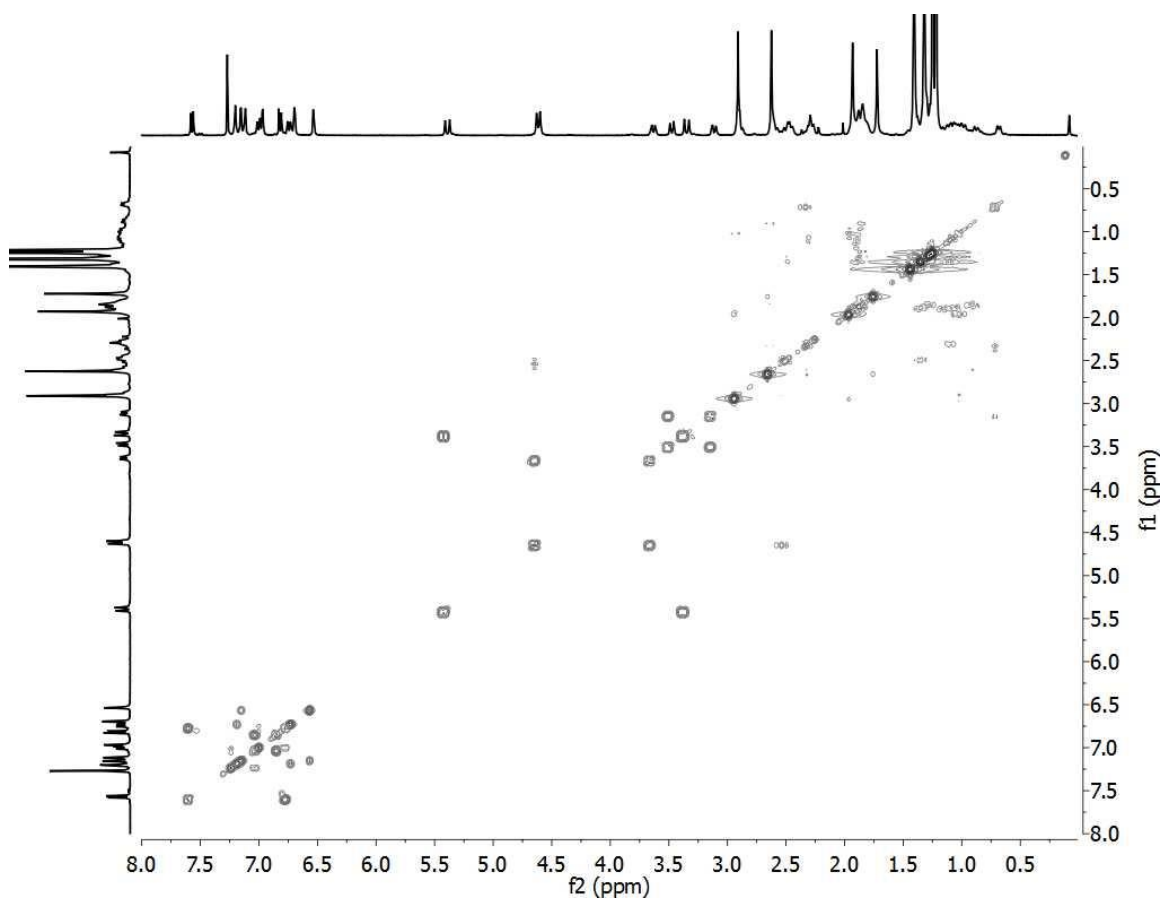
Figure C.21 $^1H - ^1H$ COSY (CDCl$_3$, 25 °C, 400MHz) spectrum of ($\pm$)-[(NNO)InCl]$_2$)(μ-Cl)(κ^2,μ-diClPh) (**6**).
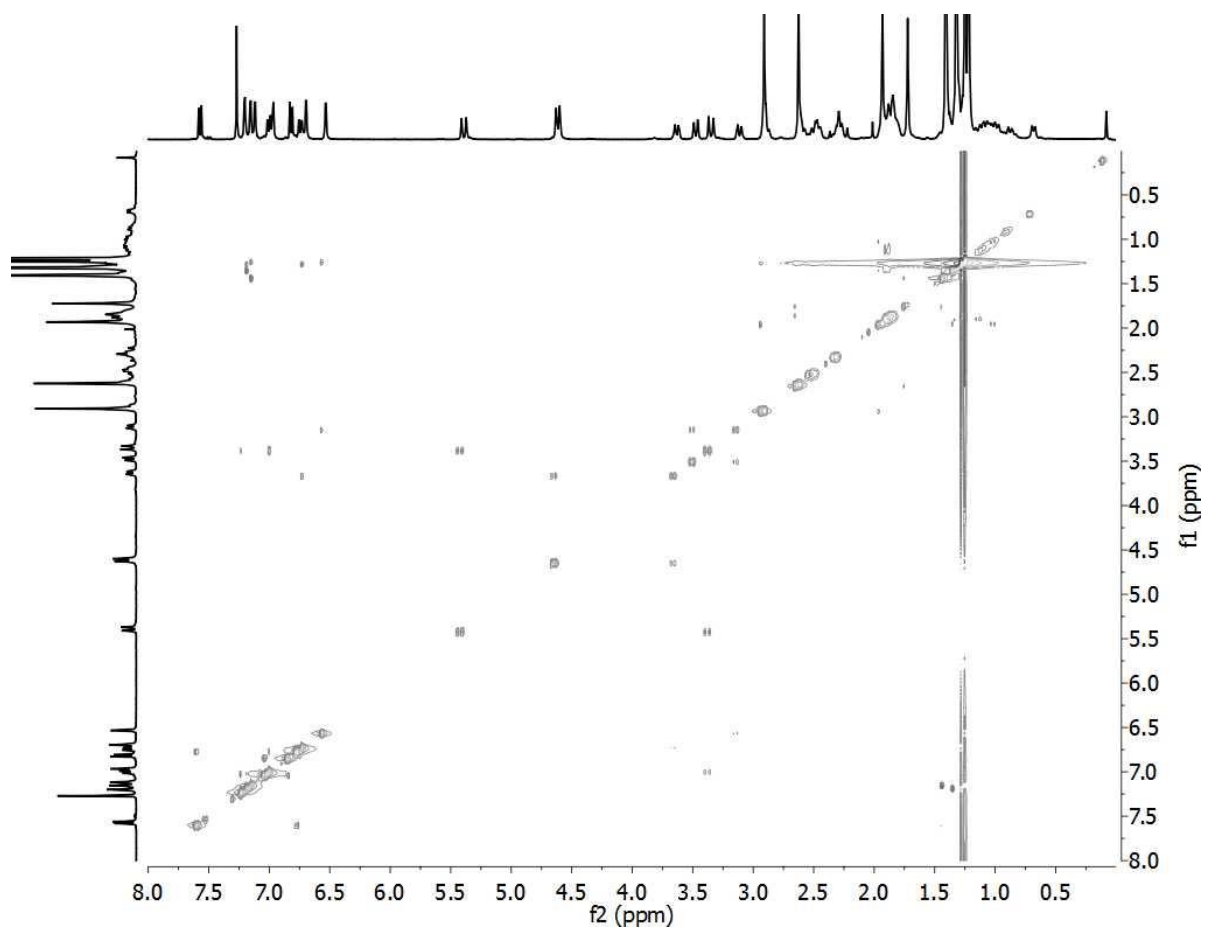
Figure C.22 ^{1}H – ^{1}H NOESY (CDCl$_3$, 25 °C, 400 MHz) spectrum of (±)-[(NNO)InCl]$_2$)(μ-Cl)(κ^2,μ-diClPh) (**6**).

C.2 Characterization of complexes 2-6 in the solid state

Table C.1 Selected crystallographic parameters.

	2	3	4	5	6
Empirical formula	$C_{60}H_{93}Cl_3In_2N_4O_3$	$C_{69.5}H_{103}Cl_3In_2N_4O_3$	$C_{69.5}H_{102}BrCl_3In_2N_4O_3$	$C_{52}H_{82}Cl_3In_2N_5O_5$	$C_{73}H_{102}Cl_4In_2N_4O_4$
Formula weight	1254.37	1378.54	1457.44	1252.90	1471.02
T (K)	90(2)	90(2)	90(2)	90(2)	90(2)
a (Å)	18.461(5)	17.272(2)	18.451(2)	17.447(2)	10.5118(4)
b (Å)	20.589(5)	21.834(3)	21.673(3)	18.137(2)	24.3030(10)
c (Å)	19.119(5)	18.317(2)	18.847(2)	21.872(3)	30.4559(11)
α (deg)	90	90	90	111.589(2)	90
β (deg)	110.389(4)	95.278(2)	111.583(3)	102.894(3)	93.687(2)
γ (deg)	90	90	90	98.066(3)	90
Volume (Å^3)	6811(3)	6878.2(15)	7008.2(15)	6081.1(13)	7764.4(5)
Z	4	4	4	4	4
Crystal system	monoclinic	monoclinic	monoclinic	triclinic	monoclinic
Space group	P2$_1$/c	P2$_1$/c	P2$_1$/c	P-1	P2$_1$/c
d$_{calc}$ (g/cm^3)	1.223	1.331	1.381	1.369	1.258
μ/mm^{-1}	0.835	0.834	1.389	1.002	0.777
F(000)	2616.0	2884.0	3020.0	2588.0	3064.0
Crystal size/mm^3	0.339 × 0.042 × 0.032	0.804 × 0.014 × 0.012	0.91 × 0.15 × 0.13	0.42 × 0.12 × 0.11	0.382 × 0.289 × 0.088
Radiation	Mo Kα (λ = 0.71073)	MoKα (λ = 0.71073)	MoKα (λ = 0.71073)	MoKα (λ = 0.71073)	MoKα (λ = 0.71073)
2Θ range for data collection/°	3.02 to 45.16	4.84 to 54.946	2.374 to 51.664	2.374 to 51.664	2.146 to 60.184

	2	3	4	5	6
Index ranges	$-19 \leq h \leq 19$, $-22 \leq k \leq 22$, $-20 \leq l \leq 20$	$-22 \leq h \leq 22$, $-28 \leq k \leq 27$, $-23 \leq l \leq 23$	$-22 \leq h \leq 21$, $-26 \leq k \leq 26$, $-17 \leq l \leq 23$	$-21 \leq h \leq 21$, $-22 \leq k \leq 22$, $-26 \leq l \leq 26$	$-14 \leq h \leq 14$, $-34 \leq k \leq 29$, $-42 \leq l \leq 39$
Total no. reflections	30942	68285	62150	104569	70649
No. independent reflections (R_{int})	8863 [R_{int} = 0.1479, R_{sigma} = 0.1418]	15706 [R_{int} = 0.0742, R_{sigma} = 0.0632]	13290 [R_{int} = 0.0548, R_{sigma} = 0.0749]	23169 [R_{int} = 0.1043, R_{sigma} = 0.1138]	22667 [R_{int} = 0.0416, R_{sigma} = 0.0494]
Data/restraints/parameters	8863/4/773	15706/0/721	13290/0/730	23169/0/1275	22667/0/833
GOF	1.045	1.003	1.041	1.008	1.089
Final R indexes [I>=2σ (I)]	R_1 = 0.0882, wR_2 = 0.2034	R_1 = 0.0410, wR_2 = 0.0899	R_1 = 0.0497, wR_2 = 0.1015	R_1 = 0.0546, wR_2 = 0.0952	R_1 = 0.0490, wR_2 = 0.1246
Final R indexes [all data]	R_1 = 0.1846, wR_2 = 0.2556	R_1 = 0.0690, wR_2 = 0.1036	R_1 = 0.0932, wR_2 = 0.1196	R_1 = 0.1182, wR_2 = 0.1138	R_1 = 0.0618, wR_2 = 0.1350
Largest diff. peak/hole / e Å^{-3}	1.57/-1.17	1.26/-1.21	3.06/-2.07	1.39/-1.75	1.63/-0.76

a $R_1 = \Sigma \, ||Fo| - |Fc|| \, / \, \Sigma \, |Fo|$; b $wR_2 = [\Sigma(w(Fo2 - Fc2)2)/\Sigma \, w(Fo2)2]1/2$.

C.3 In situ living ring-opening polymerization data with catalysts 1-4.

$[(NNO)InCl]_2(\mu\text{-}Cl)(\mu\text{-}OEt)$ (**A**)

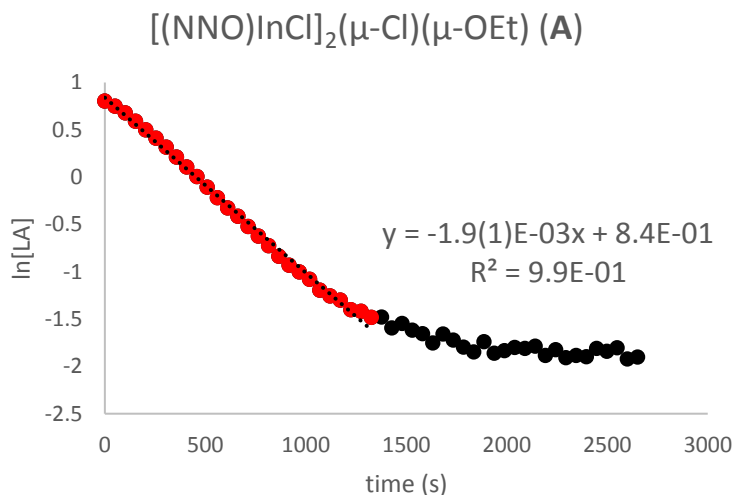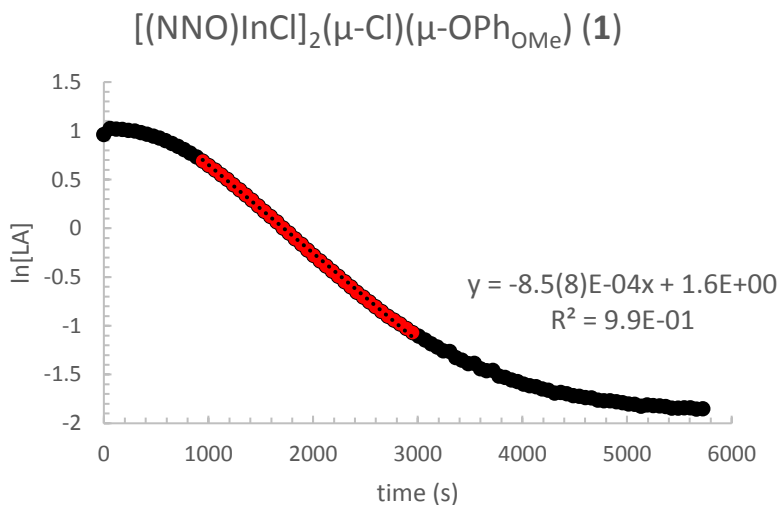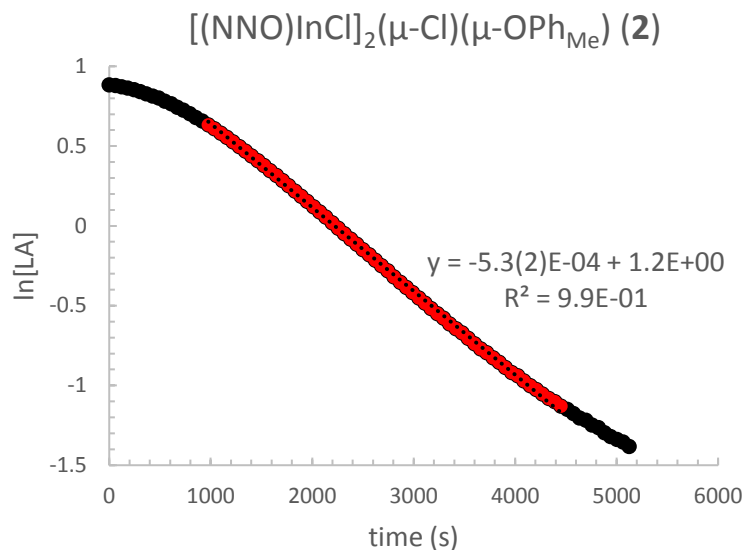$$y = -1.9(1)E\text{-}03x + 8.4E\text{-}01$$
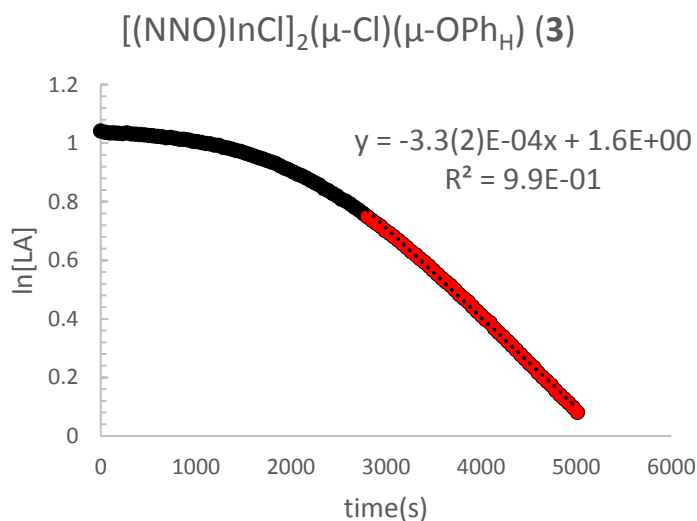$$R^2 = 9.9E\text{-}01$$

Figure C.23 Reactions were carried out in an NMR tube at 25 °C. 1,3,5-trimethoxybenzene (TMB) was used as internal standard. All reactions were carried out with 50 equivalents of LA in CD_2Cl_2 at 25 °C and followed by ^{1}H NMR spectroscopy. [**A**] = 0.0046 M, [LA] = 0.22 M The value of k_{obs} was determined from the slope of ln[LA] vs. time (shown in red), averaged from at least three experiments.

$[(NNO)InCl]_2(\mu\text{-}Cl)(\mu\text{-}OPh_{OMe})$ (**1**)

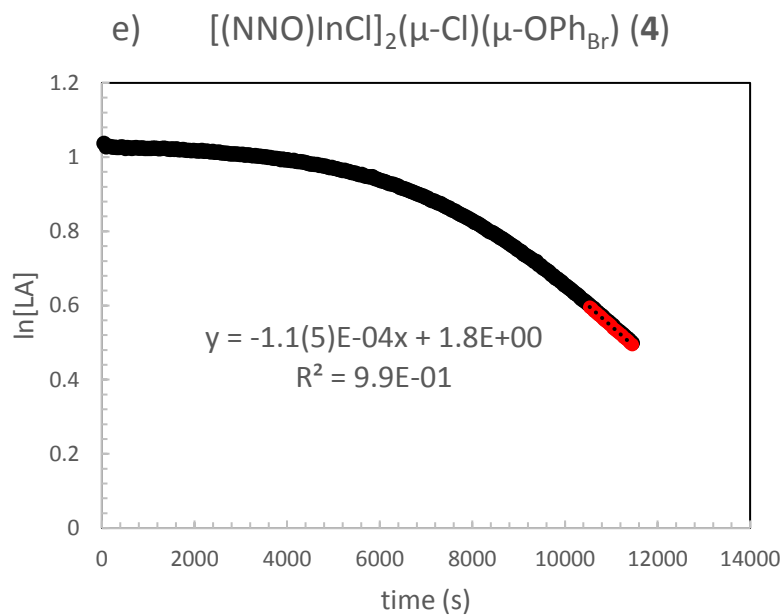$$y = -8.5(8)E\text{-}04x + 1.6E\text{+}00$$
$$R^2 = 9.9E\text{-}01$$

Figure C.24 Reactions were carried out in an NMR tube at 25 °C. 1,3,5-trimethoxybenzene (TMB) was used as internal standard. All reactions were carried out with 50 equivalents of LA in CD_2Cl_2 at 25 °C and followed by ^{1}H NMR spectroscopy. [**1**] = 0.0039 M, [LA] = 0.19 M. The value of k_{obs} was determined from the slope of ln[LA] vs. time (shown in red), averaged from at least three experiments.

Figure C.25 Reactions were carried out in an NMR tube at 25 °C. 1,3,5-trimethoxybenzene (TMB) was used as internal standard. All reactions were carried out with 50 equivalents of LA in CD_2Cl_2 at 25 °C and followed by ^1H NMR spectroscopy [2] = 0.0043 M, [LA] = 0.21 M. The value of k_{obs} was determined from the slope of ln[LA] vs. time (shown in red), averaged from at least three experiments.

Figure C.26 Reactions were carried out in an NMR tube at 25 °C. 1,3,5-trimethoxybenzene (TMB) was used as internal standard. All reactions were carried out with 50 equivalents of LA in CD_2Cl_2 at 25 °C and followed by ^1H NMR spectroscopy [3] = 0.0037 M, [LA] = 0.22 M. The value of k_{obs} was determined from the slope of ln[LA] vs. time (shown in red), averaged from at least three experiments.

e) $[(NNO)InCl]_2(\mu\text{-}Cl)(\mu\text{-}OPh_{Br})$ **(4)**

$$y = -1.1(5)E\text{-}04x + 1.8E\text{+}00$$
$$R^2 = 9.9E\text{-}01$$

x-axis: time (s)
y-axis: ln[LA]

Figure C.27 Reactions were carried out in an NMR tube at 25 °C. 1,3,5-trimethoxybenzene (TMB) was used as internal standard. All reactions were carried out with 50 equivalents of LA in CD₂Cl₂ at 25 °C and followed by ¹H NMR spectroscopy. [4] = 0.0041 M, [LA] = 0.22 M. The value of k_{obs} was determined from the slope of ln[LA] vs. time (shown in red), averaged from at least three experiments.

Appendix D

D.1 Master curves for aryl capped poly(lactide)s
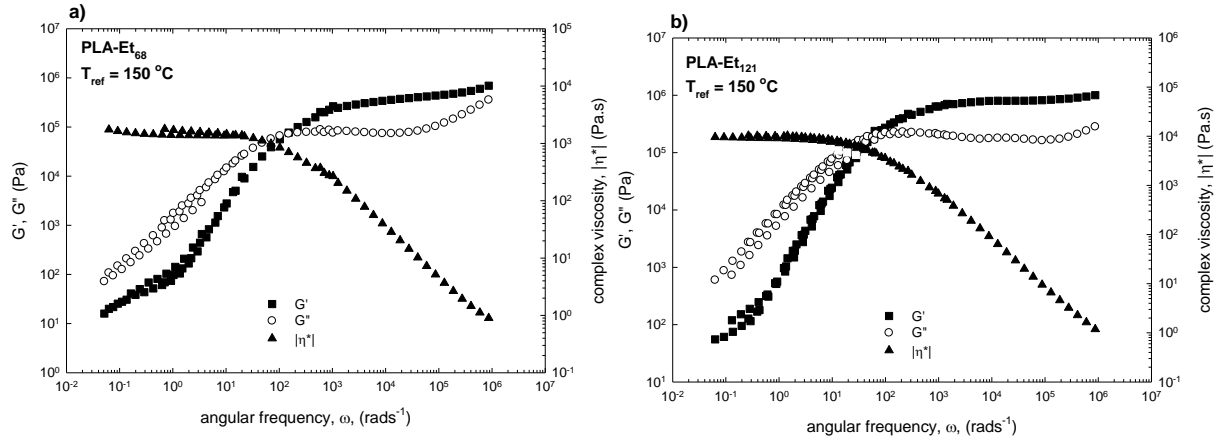
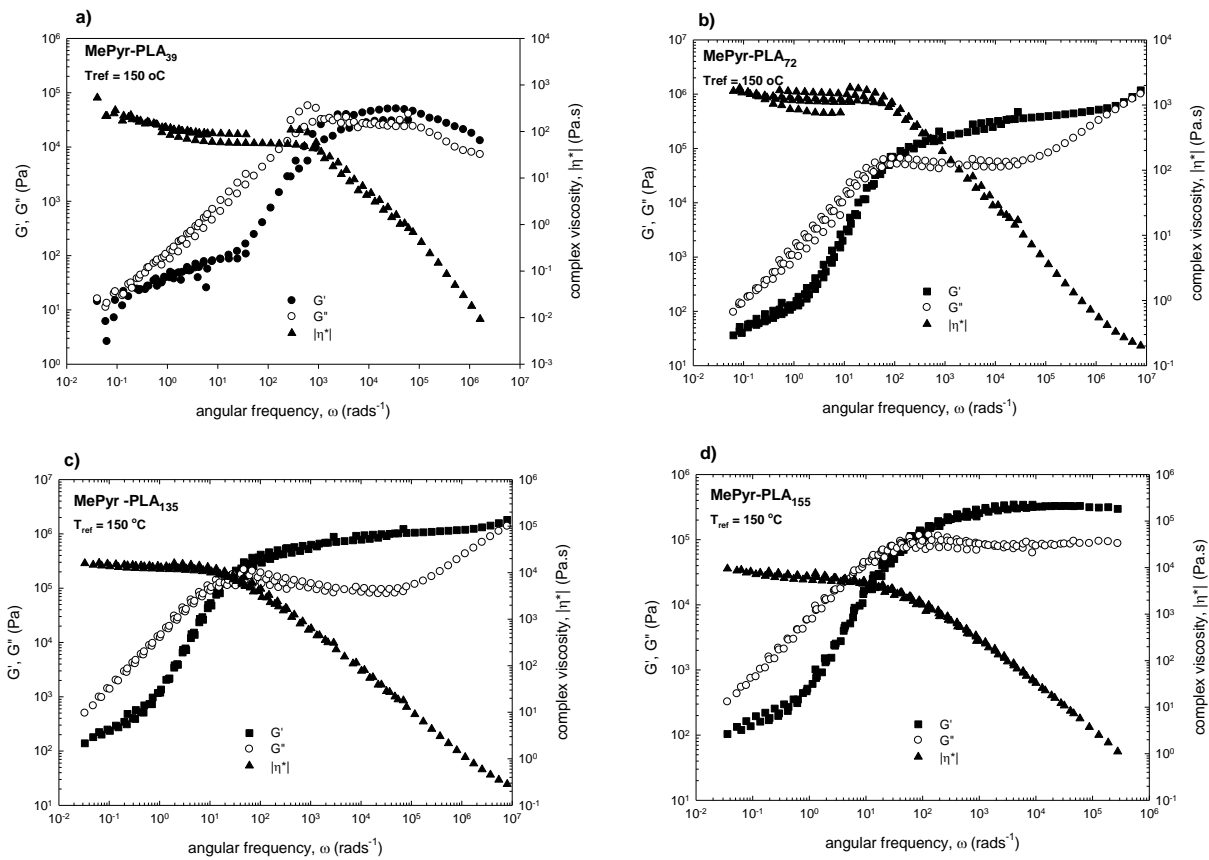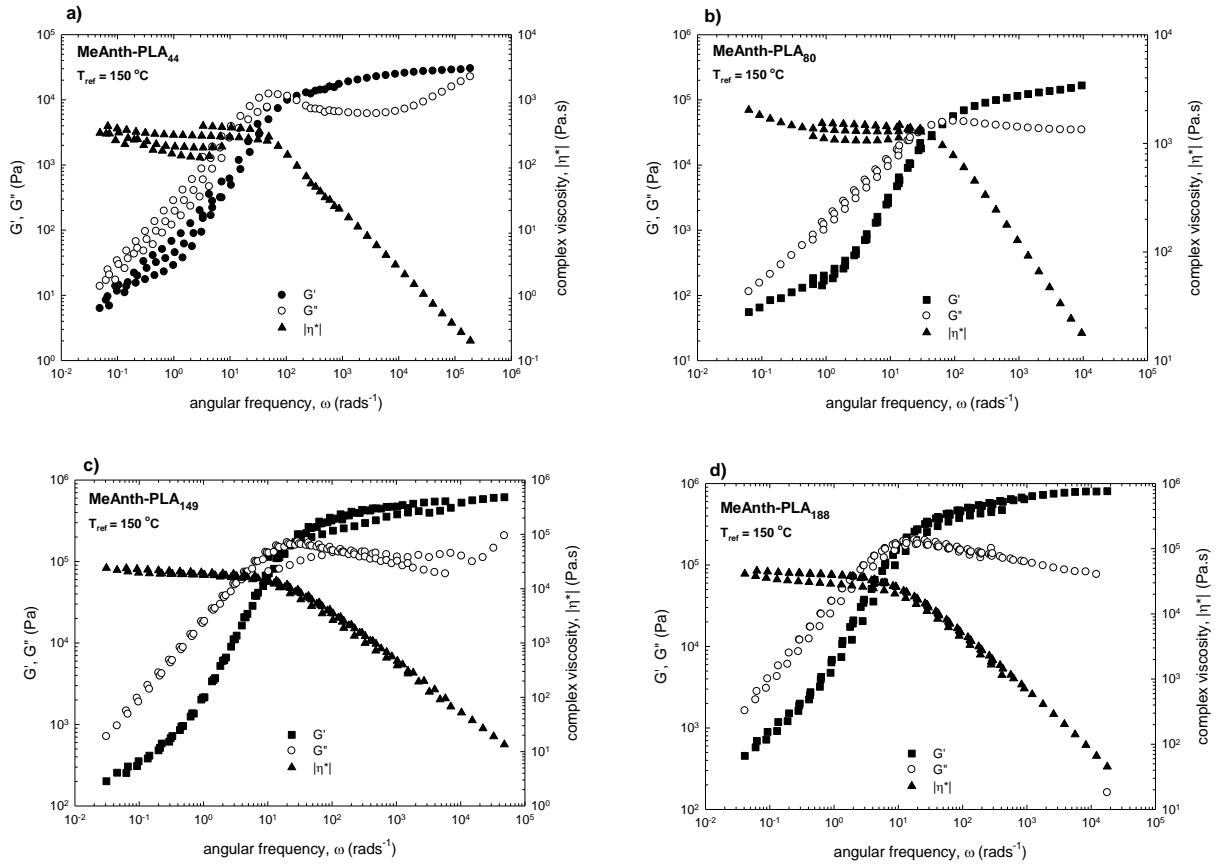**Figure D.1** Master curve of the linear viscoelastic moduli, G′ and G″, and complex viscosity, |η*| (T$_{ref}$ = 150 °C), for a) PLA-Et$_{68}$ b) PLA-Et$_{121}$ polymers.
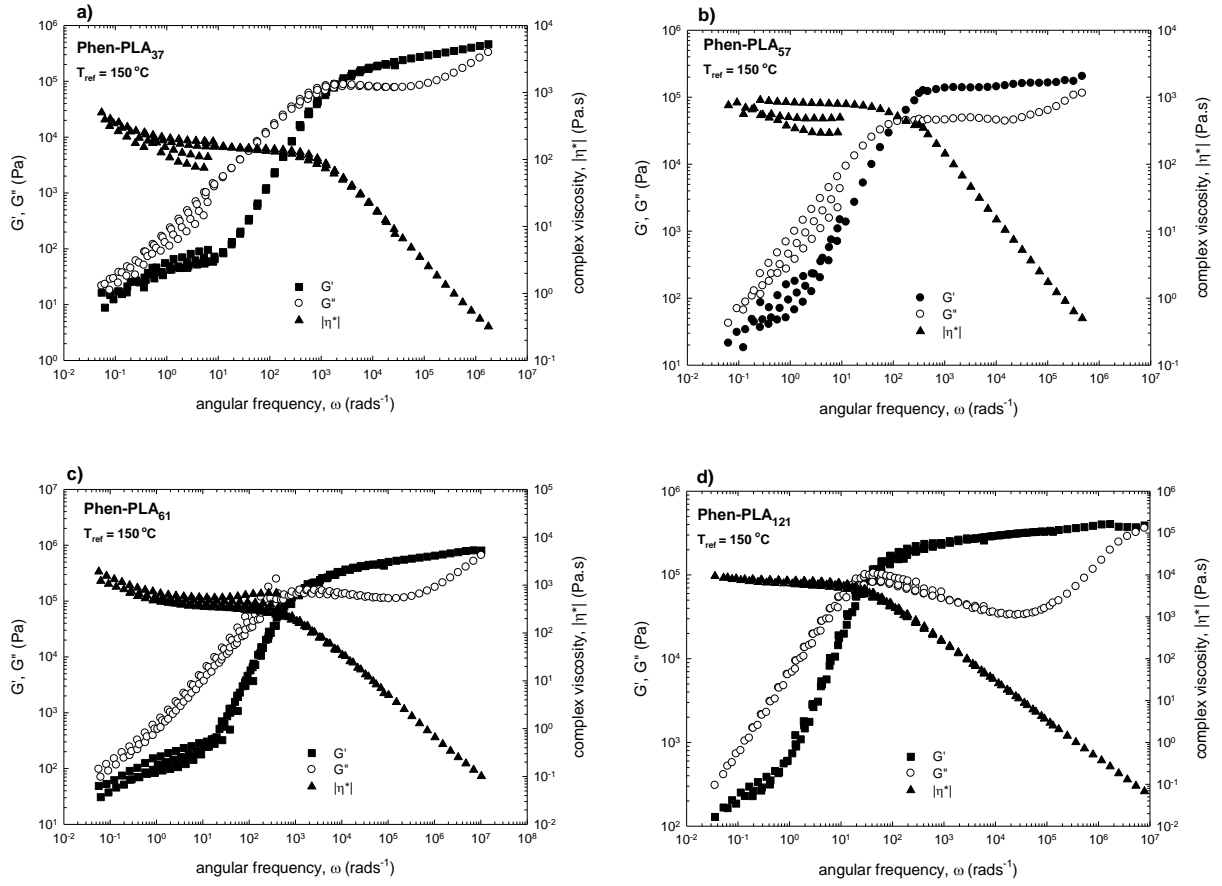
Figure D.2 Master curve of the linear viscoelastic moduli, G′ and G″, and complex viscosity, |η*| (T_{ref} = 150 °C), for a) PLA-Ph$_{37}$ b) PLA-Ph$_{57}$ c) PLA-Ph$_{61}$ and (d) PLA-Ph$_{121}$ polymers.
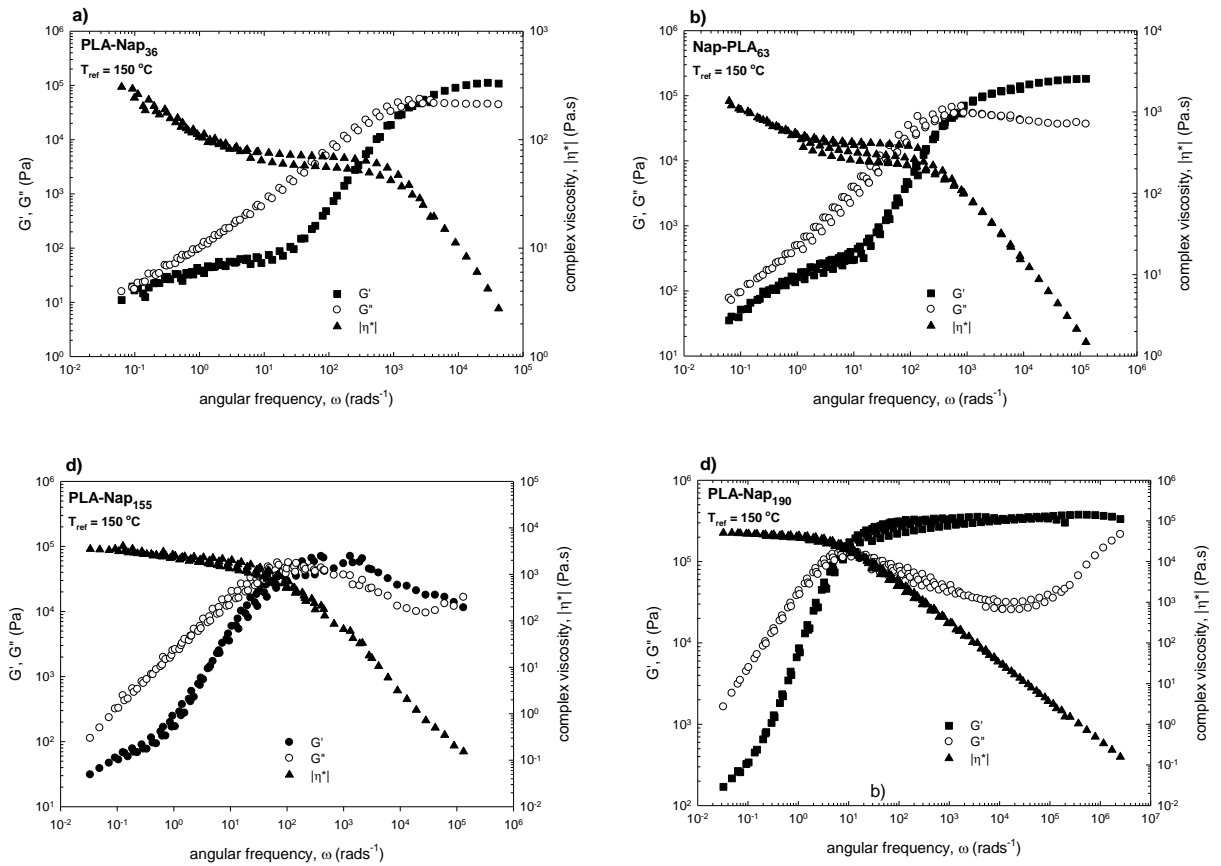
Figure D.3 Master curve of the linear viscoelastic moduli, G′ and G″, and complex viscosity, |η*| (T$_{ref}$ = 150 °C), for a) PLA-Nap$_{36}$ b) PLA-Nap$_{63}$ c) PLA-Nap$_{155}$ and (d) PLA-Nap$_{190}$ polymers.

Figure D.4 Master curve of the linear viscoelastic moduli, G′ and G″, and complex viscosity, |η*| (T_{ref} = 150 °C), for a) PLA-MePyr₃₉ b) PLA-MePyr₇₂ c) PLA-MePyr₁₃₅ and (d) PLA-MePyr₁₅₅ polymers.

Figure D.5 Master curve of the linear viscoelastic moduli, G′ and G″, and complex viscosity, |η*| (T$_{ref}$ = 150 °C), for a) PLA-MeAnth$_{44}$ b) PLA-MeAnth$_{80}$ c) PLA-MeAnth$_{149}$ and (d) PLA-MeAnth$_{188}$ polymers.

D.2 Uniaxial extension experimental plots
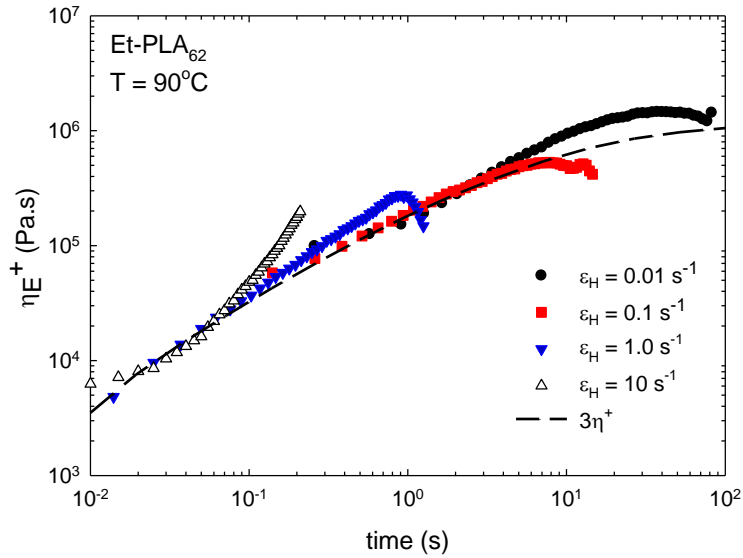
Figure D.6 Tensile stress growth coefficient (measure of elongational viscosity) as a function of time at Hencky strain rate of 0.01 to 10 s^{-1} at 90 °C for Et-PLA$_{62}$
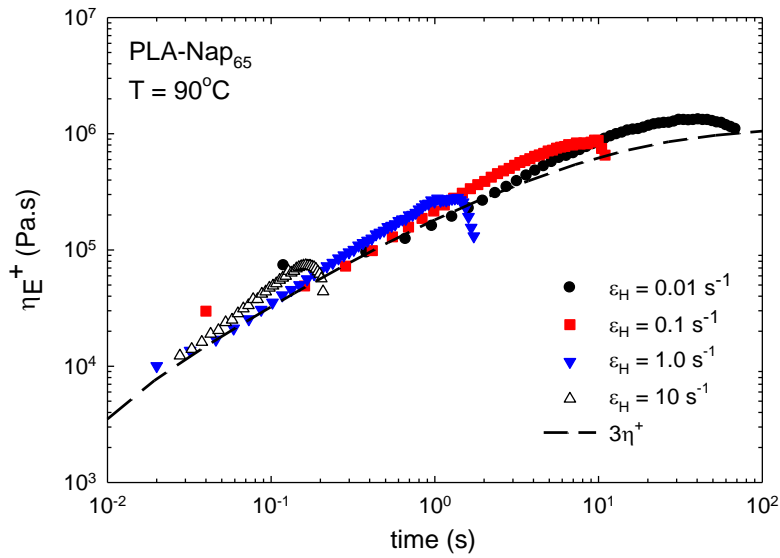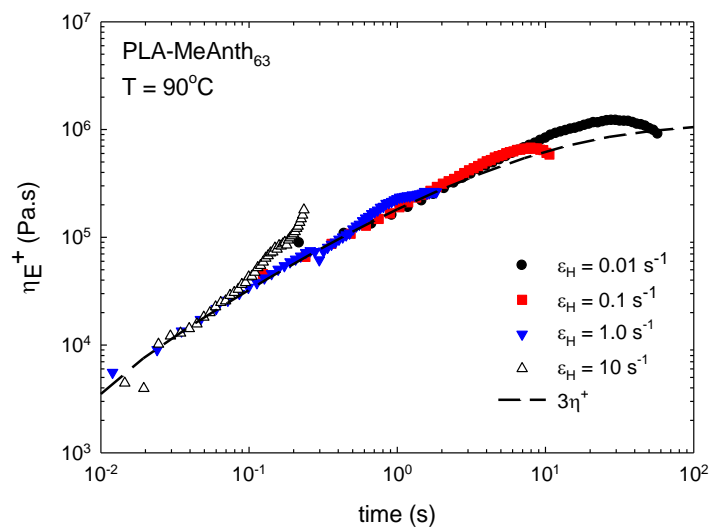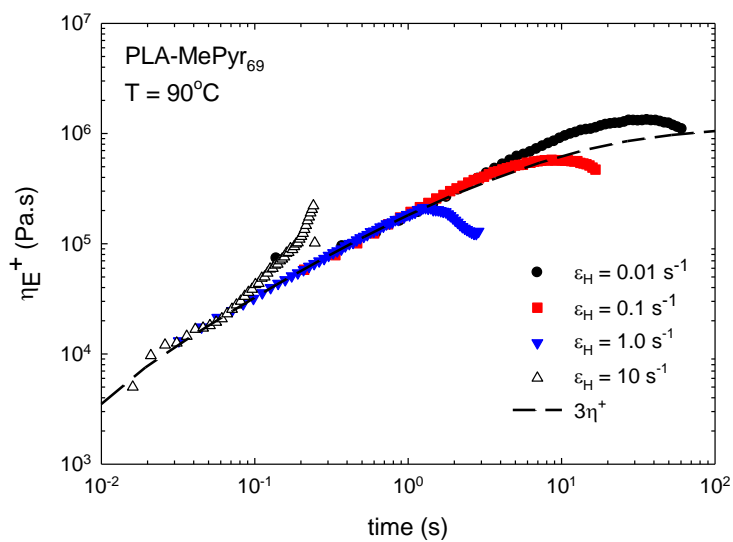

Figure D.7 Tensile stress growth coefficient (measure of elongational viscosity) as a function of time at Hencky strain rate of 0.01 to 10 s^{-1} at 90 °C for Nap-PLA$_{65}$

Figure D.8 Tensile stress growth coefficient (measure of elongational viscosity) as a function of time at Hencky strain rate of 0.01 to 10 s^{-1} at 90 °C for MeAnth-PLA$_{63}$

Figure D.9 Tensile stress growth coefficient (measure of elongational viscosity) as a function of time at Hencky strain rate of 0.01 to 10 s^{-1} at 90 °C for MePyr-PLA$_{62}$.
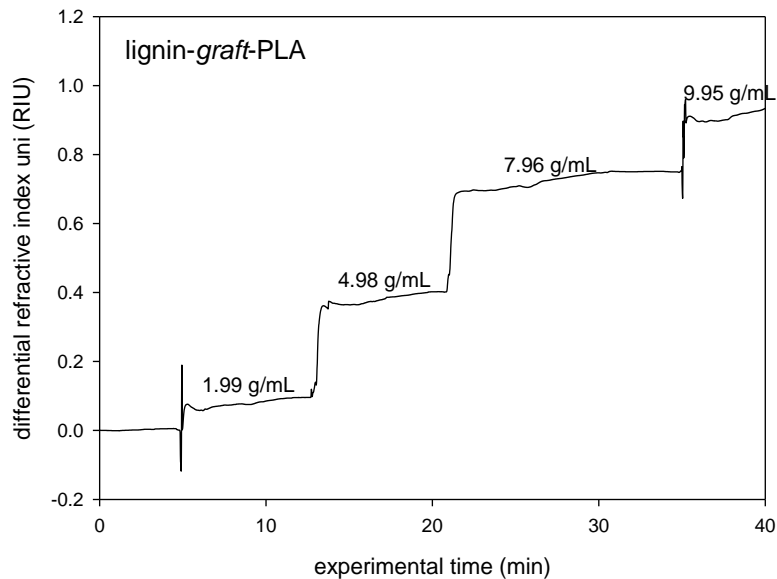
Appendix E

E.1 Calculation of dn/dc values

Figure E. 1 GPC-RI traces for THF solutions of a lignin-*graft*-PLA copolymer (arm length = 17 kg mol^{-1}).
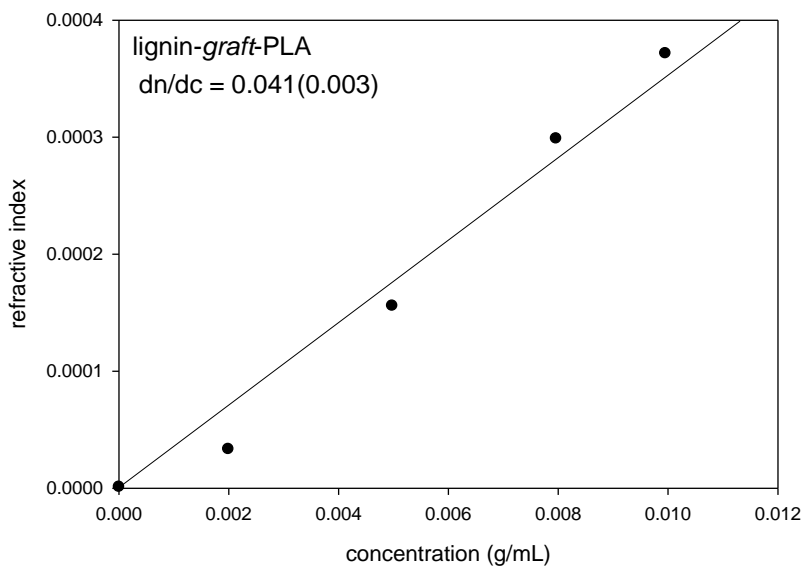

Figure E. 2 Plot of refractive index vs. concentration for THF solutions of a lignin-*graft*-PLA copolymer (arm length = 17 kg mol^{-1}).
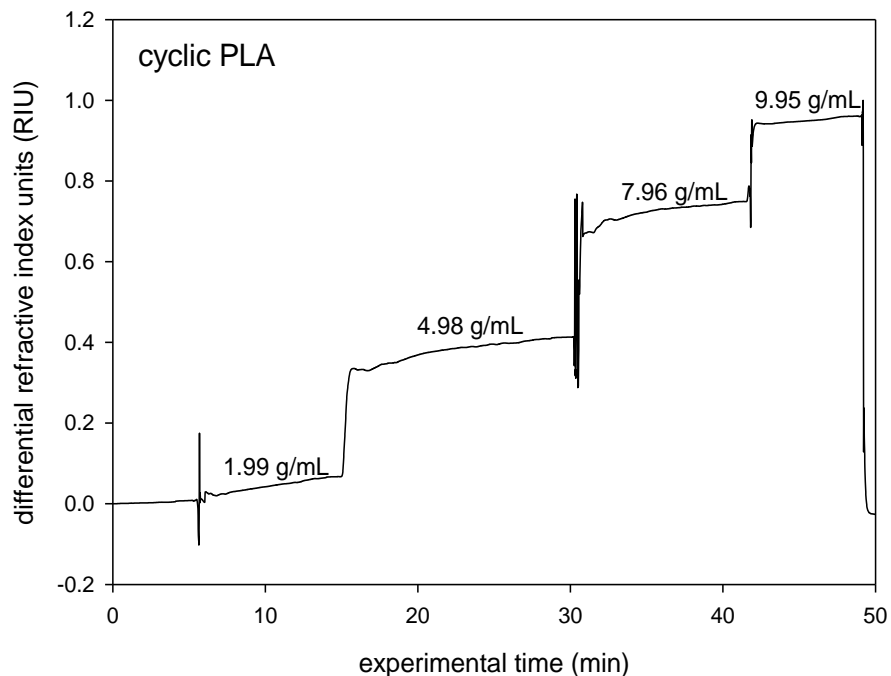
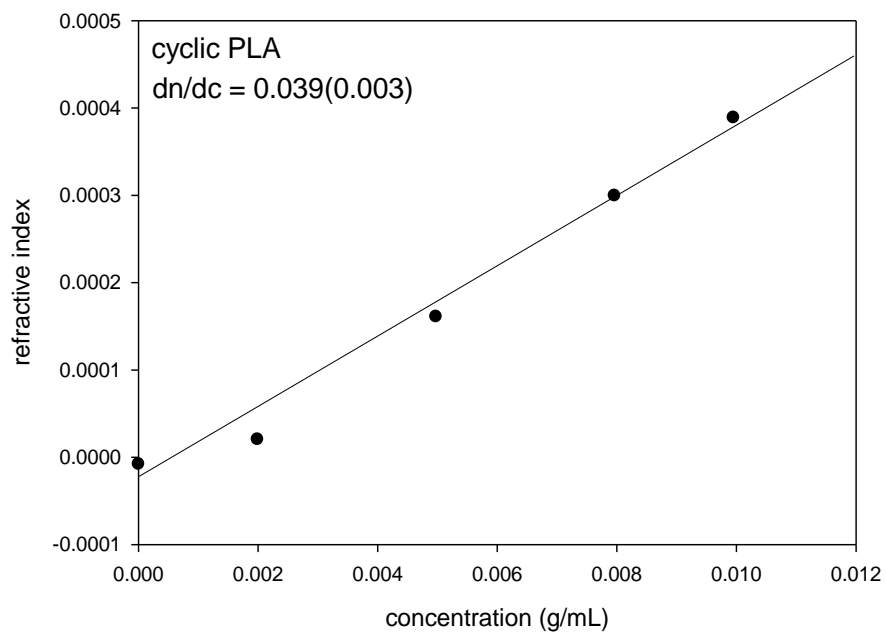**Figure E. 3** GPC-RI traces for THF solutions of a cyclic PLA (M_n = 61 kg mol^{-1}).

Figure E. 4 Plot of refractive index vs. concentration for THF solutions of a cyclic PLA (M_n = 61 kg mol^{-1}).

299